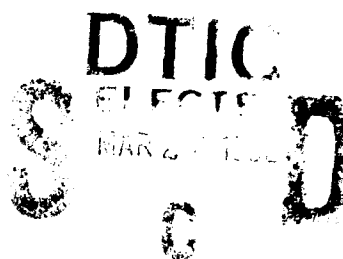


AD-A247 848



2

**FINAL REPORT**

**submitted to Office of Naval Research**

**MECHANICS OF THIN FILMS**

**ONR Grant N - 00014-87-K-0488**

**P.I. Professor John Lambropoulos**

**Department of Mechanical Engineering  
University of Rochester**



**92-05496**

**92 3 02 187**



REPORT DOCUMENTATION PAGE			Form Approved OMB No. 0704-0188	
<small>Public reporting burden for this collection of information is estimated to average 1 hour per response, including the time for reviewing instructions, searching existing data sources, gathering and maintaining the data needed, and completing and reviewing the collection of information. Send comments regarding this burden estimate or any other aspect of this collection of information, including suggestions for reducing this burden, to Washington Headquarters Services, Directorate for Information Operations and Reports, 1215 Jefferson Davis Highway, Suite 1204, Arlington, VA 22202-4302, and to the Office of Management and Budget, Paperwork Reduction Project (0704-0188), Washington, DC 20503.</small>				
1. AGENCY USE ONLY (Leave blank)	2. REPORT DATE 2/6/92	3. REPORT TYPE AND DATES COVERED Final report; 7/1/87-6/30/91		
4. TITLE AND SUBTITLE Mechanics of thin films: Elastic stresses, stress relaxation, and thermal effects		5. FUNDING NUMBERS Grant N-00014-87-K-0488		
6. AUTHOR(S) Professor J. C. Lambropoulos				
7. PERFORMING ORGANIZATION NAME(S) AND ADDRESS(ES) University of Rochester River Campus Rochester, NY 14627		8. PERFORMING ORGANIZATION REPORT NUMBER 5-28827		
9. SPONSORING/MONITORING AGENCY NAME(S) AND ADDRESS(ES) Office of Naval Research (ONR) Arlington, Virginia 22217-5000		10. SPONSORING/MONITORING AGENCY REPORT NUMBER		
11. SUPPLEMENTARY NOTES				
12a. DISTRIBUTION/AVAILABILITY STATEMENT		12b. DISTRIBUTION CODE		
13. ABSTRACT (Maximum 200 words) Problems in the mechanics and thermomechanics of thin films have been addressed. (1) Anisotropic stresses in films of cubic anisotropy oriented along the <100>, <111>, or <110> normals on a substrate; (2) Relaxation in thin films by time-independent plastic deformation along the film/substrate interface, by cracking, or by stress-induced diffusional flow during film growth. The toughening effect on brittle components of thin films in residual compression has been calculated and compared to experimental data. (3) Motivated by measurements (using the thermal comparator technique) of thin film thermal conductivity where the film conductivity was found to be up to two orders of magnitude lower than that of the corresponding solid, the thermal conductivity of thin dielectric films has been correlated to microstructural features such as grain size and film thickness. The implications of reduced film thermal conductivity were examined for laser damage where nonlinear effects were shown to be important. The effects of film anisotropy and interfacial thermal resistance have been analyzed and the contribution of microporosity to interfacial thermal resistance has been calculated. For thermally anisotropic films an equivalent isotropic film of properly chosen thickness and conductivity could be identified. Length scales have been established against which the film thickness is to be compared.				
14. SUBJECT TERMS thin films, anisotropy, diffusional flow, film growth, toughening, thin film thermal conductivity, laser damage, interfacial thermal resistance, thin film microstructure		15. NUMBER OF PAGES 56 + 9 Appendices		
		16. PRICE CODE		
17. SECURITY CLASSIFICATION OF REPORT Unclassified	18. SECURITY CLASSIFICATION OF THIS PAGE Unclassified	19. SECURITY CLASSIFICATION OF ABSTRACT Unclassified	20. LIMITATION OF ABSTRACT SAR	



# FINAL REPORT

submitted to Office of Naval Research

## MECHANICS OF THIN FILMS

ONR Grant N - 00014-87-K-0488

P.I. Professor John Lambropoulos

Department of Mechanical Engineering  
University of Rochester



Statement A per telecon Dr. Roshoy Barsoun  
ONR/Code 1132  
Arlington, VA 22217-5000  
NWW 3/23/82

Accession For	
NOT GENERAL	<input checked="" type="checkbox"/>
DTIC TAB	<input type="checkbox"/>
Unannounced	<input type="checkbox"/>
Justification	
By	
Distribution/	
Availability Codes	
Dist	Avail and/or Special
A-1	



## TABLE OF CONTENTS

Introduction		page 1
1.	ANISOTROPIC ELASTIC STRESSES IN FILMS	
1.1	Constitutive law	3
	A. Films with normal along $\langle 001 \rangle$	5
	B. Films with normal along $\langle 111 \rangle$	6
	C. Films with normal along $\langle 011 \rangle$	7
1.2	Anisotropic stresses	8
2.	STRESS RELAXATION	
2.1	Plastic deformation along the interface	9
2.2	Diffusional creep during film growth	12
2.3	Cracking of thin films	15
3.	THERMOMECHANICS OF THIN FILMS	17
3.1	Thermal conductivity of thin films	19
3.2	Film thermal anisotropy and interfacial thermal resistance	22
	3.2.1 Temperature distribution	25
	3.2.2 Limiting cases	36
3.3	Microstructural effects in film thermal conductivity	38
3.4	Laser damage in thin films	
	3.4.1 Implications of low film thermal conductivity	44
	3.4.2 Nonlinear effects in laser damage	46
3.5	Microstructural effects in interfacial thermal resistance	50
	REFERENCES	55

APPENDIX (1): J. C. Lambropoulos and S.-M. Wan, Stresses in anisotropic thin films bonded to stiff substrates, *Electronic Packaging Materials Science III*, ed. R.C. Sundahl et al., Mat. Res. Soc. Symp. Proc., vol. 108, 399 (1988).

APPENDIX (2): J. C. Lambropoulos and S.-M. Wan, Stress concentration along



interfaces of elastic-plastic thin films, *Mat. Sci. & Engin.*, A107, 169 (1989).

APPENDIX (3): J.C.M. Li, P.D. Funkenbusch, and J. C. Lambropoulos, Microstructural control through strategic materials processing, in *Ashby Symposium: The Modelling of Material Behavior and Its Relation to Design*, ed. J.D. Embury and A.W. Thompson, The Minerals, Metals & Materials Society (TMS), pp. 149-173 (1990).

APPENDIX (4): J. C. Lambropoulos, Thermomechanics of thin films and interfaces, *J. Electronic Materials*, 19, 895 (1990).

APPENDIX (5): J. C. Lambropoulos, Analysis of thermal stress, fracture strength, and the effect of ion exchange on high average power phosphate glass slab lasers, *J. Appl. Phys.*, 67, 1784 (1990).

APPENDIX (6): J. C. Lambropoulos, Toughening and crack tip shielding in brittle materials by residually stressed thin films, *J. Vac. Sci. & Technol.*, A9, 2503 (1991).

APPENDIX (7): J. C. Lambropoulos, M.R. Jolly, C.A. Amsden, M. Sinicropi, D. Diakomihalis, and S.D. Jacobs, The thermal conductivity of thin dielectric films, *J. Appl. Phys.*, 66, 4230 (1989).

APPENDIX (8): J. C. Lambropoulos and S.-S. Hwang, Implications of low film thermal conductivity for the laser damage resistance of optical thin films, *Electro-Optics and Nonlinear Optics*, ed. K.M. Nair, A. S. Bhalla, and E.M. Vogel, *Ceramic Transactions*, 14, 219-227 (1990).

APPENDIX (9): J.C. Lambropoulos, S.D. Jacobs, S.J. Burns, L. Shaw-Klein, and S.-S. Hwang, Thermal conductivity of thin films: measurement and microstructural effects, in *Thin-film heat transfer, properties and processing*, ed. M.K. Alam, M.I. Flik, G.P. Grigoropoulos, J.A.C. Humphrey, R.L. Mahajan, and V. Prasad, *American Society of Mechanical Engineers HTD-Vol. 184*, pp. 21-32 (1991).



## INTRODUCTION

Many technological areas currently use designs that rely on thin films for a variety of effects that include mechanical, thermal, electrical, optical and magnetic properties. As typical examples we mention microelectronics, optical coatings and multilayers for use in optical arrays or solid-state lasers, optical-magnetic recording and storage devices. It is becoming increasingly clear that such thin films are exposed to a variety of loadings which may be mechanical (for example coatings for tribological applications), chemical (for example anti-corrosion coatings), thermal (for example the dissipation of heat in microelectronic chip and package designs), electrical or magnetic (such as the failure of superconducting thin films at a critical value of the magnetic field). Furthermore, there often is observed a strong coupling between such loads, as for example the interplay between mechanical properties (elastic moduli), thermal properties (thermal conductivity, thermal expansion coefficient), and optical properties (absorption) in determining the laser damage resistance of thin films.

This report discusses work in three areas concerning thin films: The first area is the determination of anisotropic elastic stresses in thin films, where the primary area of application would be epitaxial films. In this work, the film thickness enters only as a geometrical parameter which otherwise does not affect the mechanical response of the film.

The second area discusses stress relaxation in thin films by plastic deformation along the film/substrate interface due to thermomechanical loading, by diffusional creep during film growth, or by cracking. The interesting point to be made is that diffusional creep introduces a length scale to which the film thickness is to be compared. This length scale, therefore, can be used to determine whether or not the film is "thin". Interestingly, this length scale depends both on film material properties as well as growth or processing properties.

The third area discusses the thermomechanical properties of thin films, and specifically addresses the issue of the thermal conductivity and interfacial thermal resistance in thin films. The work consists of an experimental part, an analytical part, and a computational part (finite elements). It is shown that thermomechanical properties of thin films may be considerably different from those of the corresponding bulk solids, and this discrepancy is resolved by



considering microstructural contributions in thin film thermal conductivity. Again, a length scale is found against which the film thickness must be compared in order to determine whether or not the film is "thin".

The report consists of two parts, a main part and a set of Appendices containing the work published in refereed journals or books. When work is described that has been already published, only the main assumptions and results are contained in the main part of the report, and the reader is referred to the enclosed Appendices for further details or for further bibliographical references. When the described work has not yet been published, the main report contains the formulation of the problem, the analysis, and the relevant results and references.



# 1. ANISOTROPIC ELASTIC STRESSES IN FILMS

The objective is to determine the effect of elastic anisotropy on the stress levels in thin films. A primary area of application would be epitaxial thin films. The two areas of particular interest are near the film's free edge and far from the free edges where the film is uniformly stressed. For the calculation of the stresses, we first find the constitutive law that applies to a specific orientation of the film with respect to the substrate, and we then use the constitutive law for the numerical calculation of the stresses.

## 1.1 CONSTITUTIVE LAW

Consider a thin film made of a material with cubic anisotropy. The elastic response of such a material is characterized by the elastic coefficients  $C_{11}$ ,  $C_{12}$ ,  $C_{44}$  so that in the crystallographic axes the stress strain relation is

$$\sigma_{11} = C_{11} \epsilon_{11} + C_{12} (\epsilon_{22} + \epsilon_{33}) \text{ etc.}, \quad \sigma_{12} = 2 C_{44} \epsilon_{12} \text{ etc.} \quad (1.1)$$

It is convenient to define an equivalent Poisson ratio  $\nu$ , and the anisotropic constants  $A$  and  $H$  via

$$\nu = \frac{C_{12}}{C_{11} + C_{12}} \quad A = \frac{2 C_{44}}{C_{11} - C_{12}} \quad H = 2 C_{44} - C_{11} + C_{12} \quad (1.2)$$

For an isotropic material  $H=0$  and  $A=1$ . The anisotropic parameters  $H$  and  $A$  are related by

$$H = C \frac{(A-1)(1-\nu)}{1+\nu} \quad C \equiv C_{11} + C_{12} - 2 \frac{C_{12}^2}{C_{11}} \quad (1.3)$$

The constant  $C$  reduces to  $E/(1-\nu)$  for isotropic materials. For typical semiconductors and metals  $A$  lies between 1 and 4, and the equivalent Poisson ratio  $\nu$  lies between 0.2 and 0.45.



Common orientations of thin anisotropic films deposited on substrates are along the  $\langle 100 \rangle$ ,  $\langle 110 \rangle$  or  $\langle 111 \rangle$  directions. For the stress analysis of such films, the stress-strain law must be converted from the crystallographic axes to axes appropriate for the orientation of the film/substrate.

Consider a cylindrical coordinate system where the  $z$  axis coincides with the film normal  $n$ , and the  $r, \theta$  directions lie in the film plane. It is convenient to evaluate the elastic constants that relate the stresses and strains in the cylindrical coordinate system  $r, \theta$ , and  $n \equiv z$ . The elastic stress-strain law relates the stress vector  $[\sigma]$  to the strain vector  $[\epsilon]$  as

$$[\sigma] = [C] [\epsilon] \quad (1.4-a)$$

$$[\sigma] = [\sigma_{rr} \ \sigma_{\theta\theta} \ \sigma_{zz} \ \sigma_{rz} \ \sigma_{\theta z} \ \sigma_{\theta r}] \quad [\epsilon] = [\epsilon_{rr} \ \epsilon_{\theta\theta} \ \epsilon_{zz} \ \gamma_{rz} \ \gamma_{\theta z} \ \gamma_{\theta r}] \quad (1.4-b)$$

The results below summarize the form of the  $6 \times 6$  matrix  $[C]$  appropriate for three commonly used film orientations.



# A. FILMS WITH NORMAL ALONG <001>

For [001] films, we denote by  $\theta$  the angle measured from [100] in the film plane. Due to symmetry, we only examine the range  $0 < \theta < \pi/4$ . The matrix [C] is given by

$$[C] = \begin{bmatrix} C'_{11} & C'_{12} & C_{12} & 0 & 0 & C'_{16} \\ & C'_{11} & C_{12} & 0 & 0 & -C'_{16} \\ & & C_{11} & 0 & 0 & 0 \\ & & & C_{44} & 0 & 0 \\ & \text{symm.} & & & C_{44} & 0 \\ & & & & & C'_{44} \end{bmatrix} \quad (1.5a)$$

$$\begin{aligned} C'_{11} &= C_{11} + \frac{H}{4}(1 - \cos 4\theta), & C'_{12} &= C_{12} - \frac{H}{4}(1 - \cos 4\theta) \\ C'_{44} &= C_{44} - \frac{H}{4}(1 - \cos 4\theta), & C'_{16} &= \frac{H}{4} \sin 4\theta \end{aligned} \quad (1.5b)$$



## B. FILMS WITH NORMAL ALONG $\langle 111 \rangle$

For  $[111]$  films,  $\theta$  measures the angle in the film plane from the projection of  $[110]$  onto that plane. Due to symmetry  $0 < \theta < \pi/3$ . The result is

$$[C] = \begin{bmatrix} C'_{11} & C'_{12} & C''_{12} & H_c & -H_s & 0 \\ & C'_{11} & C''_{12} & -H_c & H_s & 0 \\ & & C'_{33} & 0 & 0 & 0 \\ & & & C'_{13} & 0 & -H_s \\ & \text{symm.} & & & C'_{13} & -H_c \\ & & & & & C''_{13} \end{bmatrix} \quad (1.6a)$$

$$\begin{aligned} C'_{11} &= C_{11} + \frac{H}{2}, & C'_{12} &= C_{12} - \frac{H}{6}, & C''_{12} &= C_{12} - \frac{H}{3} \\ C'_{33} &= C_{11} + \frac{2H}{3}, & C'_{13} &= C_{44} - \frac{H}{3}, & C''_{13} &= C_{44} - \frac{H}{6} \end{aligned} \quad (1.6b)$$

$$H_c = \frac{H\sqrt{2}}{6} \cos 3\theta, \quad H_s = \frac{H\sqrt{2}}{6} \sin 3\theta$$



### C. FILMS WITH NORMAL ALONG $\langle 011 \rangle$

For films with normal along  $[011]$ ,  $\theta$  denotes the angle from  $[100]$  in the film plane. Now, due to symmetry the region of interest is  $0 < \theta < \pi/2$ . The result is

$$[C] = \begin{bmatrix} C'_{11} & C'_{12} & C'_{13} & 0 & 0 & C'_{16} \\ & C''_{11} & C''_{13} & & 0 & C''_{16} \\ & & C'_{33} & 0 & 0 & C'_{36} \\ & & & C'_{44} & C'_{45} & 0 \\ & \text{symm.} & & & C''_{44} & 0 \\ & & & & & C'''_{44} \end{bmatrix} \quad (1.7a)$$

$$\begin{aligned} C'_{11} &= C_{11} - \frac{H}{16} (-7 + 4 \cos 2\theta + 3 \cos 4\theta), & C''_{11} &= C_{11} - \frac{H}{16} (-7 - 4 \cos 2\theta + 3 \cos 4\theta) \\ C'_{12} &= C_{12} - \frac{3H}{16} (1 - \cos 4\theta), & C'_{13} &= C_{12} - \frac{H}{4} (1 - \cos 2\theta) \\ C''_{13} &= C_{12} - \frac{H}{4} (1 + \cos 2\theta), & C'_{33} &= C_{11} + \frac{H}{2}, & C'_{36} &= -\frac{H}{4} \sin 2\theta \\ C'_{16} &= \frac{H}{8} \sin 2\theta (1 + 3 \cos 2\theta), & C''_{16} &= \frac{H}{8} \sin 2\theta (1 - 3 \cos 2\theta) \\ C'_{44} &= C_{44} - \frac{H}{4} (1 - \cos 2\theta), & C''_{44} &= C_{44} - \frac{H}{4} (1 + \cos 2\theta) \\ C'''_{44} &= C_{44} - \frac{3H}{16} (1 - \cos 4\theta), & C'_{45} &= -\frac{H}{4} \sin 2\theta \end{aligned} \quad (1.7b)$$



## 1.2 ANISOTROPIC STRESSES

The stresses have been calculated numerically by using finite elements for the case when far from the free edges the film is in a state of residual balanced biaxial tensile or compressive strain. Such a state of strain arises either due to the thermal mismatch between the film and the substrate, or due to the film deposition process. To reduce the numerical complexity of the problem, conditions of plane strain were imposed so that the three-dimensional constitutive law of eqns (1.5)–(1.7) could be further reduced to two-dimensional. For the cases  $n=[001]$ ,  $[111]$  and  $[011]$  the plane strain conditions were imposed along the directions  $[010]$ ,  $[1 -2 1]$  and  $[100]$ , respectively. The details of the calculation and references can be found in Appendix 1.

The main conclusions are as follows for the case of a film supported on a much stiffer substrate:

The main effect of elastic anisotropy (i.e. the deviation of the anisotropic parameter from unity) is to increase the stresses both in the vicinity of the free edge of the film, as well as in the part of the film which is uniformly stressed, i.e. far from the free edges. The extent of the interface which is subjected to large shear stresses increases considerably as  $A$  increases, especially for the cases of  $n=[111]$  and  $n=[011]$ .

The stresses for  $n=[111]$  or  $[011]$  were very similar for the same level of anisotropy. These stress levels have a strong dependence on the anisotropic parameter  $A$ . For  $n=[001]$  the stresses are lower, and have a weaker dependence on the anisotropic factor  $A$ .



## 2. STRESS RELAXATION

The objective in this part of the work was to examine several mechanisms which may lead to stress relaxation in thin films, since the stresses calculated previously in Part 1 do not account for any relaxation.

Stress relaxation can occur three ways: By time-independent elastic-plastic deformation, or by time-dependent creep which may occur by dislocation climb-and-glide or by stress-driven mass diffusion, or by cracking of the film.

### 2.1 PLASTIC DEFORMATION ALONG THE INTERFACE

We assume that the film is elastic-plastic, and that far from the free edges it is in a uniform state of stress corresponding to a differential thermal mismatch between the film and the substrate. We are primarily concerned with the case when far from the free edges the stress is in the elastic region, whereas the stress concentration near the free edges leads to a concentrated zone of intense plastic deformation.

The film material is modeled as elastic-plastic, with the constitutive law in simple shear

$$\frac{\epsilon_{12}}{\epsilon_0} = \begin{cases} \frac{\tau}{\tau_0} & \text{if } |\tau| < |\tau_0| \\ \left(\frac{\tau}{\tau_0}\right)^n & \text{if } |\tau| \geq |\tau_0| \end{cases} \quad (2.1)$$

where  $\tau_0$  is the yield stress in simple shear, and  $\epsilon_0 = \tau_0/2G$  is the yield strain in simple shear,  $G$  being the shear modulus. the hardening exponent  $n$  ranges from 1 (for linear elastic material) to  $\infty$  (for elastic, perfectly plastic material).

For multiaxial states of stress, the strain  $\epsilon_{ij}$  is given by



$$\epsilon_{ij} = \epsilon_{ij}^e + \epsilon_{ij}^p + \epsilon_{ij}^T \quad (2.2)$$

where the elastic strain  $\epsilon_{ij}^e$  is related to the stress  $\sigma_{ij}$  via the usual linear elastic constitutive response, the plastic strain  $\epsilon_{ij}^p$  is related to the deviatoric stress tensor  $s_{ij} = \sigma_{ij} - \sigma_{kk} \delta_{ij} / 3$  by  $J_2$  deformation theory thus

$$\epsilon_{ij}^p = f s_{ij}, \quad f = \frac{\left(\frac{\bar{\epsilon}}{\epsilon_0}\right)^{1-\frac{1}{n}} - 1}{2 G} \quad (2.3)$$

where the equivalent shear strain  $\bar{\epsilon}$  is defined via the strain deviator

$$\bar{\epsilon} = \sqrt{\frac{e_{ij} e_{ij}}{2}} \quad e_{ij} \equiv \epsilon_{ij} - \frac{\epsilon_{kk}}{3} \delta_{ij} \quad (2.4)$$

Under these circumstances, the equivalent shear stress  $\tau \equiv (s_{ij} s_{ij} / 2)^{1/2}$  is also related to the equivalent shear strain  $\bar{\epsilon}$  by eqn (2.1).

The last term in eqn (2.2) is the misfit strain, which consists of only a volumetric component

$$\epsilon_{ij}^T = \epsilon^T \delta_{ij} \quad (2.5)$$

Thus, thermal mismatch strain can be represented by  $\epsilon^T$ , which can also represent misfit strain due to the film deposition process.

The non-dimensional loading parameter was taken to be the ratio of misfit to yield strain,

$$\theta \equiv \frac{\epsilon^T}{\epsilon_0} \quad (2.6)$$



The far-field film material will first become plastic when  $\theta=0.93$  for a Poisson ratio of 0.3.

The details of the calculations can be found in Appendices 2 and 3. The main results are as follows for the case of a film bonded to a stiff substrate:

For  $\theta < 0.93$ , the plastic deformation is localized near the free edge. The plastic zone is localized within a thin strip near the free edge and along the film/substrate interface. The length  $D$  and height  $H$  of the plastic zone are not very sensitive to the hardening exponent  $n$ , but depend strongly on the loading parameter  $\theta$ . Thus, linear elastic stress distributions may be used to approximate the extent of the plastic zone. When  $\theta=0.93$  the plastic zone extends through the whole film. This continuum estimate of the extent of plastic deformation agrees quantitatively with the fact that interfacial dislocations relieve the high stresses near the free edge by propagating along the film/substrate interface.

The stress concentration in thick films (where the areal extent of the film is comparable to the film thickness, thus modeling the island mode of film growth) is lower than in thin films. The difference in stresses between thick and thin films is largest for linear elastic materials, and it diminishes considerably as the amount of hardening diminishes.

It was found that even for small amounts of hardening the stresses along the film interface near the film's free edge can considerably exceed the yield stress of the material. For example, for  $n=30$ , within a distance of 10% of the film thickness, the shear stress along the interface is comparable to the yield stress whereas the peeling normal stress may be several times higher than the yield stress.

The calculated stresses can be also used for the case of film growth where stress relaxation along the interface occurs during film growth rather than post-processing. The observation that allows this extension is that the yield stress  $\tau_0$  of thin films is a diminishing function of the film thickness. Thus, plastic deformation is suppressed in very thin films which are expected to fail in a brittle manner. As growth continues, plasticity is enhanced and the loading parameter is thus an increasing function of the film thickness.



## 2.2 DIFFUSIONAL CREEP DURING FILM GROWTH

The structure of deposited films depends on parameters such as incident flux, film atom adsorption, density of surface nucleation sites, and adatom surface mobility. The resulting microstructure consists of small grains, which are often columnar and extend through the film thickness (Thornton, 1974, 1977; Movchan and Demchishin, 1969; Messier, 1986). The small grain size of thin films implies that inelastic stress relaxation mechanisms which are observed in bulk materials at high temperatures may be actually operative in thin films at lower temperatures. Thus, stress-driven diffusional flow in films is enhanced.

To examine the effect of microstructure and growth parameters on diffusional flow during the growth of a thin film, we first observe that the total strain vanishes for a thin film deposited onto a thick substrate due to the geometrical constraint of the substrate. Thus,

$$\epsilon^e + \epsilon^T + \epsilon^{cp} = 0 \quad (2.7)$$

where the first term is the elastic strain related to the biaxial film stress  $\sigma$  by  $\epsilon^e = (1-\nu)\sigma/E$  via the film Poisson ratio  $\nu$  and Young's modulus  $E$ , the second term  $\epsilon^T$  is the misfit strain which creates the stress in the film and is assumed to be independent of the film thickness, and the third term is the creep strain which may be due to grain-boundary diffusion (or, Coble creep, dominating at lower temperatures and higher grain sizes) or bulk diffusion (Nabarro-Herring creep, dominating at higher temperatures).

For a point in the film at a fixed distance  $x_2$  above the film/substrate interface no creep relaxation can occur if the film thickness  $h$  is less than  $x_2$ . Thus, points near the interface have undergone larger amounts of relaxation as compared to points closer to the growing film surface for two reasons: Points near the interface are exposed to diffusional flow for longer periods of time, and they have experienced creep at lower grain size. The total creep strain is thus found by



$$\epsilon^{cp} = \int_{x_2/p_0}^t \dot{\epsilon}^{cp} dt \quad (2.8)$$

The creep strain rate is given by

$$\begin{aligned} \dot{\epsilon}^{cp} &= \frac{B_s (D_b \delta)}{h^2 d} \frac{\sigma}{\sigma_0}, \quad \text{grain-boundary diffusion} \\ \dot{\epsilon}^{cp} &= \frac{B_s D_v}{h d} \frac{\sigma}{\sigma_0}, \quad \text{bulk diffusion} \\ \sigma_0 &\equiv \frac{kT}{\Omega} \end{aligned} \quad (2.9)$$

where  $h$  is the film thickness,  $d$  is the width of the columnar grains, and  $\Omega$  is the atomic volume. The current film thickness  $h_0$  increases in proportion to the film growth rate  $p_0$ , so that  $h_0 = p_0 t$ . The constants  $B_s$  and  $B_v$  are approximately equal to 10, and  $D_b \delta$  (units of  $m^3/s$ ),  $D_v$  (units of  $m^2/s$ ) are the temperature-dependent diffusivities for grain-boundary and bulk diffusion, respectively.

Eqn (2.7) leads to a differential equation for the rate at which the stress  $\sigma$  in the film evolves with time. The details of the calculation can be found in Appendix 4. The main result is that the elastic and misfit strains are of the same order of magnitude, and that the creep strain rate via grain-boundary diffusion is proportional to the non-dimensional number  $N$  defined by

$$N = \frac{E}{\sigma_0} \frac{B_s (D_b \delta)}{h_0 d p_0} = \frac{\mathfrak{L}}{h_0}, \quad \mathfrak{L} \equiv \frac{E}{\sigma_0} \frac{B_s (D_b \delta)}{d p_0} \quad (2.10)$$

where  $\mathfrak{L}$  is a length scale which depends on material properties and on the growth parameters  $d$  and  $p_0$ . When  $N > 1$  (or, equivalently, the film thickness  $h_0$  is less than the length scale  $\mathfrak{L}$ ) the effect of grain boundary diffusion is important in relaxing the stresses induced by the misfit strain  $\epsilon^T$ .



To estimate the length scale  $\ell$ , typical values were used for the film growth rate  $p_0$  (from 0.1 to 10 nm/s) and the grain width  $d$  (from 20 to 500 nm). Using these typical values, the range of the length scale  $\ell$  (from  $\ell_{\min}$  to  $\ell_{\max}$ ) was found so that grain-boundary relaxation becomes important when the film thickness is less than  $\ell$ . The results for many FCC and HCP metallic films are summarized in Appendix 4. As an example, for Ni films grown at 500 °K, the range for  $\ell$  is from 2 nm to 5  $\mu\text{m}$ . Clearly, therefore, the growth parameters can be chosen so as to minimize or maximize the effect of creep strain rate for a given film thickness in the micron or submicron range.

Another consequence of this analysis is that grain-boundary diffusion is most important for thin films, or in the early stages of film growth when the film thickness is low. As a result, the stress in the film is low near the film/substrate interface and high near the film's free surface, so that the average stress in the film (which is often measured by monitoring the radius of curvature of the supporting substrate) is a diminishing function of the film thickness.



## 2.3 CRACKING OF THIN FILMS

Recent experiments have shown that the mechanical strength of nominally brittle components can be greatly enhanced by thin films which are in a state of residual compression. Several such experiments have been summarized in Appendices 5 and 6 where references can also be found.

The films need not be distinct from the substrate itself. As an alternative example, ion-exchange in glass components can be used to significantly improve the strength of glass. For example, three different fracture experiments had been conducted at the University of Rochester on phosphate glasses whose mechanical strength was improved by ion-exchange. The first geometry involved small disks (diameter of 20 mm, thickness of 3 mm), and the second geometry was that of squat cylinders (diameter 6.4 mm, height 6.4 mm). These two geometries were tested in thermal shock tests, and a finite element analysis was performed in order to correlate the temperature drop at fracture to the magnitude of the resulting thermal stresses. For the unstrengthened specimens, the fracture strength was thus estimated to be about 25 MPa, whereas for the strengthened specimens it was about 135 MPa.

The third geometry was that of rectangular slabs ( $8 \times 15 \times 160 \text{ mm}^3$ ) which were thermally pumped to failure. Appendix 5 contains the details of the stress calculations. A finite element analysis again correlated the thermal power input to the resulting thermal stresses under steady-state thermal pumping. It was found that the unstrengthened specimens had a fracture strength of 19–23 MPa, whereas after ion-exchange the strength was improved to about 110 MPa. The conclusion from such tests was that ion-exchange can greatly improve the apparent fracture toughness of brittle glass by imparting an average compressive surface stress of approximately 90–110 MPa for phosphate glass. The value of the average compressive stress was correlated to the amount of the average dilation (due to the ion-exchange) which was found to be about 0.0034. Independent measurements of the ion concentration at the surface of the glass and of the thickness of the ion-exchange layer (50–60  $\mu\text{m}$ ) were in good agreement with the analytical predictions.

The idea of strengthening was further examined by examining the shielding imparted to a



surface crack by two individual nearby spots which undergo a volume expansion (Appendix 6). The expanding spots were further arranged in the form of a film perpendicular to the crack plane. It was found that the location of the film with respect to the crack front is an important parameter in determining the shielding due to the film. When the film is ahead of the crack front, it does not provide any shielding; It is only when the crack front traverses the film that a shielding is induced. This clearly shows that only the part of the film that is already cracked contributes to shielding.

This idea was expanded to include crack growth resistance curves by plotting the amount of crack tip shielding  $\Delta K$  vs. the crack length  $a$ . It was found that for two typical film stress distributions (either exponentially decaying from the sample's free surface, as in the case of ion-exchange, or constant over the film thickness, as in the case of physically distinct films)  $\Delta K$  reaches a maximum when the crack length is equal to the length scale characterizing the film stress distribution, and slowly decays for greater crack sizes. Thus, the maximum shielding effect is imparted when the crack reaches the interface of the film and the substrate.



### 3. THERMOMECHANICS OF THIN FILMS

In the work described above, it has been assumed that the mechanical properties of thin films are independent of temperature, and that there is no coupling between the thermal and mechanical response of the thin film. However, there are many technological applications where there is a very strong interplay between the thermal and the mechanical properties of the film, so that it is more convenient to think of the thermomechanical properties.

Three primary examples of technological areas where the thermomechanical properties of thin films are of paramount importance are microelectronic circuits (Maldonado, 1990), magneto-optical recording devices (Bartholomeusz, 1989; Evans and Nkansah, 1988; Halley and Midwinter, 1987; Koyanagi et al., 1989), and laser damage in optical films and multilayers (Guenther and McIver, 1988; Lange et al., 1984, 1985; Lowdermilk and Milam, 1981; Walker et al., 1981a, 1981b).

In microelectronic design, the removal of the generated heat due to the power consumed is controlled by the thermal properties of the electronic package which often involve a variety of thin films.

In magneto-optical recording the write process is achieved by the localized heating of the recording medium by a laser beam. The size and spacing of the written bits, and thus the density of information that may be stored, is controlled by the thermal conductivity of the recording medium.

In laser damage of optical films, which is due to the localized absorption of the incident radiation by submicron inhomogeneities embedded within the otherwise non-absorbing film, the damage resistance (the areal energy density at failure, defined as the level of energy at which the inhomogeneity melts) is directly related to the thermal conductivity of the thin film within which the absorbing inclusion is embedded. The energy density at damage for inhomogeneities embedded in infinite matrices (Hopper and Uhlmann, 1970; Lange et al. 1984, 1985) has been found from the work of Goldenberg and Tranter (1952) as



$$E_t \sim T_c \sqrt{\rho c k t_p} \quad (3.1)$$

where  $T_c$  is the melting point of the inclusion,  $\rho$ ,  $c$ ,  $k$  are the density, specific heat, and thermal conductivity of the host material, and  $t_p$  is the laser pulse duration.

Other references of technological interest where the thin film thermal conductivity is important can be found in Appendices 7, 8, and 9.

In this part of the reported work, we describe the experimental technique which was used for the measurement of the thermal conductivity of thin films (Lambropoulos et al., 1989), and the implications of such measurements for laser damage.



### 3.1 THERMAL CONDUCTIVITY OF THIN FILMS

The analysis and measurement of the thermal conductivity of thin dielectric films for optical applications was motivated from the Laboratory for Laser Energetics at the University of Rochester. The measurement is done by using the thermal comparator technique, whereby a heated tip (typically 20 °C above ambient) is brought into contact with the free surface of a thin film deposited onto a substrate. The resulting temperature drop of the tip is directly related to the combined thermal conductivity  $k_{app}$  of the film/substrate assembly which involves contributions from the film itself (thermal conductivity  $k_F$ ), the film/substrate interface (thermal resistance  $R_{int}$ ) and the substrate (thermal conductivity  $k_{sub}$ ). The measurement and the analysis required to extract the thermal conductivity  $k_F$  of the film from the measured  $k_{app}$  is described in great detail in Appendix 7 for isotropic films in which the in-plane and out-of-plane thermal conductivities are equal.

Since the original publication of the work in 1989 many other thin films have been examined, including oxides, nitrides, fluorides, amorphous metals, and superconductors Shaw-Klein et al., 1991; Shaw-Klein, 1992). The main result has been that the thermal conductivity of thin films may be up to two orders of magnitude lower than the conductivity of the corresponding bulk solid. Table 1 shows the ranking of the film thermal conductivity with respect to bulk solids, and Table 2 summarizes the results of the measurement of the thin film thermal conductivity. Further results can be found in Appendix 7.



**TABLE 1: Thermal conductivity of selected bulk and film materials**

<b>Materials</b>	<b><math>k(\text{W/m-K})</math></b>
Diamond (I and II)	1200-2300
Cu (polycrystalline)	200-500
Si (single crystal)	150
$\text{Al}_2\text{O}_3$ (single crystal)	35
$\text{Al}_2\text{O}_3$ (sintered)	20
Many oxides and fluorides, bulk solids	1.0 to 10
Oxide and fluoride films, nominally 1 $\mu\text{m}$ thick	0.05 to 1.0
Air	0.025



**TABLE 2: Measured thermal conductivity of various thin films**

Film	Microstructure	Thickness ( $\mu\text{m}$ )	$k_F$ (W/ m-K)	$k_{\text{bulk}}$ (W/ m-K)
$\text{SiO}_2$	Amorphous	0.50–2.0	0.4–1.1	1.2–10.7
$\text{TiO}_2$	–	0.50–2.0	0.5–0.6	7.4–10.4
$\text{ZrO}_2$	–	0.15–0.47	0.04	
$\text{Al}_2\text{O}_3$	–	0.17–0.46	0.72	20–46
$\text{MgF}_2$	–	0.21–0.58	0.58	15–30
AlN	Dense, polycrystalline	<0.15	0.5	70–180
		0.25–1.0	16	
Tb–Fe compound	dense, amorphous	0.25–1.0	5.3 (  )	30–40
			7.0 ( $\perp$ )	
Tb–Fe compound	columnar, amorphous	0.25–1.0	0.3 (  )	
			4.3 ( $\perp$ )	
$\text{YBa}_2\text{Cu}_3\text{O}_7$	crystalline	0.25–1.0	0.1–0.2	8–10

Notice that (||) denotes the conductivity parallel to the film, and ( $\perp$ ) perpendicular to the film.



### 3.2 FILM THERMAL ANISOTROPY AND INTERFACIAL THERMAL RESISTANCE

An interesting feature of the thermal conductivity of thin films is that it is often anisotropic, so that the conductivity in the plane of the film  $k_{||}$  is different from the thermal conductivity perpendicular to the plane of the film  $k_{\perp}$ . This anisotropy may be due to the anisotropic crystallography of the film itself, or due to the film microstructure that develops during deposition. For example, Shaw-Klein (1992) has recently measured the thermal conductivity of superconducting  $Y_1Ba_2Cu_3O_{7-\delta}$  films. It was found that both  $k_{||}$  and  $k_{\perp}$  were considerably lower than the corresponding bulk single crystal values, and that a significant anisotropy existed in the thin films with  $k_{\perp} \ll k_{||}$ .

Shaw-Klein (1992) has also measured the thermal conductivity of amorphous films of rare-earth transition metals used in magneto-optic recording. The film thickness was in the range 0.25–1  $\mu\text{m}$ , and the substrate was fused silica. When the films were deposited at low pressures, SEM analysis showed that the film microstructure did not exhibit any significant anisotropy, and measurement of the in-plane ( $k_{||}$ ) and out-of-plane ( $k_{\perp}$ ) thermal conductivities showed that the film was approximately isotropic with  $k_{||}/k_{\perp}=0.7$ . At higher deposition pressures, the films exhibited the characteristic columnar microstructure, and a significant anisotropy in the thermal conductivity developed, with  $k_{||}/k_{\perp}$  approximately equal to 0.07.

In the work of Shaw-Klein et al. the in-plane thermal conductivity was determined by measuring the electrical in-plane resistivity and converting to electronic thermal conductivity via the Wiedemann-Franz law. The phonon contribution to the thermal conductivity was estimated and added to the electronic contribution to yield  $k_{||}$ . The thermal conductivity normal to the plane of the film  $k_{\perp}$  was measured with the thermal comparator method. It is thus clear that, depending on the film material, anisotropy, and microstructure, the film's thermal anisotropy may be such that  $k_{||}/k_{\perp} \gg 1$  or  $k_{||}/k_{\perp} \ll 1$ .

Another interesting feature of film thermal conductivity is that a considerable amount of



interfacial thermal resistance may develop between the film and the substrate (Cahill et al. 1989; Swartz, 1987; Swartz and Pohl, 1987, 1989). The existence of an interfacial thermal resistance implies that the temperature is not continuous across the film/substrate interface, and that the amount of temperature discontinuity is linearly related to the power flux per unit area through the interfacial thermal resistance. For example, the measurements of Lambropoulos et al. (Appendix 7) on a wide variety of oxide and fluoride films with thickness in the submicron range may be as large as  $3 \text{ mm}^2 \text{ K/W}$  when deposited on single crystal Si or sapphire substrates.

More recently, Kuo (ongoing work at the University of Rochester, 1991-92, unpublished) has measured the interfacial thermal resistance between thin films of amorphous Si (with thickness from 0.25 to 1.8  $\mu\text{m}$ ) deposited on single crystal Si substrates. Kuo's technique did not involve any contact with the film's free surface, but relied on the local swelling in the surface of the film when a laser beam of known power illuminated the surface. Kuo found that when the Si films were deposited on the as-received Si substrates, the interfacial thermal resistance was approximately  $0.6 \text{ mm}^2 \text{ K/W}$ . When the Si substrate was cleaned with an ion beam before film deposition, the interfacial thermal resistance dropped to about  $0.2 \text{ mm}^2 \text{ K/W}$ . For comparative purposes, we mention that the thermal resistance of a 1- $\mu\text{m}$  thick layer of  $\text{SiO}_2$  (with thermal conductivity of  $10 \text{ W m}^{-1} \text{ K}^{-1}$ ) would be  $0.1 \text{ mm}^2 \text{ K/W}$ . It is thus clear that the interfacial thermal resistance between a film and a substrate may be considerable. There are cases, however, when the interfacial thermal resistance is much lower. For example, the analysis of the data for the rare-earth transition-metal amorphous films studied by Shaw-Klein (1992) showed that the interfacial thermal resistance was several orders of magnitude lower than the values quoted above.

This section of the report discusses the effective thermal conductivity due to an anisotropic film which is bonded to a substrate via an imperfect interface which is characterized by its interfacial thermal resistance. The effective thermal conductivity due to the film and the substrate is determined for a wide range of ratios of (1) film to substrate thermal conductivity, (2) film thickness to heat flow radius, (3) interfacial to substrate thermal resistance, and (4) film thermal anisotropy. For the limiting case of small interfacial thermal resistance, analytical expressions are derived for the dependence of the effective thermal conductivity on these ratios.



It is also shown that for arbitrary amounts of thermal anisotropy in the film, an equivalent thermally isotropic film can be deduced with an equivalent thickness depending on the degree of anisotropy and the actual film thickness, and an equivalent thermally isotropic conductivity which is the geometric mean of the in-plane and out-of plane film thermal conductivities.



### 3.2.1 TEMPERATURE DISTRIBUTION

Consider a film of thickness  $t$  bonded to a semi-infinite substrate as shown in Fig. 1. The film is thermally anisotropic, with thermal conductivity  $k_{\perp}$  normal to the film-substrate interface, and thermal conductivity  $k_{\parallel}$  parallel to the interface. The substrate has the isotropic thermal conductivity  $k_2$ . Under steady-state conditions, the temperature  $T_1(r, z)$  in the film satisfies

$$k_{\parallel} \left( \frac{\partial^2 T_1}{\partial r^2} + \frac{1}{r} \frac{\partial T_1}{\partial r} \right) + k_{\perp} \frac{\partial^2 T_1}{\partial z^2} = 0, \quad 0 \leq r \leq \infty, \quad 0 \leq z \leq t \quad (3.2 a)$$

whereas in the substrate the temperature  $T_2(r, z)$  satisfies

$$k_2 \left( \frac{\partial^2 T_2}{\partial r^2} + \frac{1}{r} \frac{\partial T_2}{\partial r} + \frac{\partial^2 T_2}{\partial z^2} \right) = 0, \quad 0 \leq r \leq \infty, \quad t \leq z \quad (3.2 b)$$

where  $(r, z)$  are cylindrical coordinates, with  $z=0$  at the film's free surface. The boundary conditions along the film-substrate interface are

$$\begin{aligned} k_{\perp} \frac{\partial T_1}{\partial z} &= k_2 \frac{\partial T_2}{\partial z} \quad \forall r, z = t \\ k_2 \frac{\partial T_2}{\partial z} + \frac{T_1 - T_2}{R_{\text{int}}} &= 0 \quad \forall r, z = t \end{aligned} \quad (3.3)$$

where the first of (3.3) expresses the continuity of power flux, and the second approximates the temperature discontinuity at the interface which is proportional to the interfacial thermal resistance  $R_{\text{int}}$ . Notice that if  $R_{\text{int}}=0$ , then the temperature is continuous at the interface. If  $R_{\text{int}} \rightarrow \infty$  then the interface is thermally insulated. In the case of the isotropic film and in the absence of any interfacial thermal resistance, the surface temperature distribution has been calculated by Dryden (1983).

No attempt will be made to predict the value of the interfacial resistance  $R_{\text{int}}$ . For a first principles calculation of  $R_{\text{int}}$  and its dependence on temperature, especially at low temperatures (typically less than 100–200 K), the reader is referred to the work of Cahill et al. (1989), and



Swartz and Pohl (1987, 1989). In the sequel  $R_{int}$  will be treated as a phenomenological parameter describing the film/substrate interface. However, interfacial microstructural effects on  $R_{int}$  will be discussed later on in this report.

At the free surface of the film ( $z=0$ ) it is assumed that there is a prescribed power flux so that

$$k_{\perp} \frac{\partial T_1}{\partial z} = \begin{cases} q(r), & 0 < r < a \\ 0, & a < r \end{cases} \quad z = 0 \quad (3.4)$$

The radius  $a$  over which heat flow occurs is called the thermal contact radius. It is also assumed that  $T_1, T_2 \rightarrow 0$  as  $(r^2+z^2)^{1/2} \rightarrow \infty$ .

The problem is solved by using Hankel transforms of order zero. The transforms of the temperature distributions  $T_1$  and  $T_2$  are then given by

$$\begin{aligned} \bar{T}_1(\lambda, z) &= A(\lambda) \exp(\lambda\beta z) + B(\lambda) \exp(-\lambda\beta z) \\ \bar{T}_2(\lambda, z) &= C(\lambda) \exp(-\lambda z) \end{aligned} \quad (3.5)$$

where the relative thermal anisotropy  $\beta$  is defined as

$$\beta \equiv \sqrt{k_{\parallel} / k_{\perp}} \quad (3.6)$$

In particular, if the power flux distribution  $q(r)$  of eqn (3.4) is

$$q(r) = - \frac{Q}{2 \pi a \sqrt{a^2 - r^2}} \quad (3.7)$$

so that the total power flowing through the area  $\pi a^2$  at  $z=0$  is  $Q$ , then the constants  $A, B, C$  of eqn (3.5) are found by imposing the boundary conditions of eqn (3.3) and (3.4). They are given by



$$\begin{Bmatrix} A(\lambda) \\ B(\lambda) \\ C(\lambda) \end{Bmatrix} = \chi \begin{Bmatrix} -\exp(-2\lambda\beta t) \left( 1 - \frac{\sqrt{k_{||} k_{\perp}}}{k_2} (1 + \lambda k_2 R_{int}) \right) \\ 1 + \frac{\sqrt{k_{||} k_{\perp}}}{k_2} (1 + \lambda k_2 R_{int}) \\ 2 \frac{\sqrt{k_{||} k_{\perp}}}{k_2} \exp(-\lambda(\beta-1)t) \end{Bmatrix} \quad (3.8)$$

$$\chi \equiv \frac{\frac{Q}{2 \sqrt{k_{||} / k_{\perp}}} \pi a \frac{\sin(a\lambda)}{\lambda^2}}{1 + \exp(-2\lambda\beta t) + \frac{\sqrt{k_{||} k_{\perp}}}{k_2} (1 - \exp(-2\lambda\beta t)) (1 + \lambda k_2 R_{int})}$$

The temperature in the film is now found by inverting the Hankel transform, so that

$$T_1(r, z) = \int_0^{\infty} \bar{T}_1(\lambda, z) J_0(\lambda r) \lambda d\lambda \quad (3.9)$$

$J_0$  being the Bessel function of the first kind and of order zero.

The analytical treatment of heat flow, from a circular region of radius  $a$  on the surface of a semi-infinite half-space of uniform conductivity  $k$ , can be found in Carslaw and Jaeger (1959), where the thermal constriction is defined as the ratio of temperature increase to the power flowing through a spot of size  $a$  (see also Dryden, 1983). We define the thermal resistance  $R$  in a slightly different manner, as

$$R = \frac{\Delta T}{Q/A} \quad (3.10)$$

where  $\Delta T$  is the average change in temperature over the area  $A = \pi a^2$  of the circle of radius  $a$  as compared to the temperature of the half-space far from the heated spot, and  $Q$  is the net power passing through  $A$ . The thermal resistance can be calculated if the distribution of power flux  $q(r)$  (power per unit area) is known over  $0 < r < a$ . For the specific power flux  $q(r)$  given by eqn (3.7), which also makes the circle of radius  $a$  isothermal, the thermal resistance for the



homogeneous half-space is

$$R = \frac{\pi}{4} \frac{a}{k} \quad (3.11)$$

For the case of the anisotropic film bonded to the substrate via the imperfect interface characterized by  $R_{int}$ , the thermal resistance is calculated by first finding the average temperature over the circle of radius  $a$  at the film's free surface which is not isothermal anymore. Thus,

$$T_{ave} = \frac{1}{\pi a^2} \int_0^a T_1(r, z=0) 2\pi r dr \quad (3.12)$$

with the temperature  $T_1$  in the film given by eqn (3.9). The thermal resistance is then calculated via

$$R = \frac{T_{ave}}{Q / (\pi a^2)} \quad (3.13)$$

Using eqns (3.8) and (3.9), the thermal resistance is thus found as

$$R = \frac{a}{\sqrt{k_{||} k_{\perp}}} \int_0^{\infty} \frac{J_1(\xi) \sin \xi}{\xi^2} G(\xi, \sqrt{k_{||} k_{\perp}}/k_2, \beta t/a, \rho) d\xi \quad (3.14)$$

$$G(\xi, \kappa, H, \rho) \equiv \frac{1 - \exp(-2\xi H) + \kappa (1 + \exp(-2\xi H)) (1 + \xi \rho)}{1 + \exp(-2\xi H) + \kappa (1 - \exp(-2\xi H)) (1 + \xi \rho)}$$

where we have denoted the non-dimensional interfacial thermal resistance  $\rho$  by

$$\rho = \frac{R_{int} k_2}{a} \quad (3.15)$$

On the other hand, if the half-space were homogeneous with an apparent thermal



conductivity  $k_{app}$ , the thermal resistance would be given by

$$R = \frac{\pi}{4} \frac{a}{k_{app}} \quad (3.16)$$

Equating (3.14) and (3.16) we thus find the apparent thermal conductivity  $k_{app}$  as

$$\frac{1}{k_{app}} = \frac{4}{\pi} \frac{1}{\sqrt{k_{||} k_{\perp}}} \int_0^{\infty} \frac{J_1(\xi) \sin \xi}{\xi^2} G(\xi, \sqrt{k_{||} k_{\perp}}/k_2, \beta t/a, \rho) d\xi \quad (3.17)$$

Eqn (3.17) clearly shows that the original anisotropic film of thickness  $t$  and thermal conductivity  $k_{\perp}$  normal to the film-substrate interface, and thermal conductivity  $k_{||}$  parallel to the interface, is equivalent to an isotropic film with equivalent thickness  $t_{eq}$  and equivalent thermal conductivity  $k_{eq}$  given by

$$t_{eq} = \beta t = \sqrt{\frac{k_{||}}{k_{\perp}}} t, \quad k_{eq} = \sqrt{k_{||} k_{\perp}} \quad (3.18)$$

Thus, the apparent thermal conductivity is given by

$$\begin{aligned} \frac{k_2}{k_{app}} &= \frac{4}{\pi} \frac{1}{\kappa} \int_0^{\infty} \frac{J_1(\xi) \sin \xi}{\xi^2} G(\xi, \kappa, H, \rho) d\xi \\ \kappa &= \frac{k_{eq}}{k_2} = \frac{\sqrt{k_{||} k_{\perp}}}{k_2}, \quad H = \frac{t_{eq}}{a} = \sqrt{\frac{k_{||}}{k_{\perp}}} \frac{t}{a} \end{aligned} \quad (3.19)$$

with the function  $G$  given by eqn. (3.14).

It is the apparent thermal conductivity  $k_{app}$  that the thermal comparator directly measures. Eqn (3.19) shows that the measured  $k_{app}$  depends on the film's thermal properties and thickness, on the substrate thermal conductivity  $k_2$ , on the non-dimensional interfacial



thermal resistance  $\rho$ , and on the heat flow radius  $a$ . The substrate thermal properties, the film thickness  $t$ , and the heat flow radius  $a$  can be independently measured or estimated, so that eqn (3.19) essentially relates the film thermal conductivity  $k_{eq}$  to the measured  $k_{app}$  and to the interfacial thermal resistance  $\rho$  which characterizes the microstructure of the film/substrate interface.

The integral in eqn. (3.19) was computed numerically by using version 1.2 of Mathematica. The results are shown in Figs 2A–E. In these figures, the horizontal axis is the reduced equivalent film thickness  $t_{eq}/a$ , with  $t_{eq}$  related to the actual film thickness  $t$  via eqn (3.19), and the vertical axis is the inverse of the apparent thermal conductivity of the film measured with respect to the conductivity  $k_2$  of the substrate. It is clear from these figures that the ratio  $k_2/k_{app}$  is a strong function of the film thickness  $t$ , of the anisotropy  $k_{||}/k_{\perp}$ , and of the non-dimensional interfacial thermal resistance  $\rho$ . The limiting cases of thin or thick films, and of small or large  $\rho$  will be discussed in the next section, since in these cases the integral of eqn (3.19) can be further simplified.

Figs 2A–E clearly show that as  $t_{eq}/a \rightarrow \infty$ , then  $k_{app} \rightarrow k_{eq} \equiv (k_{||}/k_{\perp})^{1/2}$ . This observation suggests the possibility of measuring a compound thermal conductivity for bulk crystals with orthotropic symmetry. Such examples include  $Y_1Ba_2Cu_3O_{7-\delta}$  bulk superconducting ceramics or crystals of hexagonal symmetry (such as graphite, Zn, or Cd) oriented so that the  $z$  axis of Fig. 1 is parallel to the crystal's  $c$ -axis, and fiber-reinforced solids with the fibers pointing along the  $z$  axis. In these cases, or for very thick coatings, it is seen that both the parallel ( $k_{||}$ ) and perpendicular ( $k_{\perp}$ ) components of thermal conductivity contribute to the resulting heat flow patterns and to the measured apparent thermal conductivity  $k_{app}$ . It is also clear that the effect of the non-dimensional interfacial thermal resistance  $\rho$  is very small when  $t \gg a$ , implying that thick coatings, as expected, are not sensitive to the presence of the interface.

For thin films (say,  $t_{eq}/a \leq 0.1$ ), on the other hand, it is clear that the apparent thermal conductivity  $k_{app}$  is a strong function of the interfacial thermal resistance  $\rho$ . For very thin films ( $t_{eq}/a \leq 0.01$ ),  $k_2/k_{app}$  depends weakly on  $k_{eq}/k_2$  for insulating films ( $k_{eq}/k_2 \leq 0.1$ ) and depends mainly on the non-dimensional thermal resistance  $\rho$ . Also for insulating films, and for



small values of  $\rho$  (say,  $\rho \leq 1$ ),  $k_{app}$  is near the substrate  $k_2$  and the presence of the film leads to a perturbation from  $k_2$ . In this case,  $k_2/k_{app}$  depends weakly on  $\rho$  and changes by not more than a factor of 2 for all film thicknesses as  $\rho$  changes from 0 to 1. However, for large values of  $\rho$ ,  $k_2/k_{app}$  is approximately equal to  $\rho$ , or  $k_{app} = a/R_{int}$ , so that the measured apparent conductivity  $k_{app}$  is dominated by the presence of the interface.

As discussed in the introduction (see also Table 2), thin films are insulating so that Figs 2A and 2B are applicable to such thin films deposited on relatively conducting substrates (for example, at room temperature Si with  $k_2 = 150$  W/m-K, sapphire with  $k_2 = 35$  W/m-K, or MgO with  $k_2 = 35$  W/m-K). For more insulating substrates (for example fused  $\text{SiO}_2$  with  $k_2 = 1.4$  W/m-K at room temperature) Fig. 2C is applicable.

Figs 2A and 2B also show that for insulating films ( $k_{eq}/k_2 \leq 0.1$ ) a value of the interfacial thermal resistance exists which makes the measured  $k_{app}$  essentially insensitive to the film thickness for  $t_{eq}/a \geq 0.001$ . For example, for  $k_{eq}/k_2 = 0.01$  the value  $\rho = 100$  makes  $k_{app}$  change from the film's  $k_{eq}$  by less than 20% for this range of film thicknesses. For  $k_{eq}/k_2 = 0.1$  the special value of  $\rho$  is about  $\rho = 10$ . This value also makes  $k_{app}$  stay to within 20% of  $k_{eq}$ . Clearly, the value of  $\rho$  which makes  $k_{app}$  independent of  $t_{eq}/a$  is approximately equal to  $k_2/k_{eq}$  for insulating films, or, equivalently  $R_{int} = a/k_{eq}$ . Thus, by choosing  $R_{int} = a/k_{eq}$ , the apparent thermal conductivity  $k_{app}$  can be made approximately equal to the film's  $k_{eq}$  for any film thickness and any value of the substrate conductivity  $k_2$  as long as the substrate is more conducting than the film (which is the usual case, as Table 2 indicates).



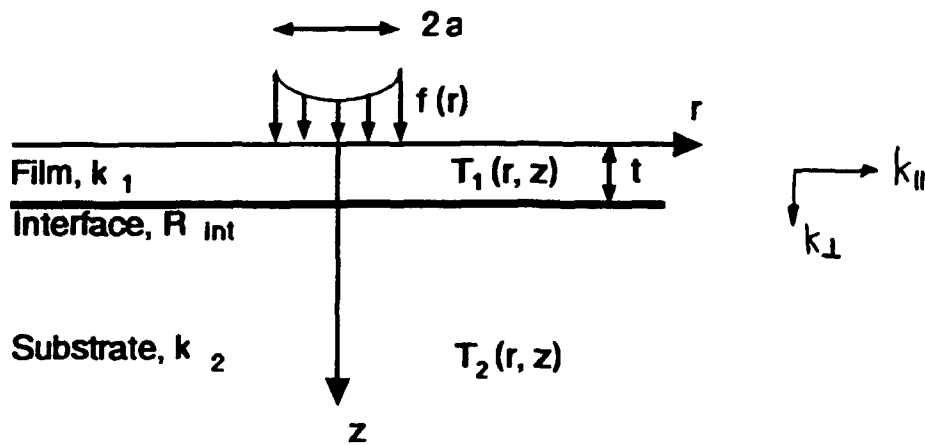


FIGURE 1: The geometry of an anisotropic thin film (thermal conductivity  $k_{||}$  parallel to film and  $k_{\perp}$  perpendicular to film). Equivalently, the film is thermally isotropic with thermal conductivity  $k_{eq}$  and thickness  $t_{eq}$ . The heat flux is specified by the function  $f(r)$ , and  $a$  is the heat flow radius.



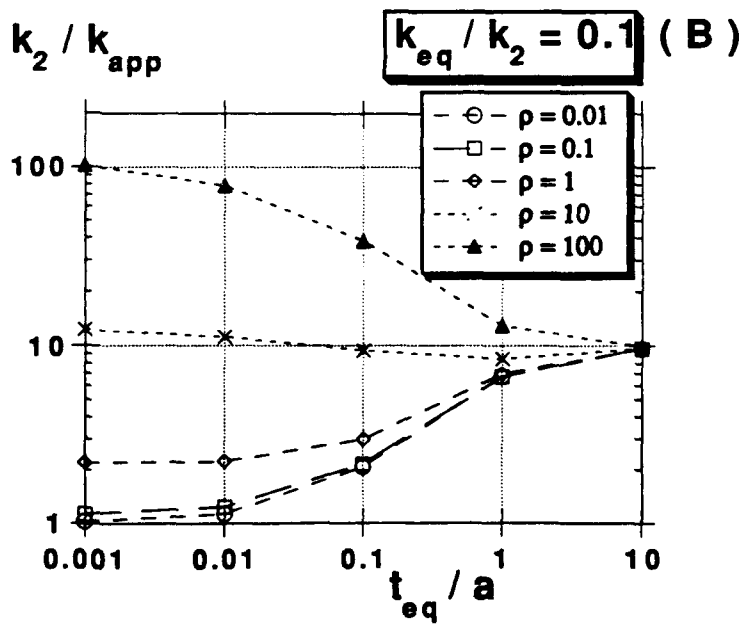
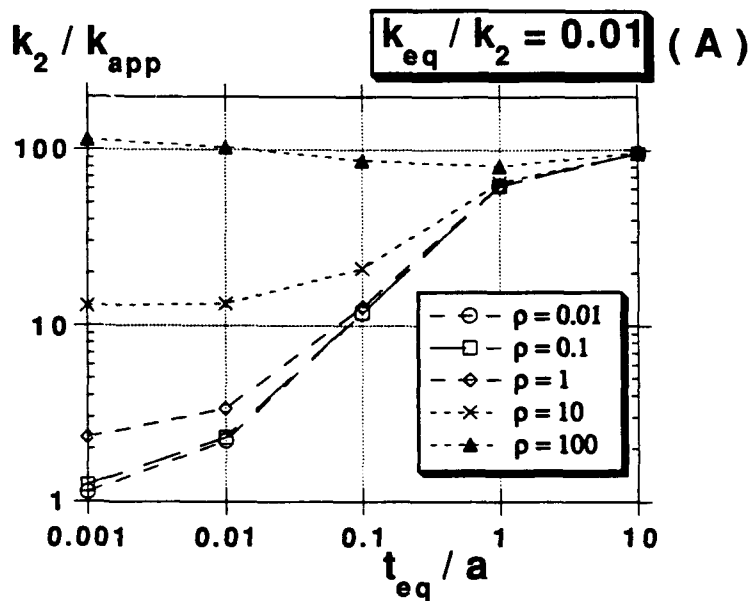
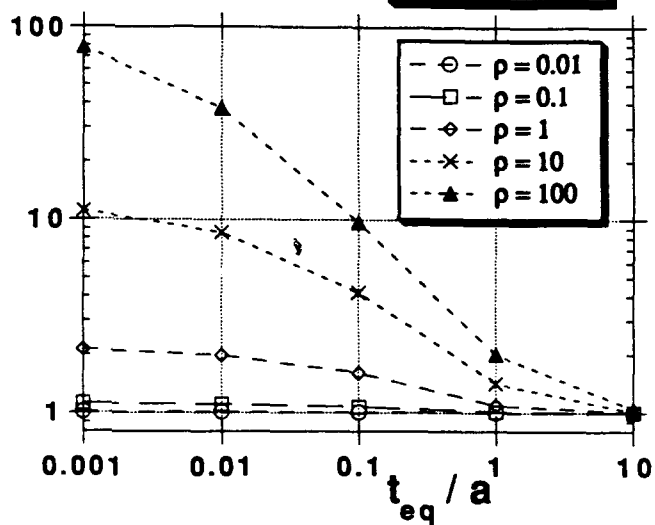


FIGURE 2



$k_2 / k_{app}$   $k_{eq} / k_2 = 1$  (C)



$k_2 / k_{app}$   $k_{eq} / k_2 = 10$  (D)

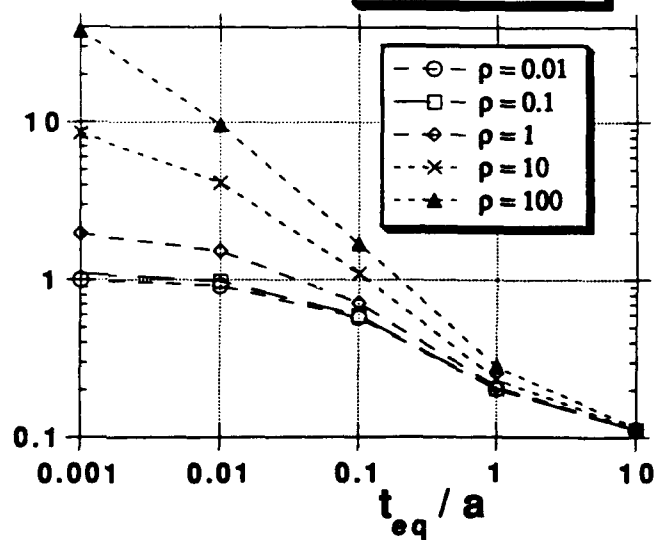


FIGURE 2, continued



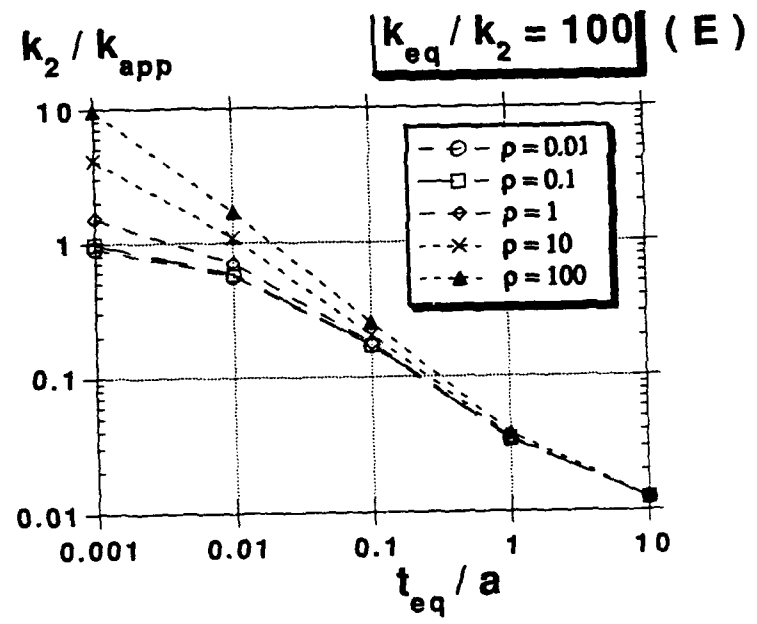


FIGURE 2, continued



### 3.2.2 LIMITING CASES

#### (A) Small interfacial thermal resistance, thin film

The function  $G(\xi, \kappa, H, \rho)$  of eqn (3.19) is expanded in series about  $\rho=0$ , and the first two terms are kept. For thin coatings ( $H \equiv t_{eq}/a \ll 1$ ) the result is

$$\begin{aligned} \frac{k_2}{k_{app}} = & 1 + \frac{4}{\pi} H \frac{1-\kappa^2}{\kappa} + \frac{32\sqrt{2}}{3\pi} H^{3/2} \frac{f_1(\kappa)}{\kappa} + O(H^{5/2}) \\ & + \rho \frac{4}{\pi} \left\{ 1 - 4\sqrt{2} H^{1/2} \frac{f_1(\kappa)}{\kappa^2-1} + 2\sqrt{2} H^{3/2} \frac{f_2(\kappa)}{\kappa^2-1} + O(H^{5/2}) \right\} \end{aligned} \quad (3.20)$$

where the functions  $f_1(\kappa)$  and  $f_2(\kappa)$  of  $\kappa \equiv k_{eq}/k_2 \equiv (k_{||}/k_{\perp})^{1/2}$  are shown in Fig. 3. It is seen that for an insulating film with respect to the substrate ( $\kappa \leq 1$ ) these functions have a small value, but they attain much larger values when the film is more conducting than the substrate.

Eqn (3.20) clearly shows that in this limiting case of thin films with small interfacial resistance the effect of the film and of the film/substrate interface is to perturb the measured thermal conductivity  $k_{app}$  from the substrate thermal conductivity  $k_2$ . For isotropic films, the term proportional to  $H$  on the RHS of eqn (3.20) is in agreement with the results of Dryden who did not directly calculate  $k_{app}$  but the total thermal resistance due to a thin film bonded to a substrate via a perfect interface.



(B) Small interfacial thermal resistance, thick film

When  $H \rightarrow \infty$ ,  $k_{app}$  is more conveniently measured with respect to the film thermal conductivity  $k_{eq} \equiv (k_{||} / k_{\perp})^{1/2}$ . The result is

$$\frac{\sqrt{k_{||} k_{\perp}}}{k_{app}} = 1 + \frac{2}{\pi H^2} \ln \frac{\kappa+1}{2} - \frac{7}{24 \pi H^3} f_3(\kappa) + O(H^{-4}) + \rho \frac{2}{\pi H^2} \left\{ \frac{\kappa}{\kappa^2 - 1} \ln \frac{\kappa+1}{2} - \frac{7}{16 H^2 \kappa^2 - 1} f_3(\kappa) + O(H^{-4}) \right\} \quad (3.21)$$

where the function  $f_3(\kappa)$  is shown in Fig. 3.

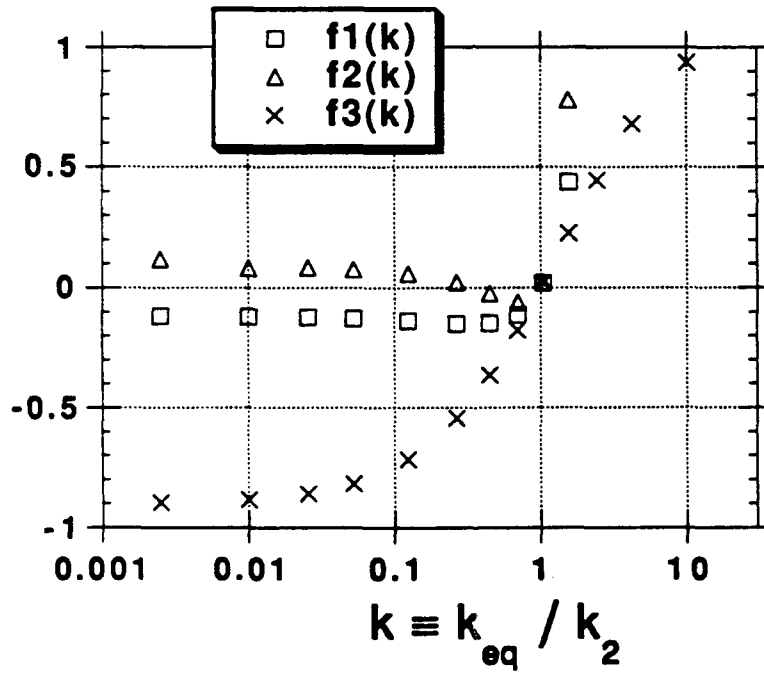


FIGURE 3: The functions  $f_1$ ,  $f_2$  and  $f_3$  required for thin films.



### 3.3 MICROSTRUCTURAL EFFECTS IN FILM THERMAL CONDUCTIVITY

To understand the basic physical mechanisms that diminish the thermal conductivity of thin films as compared to the bulk, we have considered continuum effects (such as porosity, see, for example, Brailsford and Major, 1964; Budiansky, 1970; Torquato, 1991; or interfacial thermal resistance among grains) and quasi-particle effects involving phonon scattering (Klemens, 1955, 1958, 1969; Reissland, 1973). In thin films phonons can be scattered by other phonons (Umklapp processes), or by microstructural inhomogeneities such as dislocations, stacking faults, chemical inhomogeneities or boundaries such as the film/substrate interface. An initial analysis of such effects is presented in Appendix 9, where AlN has been used as a representative material.

The main conclusion is that all these microstructural features lead to reduced film thermal conductivity. However, the same mechanisms will lead to similar reductions in bulk materials characterized by the same microstructure as the thin films. The only mechanism that leads to a dependence on the film thickness of the film thermal conductivity is scattering from the film free surface or the film/substrate mechanism. This dependence is analyzed below.

The Debye theory of specific heat (Reissland, 1973) can be used to derive an expression for the thermal conductivity  $k_0$  of a material in which the primary mode of heat transfer is via phonons. The result is

$$k_0 = \frac{k_B}{2\pi^2 v} \left( \frac{k_B T}{h/2\pi} \right)^3 \int_0^{\theta_D/T} dx \tau(x) x^2 f(x) \quad (3.22)$$

$$f(x) = \frac{x^2 e^x}{(e^x - 1)^2}, \quad x \equiv \frac{h\omega/2\pi}{k_B T}$$

where  $k_B$  is Boltzmann's constant,  $v$  is the velocity of sound in the material,  $h$  is Planck's constant,  $T$  is the absolute temperature,  $\theta_D$  is the Debye temperature,  $\tau$  is the relaxation time



(related to the phonon mean free path  $\ell$  by  $\tau = \ell/v$ ), and  $\omega$  is the phonon frequency.

For a perfect crystal of infinite extent the main scattering of phonons is due to Umklapp processes (U-processes), so that

$$\tau = \tau_U = \frac{\exp(\beta \theta_D / T)}{A x^2 T^n} = \frac{1}{x^2} \frac{L}{v} \quad (3.23)$$
$$L = L_0 \frac{\exp(\beta / \phi)}{\phi^n} \quad \phi \equiv \frac{\theta_D}{T}$$

$L_0$ ,  $n$ , and  $\beta$  are material constants which can be extracted from the dependence on temperature of the thermal conductivity of the bulk single crystal. Table 3 summarizes data for several different classes of solids such as single elements, oxides, nitrides and arsenides. The corresponding dependence of the length scale  $L$  on temperature  $T$  (normalized with respect to the Debye temperature  $\theta_D$ ) is shown in Fig. 4. It is important to note that  $L$  (which is independent of the phonon frequency  $\omega$  or  $x$ ) is *not* the phonon mean free path. Also note that the length scale  $L$  is temperature dependent.

Thin deposited films have a characteristic microstructure consisting of grains (grain size  $D$ ) in addition to the film thickness  $H$ . In this case, the total scattering time  $\tau$  is found by adding the scattering rates due to the Umklapp processes, the grain structure of the film, and the film thickness, so that

$$\frac{1}{\tau} = \frac{1}{\tau_U} + \frac{v}{H} + \frac{v}{D} \quad (3.24)$$

In this way, the ratio of the thin film to the single crystal bulk conductivity is found to be



$$\frac{k}{k_0} = \frac{\int_0^{\theta_D/T} dx \frac{x^2}{x^2 + \frac{L}{H} + \frac{L}{D}} f(x)}{\int_0^{\theta_D/T} dx f(x)} \quad (3.25)$$

Fig. 5 shows the dependence of  $k/k_0$  ( $k_0$  being the thermal conductivity of the infinite perfect crystal where only Umklapp processes contribute to phonon scattering) on the non-dimensional film thickness  $H/L$  for various values of the microstructural variable  $D/L$  at several different nondimensional temperatures  $T/\theta_D$ . At small film thickness, the film thermal conductivity is dominated by the effect of the film thickness. At large film thickness, the film conductivity becomes independent of the thickness and depends only on the microstructural variable.

It is clear, therefore, that the film thickness is to be compared to the important length scale  $L$ . This implies that a film which is thermally thin at a low temperature (compared to the Debye temperature  $\theta_D$ ) is not necessarily so at a higher temperature.



**TABLE 3:** Material constants for the calculation of the dependence on temperature of the thermal conductivity of single bulk crystals. RT denotes room temperature of 300 °K. These constants have been calculated from the experimental  $k(T)$  which was found in the following references.

For Si, Ge: C.J. Glassbrenner and G.A. Slack, Phys. Rev. 134, A1058, 1964.

For diamond: D.T. Morelli, C.P. Beetz, and T.A. Perry, J. Appl. Phys. 64, 3063, 1988; see also T.R. Anthony, J.L. Fleischer, J.R. Olson, and D.G. Cahill, *ibid.* 69, 8122, 1991.

For GaAs: F. Szmulowicz, F.A. Madarasz, P.G. Klemens, and J. Diller, J. Appl. Phys. 66, 252, 1989.

For AlN: R.B. Dinwiddie and D.G. Onn, Mat. Res. Soc. Symp. Proc. Vol. 167, 241, 1990.

For MgO: C.L. Tsai, A.R. Moodenbaugh, H. Weinstock, and Y. Chen, Thermal Conductivity, vol. 16, 139, ed. D.C. Larsen, Plenum Press, 1983.

For BeO: G.A. Slack and S.B. Austerman, J. Appl. Phys. 42, 4713, 1971.

For  $Al_2O_3$ : B. Schulz, J. Nucl. Mater. 155-157, 348, 1988.

Material	$v$ (m/s)	$\theta_D$ (K)	$n$	$\beta$	$A$ (1/s-K <sup>n</sup> )	$L_0$ (nm)	$L(RT)$ (nm)
Si	6,400	674	3	0.29	6,050	3.5	77
Ge	3,940	395	3	0.20	10,980	5.8	17
C(dia)	13,200	2,230	4	0.121	1.31	0.41	3,100
GaAs	3,860	370	3	0.33	16,600	4.6	13
AlN	5,000	950	4	0.17	10	0.61	105
MgO	7,000	945	3	0.5	24,600	0.34	51
BeO	8,900	1,280	4	0.1125	3.5	0.95	510
$Al_2O_3$	8,900	1,000	3	0.16	21,400	0.42	26



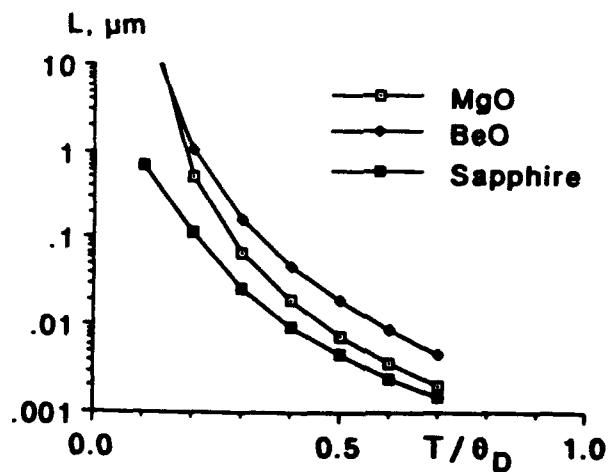
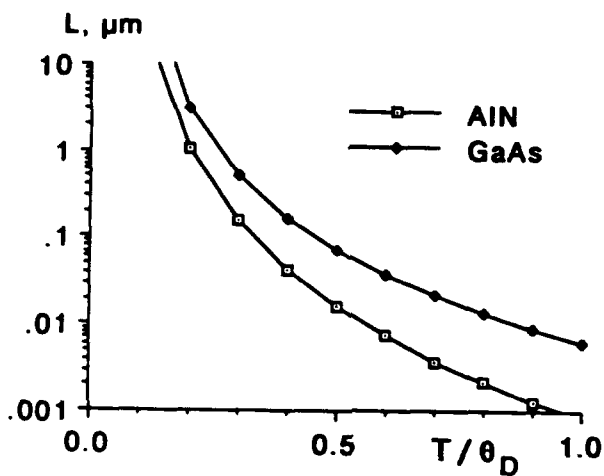
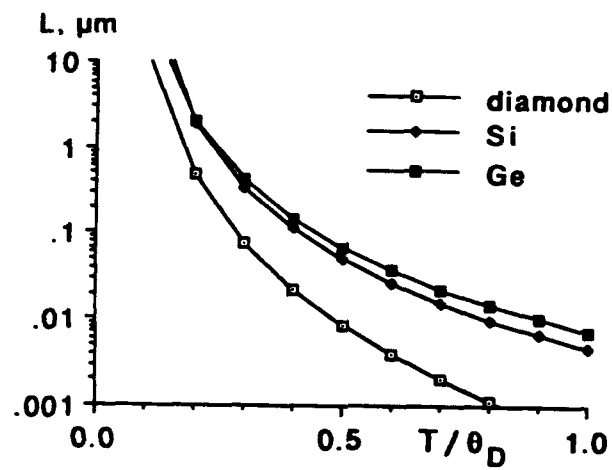


FIGURE 4: The dependence of the length scale  $L$  on temperature for various classes of solids.



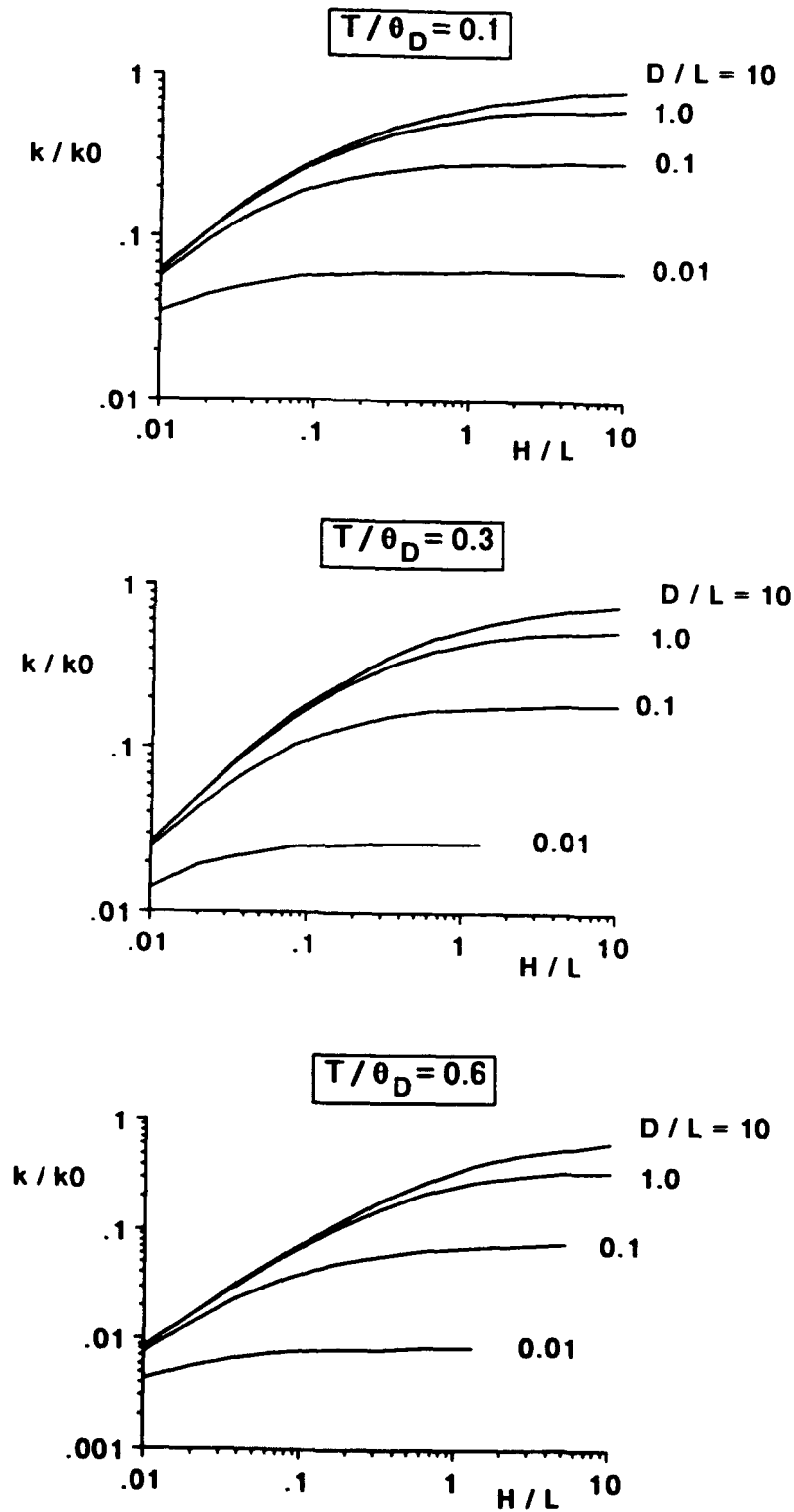


FIGURE 5: The dependence of the thin film thermal conductivity  $k$  on the film thickness  $H$ .



### 3.4 LASER DAMAGE IN THIN FILMS

#### 3.4.1 IMPLICATIONS OF LOW FILM THERMAL CONDUCTIVITY

The resistance to laser damage in optical thin films is an important consideration towards the development of powerful solid-state lasers. Appendices 8 and 9 summarize experimental data, and the damage mechanisms (avalanche ionization, multiphoton absorption, and impurity-initiated damage; see Walker et al. 1981a, 1981b).

According to the impurity model, whose predictions for the laser damage of bulk solids is eqn (3.1), an absorbing inclusion within a non-absorbing infinite matrix is heated due to the absorption of the incident radiation. The high temperature within the inclusion leads to failure when the temperature reaches some critical value. Further details and references can be found in Appendix 9.

Here we consider the effect of low film thermal conductivity, film thickness, and the proximity of the inclusion to the film's free surface, see Fig. 6. At time  $t \geq 0$  the inclusion absorbs power at the rate  $q$  per unit volume, whereas the film and the substrate do not absorb any of the incident radiation. We used finite elements to solve the time-dependent heat conduction equation assuming that the temperature and heat flux are continuous at all interfaces and that the film's free surface is insulated. The governing equations are

$$\begin{aligned} \text{Inclusion: } & k_I \nabla^2 T_I + q = (\rho c)_I \frac{\partial T_I}{\partial t}, \quad r < R \\ \text{Film: } & k_F \nabla^2 T_F = (\rho c)_F \frac{\partial T_F}{\partial t}, \quad r > R, \quad -(H-D) < z < D \\ \text{Substrate: } & k_S \nabla^2 T_S = (\rho c)_S \frac{\partial T_S}{\partial t}, \quad z < -(H-D) \end{aligned} \quad (3.26)$$

where  $z$  is the axial coordinate in a cylindrical system  $(r_1, z)$  with origin in the center of the inclusion.



The main result of the numerical solution is that the film thermal conductivity  $k_F$  plays an important role in determining the temperature at the points A, B, and C shown in Fig. 6 (see appendix 9). Low film thermal conductivity leads to very high temperatures after a certain time has elapsed. For typical material parameters and laser beam duration the effect of the reduced film conductivity is important. In effect, the reduced values of the film thermal conductivity insulate the heated inclusion so that the temperature within and in the vicinity of the inclusion rises significantly and it can easily reach thousands of degrees °K.

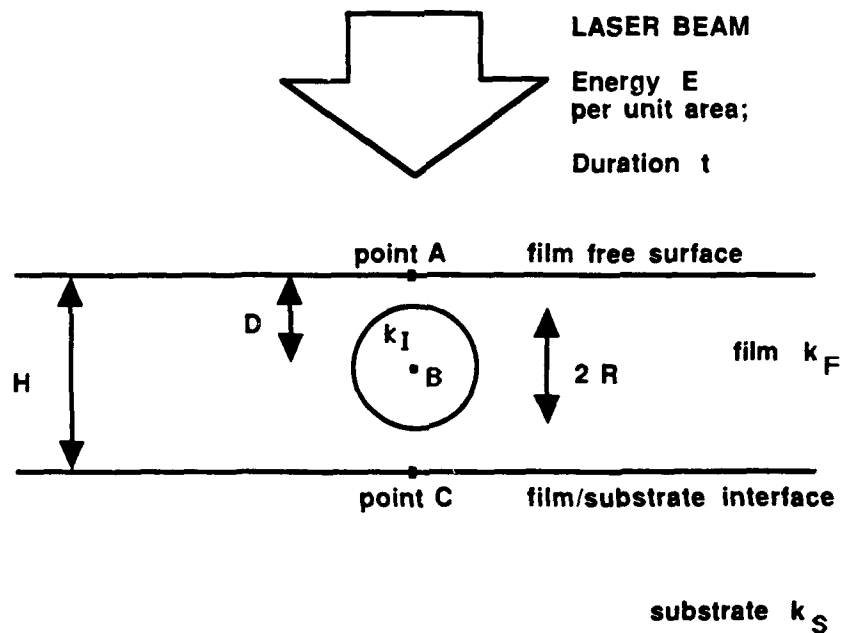


FIGURE 6: The geometry of a thin film (non-absorbing), containing an absorbing inclusion and supported on a non-absorbing substrate.



### 3.4.2 NONLINEAR EFFECTS IN LASER DAMAGE

It is clear from the discussion above that the temperature in laser damage can become very large. It is well known that the thermal conductivity of solids has a strong temperature dependence, typically diminishing with increasing temperature as eqn (3.22) shows. It is clear that if  $dk/dT < 0$ , then a non-linear insulating effect is introduced in the sense that as the temperature increases the thermal conductivity decreases which further increases the temperature.

To study this non-linear effect, we have assumed steady-state conditions so that all time dependence can be neglected, and we have looked at the model of Goldenberg and Tranter (1952) of the spherical absorbing inclusion of radius  $R$  (denoted by "1") embedded within the infinite nonabsorbing matrix ("2"). We assume that the thermal conductivity varies as

$$\text{Inclusion : } k_1(\theta) = k_1^0 \left( \epsilon_1 + \frac{1}{\theta^{m_1}} \right), \quad \text{Matrix: } k_2(\theta) = k_2^0 \left( \epsilon_2 + \frac{1}{\theta^{m_2}} \right) \quad (3.27)$$

where  $\theta$  denotes the non-dimensional temperature with respect to room temperature  $\theta = T/T_{RT}$ . The material constants  $k_1^0$  and  $k_2^0$  are the thermal conductivities at room temperature,  $\epsilon_1$  and  $\epsilon_2$  are the small thermal conductivities at very high temperature ( $\theta \gg 1$ ) and  $m_1, m_2$  are exponents which give the temperature dependence of the thermal conductivity. Typically,  $m_1, m_2$  lie in the range 1-2. We observe that  $m_1, m_2 = 0$  corresponds to the linear case of temperature-independent thermal properties.

The steady-state solution of the temperature distribution with  $\theta \rightarrow 1$  as  $\rho = r/R \rightarrow \infty$  is calculated by assuming that the temperature and the heat flux is continuous along the inclusion-matrix interface. The governing equations are

$$\begin{aligned} \text{Inclusion: } \quad \frac{d}{dr} \left[ k_1(T) r^2 \frac{dT}{dr} \right] + q &= 0, \quad r < R \\ \text{Matrix: } \quad \frac{d}{dr} \left[ k_2(T) r^2 \frac{dT}{dr} \right] &= 0, \quad r > R \end{aligned} \quad (3.28)$$



We first find the temperature  $\theta_s$  at the surface of the inclusion ( $\rho=1$ ) and the temperature  $\theta_c$  at the inclusion center ( $\rho=0$ ) by

$$\begin{aligned} \epsilon_2 \theta_s + \frac{1}{1-m_2} \theta_s^{1-m_2} &= \frac{g}{3} + \epsilon_2 + \frac{1}{1-m_2} \\ \epsilon_1 \theta_c + \frac{1}{1-m_1} \theta_c^{1-m_1} &= \frac{gk}{6} + \epsilon_1 \theta_s + \frac{1}{1-m_1} \theta_s^{1-m_1} \end{aligned} \quad (3.29)$$

where  $g$  denotes the non-dimensional heating term and  $k$  is the ratio of matrix to inclusion room temperature thermal conductivities

$$g \equiv \frac{q R^2}{k_2^0 T_{RT}}, \quad k \equiv \frac{k_2^0}{k_1^0} \quad (3.30)$$

In view of the previous discussion on the decreased thermal conductivity of the host material,  $k$  will typically be less than unity. It is interesting to note that the temperature  $\theta_s$  at the surface of the inclusion depends only on the properties of the matrix

The temperature inside the inclusion  $\theta_{in}(\rho, \rho \leq 1)$  and outside the inclusion  $\theta_{out}(\rho, \rho \geq 1)$  are then given by

$$\begin{aligned} \epsilon_1 \theta_{in} + \frac{1}{1-m_1} \theta_{in}^{1-m_1} &= \frac{gk}{6} (1-\rho^2) + \epsilon_1 \theta_s + \frac{1}{1-m_1} \theta_s^{1-m_1} \\ \epsilon_2 \theta_{out} + \frac{1}{1-m_2} \theta_{out}^{1-m_2} &= \frac{g}{3} \frac{1}{\rho} + \epsilon_2 + \frac{1}{1-m_2} \end{aligned} \quad (3.31)$$

Fig. 7 shows the temperature distribution in the vicinity of the inclusion. The linear case  $m_1, m_2 = 0$  results in low temperatures and the thermal non-linearity leads to significantly higher temperatures.

Fig. 8 shows the dependence of the inclusion surface temperature on the non-dimensional loading  $g$  defined by eqn (3.29). It is clear that for low values of  $g$  ( $g \leq 2$ ) the linear



analysis sufficiently predicts the surface temperature. At higher  $g$ , the non-linear dependence of the thermal conductivity on temperature leads to a distinctly different dependence of temperature on the absorbed power  $q$ , so that the rate at which the temperature changes with  $g$  is many times higher than the corresponding linear case in which the temperature depends linearly on  $g$ .

Although the present discussion establishes the importance of non-linear thermal effects, it is applicable only when steady-state has been achieved. Since steady-state is known to lead to considerably higher temperatures than the transient solution, the reported results are to be seen as an upper bound on the effects of non-linear dependence of the matrix thermal conductivity on the temperature.

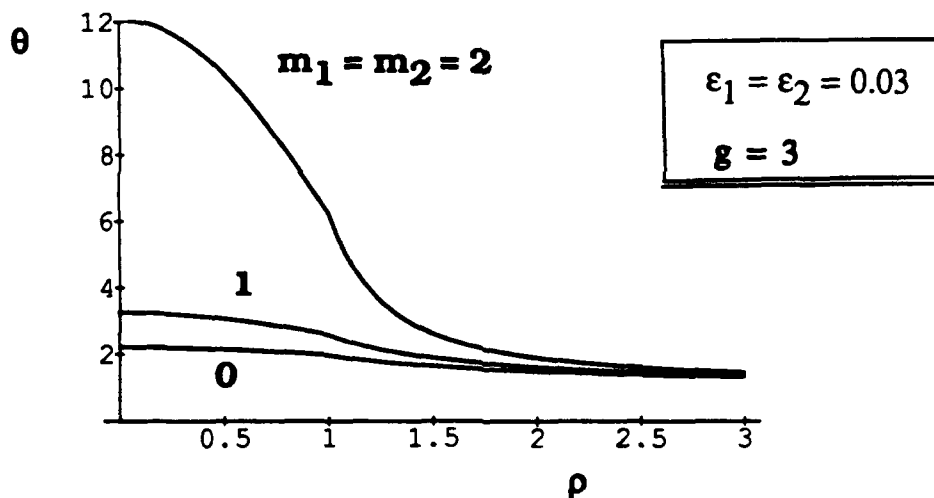


FIGURE 7: The temperature distribution (steady-state conditions) due to an absorbing inclusion embedded in an infinite, non-absorbing matrix. The inclusion-matrix interface is at  $\rho=1$ .

At room temperature, the conductivity of the matrix is one-half that of the inclusion ( $k=0.5$ ).



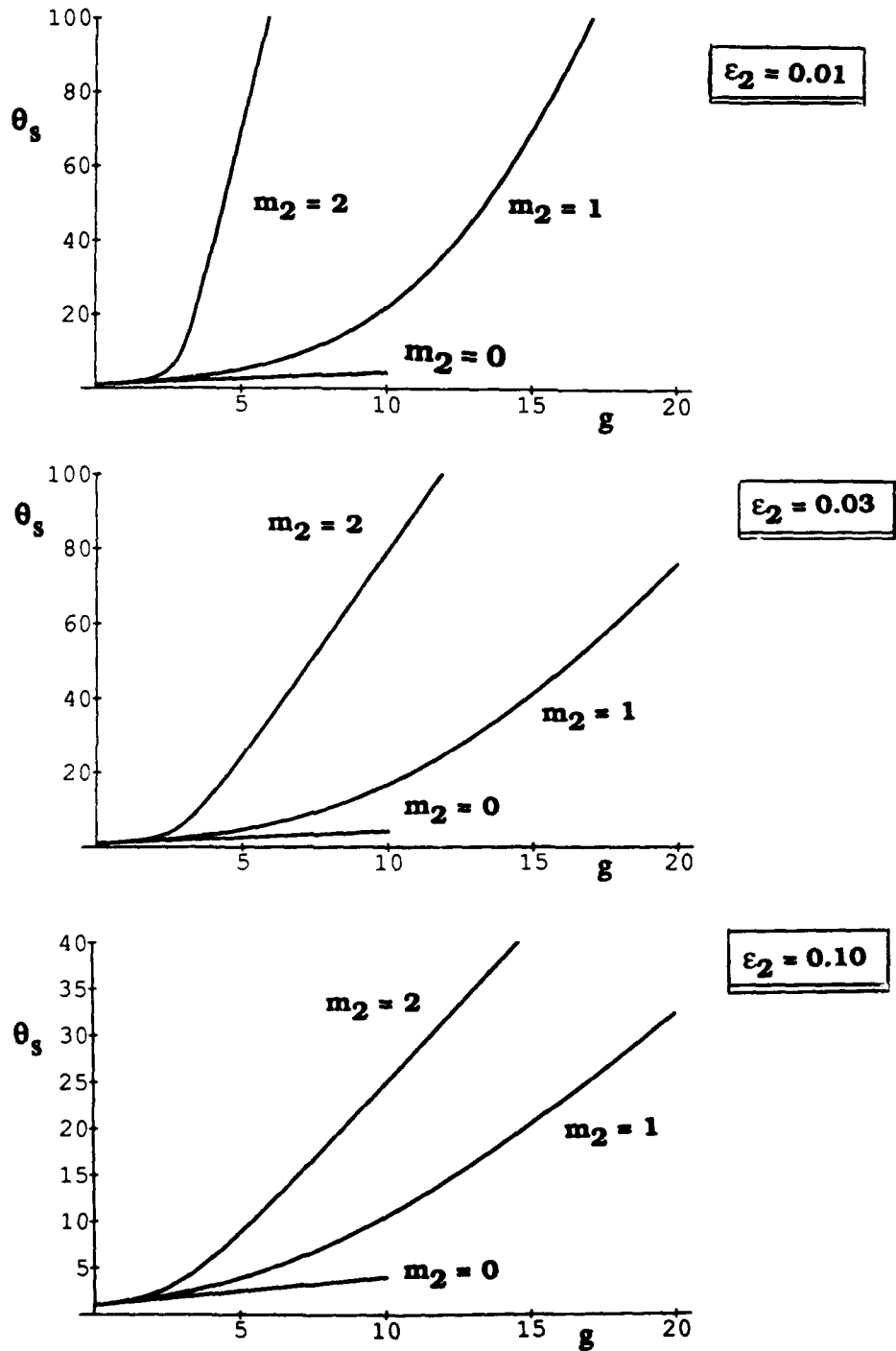


FIGURE 8: Steady-state temperature at the inclusion surface vs. the non-dimensional absorbed power  $g$ . The temperature is normalized in terms of the room temperature (300°K).  $m_2=0$  corresponds to a thermally linear material with conductivity independent of temperature.



### 3.5 MICROSTRUCTURAL EFFECTS ON INTERFACIAL THERMAL RESISTANCE

In the analyses presented above, it has been assumed that there is continuity of temperature along the film/substrate interface. Clearly, this will only be the case if no microstructural details are present along that interface. The results of Lambropoulos et al. (Appendix 7) on the measurement of the thermal conductivity of thin films by the thermal comparator suggest that such an interfacial resistance may be considerable. Furthermore, section 3.2.1 of this report showed that the interfacial thermal resistance may have a large effect on the apparent thermal conductivity of the thin film.

It is well known that due to the nucleation of the thin film, the interface has a large amount of porosity. This porosity appears to be localized near the interface in films characterized by the columnar microstructure discussed in Section 2.2. The presence of this porosity implies that the film/substrate interface is not to be viewed as a single plane, but instead as a diffuse region characterized by a distribution of voids.

To determine the effect of porosity on the interfacial thermal resistance, we have modeled the porous interface by examining a single cylindrical tapering grain, as shown in Fig. 9a. The width of the grain is  $D$ , and the area of contact of the grain with the substrate is  $2a < D$ . We assume that as  $z \rightarrow \infty$  the temperature distribution is uniform and that it corresponds to a constant heat flux  $q$  (power per unit area) in the  $(-z)$  direction. that there is not heat flow from one grain to a neighboring grain, and that the film is in contact with a conducting substrate so that the interface at  $z=0$  is kept at a constant temperature.

We denote by  $T_0(r, z)$  the temperature distribution in the absence of any porosity so that

$$T_0(r, z) = \frac{q z}{k} \quad (3.32)$$

where  $k$  is the thermal conductivity of the grain material. On the other hand, in the presence of interface porosity we denote the temperature by  $T(r, z)$ . Fig. 9b shows numerically computed isotherms in the absence of any porosity ( $2a=D$ ), and in the presence of porosity. It is clear that



porosity leads to higher temperatures in the vicinity of the film/substrate interface and this implies a higher interfacial thermal resistance.

To determine the effect of the interface porosity on the interfacial thermal resistance, we calculate the average temperature at a height  $z$  above the interface

$$T_{ave}(z) \equiv \frac{\int_0^{D/2} T(r, z) 2 \pi r dr}{\pi D^2 / 4}, \quad T_{ave}^0(z) \equiv \frac{\int_0^{D/2} T_0(r, z) 2 \pi r dr}{\pi D^2 / 4} \quad (3.33)$$

and we can then determine the interfacial thermal resistance by

$$R_{int} \equiv \frac{T_{ave}(z=H)}{q}, \quad R_{int}^0 \equiv \frac{T_{ave}^0(z=H)}{q} = \frac{H}{k} \quad (3.34)$$

This definition of the thermal resistance is identical with the definition used in Section 3.2.1 of this report, see eqn (3.13). Notice that these contributions to the interfacial thermal resistance do not include any intrinsic thermal resistance an example of which is the interfacial thermal resistance of two different solids brought into intimate contact through a perfect interface.

To examine the effect of the microstructural porosity alone on the interfacial thermal resistance, we define the fractional change in the interfacial thermal resistance

$$\frac{R_{int} - R_{int}^0}{R_{int}^0} = \frac{k}{H} T_{ave}(z=H) - 1 \quad (3.35)$$

which is plotted in Fig. 10 in two different ways.

It is clear from Fig. 10 that the effect of the pore shape is not very strong, and that tall pores (small  $H$ ) give large thermal resistance than short pores. However, the effect of porosity along the interface, i.e. the ratio  $a/(D/2)$ , is very strong so that the interfacial thermal resistance decreases by almost two orders of magnitude as  $a/(D/2)$  increases from 0.2 to 0.9.



It is concluded, therefore, that a large contribution to interfacial thermal resistance may be due to the interfacial pore microstructure.



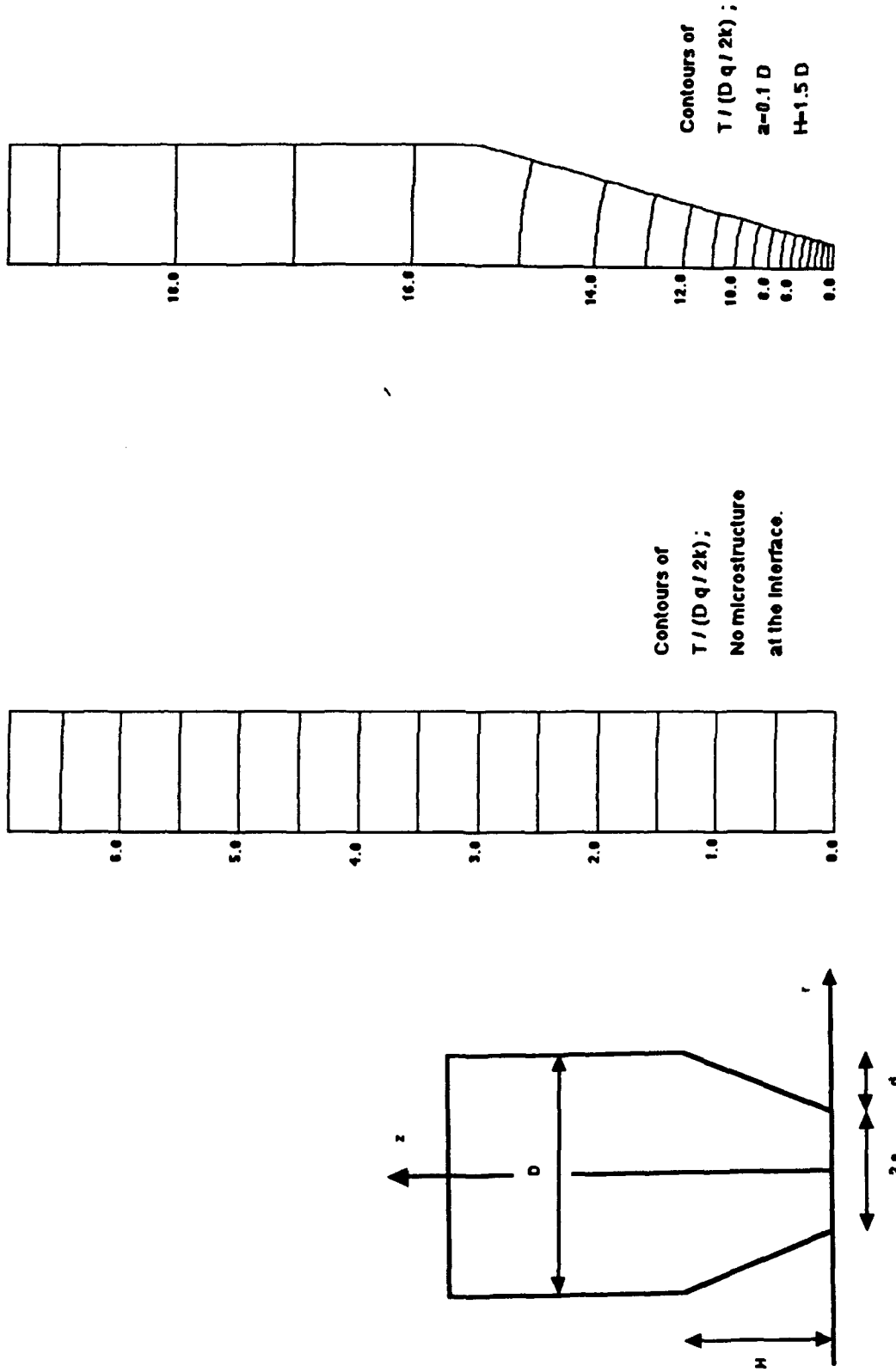


FIGURE 9: (A) The geometry of a cylindrical grain (width  $D$ ) of a film. The substrate is at  $z=0$ .  
(B) Isotherms in the presence and in the absence of interfacial porosity.



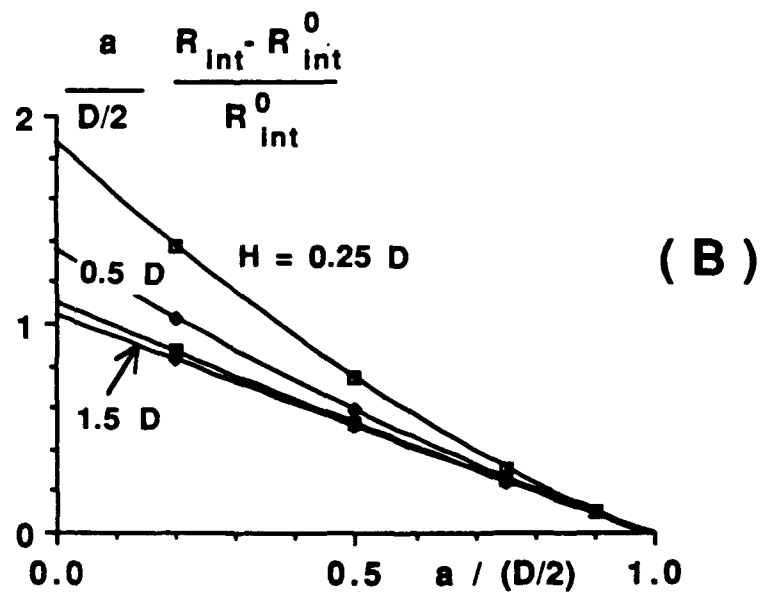
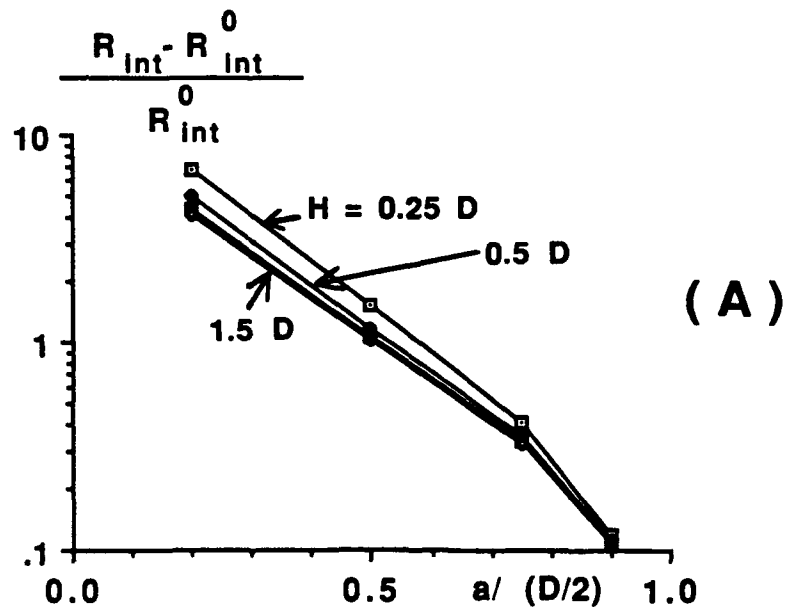


FIGURE 10: Fractional change in interfacial thermal resistance due to the presence of interfacial porosity.



## REFERENCES

- Bartholomeusz, B.J., 1989, "Thermomagnetic marking of rare-earth-transition-metal thin films", Journal of Applied Physics, vol. 65, p. 262.
- Brailsford, A.D. and K. G. Major, K.G., 1964, "The thermal conductivity of aggregates of several phases, including porous materials", British Journal of Applied Physics, vol. 15, p. 313.
- Budiansky, B., 1970, "Thermal and thermoelastic properties of isotropic composites", Journal of Composite Materials, vol. 4, p. 286.
- Cahill, D.G., Fischer, H.E., Klitsner, T., Swartz, E.T. and Pohl, R.O., 1989, "Thermal conductivity of thin films: measurements and understanding", Journal of Vacuum Science and Technology, vol. A7, p. 1259.
- Carslaw, H.S. and Jaeger, J.C., 1959, Conduction of heat in solids, Oxford University Press, London, Chapter 8.
- Casimir, H.B.G., 1938, "Note on the conduction of heat in crystals", Physica, vol. 5, p. 495.
- Dryden, J.R., 1983, The effect of a surface coating on the constriction resistance of a spot on an infinite half plane, J. Heat Transfer, vol. 105, 408.
- Evans, K.E. and Nkansah, M.A., 1988, "Finite element analysis of thermal stresses in optical storage media", Journal of Applied Physics, vol. 64, p. 3398.
- Goldenberg, H. and Tranter, M.A., 1952, "Heat flow in an infinite medium heated by a sphere", British Journal of Applied Physics, vol. 3, p. 296.
- Guenther, A.H. and McIver, J.K., 1988, "The role of thermal conductivity in the pulsed laser damage sensitivity of optical thin films", Proceedings of Society of Photo-instrumentation Engineers (SPIE), vol. 895, p.246.
- Halley, J.M. and Midwinter, J.E., 1987, "Thermal analysis of optical elements and arrays on thick substrates with convective cooling", Journal of Applied Physics, vol. 62, p. 4055.
- Hopper, R.W. and Uhlmann, D.R., 1970, "Mechanism of inclusion damage in laser glass", Journal of Applied Physics, vol. 41, p. 4023.
- Klemens, P.G., 1955, "The scattering of low-frequency lattice waves by static imperfections", Proceedings of the Physical Society, vol. 68, p. 1113.
- Klemens, P.G., 1958, "Thermal conductivity and lattice vibrational modes", in Solid State Physics, vol. 7, ed. F. Seitz and D. Turnbull, Academic Press, New York, p. 1.
- Klemens, P.G., 1969, "Theory of the thermal conductivity of solids", in Thermal Conductivity, vol. 1, ed. R. P. Tye, Academic Press, New York, p. 1.
- Koyanagi, H., Ito, T., Miyamoto, N., Sato, Y., and Ando, H., 1989, "Optical and thermal analyses on multilayered thin films of a phase-change optical recording disk", Journal of Applied Physics, vol. 66, p. 1045.
- Lange, M.R., McIver, J.K., and Guenther, A.H., 1984, "The influence of the thermal and mechanical properties of optical materials in thin film form on the damage resistance to pulsed lasers", Thin Solid Films, vol. 118, p. 49.
- Lange, M.R., McIver, J.K., and Guenther, A.H., 1985, "Pulsed laser damage in thin film coatings: fluorides and oxides", Thin Solid Films, vol. 125, p. 143.
- Lambropoulos, J.C., Jolly, M.R., Amsden, C.A., Sinicropi, M., Diakomihalis, D., and Jacobs, S.D., 1989, "Thermal conductivity of dielectric thin films", Journal of Applied Physics.



vol. 66, p. 4230.

Lambropoulos, J.C. and Hwang, S.-S., 1990, "Implications of low film thermal conductivity for the laser damage resistance of optical thin films", in Electro-Optics and Nonlinear Optic Materials, Ceramic Transactions vol. 14, ed. K. M. Nair, A. S. Bhalla, and E. M. Vogel, American Ceramic Society, p. 219.

Lowdermilk, W.H. and D. Milam, D., 1981, "Laser-induced surface and coating damage", IEEE Journal of Quantum Electronics, vol. QE-17, p. 1888.

Maldonado, J.A., 1990, "X-Ray lithography, where it is now, and where it is going", Journal of Electronic Materials, vol. 19, p. 699.

Messier, R., 1986, "Toward quantification of thin film morphology", Journal of Vacuum Science and Technology, vol. A4, p. 490.

Movchan, B.A. and Demchishin, A.V., 1969, Fiz. Met. Metalloved., vol. 28, p. 653 (in Russian).

Powell, R.W., 1969, "Thermal conductivity determinations by thermal comparator methods", in Thermal Conductivity, vol. 2, ed. R. P. Tye, Academic Press, New York, p. 276.

Reissland, J.A., 1973, The Physics of Phonons, John Wiley, London, p. 117.

Shaw-Klein, L., Microstructural effects in thin film thermal conductivity, Ph. D. Thesis, University of Rochester, February 1992.

Shaw-Klein, L., Burns, S.J., and Jacobs, S.D., 1991, "Thermal conductivity of aluminum nitride thin films", in Electronic Packaging Materials Science, ed. E. D. Lillie et al., Materials Research Society Symposium Proceedings, vol. 203, MRS, Pittsburgh, (to be published).

Swartz, E.T., 1987, "Solid-solid thermal boundary resistance", Ph. D. thesis, Cornell University.

Swartz, E.T. and Pohl, R.O., 1987, Thermal resistance at interfaces, Appl. Phys. Lett., vol. 51, p. 2200.

Swartz, E.T. and Pohl, R.O., 1989, Thermal boundary resistance, Rev. Modern Physics, vol. 6, p. 6051.

Thornton, J.A., 1974, "Influence of apparatus geometry and deposition conditions on the structure and topography of thick sputtered coatings", Journal of Vacuum Science and Technology, vol. 11, p. 666.

Thornton, J.A., 1977, "High rate thick film growth", in Annual Review in Materials Science, vol. 7, ed. R. A. Huggins et al., p. 239.

Torquato, S., 1991, Random heterogeneous media: Microstructure and improved bounds on effective properties, Appl. mech. Rev., vol. 44, 37.

Walker, T.W., Guenther, A.H., and Nielsen, P.E., 1981a, "Pulsed laser-induced damage to thin-film optical coatings-Part I: Experimental", IEEE Journal of Quantum Electronics, vol. QE-17, p. 2041.

Walker, T.W., Guenther, A.H., and Nielsen, P.E., 1981b, "Pulsed laser-induced damage to thin-film optical coatings-Part II: Theory", IEEE Journal of Quantum Electronics, vol. QE-17, p. 2053.



## APPENDIX (1)

J. C. Lambropoulos and S.-M. Wan, Stresses in anisotropic thin films bonded to stiff substrates, Electronic Packaging Materials Science III, ed. R.C. Sundahl et al., Mat. Res. Soc. Symp. Proc., vol. 108, 399 (1988).

### STRESSES IN ANISOTROPIC THIN FILMS BONDED TO STIFF SUBSTRATES

JOHN C. LAMBROPOULOS AND SHIH-MING WAN  
Department of Mechanical Engineering, University of Rochester, Rochester,  
NY 14627

#### ABSTRACT

Numerical techniques are used to calculate the stress concentrations arising near the interface of a single-crystalline film which is bonded to a stiff substrate. The film has cubic elastic symmetry, and it is characterized by the anisotropic constants A and H which show the deviation of the material from elastic isotropy. The normal to the film-substrate interface is taken to be along the 100, 111 or 110 directions. The inhomogeneous stresses near the free edge and the uniform stresses far from the free edge are calculated, and the effects of cubic elastic anisotropy and of film growth direction are established for material parameters typical of metallic and semiconducting films.

#### INTRODUCTION

It is well known that thin films grown on substrates by various techniques are in a state of internal stress which arises as a result of the deposition process (intrinsic stress) or as a result of differential thermal mismatch between film and substrate at a temperature different than the deposition temperature (thermal stress) [1]. Large values of the internal stress may lead to failure by delamination from the film's free edge [2], by buckling [3] or by cracking along the interface [4].

Stresses near the vicinity of the free edge of an isotropic film were calculated by Aleck [5], and later by Zeyfang [6] and Blech and Levi [7], who established that close to the free edge large peeling and shear stresses develop. Williams [8] showed that for an isotropic film bonded to a rigid substrate stress singularities develop near the point where the interface meets the free edge. Hein and Erdogan [9] calculated the stress singularity for varying stiffness between film and substrate. They showed that when the film is much stiffer the singularity is  $-\frac{1}{2}$  for large values of the film material angle. When the substrate is much stiffer, the singularity is generally milder [9]. Approximate solutions for the stresses along the interface have been presented by Suhir [10], and by Yang and Freund [11], who have approximated the variation of the stresses through the thickness of the film.

In all works cited above, it has been assumed that the film and substrate are elastically isotropic. Still, situations often arise where the films are not isotropic. Examples are epitaxial films which may have a considerable amount of anisotropy [12], and magnetic films in which the material properties normal to the interface differ from the properties parallel to it [13].

It is the objective of this note to establish the effect of elastic anisotropy on the stresses near and far from the free edge in thin films of cubic symmetry which are bonded to stiff substrates.

#### ANISOTROPIC ELASTIC STRESSES

The geometry of the film and the substrate is shown inserted in Fig. 1. The z direction is normal to the film-substrate interface, and it is assumed that plane-strain conditions exist along the y direction. The substrate is modelled as being rigid and rigidly bonded to the film whose constitutive relation in the coordinate system of the crystal is

$$\sigma = C(\epsilon - \epsilon^T I) \quad (1)$$



where  $\sigma, \epsilon$  denote the stress and strain tensors, respectively,  $I$  is the identity tensor, and  $C$  is the 4-th order tensor of elastic stiffness with the usual symmetries and the non-zero entries

$$\begin{aligned} C_{1111} &= C_{2222} = C_{3333} = C_{11} \\ C_{1122} &= C_{2233} = C_{3311} = C_{12} \\ C_{1212} &= C_{2323} = C_{3131} = C_{44} \end{aligned} \quad (2)$$

The quantity  $\epsilon^T$  denotes a misfit strain and it may be due to differential thermal mismatch or due to the intrinsic stress.

It is convenient to define the anisotropic factors  $A$  and  $H$  by [14]

$$A = 2C_{44}/(C_{11} - C_{12}), \quad H = 2C_{44} - (C_{11} - C_{12}) \quad (3a)$$

For an isotropic material  $A=1$  and  $H=0$ . An equivalent Poisson ratio  $\nu$  is also defined

$$\nu = C_{12}/(C_{11} + C_{12}) \quad (3b)$$

For typical metals [14] and semiconductors (elemental or III-V compounds) [15]  $A$  lies between 1.5 and 4, and  $\nu$  between 0.2 and 0.45.

The orientation of the interface normal  $n$  is taken along the 100, 111 or 110 directions. Knowledge of  $n$  allows equation (1) to be expressed in the coordinate system of the film which is inserted in Fig.1.

The far field uniform stresses are found by noting that far from the free edge

$$\epsilon_{xx} = \epsilon_{yy} = \epsilon_{xy} = 0, \quad \sigma_{zz} = \sigma_{zx} = \sigma_{zy} = 0 \quad (4)$$

The only non-zero stresses are, in general,  $\sigma_{xx}, \sigma_{yy}$  and  $\sigma_{xy}$ . For  $n=100$  or  $111$   $\sigma_{xx} = \sigma_{yy}$  and  $\sigma_{xy} = 0$ , whereas for  $n=110$   $\sigma_{xx} - \sigma_{yy} \neq 0$  and  $\sigma_{xy} \neq 0$ . The insert in Fig. 1 shows the far field  $\sigma_{xx}$  for  $n=110$  or  $111$  for various values of the anisotropic parameter  $A$ . For  $n=100$  it can be easily shown that the far field stresses do not depend on  $C_{44}$  or  $A$ , but only on  $C_{11}$  and  $C_{12}$ . Thus for arbitrary  $A$  with  $n=100$  the far field stresses are equal to the  $n=111$  or  $110$  values with  $A=1$ .

To find the stresses distribution near the free edge, finite element techniques were used employing 4-node bilinear isoparametric elements. The half-length of the film (parallel to the interface) was taken to be five times the thickness of the film. The Poisson ratio was taken to be  $\nu=0.2$ , and  $A$  was equal to 1 (isotropic), 2 or 4. For  $n=100$  the plane-strain condition was enforced along the 010 direction; For  $n=110$  the plane-strain condition was along 001, and for  $n=111$  the plane-strain condition was along  $\bar{1}\bar{2}1$ .

Figures 1 and 2 show the stress distribution near the free edge and along the interface ( $z=0.008h$ ) for  $n=111$ . Figures 3 and 4 show the same results for  $n=100$ . The insert in Fig. 1 and Fig. 3 shows the levels of the uniform far field stresses  $\sigma_{xx}$  for  $n=110$  and  $111$ . In order to clearly show the effect of anisotropy and the effect of the interface normal  $n$ , the stresses are measured in units such that the far field stress  $\sigma_{xx}=1$  for an isotropic material with the same Poisson ratio.

#### DISCUSSION

It is seen from Figures 1-4 that the main effect of elastic anisotropy is to increase the stresses both in the vicinity of the free edge, as well as in the part of the film which is uniformly stressed. Furthermore, the extent of the interface which is subjected to large shear stresses is seen to increase considerably as  $A$  increases, especially for the case  $n=111$  (Fig. 2). Although the peeling stress  $\sigma_{zz}$  has diminished considerably by the time  $x=0.1$  or  $0.2 h$ ,



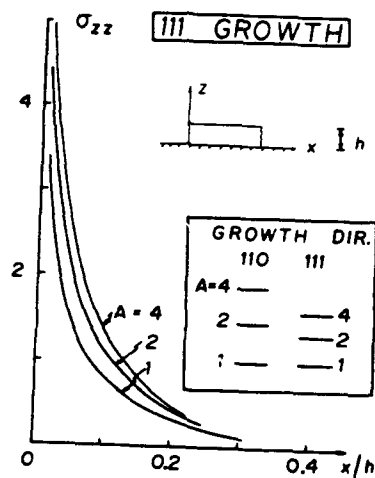


Figure 1: The peeling stress  $\sigma_{zz}$  for  $n=111$ . The insert shows the far field uniform  $\sigma_{xx}$ . Units are such that far field uniform  $\sigma_{xx}=1$  for isotropic material ( $A=1$ ).

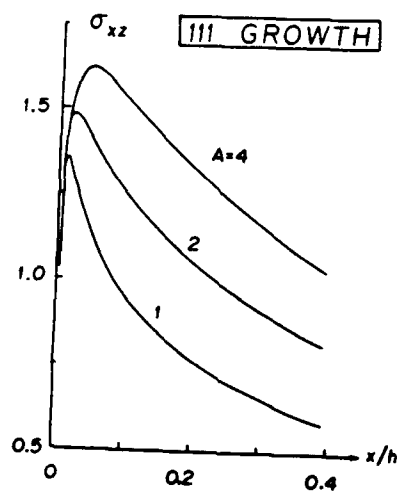


Figure 2: The shear stress  $\sigma_{xz}$  for  $n=111$ . Units are such that far field uniform  $\sigma_{xx}=1$  for isotropic material ( $A=1$ ).



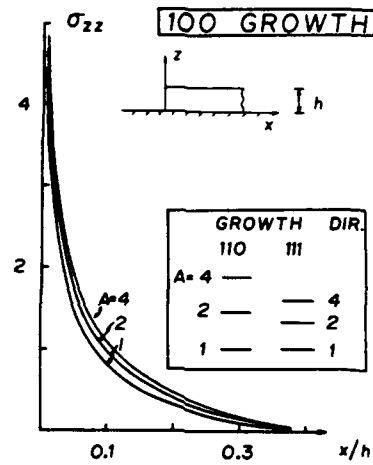


Figure 3: The peeling stress  $\sigma_{zz}$  for  $n=100$ . The insert shows the far field uniform  $\sigma_{xx}$ . Units are such that far field uniform  $\sigma_{xx}=1$  for isotropic material ( $A=1$ ).

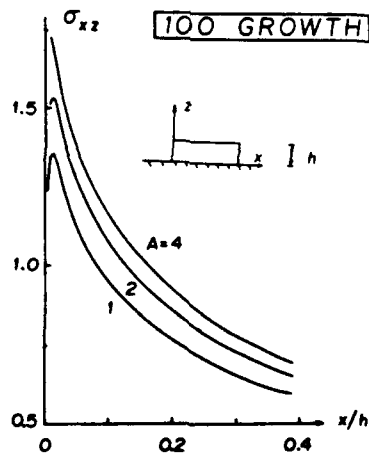


Figure 4: The shear stress  $\sigma_{xz}$  for  $n=100$ . Units are such that far field uniform  $\sigma_{xx}=1$  for isotropic material ( $A=1$ ).



the levels of the shear stress still remain close to the far field value of the internal stress. When compared to the isotropic results ( $A=1$ ), it is seen that anisotropy does not change the qualitative features of the stress distribution along the interface.

Concerning the effect of the interface orientation  $n$  on the resulting stress distribution along the interface, the numerical results showed that the stresses near the free edge with  $n=110$  were within 5% or less of the stresses with  $n=111$  for the same value of  $A$ . Thus, it was concluded that the effect of anisotropy is essentially the same when  $n=111$  or  $110$ . On the other hand, when  $n=100$  the numerical results show that the effect of  $A$  on the peeling stress  $\sigma_{zz}$  is much smaller than when  $n=111$  or  $110$ ; The effect of  $A$  on the shear stress  $\sigma_{xz}$  is stronger, but still weaker than the case with  $n=111$  or  $110$ . A more detailed analysis of the effect of anisotropy is forthcoming.

Several assumptions had to be made in this work, such as the isotropy of the misfit strain  $\epsilon^T$ , or that the substrate is rigid, or that the assumption of plane-strain is valid (thus reducing the problem from three to two dimensions), or that the film remains linearly elastic at the high levels of stress present near the free edge, whereas plastic deformation is expected to relieve the high stresses by a variety of deformation mechanisms, such as dislocation flow or diffusional creep depending on the level of the temperature and on the level of the far field uniform stress [12]. A careful examination of these assumptions is currently under way.

#### ACKNOWLEDGEMENT

This work has been supported by the ONR under Grant N00014-87-K-0488 and in part by the DOE Office of Inertial Fusion under Agreement No. DE-FC0B-85DP 40200 and by the Laser Fusion Feasibility Project at the Laboratory for Laser Energetics which has the following sponsors: Empire State Electric Energy Research Corporation, GE Company, NY State Energy Research and Development Authority, Ontario Hydro, and the University of Rochester, and the Office of Naval Research.

#### REFERENCES

1. R.W. Hoffman, in *Physics of Thin Films*, edited by G. Hass and R.E. Thun (Academic Press, New York, 1966), p. 211.
2. J.W. Hutchinson, M.E. Mear and J.R. Rice, Report MECH-95, Harvard University, 1987.
3. A.G. Evans and J.W. Hutchinson, *Int. J. Solids Structures*, **20**, 455 (1984).
4. D.B. Marshall and A.G. Evans, *J. Appl. Phys.*, **56**, 2632 (1984).
5. B.J. Aleck, *J. Appl. Mech.*, **16**, 118 (1949).
6. R. Zeyfang, *Solid State Electronics*, **14**, 1035 (1971).
7. I.A. Blech and A.A. Levi, *J. Appl. Mech.*, **48**, 442 (1981).
8. M.L. Williams, *J. Appl. Mech.*, **19**, 526 (1952).
9. V.L. Hein and F. Erdogan, *Int. J. Fract. Mech.*, **7**, 317 (1971).
10. E. Suhir, *J. Appl. Mech.*, **53**, 657 (1986).
11. W. Yang and L.B. Freund, Brown University, 1986 (to be published).
12. M. Murakami, in *CRC Critical Reviews in Solid State and Materials Science*, vol. 11, edited by D.E. Schuele and R.W. Hoffman (CRC Press, Boca Raton, 1984), p.317.
13. J.K. Howard, *J. Vac. Sci. Technol.*, **A4**, 1 (1986).
14. J.P. Hirth and J. Lothe, *Theory of Dislocations*, 2nd edition, (John Wiley, New York, 1982), p. 42, 430-431.
15. J.C. Lambropoulos, *J. Crystal Growth*, **80**, 245 (1987).



## Stress Concentration Along Interfaces of Elastic-Plastic Thin Films\*

J. C. LAMBROPOULOS and S.-M. WAN

Department of Mechanical Engineering, University of Rochester, Rochester, NY 14627 (U.S.A.)

(Received June 1, 1988)

### Abstract

Finite element techniques are used to calculate the stress concentrations near the free edge and along the interface of thin films which are bonded to stiff substrates. The material of the film is modeled as elastic-plastic with a linear power-law hardening stress-strain curve in simple shear. It is assumed that the film material is characterized by  $J_2$  deformation theory, and that far from the free edges the film is in a state of uniform balanced biaxial stress which may be due to misfit strain, to thermal strain or to intrinsic stress. Emphasis is placed on the stress concentrations in films of small aspect ratio (modeling the early stages of island growth) or of large aspect ratio (modeling epitaxial or layer-by-layer growth) and on the effect of the hardening exponent on the resulting stress concentrations. It is found that stress concentrations are localized near the film-substrate interface, that films of small aspect ratio have smaller stress concentrations than films of large aspect ratio, and that plastic deformation significantly reduces the stress levels near the interface, although close to the free edge the stress levels are still higher than the far field uniform stresses.

### 1. Introduction

It is well known that thin films grown on substrates are in a state of internal stress which arises as a result of the deposition process (intrinsic stress) or as a result of differential thermal mismatch between film and substrate when the temperature is different from the deposition temperature (thermal stress) [1, 2]. Large values of the internal stress may lead to failure by delamination from the free edge of the film [3], or by

buckling and cracking along the interface between film and substrate [4, 5]. The film materials are used in a wide variety of applications, such as optical [6], electronic [7], or magnetic [8].

Stresses near the vicinity of the free edge of an isotropic film were calculated by Aleck [9], and later by Zeyfang [10] and Blech and Levi [11], who established that close to the free edge large peeling and shear stresses develop. Such stresses considerably exceed the far field internal stress of the film [11]. Williams [12] showed that for a film bonded to a rigid substrate stress singularities develop near the point where the interface meets the free edge. Hein and Erdogan [13] calculated the stress singularity for varying stiffness between film and substrate. They showed that when the film is much stiffer the singularity is  $\sim 1/2$  for large values of the film material angle. When the substrate is much stiffer, the singularity is generally milder [13]. More recently, Lau, Rahman and Delale calculated the free edge singularity for power-law hardening materials and for a variety of different free-edge material angles [14]. Approximate solutions for the stresses along the interface have been presented by Suhir [15, 16], and by Yang and Freund [17], who have approximated the variation of the stresses through the thickness of the film. Stresses in elastic substrates have been calculated by Hu [18] and by Isomae [19] who were mostly interested in evaluating defect densities induced in silicon substrates due to the thin film internal stresses. Interfacial stress distribution in epitaxial films, which are characterized by considerable elastic anisotropy, have been calculated by Lambropoulos and Wan [20].

As Lau *et al.* have pointed out [14], most studies to date have concentrated on linearly elastic constitutive response for the film or substrate materials. More recently, attempts have been made to include material nonlinearities in the analysis of stresses in film-substrate assemblies. Yang and Freund examined plastic and vis-

\*Paper presented at the symposium on Interfacial Phenomena in Composites: Processing, Characterization, and Mechanical Properties, Newport, RI, June 1-3, 1988.



cous material response for the film [17] but, due to the approximation involved, their solution is not valid within 1-2 thickness from the film's free edge. Suhir [16] allowed for nonlinear stiffness of the solder in soldered film-substrate assemblies. Due to the approximations invoked in Suhir's work [15, 16] the traction-free boundary conditions are not satisfied near the film's free edge. As noted above, Lau *et al.* [14] examined singularities in power-law hardening composite wedges. Isomae [21] allowed for linearly viscous response of the film material in an effort to model dislocation generation in silicon substrates with  $\text{SiO}_2$  or  $\text{Si}_3\text{O}_4/\text{SiO}_2$  films. In Isomae's work primary emphasis was placed on the stresses induced in the substrate.

Inelastic effects have long been recognized as leading to significant stress relaxation in metallic films. As examples we mention the work of Murakami *et al.* on Pb [22] and the work of Hershkovitz *et al.* on aluminum [23]. Reviews of the deformation mechanisms in thin films have been provided by Koleshko *et al.* [24], by Murakami [25], and by Chaudhari [26]. Kinoshita [27] has summarized methods for measuring thin film mechanical properties. Deformation mechanisms include diffusional creep, power-law creep and, at lower temperatures and higher stresses, dislocation glide [25, 26]. As noted above, Isomae [21] used linearly viscous constitutive response for  $\text{SiO}_2$  films interacting with silicon substrates.

Concerning plastic deformation of films on substrates by dislocation glide, Hoffman has pointed out that the high stresses along the interface and near the free edge of the film must necessarily lead to plastic flow or fracture, and that the strain gradients are localized near the film edge [3, 28, 29]. Stress-strain curves for gold films measured by Catlin and Walker [30] show a considerable nonlinearity, as do the data of Henning *et al.* on copper and nickel [31].

It is the objective of this report to account for the effect of elastic-plastic relaxation near the free edge and along the film-substrate interface in films which are subjected to a uniform far-field stress (due either to misfit or thermal strain). To simplify the problem, and in view of the studies on stresses in the substrate by Hu [18] and by Isomae [19, 21], we assume that the substrate is rigid, and thus focus our attention exclusively on the film and on the film-substrate interface. We assume that the film is in a state of plane strain, and we account for plastic deformation of the

film material via  $J_2$  deformation theory fitted to a linear-power law hardening stress-strain behavior in simple shear. To account for three-dimensional island-like growth (Volmer-Weber growth [32]) and for epitaxial layer growth (Frank and van der Merwe [32]), we consider films whose lateral extent is similar to the thickness of the film or greatly exceeds it. The basic parameters characterizing our model are the ratio of film lateral extent to film thickness, the ratio of misfit to yield strain, and the hardening exponent of the film material.

## 2. Problem formulation

Figure 1 shows the geometry of a film with thickness  $h$  and lateral extent  $L$ . The free edge of the film is located along  $x=0$ , and the film-substrate interface is at  $y=0$ . For simplicity, and in order to avoid three-dimensional effects, it is assumed that plane-strain conditions prevail along the  $z$  direction. For reasons explained in the Introduction, we concentrate our attention on the film and interface. Thus, we assume that the substrate is rigid, and that displacement and traction continuity is satisfied along the interface  $y=0$ . The sides  $x=0$ ,  $x=L$ , and  $y=h$  are free of tractions. Far from the free edges the film is in a state of balanced biaxial stress, *i.e.*  $\sigma_{xx} = \sigma_{zz}$ , which, furthermore, is uniform in the  $y$  direction.

The film material is taken to be elastic-plastic. Specifically, we assume that in a simple shear test the film material obeys

$$\frac{\epsilon_{12}}{\epsilon_0} = \begin{cases} \tau/\tau_0 & \text{if } |\tau| < \tau_0 \\ (\tau/\tau_0)^n & \text{if } |\tau| \geq \tau_0 \end{cases} \quad (1)$$

where  $\tau_0$  is the yield stress in simple shear,  $\epsilon_0$  is the yield strain which is related to  $\tau_0$  by  $\tau_0 = 2G\epsilon_0$ ,  $G$  being the elastic shear modulus, and  $n$  is the hardening exponent (Fig. 2). For multi-axial stress states the total strain  $\epsilon_{ij}$  is given by

$$\epsilon_{ij} = \epsilon_{ij}^e + \epsilon_{ij}^p + \epsilon_{ij}^T \quad (2)$$

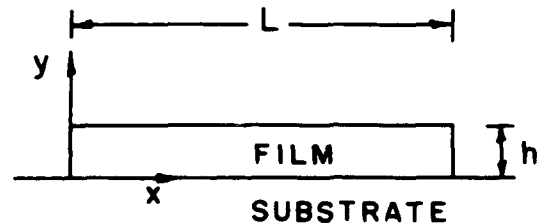


Fig. 1. Film geometry.



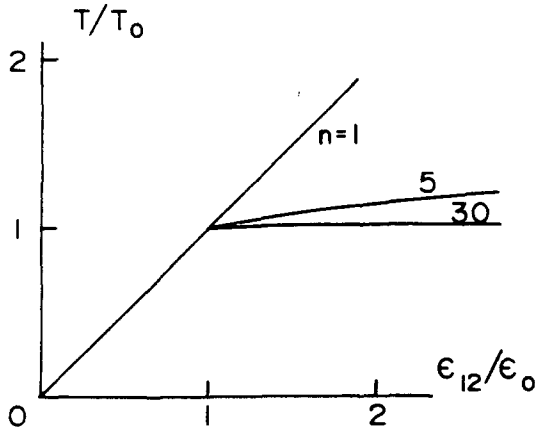


Fig. 2. Linear power-law hardening stress-strain curve in simple shear.

where the elastic strain  $\epsilon_{ij}^e$  is related to the stress tensor  $\sigma_{ij}$  via the usual linear elastic constitutive response, the plastic strain  $\epsilon_{ij}^p$  is related to the stress deviator  $S_{ij} = \sigma_{ij} - \sigma_{kk}\delta_{ij}/3$  by

$$\epsilon_{ij}^p = f S_{ij} \quad (3)$$

where  $f$  is found by invoking  $J_2$  deformation theory, and by fitting eqns. (2), (3) to eqn. (1) with  $\epsilon_{ij}^T = 0$ . Thus, we find that

$$f = \left[ \left( \frac{\bar{\epsilon}}{\epsilon_0} \right)^{1-1/n} - 1 \right] / 2G \quad (4)$$

where  $\bar{\epsilon}$  is the equivalent shear strain defined as  $\bar{\epsilon}^2 = e_{ij}e_{ij}/2$ , with  $e_{ij}$  the strain deviator. Denoting by  $\tau$  the equivalent shear stress defined by  $\tau^2 = S_{ij}S_{ij}/2$ , then  $\tau$  and  $\bar{\epsilon}$  are also related by (1). The last term in eqn. (2) is the misfit strain, which is assumed to consist of only a volumetric component, thus

$$\epsilon_{ij}^T = \epsilon^T \delta_{ij} \quad (5)$$

where  $\delta_{ij}$  is the Kronecker delta. The assumption that  $\epsilon_{ij}^T$  is isotropic is exact when  $\epsilon_{ij}^T$  represents thermal strain due to differential thermal mismatch. For the case of intrinsic stress, the assumption (5) is validated by the physical models of intrinsic stress (such as  $H_2O$  vapor, oxygen or impurity absorption in optical thin films [27, 33], or lattice misfit in epitaxial films [34]). For epitaxial films, nevertheless, it may be more appropriate to take  $\epsilon_{xx}^T = \epsilon_{zz}^T$ ,  $\epsilon_{yy}^T = 0$ .

It is convenient to normalize stresses by the yield stress  $\tau_0$ , strains by the yield strain  $\epsilon_0$ , and distances by the film thickness  $h$ . Thus, it is clear

that the parameters characterizing the present problem are the aspect ratio  $L/2h$ , the ratio of misfit to yield strain  $\epsilon^T/\epsilon_0$ , and the hardening exponent  $n$ .

Solving eqns. (2)–(5) for the stresses, we find

$$\sigma_{ij} = \frac{\epsilon_{ij}}{\eta} + \frac{1}{3} \delta_{ij} \epsilon_{kk} \left( -\frac{1}{\eta} + \frac{1+\nu}{1-2\nu} \right) - \delta_{ij} \frac{1+\nu}{1-2\nu} \theta \quad (6)$$

where  $i, j = 1, 2, 3$  and

$$\epsilon_{zz} = 0 \quad (7)$$

from the plane-strain condition.  $\eta$  is defined by

$$\eta = \begin{cases} \bar{\epsilon}^{(1-1/n)}, & \text{for } \bar{\epsilon} \geq 1 \\ 1, & \text{for } \bar{\epsilon} < 1 \end{cases} \quad (8)$$

and  $\nu$  is the Poisson ratio. The parameter  $\theta$  is defined by

$$\theta = \epsilon^T/\epsilon_0 \quad (9)$$

It is immediately clear that the constitutive law of eqns. (6)–(10) is equivalent to that of a non-linear elastic material. As expected, this is due to the fact that the elastic-plastic response of the film is modeled by using deformation theory of plasticity.

The stresses corresponding to the constitutive law of eqns. (6)–(8) were determined by a displacement-based finite element calculation. Due to the symmetry of the problem, only the domain  $0 \leq x \leq L/2$  was discretized with the boundary condition that the displacement in the  $x$  direction and the shear stress  $\tau_{xy}$  vanish at  $x = L/2$ .

The elements used were bilinear isoparametric rectangles with  $3 \times 3$  Gaussian quadrature. The grid used had approximately 50 nodes in the  $x$  direction and 30 nodes in the  $y$  direction with higher concentration of elements near the interface and near  $x = 0$ . Convergent solutions were achieved for a given  $n$  by using as a first approximation the convergent stress distribution corresponding to the previous value of  $n$ . The results for the stress distributions thus determined will be presented and discussed in the next section.

### 5. Results and discussion

Figures 3 and 4 show the stress distributions  $\sigma_{xy}$  and  $\sigma_{yy}$  versus distance  $x$  along the film-substrate interface for several values of the hardening exponent  $n$ . To avoid interpolation from the Gaussian quadrature points to  $y = 0$ , we



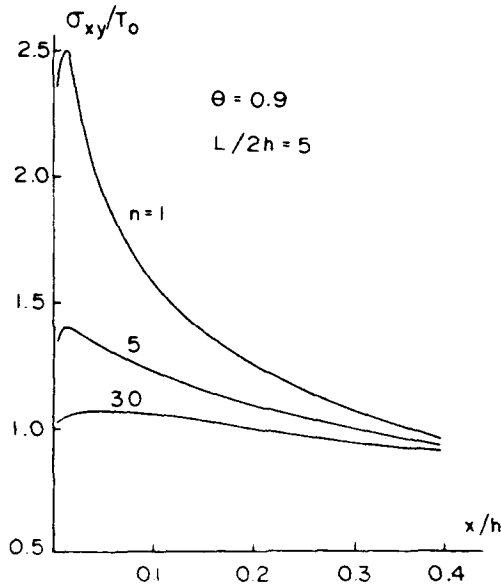


Fig. 3. Shear stress  $\sigma_{xy}$  vs.  $x$  immediately above the film-substrate interface ( $y=0.009h$ ) for various hardening exponents.

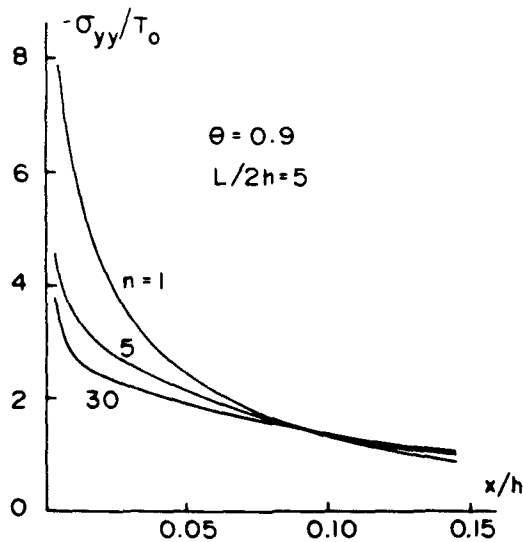


Fig. 4. Peeling stress  $\sigma_{yy}$  vs.  $x$  immediately above the film-substrate interface ( $y=0.009h$ ) for various hardening exponents.

have plotted the stresses along the centers of the elements closed to the interface, which were located at  $y/h=0.009$ . These stress distributions can be converted to stress concentrations by picking the maximum value of  $\sigma_{xy}/\tau_0$  (see Fig. 3) or the value of  $\sigma_{yy}/\tau_0$  at the center of the element closest to  $x=y=0$  (see Fig. 4), dividing by  $\theta$ , and

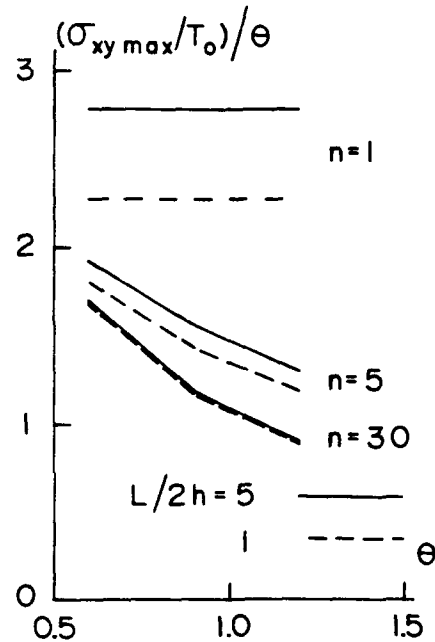


Fig. 5. Non-dimensional shear stress concentration vs. non-dimensional load for  $n=1, 5, 30$ . Solid lines are for thin films ( $L/2h=5$ ). Dashed lines are for thick films ( $L/2h=1$ ).

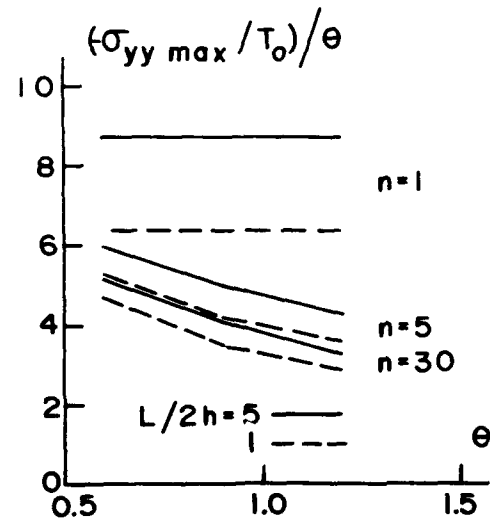


Fig. 6. Non-dimensional peeling stress concentration vs. non-dimensional load for  $n=1, 5, 30$ . Solid lines are for thin films ( $L/2h=5$ ). Dashed lines are for thick films ( $L/2h=1$ ).

by plotting vs.  $\theta$ . The resulting stress concentration factors vs. the dimensionless load parameter  $\theta$  are shown in Figs. 5 and 6 for the shear stress  $\sigma_{xy}$  and for the peeling stress  $\sigma_{yy}$ , respectively, for various values of the hardening exponent  $n$  and



for two values of the aspect ratio, 5 and 1, corresponding to thin films ( $L \gg h$ ) and three-dimensional island-like growths ( $L \approx h$ ).

Finally, Figs. 7 and 8 show the development of the dimensions of the plastic zone with the load parameter  $\theta$ . Specifically, Fig. 7 shows contours of the equivalent shear stress  $\tau$  for the case of thin films with  $n = 30$ , for several values of  $\theta$ ; Fig. 8 shows the dependence of the dimensions  $H$ ,  $D$  of the plastic zone on the hardening exponent  $n$  for thin films ( $L/2h = 5$ ). In the results shown in Figs. 3-8 the Poisson ratio is taken as 0.3.

It can be easily shown that the far-field material becomes plastic (i.e.  $\tau$  exceeds  $\tau_0$ ) when  $\theta = 0.93$ . Thus, when  $\theta < 0.93$  the plastic deformation is localized near the free edge  $x = 0$ . As  $\theta$  approaches 0.93 from below, the extent  $D$  of the plastic zone increases rapidly, and extends through the whole of the film as  $\theta$  exceeds 0.93. Figure 8 shows that the dimension  $D$ ,  $H$  of the plastic zone depend weakly on the hardening exponent  $n$ , implying that, for example, linear elastic solutions [9-11, 15, 16] can be used to estimate  $D$  and  $H$ . On the other hand, as expected,  $D$  depends very strongly on the loading parameter  $\theta$ . Examination of Fig. 7 shows that plastic deformation is localized within a narrow strip which starts at the free edge  $x = 0$  and extends parallel to the film-substrate interface. Outside this zone of intense plastic deformation the film material is weakly stressed. If one were to think of plastic deformation in terms of the

propagation of interfacial dislocations, Fig. 7 shows that a continuum plasticity approach agrees qualitatively with the fact that interfacial dislocations propagate along the film-substrate interface [32, 34]. Our calculation presently establishes the interface between film and substrate as being extensively deformed into the plastic region. This observation is in agreement with the results of Lau *et al.* [14] in which the angular variation of the stress components resulting from the asymptotic analysis is such that the peeling stress is maximum along the interface.

The stress concentration plots of Figs. 5 and 6 show that bulky films ( $L \approx h$ , modeling thus island mode of film growth) are in general less stressed than thin films ( $L \gg h$ , modeling epitaxial mode of film growth [32]). The difference is largest for linear elastic films; it diminishes considerably as hardening diminishes. As the films are progressively stressed into the plastic region, the stress

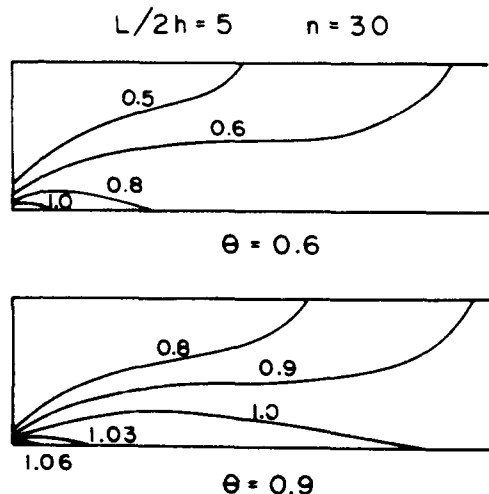


Fig. 7. Contours of equivalent shear stress  $\tau$  normalized with respect to yield stress  $\tau_0$ . General yield occurs in the far-field material for  $\theta = 0.93$ .

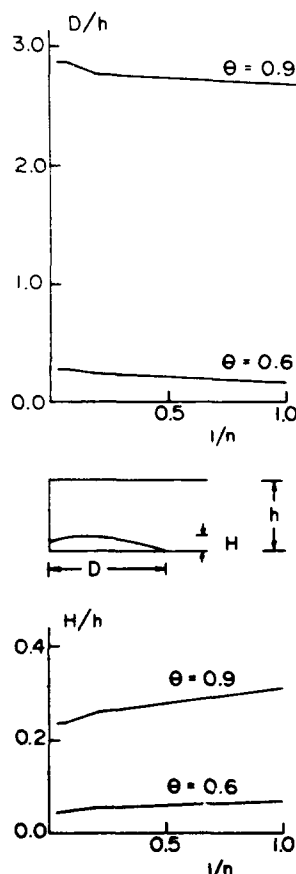


Fig. 8. Variation of extent  $D$  and height  $H$  of plastic zone vs. strain hardening exponent  $n$ . The aspect ratio is  $L/2h = 5$ .



concentrations diminish as a result of stress relaxation by plastic deformation. Thus, the absolute values of the stresses increase as  $\theta$  increases, but less rapidly than  $\theta$  itself.

Figures 3 and 4 show that smaller amount of hardening leads to considerably lower stress values. We note from these figures that within, say,  $0.1 h$  along the interface the stresses exceed considerably the yield stress of the material. Even when  $n = 30$  the peeling stress is as large as  $2-4 \tau_0$ , while the shear stress is no less than  $\tau_0$ . We note that these stress concentrations are localized within a fraction of the film's thickness from the free edge, and close to the interface (see Fig. 7). As  $x/h \rightarrow \infty$  both  $\sigma_{yy}$  and  $\sigma_{xy}$  must vanish. When  $\theta > 0$  (implying that the far-field material is in compression) the largest value of  $\sigma_{yy}$  is also compressive (Fig. 4), but  $\sigma_{yy}$  changes to tensile with a maximum positive value at a distance of about  $0.5-1$  thickness along the interface [9-11]. This maximum is diffuse and only a fraction of the far-field stress. It is concluded that when the film is in far-field compression, the anticipated mode of failure is by shearing along the interface. When  $\theta < 0$  other modes of failure are also observed (e.g. buckling and interfacial delamination [4]). In this context we note that thin polycrystalline metallic films exhibit hardening behavior and yield stress which is quite different from the corresponding quantities for bulk materials. Hoffman [1] has compiled data which show that the hardening (about  $1/n$ ) diminishes as the film thickness increases. Similarly, the yield stress decreases as the thickness increases. Thus, when the thickness is too small, the film may fail in a brittle manner. Such observations are in agreement with experimental observations of Pashley in gold films thinner than  $50 \text{ nm}$  [35]. For other film materials, such as nickel [1], the plastic and elastic strains at fracture are comparable. The dependence of yield stress on thickness has been modeled by Chaudhari [26, 36] and Ronay [37] who argue that a critical film thickness exists below which plastic flow does not occur and above which the residual elastic strain shows an inverse thickness dependence. When  $\theta < 0$  (implying that the far-field film material is in tension), then the large values of the peeling stress along the interface are tensile and considerably exceed the yield stress  $\tau_0$  of the film material. We conclude that in this case the anticipated failure mode is by peeling away from the interface. Again, other modes of failure are possible [3].

The use of deformation theory of plasticity to describe the inelastic deformation of the film material is justified by observing that the stresses increase monotonically as the loading parameter  $\theta$  increases. Furthermore, the calculation presented herein can be used in film growth when  $h$  is a monotonically increasing function of time. As discussed above,  $\tau_0$  is a decreasing function of  $h$ , and  $\theta (= \epsilon^T/\epsilon_0)$  is a decreasing function of  $\epsilon_0$  or  $\tau_0$ . We conclude that  $\theta$  is an increasing function of  $h$ , so that deformation theory can be used to model the elastic-plastic deformation of thin films during film growth. Still, deformation theory would be inadequate when significant amounts of unloading are involved. This would be the case when for a film of fixed thickness  $h$  the temperature has a sinusoidal dependence on time with a maximum value  $\Delta T$  such that  $\Delta \alpha \Delta T > \epsilon_0$ ,  $\Delta \alpha$  being the differential thermal mismatch between film and substrate.

All calculations presented herein refer to the case when the angle between the free surface of the film and the interface is  $\pi/2$ . Once a crack is nucleated (by shearing deformation for  $\theta > 0$ , and by peeling for  $\theta < 0$ ), the geometry changes radically since now a crack exists along the interface between the film and the substrate. In such a case, the extensive work of Shih and Asaro [38] on cracks between dissimilar elastic-plastic media is to be consulted.

#### 4. Conclusions

Finite element methods were used to determine the stress distributions near the free edge and along the interface in film-substrate assemblies. The film material was assumed to be elastic-plastic characterized by a linear, power-law hardening stress-strain curve in pure shear, and by  $J_2$  deformation theory for multiaxial stress states. The main parameters describing the problem are the hardening exponent  $n$ , the ratio of misfit to yield strain, and the aspect ratio of the film. It was found that near the free edge plastic deformation relaxes the elastic stress concentration. Still, near the free edge the shear stresses are no less than the yield stress, and the peeling stresses are at least several times higher than the yield stress. These concentrations are localized within a small fraction ( $0.1-0.5$ ) of the film thickness from the film's free edge. Far from the free edge the film is in a state of balanced biaxial tension or compression.



The extent of the plastic zone depends weakly on the hardening exponent  $n$ , and strongly on the ratio of misfit to yield strain. The zone of plastic deformation is localized within a narrow region along the film-substrate interface, and it propagates parallel to the interface as the misfit strain increases in relation to the yield strain. Plastic deformation reduces the elastic stress concentration both for thin and thick films. When the far-field film material is in compression, the anticipated mode of local failure in the vicinity of the free edge is by shear; when in tension, the local mode of failure is expected to be by peeling. The applicability of deformation theory of plasticity was justified since stresses increase monotonically with the misfit strain. For film growth, deformation theory is again applicable since the yield strain is a decreasing function of film thickness.

#### Acknowledgments

This work was supported by the Office of Naval Research via grant N00014-87-K-0488, and by the National Science Foundation via a 1988 Presidential Young Investigator Award.

#### References

- 1 R. W. Hoffman, in G. Hass and R. E. Thun (eds.), *Physics of Thin Films*, Vol. 3, Academic Press, New York, 1966, p. 211.
- 2 K. L. Chopra, *Thin Film Phenomena*, McGraw-Hill, New York, 1969.
- 3 R. W. Hoffman, *Mater. Sci. Eng.*, 53 (1982) 37.
- 4 A. G. Evans and J. W. Hutchinson, *Int. J. Solids Struct.*, 20 (1984) 455.
- 5 D. B. Marshall and A. G. Evans, *J. Appl. Phys.*, 56 (1984) 2632.
- 6 R. R. Austin, R. Michaud, A. H. Guenther, and J. Putman, *Appl. Optics*, 12 (1973) 665.
- 7 R. Rosenberg, T.-S. Kuan, and H. J. Hovel, *Phys. Today*, 33 (1980) 40.
- 8 J. K. Howard, *J. Vac. Sci. Technol. A*, 4 (1986) 1.
- 9 B. J. Aleck, *J. Appl. Mech.*, 16 (1949) 118.
- 10 R. Zeyfang, *Solid State Electron.*, 14 (1971) 1035.
- 11 I. A. Blech and A. A. Levi, *J. Appl. Mech.*, 48 (1981) 442.
- 12 M. L. Williams, *J. Appl. Mech.*, 19 (1952) 526.
- 13 V. L. Hein and F. Erdogan, *Int. J. Fract. Mech.*, 48 (1981) 442.
- 14 C. W. Lau, A. Rahman and F. Delale, in W. E. Moddeman et al. (eds.), *Technology of Glass, Ceramic, or Glass-Ceramic to Metal Sealing*, ASME MD Vol. 4, 1987, p. 89.
- 15 E. Suhir, *J. Appl. Mech.*, 53 (1986) 657.
- 16 E. Suhir, *Calculated Thermally Induced Stresses in Adhesively Bonded and Soldered Assemblies*, AT&T Bell Labs, 1986, to be published.
- 17 W. Yang and L. B. Freund, *Shear Stress Concentration Near the Edge of a Thin Film*, Brown University, 1986, to be published.
- 18 S. M. Hu, *J. Appl. Phys.*, 50 (1979) 4661.
- 19 S. Isomae, *J. Appl. Phys.*, 52 (1981) 2782.
- 20 J. C. Lambropoulos and S.-M. Wan, in R. C. Sundahl et al. (eds.), *Electronic Packaging Materials Science, Mater. Res. Soc. Symp. Proc.*, 108 (1988) 399.
- 21 S. Isomae, *J. Appl. Phys.*, 57 (1985) 216.
- 22 M. Murakami, *Acta Metall.*, 26 (1978) 175.
- 23 M. Hershkovitz, I. A. Blech and Y. Komen, *Thin Solid Films*, 130 (1985) 87.
- 24 V. M. Koleshko, V. F. Belitsky and I. V. Kiryushin, *Thin Solid Films*, 142 (1986) 199.
- 25 M. Murakami, in D. E. Schuele and R. W. Hoffman (eds.), *Critical Reviews in Solid State and Materials Sciences*, Vol. 11, CRC, Cleveland, OH, 1984, p. 317.
- 26 P. Chaudhari, *IBM J. Res. Dev.*, 13 (1969) 197.
- 27 K. Kinoshita, *Thin Solid Films*, 12 (1972) 17.
- 28 R. W. Hoffman, *Surf. Interface Anal.*, 3 (1981) 62.
- 29 R. W. Hoffman, *Thin Solid Films*, 89 (1982) 155.
- 30 A. Cathin and W. P. Walker, *J. Appl. Phys.*, 31 (1960) 2135.
- 31 C. A. Henning, F. W. Boswell and J. M. Corbett, *Acta Metall.*, 23 (1975) 177.
- 32 R. W. Vook, *Opt. Eng.*, 23 (1984) 343.
- 33 H. K. Pulker and J. Maser, *Thin Solid Films*, 59 (1979) 65.
- 34 I. Markov and S. Stoyanov, *Contemp. Phys.*, 28 (1987) 267.
- 35 D. W. Pashley, *Proc. R. Soc. London, Ser. A*, 255 (1960) 218.
- 36 P. Chaudhari, *Philos. Mag. A*, 39 (1979) 507.
- 37 M. Ronay, *Philos. Mag. A*, 40 (1979) 145.
- 38 C. F. Shih and R. J. Asaro, *Elastic-Plastic Analysis of Cracks on Bimaterial Interfaces. Part I: Small Scale Yielding*, Brown University, 1987.



## **APPENDIX (3)**

J.C.M. Li, P.D. Funkenbusch, and J. C. Lambropoulos,  
Microstructural control through strategic materials processing, in  
Ashby Symposium: The Modelling of Material Behavior and Its  
Relation to Design, ed. J.D. Embury and A.W. Thompson, The  
Minerals, Metals & Materials Society (TMS), pp. 149-173 (1990).



## MICROSTRUCTURAL CONTROL THROUGH

### STRATEGIC MATERIALS PROCESSING

P. D. Funkenbusch, John Lambropoulos and J. C. M. Li

Materials Science Program,  
Department of Mechanical Engineering,  
University of Rochester,  
Rochester, NY 14627 USA

#### Abstract

Innovative application of known principles can optimize processing variables to create new materials with desirable properties. Examples are illustrated in solute transport without generating dislocations, strengthening by deformation processing of two-phase composites, growth of single crystals with controlled dislocation density, thin film deposition with minimum interfacial stresses, and powder consolidation by hot isostatic pressing. Computer aided materials design is expected to make significant contributions in the near future.

#### Introduction

The selection of materials to construct a component or a device is always a major problem in design. In many instances the limitation is not a lack of physical principles but a lack of proper materials. A good example is the recent attention to superconductors. Imagine what kind of world we will be living in when room temperature superconducting materials exist. Because of such a material limitation, many current design problems must include not only the selection of existing materials but also the design of new materials. We would like to propose "Materials Design" as a new field of study which, like any other design, is to apply known principles to create new materials or to find new usage. It may include new processing techniques, new characterization techniques and new property studies. As just discussed it is becoming increasingly important in the design of components, devices, and systems.

In this paper we would like to show several examples of how "Materials Design" would allow sophisticated techniques to control the materials microstructure and hence their properties.

#### Transport of Solutes without Introducing Dislocations

A common practice in materials processing is to alter composition by transporting the desired component through the external surfaces. The accompanying problem is that diffusion induced stresses could be so large as to generate dislocations (1-4) from the free surfaces or grain boundaries and other interfaces. This altered microstructure is sometimes beneficial (as in case hardening) but other times detrimental (as in electronic materials).

As an example (5) a slab of thickness  $2a$  has no solute to begin with and at time zero the surface concentration is maintained at  $C_s$ . It is seen from the top of Fig. 1 how the concentration profile develops and progresses to reach a uniform concentration. Let us assume that the slab has no stress in the beginning. Then after the concentration becomes uniform, again there will be no stress. In the interim, however, large stresses could be developed as shown in Fig. 1. The unit of stress is  $VEC_p/3(1-\nu)$  where  $V$  is the partial molar volume of the solute,  $E$  is Young's modulus of the material,  $C_p$  is the surface concentration in moles per unit volume, and  $\nu$  is Poisson's ratio. If  $V$  is positive, the stress is compressive near the surfaces and tensile in the middle. Since there is no applied stress, the average internal stress must be zero.

It is seen from Fig. 1 that the stress developed at the surface in the beginning is the largest. All the stresses developed subsequently are smaller. The center of the slab can have stresses even before the solutes reach there. The more solutes diffuse into the material, the less the stress is everywhere in the slab. Finally when the concentration is uniform, the stress is everywhere zero.

If the solute addition is not by maintaining the surface concentration at  $C_s$  but rather by plating or depositing the whole amount on the surfaces and if the whole amount is soluble in the material, the situation is shown in Fig. 2. It turns out that the concentration distribution and the stress distribution at any time can be represented in one graph. The left scale is concentration and the right scale is stress. The unit of stress is now  $VEC_p/3(1-\nu)$  where  $\bar{C}$  is the average concentration (or the final uniform concentration) and is a constant. It is seen that the center



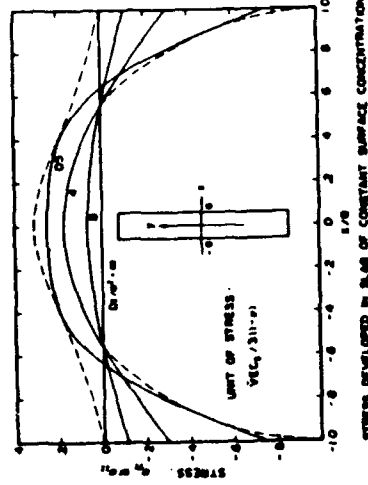
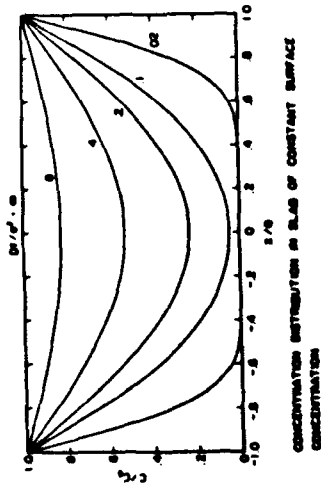


Fig. 1 Concentration Distribution and Stress Developed in Slab of Constant Surface Concentration

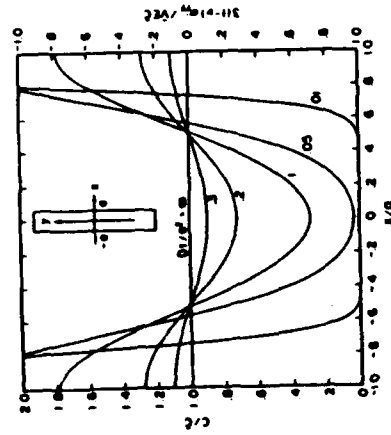


Fig. 2 Concentration and Stress Distribution in Slab with a Fixed Amount of Solute Deposited Initially on the Surface

of the slab has stresses right from the beginning which are larger than those anywhere inside the slab except near the surfaces. The stresses are tensile near the center of the slab and compressive near the surfaces if  $V$  is positive. The sign of stresses is changed if  $V$  is negative. The average is of course zero without applied stresses. If the whole amount is not soluble in the material, it reduces to the previous case in which  $C_s$  is the solubility. In both cases the maximum stress occurs at the surface.

The variation of surface stress with time is shown in Fig. 3. It is seen that it monotonically decreases to zero in both situations. If the largest stress is set below the yield stress by adjusting the surface concentration  $C_s$ , it is obvious that during diffusion we will never have a stress exceeding the yield stress of the material. Hence this is one way to alter the composition without generating dislocations.

However, this may not be the fastest way. While in the beginning the surface concentration must be chosen so that the surface stress is below the yield stress, the surface concentration may be increased later such that the surface stress is maintained close to but below the yield stress. This problem was solved analytically (6) and the result is shown in Fig. 4. It is seen that the surface concentration can be increased continuously without anywhere exceeding the yield stress. It was shown (6) that this scheme is the fastest possible way of transporting solutes from the surfaces without generating dislocations.

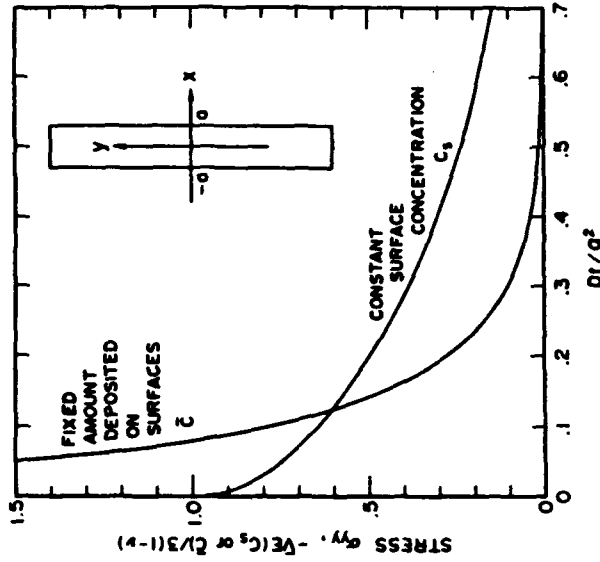


Fig. 3 Surface Stress Developed in Slab during Diffusion



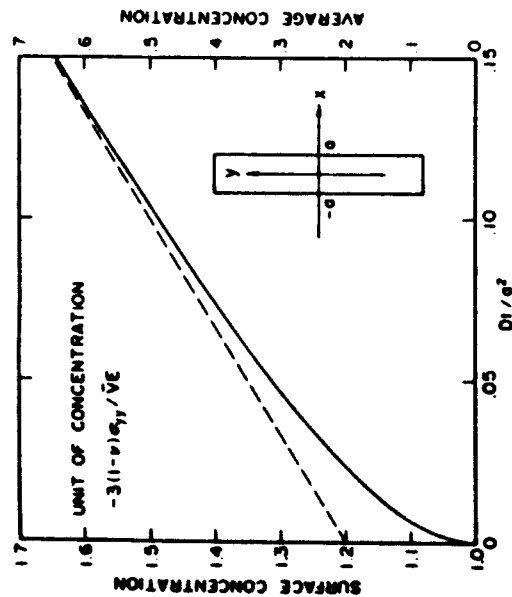


Fig. 4 Programmed Diffusion for Constant Surface Stress

#### Deformation Processed Composite Materials

If any alloy containing two deformable phases is heavily worked a composite microstructure of very fine scale can be developed (e.g. 7,8). Such "Deformation Processed Composite Materials" (DPCM) exhibit interesting properties including very rapid increases in strength with processing strain. This behavior can be understood in terms of the general tendency for two-phase materials to work harden rapidly as a result of the presence of finely spaced interphase boundaries, coupled with a rapid decrease in boundary spacing with deformation (9).

Composite work hardening can be modeled using the dislocation density in each phase as the sole determinant of the strength of that phase (9, 10). Such "one parameter" models neglect the potential for interphase boundaries to act as direct (pile-up) barriers to dislocation motion. They also gloss over the finer details of substructural development (e.g. the potential for dislocation rearrangement into cell walls (11)). However, they are consistent with most direct and indirect observations of composite substructure (7, 8, 12) and correctly predict the importance of deformation processing, temperature and annealing on strength (e.g. 9, 13, 14).

Development of "extra" or geometrical dislocation line length during deformation as a result of grain boundaries has been considered by Ashby (15). He predicted a dislocation density,  $\rho$ , of

$$\rho \approx K \left( \frac{\epsilon}{D} \right) \quad (1)$$

where  $\epsilon$  is the strain,  $D$  the grain size, and  $K$  a geometrical constant. For the two-phase, high strain case  $D$  must refer to the interphase boundary spacing and will vary exponentially with strain. In addition the dislocations generated may be in either of the phases. These considerations lead to a new equation for the dislocation density in phase A (with an equivalent expression for phase B):

$$\rho_A = 2K \left( \frac{P_A}{V_A} \right) \left[ 1 - \exp \left( -\frac{\epsilon_T}{2} \right) \right] / D \quad (2)$$

where  $D$  is now the final interphase boundary spacing,  $\epsilon_T$  is the total processing strain,  $V_A$  is the volume fraction of phase A and the factor  $P_A$  is a "partitioning" coefficient. In effect  $P_A$  and  $V_A$  together act to "divide" the geometrical dislocations between the phases. (For a more detailed discussion of this point please see reference 9. Although included for completeness in the original derivation, final modeling results are not very sensitive to  $P$  and it can be approximated as 1/2).

Equation 2 considers only geometrical dislocations. The potential for "statistical" dislocation multiplication and annihilation also needs to be considered. A very simple model, based on the Kocks' model for low temperature creep (16) is:

$$d\rho_A \approx \left[ C_{1A} \sqrt{\rho_A} - C_{2A} \rho_A \right] d\epsilon_T \quad (3)$$

with, again, an equivalent expression written for the second phase.  $C_{1A}$  and  $C_{2A}$  are constants reflecting the relative tendency for dislocation multiplication and annihilation, respectively, and can be derived from single phase work hardening data for each phase. Note that since the increase or decrease in dislocation density predicted by Equation (2) is itself dependent on the total dislocation density, there will be an interaction between the "geometrical" and "statistical" terms in a composite. Materials with a strong tendency toward dislocation annihilation/recovery in single phase form are predicted to strengthen more slowly in the composite as well.

Equations (2) and (3) can be combined and numerically integrated to predict the change in dislocation density with deformation strain and, thus, the strength of each of the component phases. A modified rule of mixtures is then used to estimate composite strength. The constant  $K$  remains in these calculations as an adjustable parameter and must, in effect, compensate for the various first-order approximations required in this derivation. Unfortunately, therefore, we are unable to predict  $K$  (and hence the composite strength) a priori. However, from examination of Equations (2) and (3) there are clearly several general guidelines that can be advanced for "designing" high strength DPCM:

1. The final microstructural scale (i.e.  $D$ ) should be as fine as possible.
2. At least moderate deformation (i.e.  $\epsilon_T > 1$ ) should be incorporated in the processing. Very fine scale microstructures can also be produced by techniques other than deformation processing. Everett (13) has recently



compared the strengthening in such composites with that obtained in comparable DPCM and, as expected from Equation [2], the DPCM was significantly stronger in all cases. This confirms the importance of substructural development during deformation in the strengthening of these materials. On the other hand, at high strains Equation [2] predicts that the direct effects of  $\epsilon$  should "saturate" and strength will be determined chiefly by the final value of  $D$ . This is also observed experimentally (e.g. 7).

3. Since statistical dislocation multiplication and annihilation are also important in composite strengthening, phases with "strong" high strain work hardening behavior should be included in DPCM. This is limited somewhat, however, by the need to consider composite deformability (17). A common observation in DPCM, again recently summarized by Everett (13), is that fcc-bcc composites strengthen more quickly with deformation than fcc-fcc combinations. This observation is, then, explicable in terms of the generally stronger high-strain work hardening behavior observed in bcc materials at room temperature. Annealing experiments also suggest that the bcc component in fcc-bcc composites plays the predominant role in strengthening (e.g. 9).

The extent to which the above concepts have been consciously applied to design of DPCM is unclear. However the materials of most active research interest in the DPCM area are precisely those indicated by this analysis, (i.e. fine, heavily deformed composites containing a bcc phase, for example Cu-Nb).

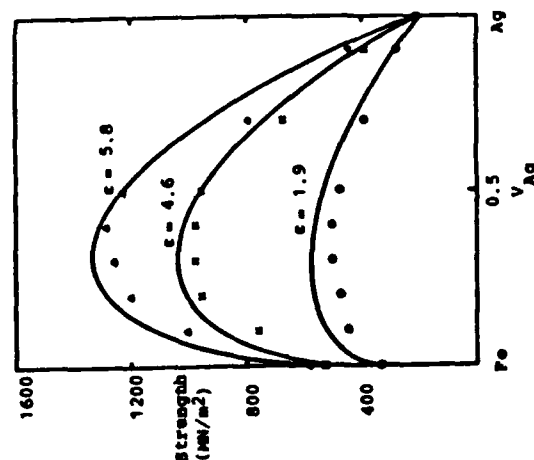


Fig. 5 Tensile strain vs. volume fraction relationship for Fe-Ag deformation processed composites. Experimental data from reference 18 (Wahl and Wassermann). The solid lines are model predictions based on a value of the adjustable parameter,  $K$ , determined using the data for a single (iron - 47 vol. % silver) composite. (Reproduced from reference 10)

Finally, although  $K$  cannot be predicted a priori, once it has been found for a given material combination it can then be used to predict the strength of other alloys in that system as a function of volume fraction, deformation strain, and microstructural scale. Figure 5 is an example of this approach and uses the data of Wahl and Wassermann (18) for a series of Ag-Fe DPCM. In this case  $K$  was estimated from the data for a Fe-47 vol.% Ag composite, and this value was then used to estimate the strength of the other composites as a function of deformation strain (10). Very good agreement is obtained overall. Further, the experimental "peak" in composite strength occurs very close to that predicted from the model. (This peak is dependent on an underlying variation of microstructural scale with volume fraction as well as on the direct effect of changing the volume fraction of the two phases.)

#### Single Crystal Growth with Controlled, or Minimized, Dislocation Density

The growth of single crystals with minimized dislocation density is a necessary prerequisite for the reliable design of electronic and photovoltaic components. Typical materials grown are Si, GaAs and InP among others (19,20). Dislocations have been attributed to excessive thermal stresses which are induced as a result of excessive temperature gradients near the solid-liquid interface of the growing crystal (19,21). As typical examples of such crystal growth techniques from the melt we mention Czochralski growth (19), edged-defined film-fed growth (EFG) of flat plates (20) and EFG growth of thin walled polygonal tubes whose cross section is hexagonal, nine-sided, or circular (12).

The thermal stresses during shaped cylindrical crystal growth, as shown in Figure 6, have been calculated, by using various approximations, by Penning (21), and by Jordan et al. (19). Numerical solutions have been presented by Motakef and Witt (23), by Kobayashi and coworkers (24), by Szabo (25), by Duseaux (26), by Schvezov et al. (27) and by Lambropoulos (28, 29). A common conclusion of these workers has been that all significant stress extremes occur within one length scale from the solid-liquid interface during crystal growth.

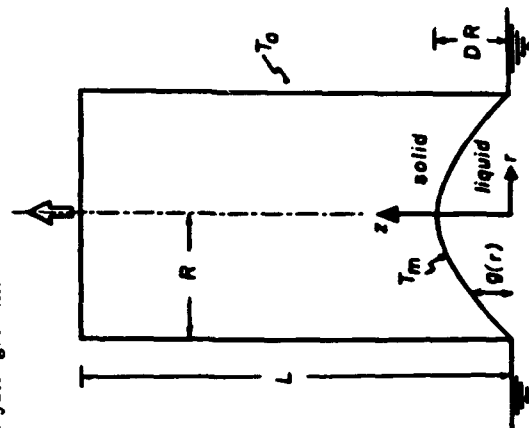


Fig. 6 The geometry of cylindrical shaped crystal growth from the melt (Czochralski)



The density of grown dislocations can be controlled in either of two manners: For a given crystal growth technique, the thermal stresses can be minimized essentially by reducing the thermal gradients. This is achieved by reducing the size of the grown crystal: Si and GaAs crystals of small dimensions can be easily grown, although it is desirable to grow as large a crystal as possible. Thermal stresses can also be reduced by diminishing, for example, the difference between the melting point and the ambient temperature of the furnace within which the crystal is growing. On the other hand, for a given crystal size, temperature gradient and growth rate it is possible to control and minimize the density of grown dislocations by controlling the orientation of the grown crystal or the shape of the solid-liquid interface or the geometry and shape of the outer periphery of the crystal. Finally, for a given material, the different crystal growth techniques may produce widely different thermal stresses and, consequently, dislocation density levels.

The effect of crystal growth orientation is shown in Figures 7 and 8 for the case of Czochralski growth (30). The temperature distribution is calculated first: it satisfies the steady state heat conduction equation (19)  $k \nabla^2 T = \rho_0 \sigma T / \alpha z$ , where  $\rho_0$  is the rate of growth,  $z$  is the growth direction,  $R$  is the radius of the growing crystal, and  $k$  is the thermal conductivity of the crystal, and the boundary conditions are  $T = T_m$  at the solid-liquid interface which is assumed to be planar, and  $K \partial T / \partial n + h(T - T_0) = 0$  at the lateral cylindrical surface  $r = R$ , where  $n$  is the outward pointing unit normal,  $h$  is the cooling coefficient, and  $T_0$  is the ambient temperature of the furnace. The thermoelastic stresses are calculated numerically using finite elements with the constitutive law  $\sigma_{ij} = C_{ijkl}(\epsilon_{ij} - \alpha_i \delta_{ij})$ ,

where  $\sigma_{ij}$ ,  $\epsilon_{ij}$  are the stress and strain tensors, respectively, in the crystal's

coordinate system,  $C_{ijkl}$  is the elastic stiffness matrix with cubic symmetry,  $\alpha$  is the coefficient of thermal expansion, and  $\delta_{ij}$  is the Kronecker delta. Having found the stresses, the dislocation density is approximated by (19, 23, 27, 29)

$$\rho = \sum_{i=1}^{12} \langle \sigma_{ij} n_i m_j - \tau_c \rangle \quad [4]$$

where  $\langle x \rangle = x$  if  $x > 0$  and  $= 0$  otherwise,  $n, m$  represent the crystallographic slip system of the type  $\{111\}\{110\}$ , the sum extends over all 12 slip systems, and  $\tau_c$  is the critical resolved shear stress. Although a dislocation density measure of the type shown in Equation (4) is approximate, it has been used extensively in the crystal growth literature, and it becomes increasingly accurate when the resolved shear stress does not greatly exceed the critical resolved shear stress  $\tau_c$ . Figures 7 and 8 show the dislocation density distribution for several crystal growth directions, as calculated via Eq. (4), at  $z = R/2$ ,  $r = R$  and at  $z = R/2$ ,  $r = 0$  as a function of the circumferential angle  $\theta$  for several values of the anisotropic parameter  $A = 2C_{44}/(C_{11} - C_{12})$ , which has a value of 1 for isotropic materials. It has been established previously, that at about half a radius above the solid-liquid interface the thermal stresses are maximized (23, 29). In the results of Figures 7 and 8, the Biot number  $B = hR/k$  is taken to be equal to 1, a value typical for the growth of GaAs, and the critical resolved shear stress  $\tau_c$  was taken equal to  $0.004 \alpha C(T_m - T_0)$ , where  $C = C_{11} + C_{12} - 2C_{13}^2/C_{11}$  (C reduces to the familiar term  $E/(1-\nu)$  for isotropic materials,  $\nu$  being the Poisson ratio). Such a value of the critical resolved shear stress corresponds to GaAs near its melting point and with  $T_m - T_0 = 140$  K. For InP, the temperature difference would be 80 K; for Si it would be 1000 K (30).

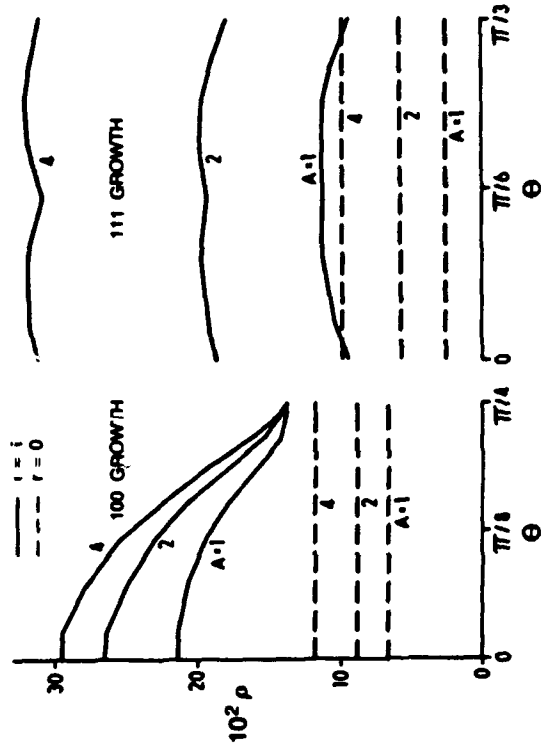


Fig. 7 Dislocation density  $\rho$  at the center and outer periphery versus angle  $\theta$ , at one-half radius above the solid-liquid interface for  $<100>$  and  $<111>$  growth and for several values of the anisotropic parameter  $A$ .

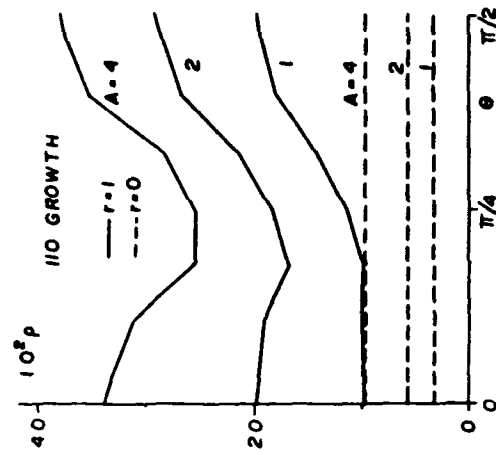


Fig. 8 Dislocation density  $\rho$  at the center and outer periphery versus angle  $\theta$ , at one-half radius above the solid-liquid interface for  $<110>$  growth and for several values of the anisotropic parameter  $A$ .



It is clear from Figures 7 and 8 that the effect of crystal growth orientation is not negligible, and that, since the anisotropic parameter  $A$  for semiconductors is between 2 and 4 [19, 29, 30], crystal growth directions exist which minimize the resultant dislocation densities during growth. These results also help to explain the experimental observation that growth along  $\langle 111 \rangle$  produces more dislocations than along  $\langle 100 \rangle$  (31), although isotropic elasticity calculations would predict the opposite effect. Furthermore, Figures 7 and 8 show that the dislocation density is maximum in the outer periphery of the crystal. There is an absolute minimum near  $r=R/2$ , and a relative minimum or maximum at  $r=0$ , so that the dislocation density levels across a diameter of the grown crystal produce a characteristic W or U shape (19, 24, 28).

The effect of the solid-liquid interface shape during Czochralski growth (32) is shown in Figure 9 where the maximum values (occurring in the center of the interface and at some small distance above it at the outer periphery of the crystal) of the equivalent shear stress  $\sigma_m$  and the hydrostatic stress  $\sigma_m = (\sigma_{rr} + \sigma_{\theta\theta} + \sigma_{zz})/3$  are shown as functions of the deviation  $D$  from planarity of the interface. It is assumed that the interface has a parabolic shape given by  $z = D(1 - (r/R)^2)$  where  $D$  is the maximum deviation from planarity in the center of the solid-liquid interface. The deviation  $D$  depends on the cooling coefficient  $h$ , the pulling rate  $p_0$ , and the detailed heat transfer along the interface (33,34). It is seen that when the interface extends into the crystal a notch-like effect develops which leads to significant stresses in the center of the solid-liquid interface. It is concluded that control of the interfacial shape during crystal growth can be used to control the resulting thermal stresses and dislocation densities.

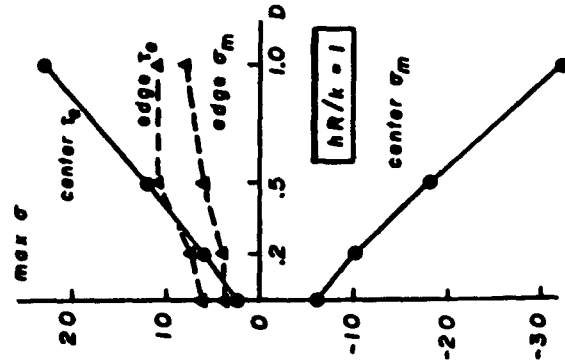


Fig. 9 Variation with  $D$  of the maximum values of equivalent shear stress and hydrostatic tension near the center ( $r=0$ ) and near the outer periphery of the crystal ( $r=1$ ). The units of stress are  $E\alpha(T_m - T_c)/100$ .

In comparing different crystal growth techniques, it is useful to keep in mind that different length scales dominate the generation of thermal stresses and, hence, dislocation densities. For example, it is obvious that during Czochralski growth the only relevant length scale is the radius or diameter of the growing crystal which is typically between 5 and 10 cm. For the EFG growth of thin flat plates (typical thickness 100  $\mu$ m), the relevant length scale is the width of the plate which, again, has typical values of 5-10 cm. On the other hand, for the growth of thin cylindrical tubes of similar radial extent ( $R=5-10$  cm and similar thickness  $t=100$   $\mu$ m), the length scale is now  $\sqrt{(Rt)}$  which is an order of magnitude smaller than the length scale of EFG growth of flat plates. Thus, the growth of flat plates vs. the growth of thin cylindrical tubes, both by the EFG method, can lead to significantly different stress levels.

Due to the presence of the solid-liquid interface, which is free of any tractions, the calculation of thermal stresses by analytical means has proven a tedious task. When more realistic material properties are employed (e.g. temperature dependent), or more accurate temperature distributions are calculated, analytical solutions are not feasible anymore and the use of numerical techniques, principally finite elements, becomes an indispensable tool. When the inelasticity of the growing crystal is also accounted for, as in the work of Lambropoulos et al. on the EFG growth of Si (20), it appears that numerical work is greatly advantageous over analytical approximations, although asymptotic behavior of the solution can be extracted analytically in some cases (28).

#### Control of Interfacial Stresses During Deposition of Thin Films

It is well known that thin films grown on substrates are in a state of internal stress which arises as a result of the deposition process (intrinsic stress) or as a result of differential thermal mismatch between film and substrate when the temperature is different from the deposition temperature (thermal stress) (35). Large values of the internal stress thus generated may lead to failure by delamination from the free edges, or by internal buckling and crack propagation (36). Stresses near the vicinity of the free edge of an isotropic film have been calculated by Aleck (37), Zeyfang (38), and Blech and Levi (39) who established that near the free edges large peeling and shearing stresses develop. These stresses exceed considerably the far field uniform internal stress in the film. Williams (40) and Hein and Erdogan (41) showed that singularities may develop near the free edge. Although these singularities are generally milder than the familiar  $-1/2$  singularity present near crack tips, they can become severe and equal to  $-1/2$  when, for example, the film material is much stiffer than the substrate. Approximate solutions for the stresses near the free edge have been presented by Suhir (42) and Yang and Freund (43). Due to the nature of the approximation invoked, these solutions are not applicable within one film thickness from the free edge. It must be pointed out that besides delamination and cracking, these high stress levels may also lead to the generation of dislocations in the film, substrate, or film/substrate interface (44, 45). Such dislocations have detrimental effects on the optical and electronic properties of the films.

The stress singularity analysis is based on the asymptotic solutions of the Navier-Stokes equations for the displacements of an isotropic elastic body, viz. (40)

$$2GU_r = -\partial\chi/\partial r + (1 - \nu)r\partial\psi/\partial\theta \quad (5)$$

$$2GU_\theta = -\partial\chi/r\partial\theta + (1 - \nu)r^2\partial\psi/\partial r$$



under plane-strain conditions.  $G$  is the shear modulus,  $\nu$  is the Poisson ratio (to be changed to  $\nu/(1+\nu)$  for plane stress) and  $r, \theta$  are cylindrical coordinates measured from the point where the asymptotic analysis is performed. The radial and tangential displacements are  $U_r$  and  $U_\theta$ , respectively. The function  $\psi$  is harmonic, and  $\chi$  is related to  $\psi$  by  $\nabla^2 \chi = \partial(r\partial\psi/\partial\theta)/\partial r$ . The stresses are related to the function  $\chi$  by

$$\sigma_{rr} = \partial^2 \chi / \partial r^2 \partial \theta^2 + \partial \chi / \partial r \partial \theta$$

$$\sigma_{\theta\theta} = \partial^2 \chi / \partial \theta^2$$

[6]

$$\sigma_{r\theta} = -\partial^2 \chi / \partial r \partial \theta + \partial \chi / \partial r^2 \partial \theta$$

Under homogeneous boundary conditions representing continuity of tractions and displacements, it is possible to derive solutions of the form  $\psi = r^m f(\theta)$  where  $m$  is an eigenvalue. The resulting stresses have the general form

$$\sigma_{ij} = K (m/r)^{1/2} f_{ij}(\theta)$$

[7]

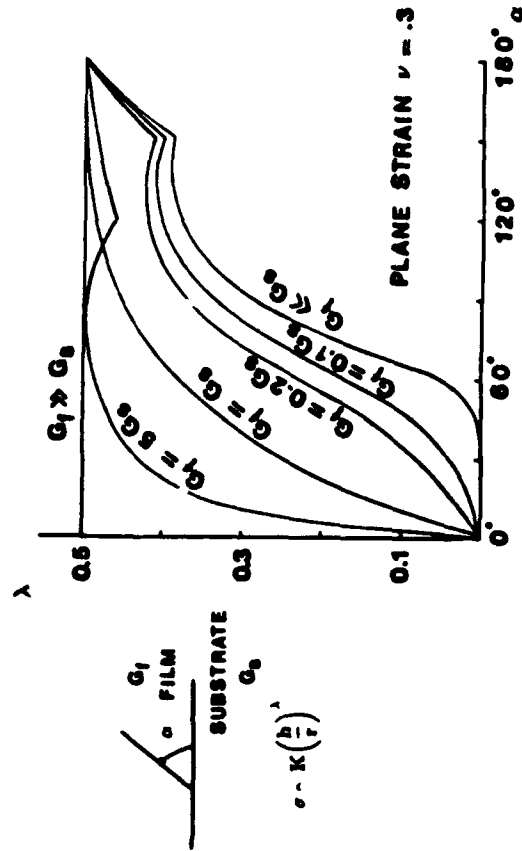


Fig. 10 Plot of the real part of the eigenvalue  $\lambda$  versus the film angle  $\alpha$  for the geometry shown.

where  $K$  is a stress intensity factor, and  $h$  is a characteristic length scale. It is seen that if the real part of  $\lambda$  is positive, then the stresses become unbounded as  $r \rightarrow 0$ . The real part of  $\lambda$  is shown in Figures 10 and 11 for two geometries which often occur in thin film design. Figure 10 represents the case where the point  $r=0$  is common to the vacuum/film/substrate intersection (41). It is seen that when the film is much stiffer than the substrate, the singularity is as strong as that for a crack. On the other hand, when the substrate is much stiffer, the singularity is weaker. When the angle subtended by the film is less than approximately 50 degrees, then the singularity disappears completely. Figure 11 shows the stress singularity when the point  $r=0$  is common to the film/substrate, i.e. the case where the film is completely buried within the substrate. It is seen that the singularity becomes weak or disappears when the angle subtended by the film is 0, 180, or 360 degrees. Still, when the film angle is very small, it is possible to get a strong singularity when the substrate is much stiffer than the film, or a weak singularity when the film is much stiffer than the substrate.

The effect of elastic anisotropy is another factor which is of importance in epitaxial films. As was shown in the previous section on control of stresses during bulk crystal growth, the effect of anisotropy is to produce higher stresses than the isotropic case. This observation can be extended to the case of thin film growth (46). Figure 12 shows the stress distribution near the free edge and at a small distance above the film/substrate interface ( $z=0.008h$ ) for a film bonded to a rigid substrate. The film is anisotropic and characterized by the anisotropic parameter  $A$  which was defined in the previous section. The film normal is along the  $\langle 111 \rangle$  direction. It is seen that the effect of elastic anisotropy is again to create higher stress levels in the vicinity of the free edge, as well as far from the free edge; the insert in Figure 12 shows the far field values of the biaxial stress in the plane of the film for  $\langle 110 \rangle$  and  $\langle 111 \rangle$  orientation. For the case of  $\langle 100 \rangle$  growth, the far field stress values are independent of the anisotropic parameter  $A$  (46).

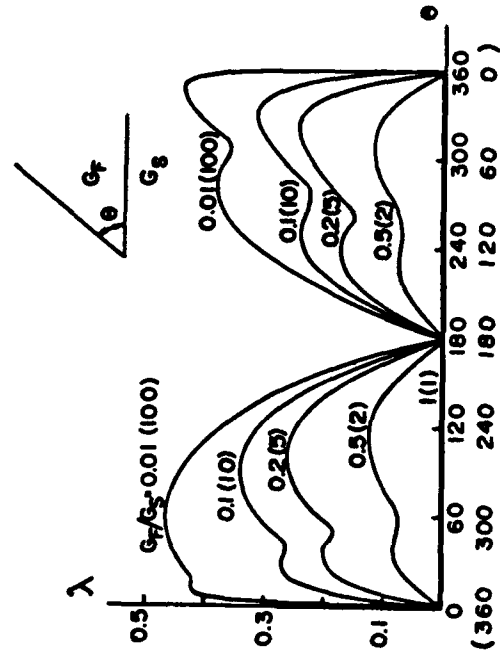


Fig. 11 Plot of the real part of the eigenvalue  $\lambda$  versus the film angle  $\theta$  for the geometry shown.



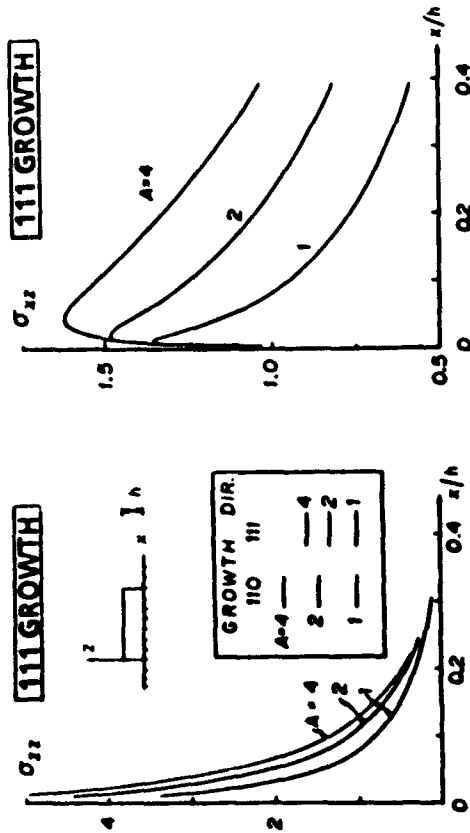


Fig. 12 Shear and peeling stresses near the film/substrate interface ( $y = 0.008h$ ) for  $\langle 111 \rangle$  growth. The insert shows the far field values of the balanced biaxial stress for  $\langle 110 \rangle$  and  $\langle 111 \rangle$  growth.

It is evident that the high levels of stress in the vicinity of the free edge may lead to inelastic deformation and subsequently to stress relaxation. To model these relaxation effects, it is assumed that the constitutive law for the film material is given by  $\epsilon_{ij} = \epsilon_{ij}^e + \epsilon_{ij}^p + \epsilon_{ij}^d$ , where the elastic strain  $\epsilon_{ij}^e$  is related to the stress  $\sigma_{ij}$  via the usual elastic stress-strain equations, the plastic strain  $\epsilon_{ij}^p = F \delta_{ij}$  where the function  $F$  is chosen to agree with a piecewise linear-power law hardening stress-strain curve in pure shear with yield stress  $\tau_0$ , yield strain  $\epsilon_0 = \tau_0/2G$ , and hardening exponent  $1/n$ , as shown in Figure 13 (47). The strain  $\epsilon^T$  represents an isotropic misfit strain which may be due to thermal mismatch, lattice misfit, or any other source of internal stress (35).

It is convenient to define the dimensionless load parameter  $\theta$  by

$$\theta = \tau^T / \epsilon_0 \quad [8]$$

The stress concentration factors are defined as the ratio of the shear stress and normal peeling stress  $\sigma_{xy}$  and  $\sigma_{yy}$ , respectively, to the load parameter  $\theta$ . Figures 13, 14. Although the stress is infinite at  $x = y = 0$ , the stresses were calculated at  $x = y = 0.009h$ , normalized with respect to  $\theta$  and plotted vs.  $\theta$  in Figures 14 and 15. These figures show the stress concentrations for long, thin films with an aspect ratio of  $L/2h = 5$ , and for thick films with an aspect ratio of 1. It is evident that the thick films experience smaller stress levels than the thin films, a conclusion which

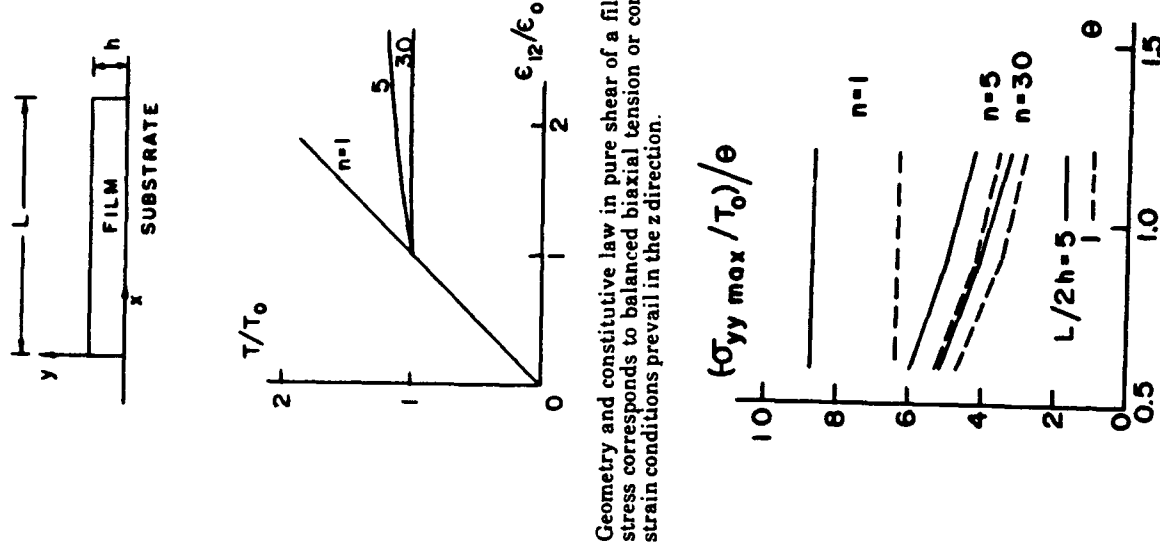


Fig. 13 Geometry and constitutive law in pure shear of a film whose far field stress corresponds to balanced biaxial tension or compression. Plane strain conditions prevail in the  $z$  direction.

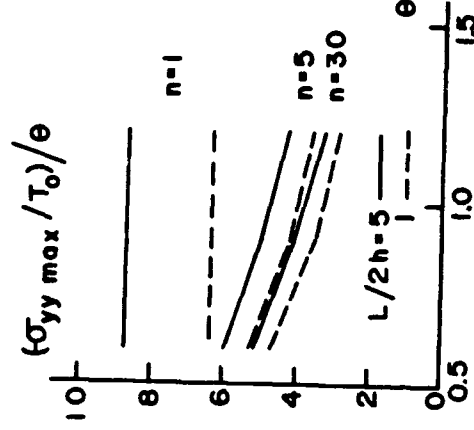


Fig. 14 Stress concentration factor at the point  $x = y = 0.009h$  versus the dimensionless load  $\theta$ .



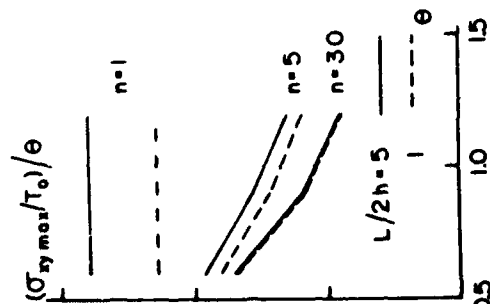


Fig. 15 Stress concentration factor at the point  $x=y=0.009h$  versus the dimensionless load  $\theta$ .

is also drawn from the analysis of elastic films (42). It is also seen that in spite of the plastic deformation, stresses considerably in excess of the yield stress are present near the free edge  $x=y=0$ . These high levels of stress are generally present within 0.2 to 0.4  $h$  along the film/substrate interface, and they may lead to the nucleation of flaws or cracks along the film/substrate interface. This is seen in Figure 16 which shows the development of the dimensions of the elastic-plastic boundary for two values of the load  $\theta$  vs. the hardening exponent  $1/n$ . It is seen that the extent of the plastically deforming region is well approximated by the linear elastic solution, and that the deforming portion of the film is localized within a diffuse zone along the film substrate interface.

For crystal growth both in the bulk from the melt and in thin film form on a substrate, considerable spatially inhomogeneous stresses develop as a result of misfit which may be due to thermal strains, lattice mismatch, or intrinsic stresses. These stresses are localized within one characteristic length scale from the interface and they must be controlled in order to avoid the degradation of the electronic or optical properties of the assembly. For the case of bulk crystal growth the stresses may be controlled by reducing the temperature gradient between the solid-liquid interface and furnace, by reducing the cooling coefficient, by reducing the size of the grown crystal, by maintaining a flat solid-liquid interface, by careful choice of the crystal growth direction, or by choosing a crystal growth technique characterized by a small characteristic length scale which is not always the same as the overall size of the grown crystal. For the case of growth in the form of thin films, the localized high stresses near the free edge and along the interface are harder to control besides controlling the far field internal stress in the film which may be due to a variety of sources. Plastic deformation does reduce the stresses at the expense of increased plastic strains. Careful choice of the crystal growth direction may be another means of controlling these high stress levels.

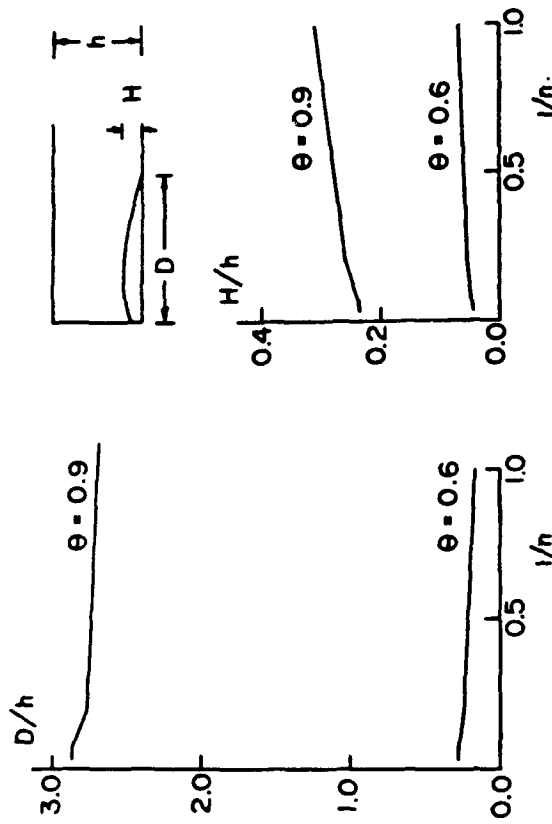


Fig. 16 Development of the plastic zone size versus the hardening exponent  $1/n$  for two values of the dimensionless load  $\theta$ .

### Optimization of the HIP Process for Powder Consolidation

Finally we would like to consider a relatively new area, the prediction of densification behavior during Hot Isostatic Pressing ("HIPing"). Changes in microstructure (i.e. particle/contact shape and number) during densification coupled with the existence of several densification mechanisms make this potentially a very complicated problem. However, Arzt, Ashby, and Easterling (48) were able to reduce the problem geometrically and used deformation mechanism maps to express their results. Recent developments include the consideration of bimodal powder mixes.

### Basic Assumptions

For densities less than 90%, Arzt et al. (48) assumed a dense packing of uniformly sized spherical particles with densification occurring entirely by deformation of the particle contacts (i.e. no particle rearrangement). This is not strictly true but is plausible for closely packed particles under isostatic pressure, becomes a better assumption as consolidation proceeds, and is generally consistent with cold compaction experiments (49). The contraction of the structure due to the approach of particle centers was modeled by fixing the particle centers and allowing a fictitious "expansion" of the particles. This produced an equivalent geometry while simplifying the calculation. These assumptions, coupled with knowledge of the initial radial distribution function (RDF) and packing density of the particles, permit the geometry of the system (i.e. number and size of interparticle contacts) to be determined for any density of the sample. It is then merely necessary to "distribute" the applied isostatic stress



among these contacts. Densification rates for various mechanisms can be calculated from a knowledge of the material properties and temperature and the dominant mechanism and overall densification rate determined. (For densities higher than 90%, individual particles begin to lose their identities in the densifying mass and so the model instead assumes an array of spherical pores formed in the particle interstices and examines their behavior.) Arzt et al. originally considered yielding, power-law creep, and volume diffusion as potential densification mechanisms.

This simple model is remarkably successful in providing a general guide to the densification behavior expected for real systems during HIPing. That is to say, it can provide a useful estimate of the temperatures and pressures required to obtain a desired final density in a reasonable time period. To obtain this result, however, a number of potentially important factors were not considered. Since the publication of this work, therefore, several additional studies have attempted to build on its foundation. Helle et al. (50) expanded the list of potential densification mechanisms to include the possibility of Nabarro-Herring and Coble creep in polycrystalline powders. Li et al. (51) considered the potential effect of thermal gradients (established in finite sized powder compacts during the ramp-up of temperature and pressure for HIPing) on the densification of compacts, in particular the potential for density gradients or inhomogeneous densification to occur. Finally both Nair and Tien (52) and Li and Funkenbusch (53) have attempted to extend the original monosized particle model to consider the effect of particle size distributions. This last topic will be the main focus of our discussion.

#### Particle-size Distributions

All real powder mixes contain a distribution of particle sizes. The reason for studying distribution effects is not, however, primarily to "fine tune" this one aspect of the Arzt et al. model. Rather, by introducing the particle size distribution as a variable, we open the possibility of optimizing this distribution to improve densification behavior and control microstructure (e.g. final pore size). Since HIP is a capital intensive operation and since final properties in powder materials are crucially dependent on the size and distribution of residual pores, even modest improvements in these areas are of interest. Unfortunately, in comparison with the monosize case, considerable additional information on particle distributions is necessary to make bimodal models work. Work in this area is, therefore, still in its infancy and "optimization" of the distributions remains an unrealized goal. Nevertheless, preliminary modeling efforts are underway and the key assumptions and information necessary for such modeling is becoming clearer.

Introducing a bimodal particle size distribution produces three distinct types of interparticle contact in contrast to the one type produced in the monosize case. The central question in modeling is, therefore: How is the applied pressure to be distributed among these contacts? So far two distinct assumptions about this distribution have been used in modeling compact behavior.

Nair and Tien (52) have assumed that the force on all contacts will be equal and have compared the behavior of a bimodal and monosize particle arrangement on this basis. This work represents an important contribution in extending HIP modeling to the bimodal case. However, the assumption of equal forces leads to significant problems. Contacts between small particles necessarily involve relatively small contact areas and hence high contact stresses. Thus contraction of the structure should be much higher around small particles. Such differential contraction can only be maintained by extensive particle rearrangement, contradicting one of the basic assumptions in the Arzt et al. model. This internal contradiction prevents the model from maintaining a truly consistent particle/contact geometry.

Recognizing this difficulty, Li and Funkenbusch (53) have developed a model which distributes the applied stress so that the relative contraction of the structure is uniform around all particle centers. This is certainly not completely correct as some particle rearrangement must occur. However, it is a reasonable first approximation, as discussed previously. In addition it is necessary if the basic approach utilized in the original monosize model is to be maintained. Knowledge of the particle distribution functions then allows the sample geometry (i.e. number and size of the interparticle contacts) to be determined from the density in a fashion identical to that used in the monosize case.

The applied stress,  $\sigma_{app}$  can be related to the average force on each type of contact,  $F_{ij}$ , by an equation of the form (52):

$$\sigma_{app} = \frac{1}{V} \sum_i \sum_j \frac{N_{ij} F_{ij} f_i}{4\pi R_i^2} \quad [9]$$

where  $N$  is the number of contacts,  $R$  is the particle radius, and  $f$  is the volume fraction of that particle type. Single subscripts (i.e.  $i$  or  $j$ ) serve to distinguish between the various particle "types" (i.e. large or small in the bimodal case). Double subscripts indicate a contact type, with the first subscript indicating the particle of interest and the second the contacting particle. Significantly, all of these parameters are known from the geometry of the system, except for the contact forces. However, for an assumed densification mechanism, the force required on each contact can also be expressed in terms of geometry and of the overall rate of particle center approach (i.e. the rate of contraction). For example, for power law creep we can write (53):

$$F_{ij} = n \rho_u^2 \left( \frac{\dot{\gamma}_{ij}}{A_{p_{ij}}} \right)^{1/n} \quad [10]$$

where  $A$  and  $n$  are materials constants,  $\rho_u$  is the radius of contact, and  $\dot{\gamma}$  is one half of the net apparent rate at which the  $i$  and  $j$  particle centers are approaching each other. Under the assumption of uniform rates of contraction around all particle centers, all of the  $\dot{\gamma}_{ij}$  can be related to each other and to the average rate of particle center approach by simple geometrical factors. Hence all of the  $F_{ij}$  terms can be expressed in terms of this average rate and Equation [9] can then be solved to find this densification rate as a function of  $\sigma_{app}$ .

The main limitation on application of this type of model to bimodal particle distributions is the current lack of information on the radial distribution of particle centers in such systems (necessary for calculating the number and size of contacts). However, some information is available from the work of Nair, Hendrix, and Tien (54). These authors present RDFs for two alloys: a mono-sized Rene 95 powder with a particle diameter of 80  $\mu\text{m}$  and an uncompacted density of 55.3%, and a bimodal alloy with 20 wt.% of 30  $\mu\text{m}$  diameter particles, 80 wt.% of 80  $\mu\text{m}$  particles, and a density of 61%. This data was used (53) to produce deformation mechanism maps and examine other aspects of compact behavior. Power-law creep and yielding were considered as the two potential densification mechanisms and attention was restricted to densities of up to 90%. Hence, only



partial maps have been calculated at the present time. Some results are reproduced in Figures 17-19.

Figure 17 shows the boundary between power-law-creep and yielding dominance of densification predicted for both the bimodal and monosize powders (solid curves). The dashed curves are the same boundary calculated by assuming that particle coordination does not increase during densification. Clearly the increase in particle coordination during densification has an important effect. This parallels Arzi's findings for monosize particles (55) and indicates the need for RDFs as input to the model.

A large difference between the monosize and bimodal curves is also evident in Figure 17. In part this reflects the difference in initial packing densities. However, the development of interparticle contact area may also be different in the two cases and this will also alter the densification behavior. To separate these two effects it would be useful to compare the behavior of two mixes with identical initial densities. Mason (55) has provided an RDF for a random packing of monosized spheres with a density of 63.6%. Although not exactly the same as that for Nair, Hendrix, and Tien's bimodal distribution it is close enough to permit a comparison (Figure 18). It is again clear that much of the difference seen in Figure 17, was due to differences in packing density. However, the fact that these curves "cross" also indicates that there can be significant differences in the development of particle contact areas as a function of particle distribution/size effects.

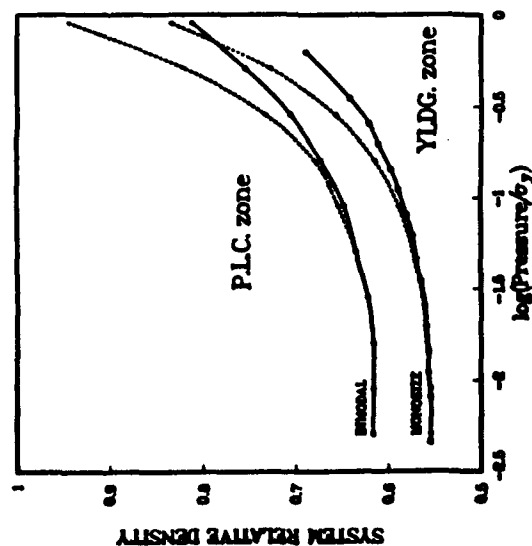


Fig. 17 Partial deformation mechanism map for a monosize and a bimodal particle mix (solid lines), obtained using particle distribution data from reference 54. Dashed lines show the effect of ignoring the increase in particle coordination number with densification. (Reproduced from reference 53)

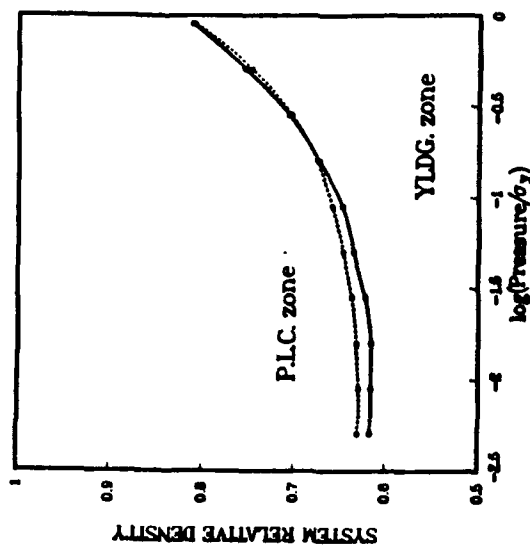


Fig 18

Deformation mechanism map for a monosize (dashed line) and bimodal (solid line) particle mix with similar initial densities. Particle distribution data from references 55 (monosize) and 54 (bimodal). (Reproduced from reference 53)

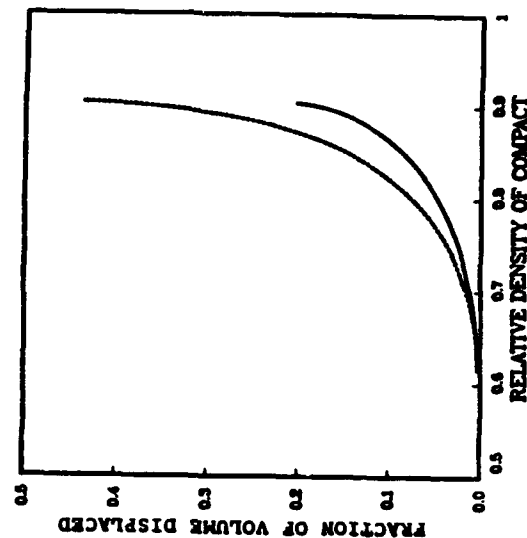


Fig. 19

Fraction of total particle volume displaced from interparticle contacts vs. compact density in the bimodal particle mix. Dashed line - small particle, solid line - large particle. (Reproduced from reference 53)



Finally, it is worthwhile to examine the behavior of the individual particle types in the bimodal mix. Although the contraction rate is fixed, the deformation (i.e. % of the total particle volume displaced at interparticle contacts) may vary significantly due to differences in the number and size of contacts formed. This is illustrated in Figure 19 where it can be seen that, for this particular bimodal mix, small particles are predicted to deform to a much greater extent than large particles. This is consistent with qualitative observations made after HIPping a bimodal mix of René 95 (56). The "breakdown" of the spherical particle model at roughly 90% density is also evident in this figure.

#### Concluding Remarks

It is seen from the examples given that we do have sufficient understanding of micromechanical principles to deal with a variety of materials processing problems. Analytical methods require many simplifying assumptions so that the results do not seem to have as much predictive power as desired. However, these methods help to define the necessary assumptions and key variables. In the immediate future increasing use of supercomputers is expected to simulate complex situations such as crystal growth and hot isostatic pressing. The operating parameters can be optimized in the computer before being put into practice. The era of computer aided materials design will be with us sooner than we think.

#### Acknowledgements

PDF acknowledges interactions with many current and former colleagues including Prof. T.H. Courtney, Prof. J.K. Lee, Dr. Jean Malzahn Kampe, and Mr. E.K.H. Li. This work was supported by the National Science Foundation under grants MSM-8657038, MSM-8857096, and MSM-8503984, by the Office of Naval Research under grants N00014-87-K0488 and N00014-85-K-0758 and by the Department of Energy under grant DE-FG02-85ER45201.

#### References

1. J. K. Boah and P.G. Winchell, Metal. Trans. 6A (1975), 717.
2. E. Levine, J. Washburn and G. Thomas, J. Appl. Phys. 38 (1967), 81, 87.
3. J. Washburn, G. Thomas and J.J. Queisser, J. Appl. Phys. 35 (1964), 1909.
4. D.P. Miller, J.E. Moore and C.R. Moore, J. Appl. Phys. 33 (1962), 2648.
5. J.C.M. Li, Metal. Trans. 9A (1978) 1353.
6. Sanboh Lee and J.C.M. Li, J. Appl. Phys. 52(3) (1981), 1336.
7. G. Frommeyer and G. Wasserman, Acta Metall. 23 (1975), 1353-1360.
8. J. Bevk, J.P. Harbison, and J.L. Bell, J. Appl. Phys. 49 (1981), 6031-6038.
9. P.D. Funkenbusch, and T.H. Courtney, Acta Metall. 33 (1985), 913-922.
10. P.D. Funkenbusch, J.K. Lee, and T.H. Courtney, Met. Trans. 18A (1987), 1249-1256.

11. W.A. Spitzig, A.R. Pelton, and F.C. Laabs, Acta Metall. 35 (1987), 2427-2442.
12. K.R. Karasek and J. Bevk, Scripta Metall. 14 (1980), 431-435.
13. R.K. Everett, Scripta Metall. 22 (1988), 1227-1230.
14. J. Bevk and Keith Karasek, New Developments and Applications in Composites, D. Kuhlman-Wilsdorf and W.C. Harrigan eds., (TMS-AIME, Warrendale, PA, 1979), 103-113.
15. M.F. Ashby, Phil. Mag. 21 (1970), 399.
16. U.F. Kocks, J. Engng. Mater. Technol. 98 (1976), 76.
17. P.D. Funkenbusch, T.H. Courtney, and D.G. Kubisch, Scripta Metall. 18 (1984), 1099-1104.
18. H.P. Wahl and G. Wassermann, Z. Metall. 61 (1973), 326-339.
19. A.S. Jordan, A.R. Von Neida, and R. Caruso, Bell System Tech. J. 59 (1980), 593.
20. J.C. Lambropoulos, J.W. Hutchinson, R.O. Bell, B. Chalmers, and J.P. Kalejs, J. Cryst. Growth 65 (1983), 324.
21. P. Penning, Philips Res. Rep. 13 (1958) 79.
22. A.S. Taylor, B.H. Mackintosh, L. Eriss, and F.V. Wald, J. Cryst. Growth 82 (1987), 134.
23. S. Motakef and A.F. Witt, J. Cryst. Growth 80 (1987), 37.
24. T. Iwaki and N. Kobayashi, J. Applied Mechanics 48 (1981), 866.
25. G. Szabo, J. Cryst. Growth 73 (1985), 131.
26. M. Duseaux, J. Cryst. Growth 61 (1983), 576.
27. C.E. Schvezov, I.V. Samarasekera, and F. Weinberg, J. Cryst. Growth 85 (1987), 142.
28. J.C. Lambropoulos, J. Cryst. Growth 80 (1987), 245.
29. J.C. Lambropoulos, J. Cryst. Growth 84 (1987), 349.
30. J.C. Lambropoulos, J. Mater. Res. (1988) 531.
31. A.G. Elliott, C.L. Wei, and R. Farraro, J. Cryst. Growth 70 (1984), 169.
32. J.C. Lambropoulos, to be published in J. Cryst. Growth (1989).
33. N. Kobayashi, in Preparation and Properties of Solid State Materials, 6 (ed. W.R. Wilcox, M. Dekker 1981), 119.
34. P.A. Ramachandran and M.P. Dudukovic, J. Cryst. Growth 71 (1985) 399.
35. R.W. Hoffman, in Physics of Thin Films 3 (ed. G. Hass and R.E. Thun, Academic Press 1966) 211.



36. A.G. Evans, M.D. Drory, and M.S. Hu, J. Mater. Res. 3 (1988), 1043.
37. B.J. Aleck, J. Appl. Mech. 16 (1949), 118.
38. R. Zeyfang, Solid State Electron. 14 (1971), 1035.
39. I.A. Blech and A.A. Levi, J. Appl. Mech. 48 (1981), 442.
40. M.L. Williams, J. Appl. Mech. 19 (1952), 526.
41. V.L. Hein and F. Erdogan, Int. J. Fract. Mech. 48 (1971), 442.
42. E. Suhir, J. Appl. Mech. 53 (1986), 657.
43. W. Yang and L.B. Freund, Shear Stress Concentration Near the Edge of a Thin Film (Brown University report 1986).
44. S.M. Hu, J. Appl. Phys. 50 (1979), 4661.
45. S. Ioannidis, J. Appl. Phys. 52 (1981), 2782.
46. J.C. Lambropoulos and S.M. Wan, in Electronic Packaging Materials Science III Materials Research Society Symposium Proceedings 108 (ed. R.C. Sundahl et al. 1988), 399.
47. J.C. Lambropoulos and S.M. Wan, Mater. Sci. and Engin. A107 (1989), 169-175.
48. E. Arzt, M.F. Ashby, and K.E. Easterling, Met. Trans. A 14A (1983), 211-221.
49. H. Fischmeister, E. Arzt, and L. Olsson, Powder Metall. 21 (1978), 179-187.
50. A.S. Helle, K.E. Easterling, and M.F. Ashby, Acta Metall. 33 (1985), 2163-2174.
51. W.B. Li, M.F. Ashby, and K.E. Easterling, Acta Metall. 35 (1987), 2831-2842.
52. S.V. Nair and J.K. Tien, Met. Trans. A 18A (1987), 97-107.
53. E.K.H. Li and P.D. Funkenbusch, Acta Metall. 37 (1989), 1645-1655.
54. S.V. Nair, B.C. Hendrix, and J.K. Tien, Acta Metall. 34 (1986), 1599-1605.
55. E. Arzt, Acta Metall. 30 (1982), 1883-1890.
56. R.D. Kissinger, S.V. Nair, and J.K. Tien, Superalloys 1984 (TMS-AIME Warrendale, PA, 1984) 287, as described in reference 52.



## Thermomechanics of Thin Films and Interfaces

JOHN C. LAMBROPOULOS

Department of Mechanical Engineering, University of Rochester, Rochester, N.Y. 14627

Several mechanics and thermomechanics problems associated with the deposition of thin films on substrates are reviewed. They include: (1) Stress concentrations in interfacial cracks, and the corresponding calculation of the energy release rate for crack growth along the film-substrate interface. (2) The effect of microstructure and of stress relaxation by diffusional creep during the growth of a thin film on the residual stresses present in the film; and (3) the thermal conductivity in film-substrate assemblies, and the issue of extracting film thermal properties from composite measurements. The relation between bulk and thin film values of the thermal conductivity is discussed. The issue of interfacial thermal resistance, which may lead to interfacial temperature drops of the order of  $0.6^\circ\text{K}$  is also addressed, and discussed in view of the inhomogeneous interface in films deposited by electron beam evaporation or ion beam sputtering.

**Key words:** Thermomechanics, thin films, interfaces

## INTRODUCTION

The design of film-substrate assemblies for electronic, optical, or magnetic applications must address a variety of problems regarding the mechanical and physical properties of thin films. It is well known that the stress in thin films may be due either to differential thermal mismatch between film and substrate (thermal stress), or it may be an intrinsic stress which arises during the deposition process itself. In addition, the film may be subjected to thermal loads such as the ones arising during the laser damage or laser processing of films. It is thus clear that both mechanical and thermal properties must be measured, and that in a given application there is an interplay between thermal and mechanical loads.<sup>1</sup>

We review several issues in this report which address the thermomechanical properties of thin films. The first issue is the interplay between the film stress and the fracture toughness of the interface, with the goal of establishing either a critical thickness for a given film stress, or the opposite, at fracture. The issue has been addressed in detail in a recent review article by Evans *et al.*<sup>2</sup> where several other important considerations are addressed: For example, the fact that the crack may not grow along the interface, but at some distance below the interface, or, for a brittle film on a ductile substrate, the fact that extensive ductility may accompany crack growth. For the issue of bimaterial brittle fracture, the reader is referred to the articles by Rice,<sup>3</sup> or by Hutchinson *et al.*,<sup>4</sup> for small scale yielding to the article by Shih and Asaro<sup>5</sup>; for cracks on bicrystal interfaces to the article by Qu and Bassani.<sup>6</sup>

Stress concentrations may arise in geometries other than those involving cracks. For example, the issue of crack nucleation near the free-edge of a film bonded to a substrate is related to the stress concentration that may develop in a notch involving a

bimaterial interface. The issue of elastic notches in isotropic bimaterials has been addressed by Hein and Erdogan.<sup>7</sup>

Most of these analyses examine the notch or crack from the point of view of bimaterial interfaces, so that the film thickness does not enter the analysis. The stress distribution in thin films, with account given to the film thickness, has been addressed by Aleck,<sup>8</sup> by Zeyfang,<sup>9</sup> and by Suhir<sup>10</sup> for elastic isotropic materials. The stresses in anisotropic films have been calculated by Lambropoulos and Wan,<sup>11</sup> who showed that anisotropy leads to higher stresses. For a plastically deforming film material bonded to a stiff substrate, Lambropoulos and Wan<sup>12</sup> have shown that the inelastic deformation is localized near a film free edge and within a diffuse zone along the film-substrate interface in a manner similar to the creation of interfacial dislocations in epitaxial structures. All these works thus identify the film-substrate interface as a region of high stresses.

A basic assumption in the thin film studies mentioned above is that the far field film stress is uniformly distributed through the thickness of the film. This is not the case when stress relaxation occurs during the growth of the film. The second issue addressed in this report is the effect of stress relaxation by grain-boundary diffusion (Coble creep) and by bulk diffusion (Nabarro-Herring creep).<sup>13</sup> A simple model is presented which accounts for the microstructure of thin films as proposed by Movchan and Demchishin<sup>14</sup> and by Thornton,<sup>15-16</sup> whereby at temperatures less than about 0.45–0.5 on the homologous scale the film consists of equiaxed, columnar grains perpendicular to the interface. The model is used to construct a composite length scale which depends on the material properties of the film, and on growth parameters such as the temperature, rate of growth, and grain size parallel to the interface. When this length scale exceeds the film thickness, relaxation effects are important. The data from Frost and Ashby<sup>17</sup> are used in order to estimate this critical length scale for a variety of metals.

The interplay between mechanical and thermal

(Received October 5, 1989; April 24, 1990)



properties is addressed in the third topic reviewed which concerns the measurement of the thermal conductivity of thin films. Such measurements are important since it has been established that when the film thickness is less than about one micron, the film conductivity is considerably lower than that of the corresponding bulk solid. Thus, in correlating thermal loads (such as the critical energy density for laser damage of thin films) to critical thermo-mechanical material parameters (such as the temperature at damage, or the fracture toughness of the interface), the bulk values are not appropriate. The interplay between thermal and mechanical loads is discussed in the review article by Nakayama,<sup>17</sup> and in the text edited by Bar-Cohen and Kraus.<sup>1</sup> The issue of thermal conductivity measurements is also reviewed by Guenther and McIver.<sup>18</sup>

We present an overview of a non-destructive method used by Lambropoulos *et al.*<sup>19</sup> to measure the thermal conductivity of thin dielectric films (oxides and fluorides), and to extract the film thermal properties from the measurement of the composite properties. Estimates are presented for the volume fraction of voids necessary to induce the measured reduction from the bulk value, and although these estimates are comparable to the void fractions predicted from atomistic models of non-equilibrium film growth, it is not clear whether or not the enhanced porosity of films is the only reason for the reduced thermal conductivity. This technique also allows the determination of the interfacial thermal resistance, i.e. the ratio of temperature drop to power flux across the interface, and some correlations of this quantity to the measured power fluxes are discussed.

## INTERFACIAL FRACTURE IN THIN FILMS

Consider a film of thickness  $t$  which is bonded to a semi-infinite substrate. A Cartesian coordinate system  $x_1, x_2, x_3$  is used such that the film-substrate interface is at  $x_2 = 0$ . The axis  $x_1$  lies in the film-substrate interface. The film and substrate are linear elastic and isotropic materials, each characterized by its own Young's modulus and Poisson ratio. The film is assumed to be in a state of balanced biaxial tension or compression in the plane of the film. The state of stress is characterized by the misfit strain  $\epsilon^T$  which may be identified with the differential thermal mismatch strain between film and substrate, so that

$$\epsilon^T = (\alpha_F - \alpha_S) \Delta T \quad (1)$$

where  $\Delta T$  is the difference between the film deposition and actual temperatures.  $\epsilon^T$  may also be identified with an epitaxial mismatch strain, or with a misfit strain giving rise to intrinsic stress during the film deposition process.

Due to the fact that the film thickness is much smaller than any dimension of the supporting substrate  $\epsilon_{11}$  and  $\epsilon_{33}$  both vanish far from any inhom-

ogeneities such as free edges or interfacial cracks so that

$$\begin{aligned} \epsilon_{11} = 0 &= \frac{\sigma_{11} - \nu \sigma_{33}}{E} + \epsilon^T \\ \epsilon_{33} = 0 &= \frac{\sigma_{33} - \nu \sigma_{11}}{E} + \epsilon^T \end{aligned} \quad (2)$$

where  $E, \nu$  are the elastic properties of the film. Hence, the far field state of stress is that of balanced biaxial tension or compression given by

$$\sigma_{11} = \sigma_{33} = \sigma_0 = -\frac{E}{1-\nu} \epsilon^T \quad (3)$$

We consider a crack of length  $a$  which lies along the film-substrate interface with a crack tip at  $x_1 = x_2 = 0$ . The uncracked material is at  $x_1 > 0$ . The crack may be internal, or it may extend to the outer edge of the film.

It has been shown by Rice<sup>3</sup> and by Hutchinson *et al.*<sup>4</sup> from an asymptotic stress analysis (under the assumption of plane strain or plane stress deformation in the  $x_3$  direction) in the vicinity of the crack tip in a bimaterial interface that along the crack line  $x_2 = 0, x_1 > 0$  the stress distribution is given by

$$(\sigma_{22} + i\sigma_{12})_{\theta=0} = \frac{K}{\sqrt{2\pi r}} r^\mu \quad (4)$$

with  $r^\mu = \cos(\epsilon \ln r) + i \sin(\epsilon \ln r)$  and where  $r$  is distance from the crack tip,  $\theta$  measures the angle from the crack line ahead of the crack tip, and  $K = k_1 + ik_2$  is a complex stress intensity factor, and  $i$  is the imaginary unit. The asymptotic analysis shows that<sup>3</sup>

$$\epsilon = \frac{1}{2\pi} \ln \left( \frac{\frac{\kappa_1}{\mu_1} + \frac{1}{\mu_2}}{\frac{1}{\mu_1} + \frac{\kappa_2}{\mu_2}} \right) \quad (5)$$

where  $\mu$  is the shear modulus, and  $\kappa = 3 - 4\nu$  for plane strain and  $(3 - \nu)/(1 + \nu)$  for plane stress, with  $\nu$  denoting the Poisson ratio. In this expression 1 denotes the film material, and 2 denotes the substrate. The magnitude of  $K$  is undetermined from the asymptotic analysis.

The crack opening displacements are given by<sup>3</sup>

$$\Delta(u_2 + iu_1) = \frac{(c_1 + c_2) K r^\mu \sqrt{\frac{r}{2\pi}}}{2(1 + 2i\epsilon) \cosh(\pi\epsilon)} \quad (6)$$

where we have denoted  $\Delta() = ()_{\theta=\pi} - ()_{\theta=-\pi}$ . The energy release rate per unit new crack area is given by<sup>3</sup>



$$G = \frac{(c_1 + c_2) K \bar{K}}{16 \cosh^2(\pi \epsilon)} \quad (7)$$

where  $c_i = (\kappa_i + 1)/\mu$ , for  $i = 1, 2$  and the overbar denotes the complex conjugate. For a homogeneous solid ( $c_1 = c_2$ ,  $\epsilon = 0$ )  $K = K_I + iK_{II}$  with I and II denoting the corresponding modes. When 1 is elastic but 2 is rigid, then  $\epsilon = 0.094$  and  $0.12$  under, respectively, plane strain or plane stress conditions with  $\nu = 0.3$ . Rice<sup>3</sup> discusses extensively the units of measuring  $K$ , and he has shown that the largest value of  $\epsilon$  is  $0.175$ .

In order to determine the stress intensity factor  $K$ , it is required to solve the complete boundary value problem for an interfacial crack. The stresses and displacements are calculated by using finite elements with linear, 4-noded, isoparametric rectangular elements. The stress intensity  $K = k_1 + ik_2$  can be calculated either from the stress distribution along  $\theta = 0$  of Eq. (4), or from the displacement distribution along  $\theta = \pm\pi$ , see Eq. (6). For the case of the stress distribution along  $\theta = 0$ , the numerically computed stresses are multiplied by  $r^{1/2}$ , in order to remove the strong singularity. The result is

$$\begin{aligned} \sigma_{22} \sqrt{r} &= [k_1 \cos(\epsilon \ln r) - k_2 \sin(\epsilon \ln r)] / \sqrt{2\pi} \\ \sigma_{12} \sqrt{r} &= [k_1 \sin(\epsilon \ln r) + k_2 \cos(\epsilon \ln r)] / \sqrt{2\pi} \end{aligned} \quad (8)$$

so that  $k_1$  and  $k_2$  can be determined for each value of  $r$  by solving the equations above. A similar procedure can be followed when the numerically computed crack opening displacements are used instead of the stresses. When the variation of the computed  $k_1$  and  $k_2$  is now plotted vs  $r$ , it is found that as  $r \rightarrow 0$ , the two approaches give identical results for  $k_1$  and  $k_2$ . Finally, the energy release rate is computed from Eq. (7).

For the case of a double edge crack in a film of length  $10t$  in the  $x_1$  direction and bonded to a rigid substrate under plane strain conditions in the  $x_3$  direction ( $\epsilon_{33} = 0$ ), it was found that the energy release rate varied from  $0.9$  to  $1.0 \sigma_0^2 (1 - \nu^2) t / 2E$  when  $a/t$  varied from  $0.5$  to  $3.0$ . In this notation  $\sigma_0$  is the far field uniform stress, which is defined by Eq. (3). For  $a/t = 3$  it was also found that

$$k_2/k_1 = 2.7 \quad (9)$$

implying that the shear stress effects along the interface dominate over the normal stress effects.

For the case of an internal crack of total length  $2a$ ,  $G$  varied from  $0$  to  $0.1 \sigma_0^2 (1 - \nu^2) t / 2E$  as  $a/t$  varied from  $0.5$  to  $3.0$ .

The computed energy release rate can be checked against an analytically derived energy release rate when the edge crack is semi-infinite. When  $a \gg t$ , for an observer stationary with respect to the crack tip, the stress field does not change when the crack advances by  $\Delta a$ . Under such steady-state conditions, and assuming that  $\epsilon_{33} = 0$  both ahead and

behind the crack tip, the energy release rate  $G$  can be calculated analytically from

$$G = - \frac{\Delta U}{w \Delta a} \quad (10)$$

where  $w$  is the thickness in the  $x_3$  direction and  $\Delta U$  is the change in the strain energy of a volume element  $w$  by  $t$  by  $\Delta a$  when this element is transported from  $x_1 = +\infty$  (where it is in a state of biaxial tension or compression along the  $x_1$  and  $x_3$  directions) to  $-\infty$  (where it is in a state of tension or compression along the  $x_3$  direction only.) The result is

$$G = \frac{\sigma_0^2 t (1 - \nu^2)}{2E} \quad (11)$$

If we assume that  $\epsilon_{33} = 0$  ahead of the crack tip but  $\sigma_{33} = 0$  behind the crack tip, the energy release rate is found to be

$$G = \frac{\sigma_0^2 t}{2E} \quad (12)$$

It is clear from the discussion above that any three dimensional effects have been neglected in computing the stress distributions near the crack tip.

Assuming that the crack grows when  $G = G_c$ , where  $G_c$  is the fracture toughness of the interface, it is concluded that the critical value of the far field film stress at fracture is given by

$$\sigma_0 = \sqrt{\frac{2EG_c}{t(1 - \nu^2)}} \quad (13)$$

Viewed in another way, we conclude that for a given far field internal stress, there is a critical thickness  $t_c$  above which the interface crack will grow, so that thick films are intrinsically more unstable than thinner films. For other film-substrate combinations, we refer to the work by Evans *et al.*<sup>2</sup> It is obvious that the simple analysis leading to Eq. (13) does not distinguish between the normal and shear contributions to the crack growth behavior. To do so, the exact mechanism of crack growth is required.

A basic assumption in the analysis presented above has been that the far field stress is uniformly distributed through the film thickness, so that the average (through the thickness) film stress is independent of the film thickness. We next turn to the issue of stress relaxation during the growth of the film, and on its effect on the average film stress.

### STRESS RELAXATION BY DIFFUSION DURING FILM GROWTH

The structure of vacuum-deposited films depends on parameters such as incident film flux, the film atom adsorption probability, the density of surface



sites, and the adatom surface mobility. These parameters depend, in turn, on the film atom energy and angle of incidence, the exposed crystallographic surfaces, and most important the temperature of the substrate. Movchan and Demchishin<sup>14</sup> examined films of Ni, Ti, W, Al<sub>2</sub>O<sub>3</sub>, and ZrO<sub>2</sub>, and they have divided the  $T/T_m$  scale ( $T_m$  being the melting point of the film material) into three zones: Zone 1 ( $T/T_m < 0.25-0.30$ ) consisting of tapered crystalites of width which increases with  $T$ ; Zone 2 ( $0.25-0.3 < T/T_m < 0.45$ ) consisting of columnar grains with a smooth surface; and Zone 3 ( $T/T_m > 0.45$ ) consisting of equiaxed grains. Thornton<sup>15-16</sup> has examined sputtered films of Mo, Cr, Ti, Fe, Cu, and Al and observed microstructures consistent with the three-zone model of Movchan and Demchishin.

The small grain size of thin films implies that inelastic stress relaxation mechanisms which are observed in bulk materials at high temperatures may be actually operative in thin films at much lower temperatures. Murakami<sup>20</sup> has shown that a large part of the deformation mechanism map of Pb films of grain size 0.2  $\mu\text{m}$  and film thickness 0.5  $\mu\text{m}$  is occupied by grain-boundary diffusional flow. Similar conclusions have been derived by Koleshko *et al.* for Al films.<sup>21</sup>

In order to examine the effect of the microstructure and growth parameters on diffusional flow during the growth of a thin film, we observe that the total strain for a film growing onto a thick substrate must vanish due to the geometrical constraint of the non-deforming substrate, thus

$$0 = \epsilon^e + \epsilon^T + \epsilon^{cp} \quad (14)$$

where the first term is the elastic strain, the second term is the misfit strain which induces the stress in the film and is assumed to be independent of the film thickness, and the third term is the creep, or inelastic strain. The elastic strain is given by

$$\epsilon^e = \frac{1 - \nu}{E} \sigma \quad (15)$$

( $E$ ,  $\nu$  being the Young's modulus and Poisson ratio, respectively) and the creep strain is given by

$$\epsilon^{cp} = \int_{x_2/p_0}^t \dot{\epsilon}^{cp} dt, \quad \dot{\epsilon}^{cp} = \epsilon_0 \frac{\sigma}{g s_0} \quad (16)$$

for a material particle located at a distance  $x_2$  above the interface of a film whose thickness  $h$  increases linearly with time at the rate  $p_0$ . For the inelastic constitutive expression we assume that either grain-boundary (Coble creep<sup>22</sup>) or bulk (Nabarro-Herring creep<sup>23-24</sup>) diffusion operates, so that

$$\begin{aligned} \epsilon_0 &= \frac{B_s (D_b \delta)}{h^2 d} (g - b. \text{diffusion}), \\ \epsilon_0 &= \frac{B_s D_v}{h d} (\text{bulk diffusion}) \end{aligned} \quad (17)$$

where  $h$  is the current thickness of the film ( $h = p_0 t$ ) which is identical to the grain size perpendicular to the interface according to the model of Movchan and Demchishin,<sup>14</sup> and  $d$  is the grain size parallel to the interface. It is assumed that  $d$  remains constant during growth. The constants  $B_s$  and  $B_v$  are approximately equal to 10, from the work of Gibbs,<sup>25</sup> and  $D_b \delta$  and  $D_v$  are the temperature dependent diffusivities for grain-boundary and bulk diffusion, respectively. The material constant  $\sigma_0 = kT/\Omega$  where  $\Omega$  is the atomic volume.

Let the current film thickness be  $h_0$ . We non-dimensionalize the stress by  $\sigma_0$ , the strain by  $\sigma_0/E$ , and time by  $h_0/p_0$ , so that Eq. (12) becomes

$$0 = (1 - \nu) \frac{\sigma}{\sigma_0} + \frac{\epsilon^T}{(\sigma_0/E)} + \frac{E B_s (D_b \delta)}{\sigma_0 h_0 d p_0} \int_{x_2/h_0}^1 \frac{(\sigma/\sigma_0)}{(h/h_0)^2} d \left( \frac{tp_0}{h_0} \right) \quad (18)$$

for the case of grain-boundary diffusion, which is expected to dominate at lower temperatures. A similar expression can be derived for bulk diffusion. From Eq. (18) it becomes clear that the elastic and misfit strains are of the same order of magnitude, and that the creep strain via grain-boundary diffusion is proportional to the non-dimensional number  $N$  defined by

$$N = \frac{E B_s (D_b \delta)}{\sigma_0 h_0 d p_0} = \frac{l}{h_0}, \quad l = \frac{E B_s (D_b \delta)}{\sigma_0 d p_0} \quad (19)$$

where  $l$  is a length scale which depends on material properties and on the growth parameters  $d$  and  $p_0$ . When  $N > 1$  (or  $l > h_0$ ), the effect of grain-boundary diffusion is important in relaxing the stresses induced by the misfit  $\epsilon^T$ .

To estimate the length scale  $l$ , we used typical ranges of film growth parameters:  $p_0 = 0.1$  to 10 nm/s and  $d = 20$  to 500 nm. For the diffusivities we used the data from Frost and Ashby.<sup>13</sup> Thus, the range of values of  $p_0$  and  $d$ , via Eq. (17), allows the calculation of a minimum  $l_{\min}$  and maximum value  $l_{\max}$  for the parameter  $l$ , which are shown below in Table 1. Depending on the growth temperature, grain size  $d$ , and growth rate  $p_0$ , it is seen from Table 1 that the effect of grain-boundary diffusion may be considerable.

For the FCC metals the ratio  $E/\sigma_0$  ranges from  $2 \times 10^2$  to  $5 \times 10^2$ , with the exception of lead where  $E/\sigma_0$  is about  $1 \times 10^3$ . For the HCP metals  $E/\sigma_0$  ranges from  $1 \times 10^3$  to  $5 \times 10^3$ , with the exception of Ti where  $E/\sigma_0$  is one order of magnitude lower. Depending on the misfit strain  $\epsilon^T$  the relative magnitude of the elastic strain can thus be calculated via Eq. (18).

Although the assumption has been made that grain size  $d$  remains constant during growth, this is not necessarily so. Goyal *et al.*<sup>26</sup> have shown for Ni films grown by thermal evaporation on Si substrates that the grain size  $d$  increases linearly with film thick-



Table 1. Values of  $l_{\min}$  and  $l_{\max}$  (units of microns) for some temperatures for some fcc and bcc metals. The material data for the diffusivities are from Frost and Ashby.<sup>15</sup>

$T_m$ (K)	T = 300 K		T = 400 K		T = 500 K		
	$l_{\min}$	$l_{\max}$	$l_{\min}$	$l_{\max}$	$l_{\min}$	$l_{\max}$	
FCC							
Ni	1726	4E-11	1E-7	4E-6	1E-2	2E-3	5
Cu	1356	2E-9	5E-6	6E-5	0.2	0.02	50
Ag	1234	6E-7	0.002	0.004	10	0.8	2,000
Al	933	8E-5	0.2	0.2	500	40	1E + 5
Pb	601	8E-2	200	40	1E + 5	2E + 3	5E + 6
HCP							
Zn	693	4	1E + 4	1,000	2E + 6	4E + 4	1E + 8
Cd	594	100	3E + 5	2E + 4	5E + 7	4E + 5	1E + 9
Mg	924	0.004	10	400	1E + 6	4,000	1E + 7
alpha-Ti	1933		1.5E-5	8E-5	0.2	0.02	50
beta-Ti	1933		2E-16	2E-13	5E-10	2E-9	5E-6

ness (from about 5 nm at a thickness of 50 nm to about 30 nm at a thickness of 500 nm). Such a feature can be easily included into the analysis.

Since the film thickness (and, correspondingly the grain size  $d$ , since  $d(d)/d(h) > 0$ ) increases continuously during growth, the main consequence of Eq. (17) is that grain-boundary diffusion is most important for thin films, so that in the early stages of growth we expect the stress due to the misfit to be largely relaxed. When the film gets to be thicker, diffusion is diminished, so that for a given thickness of the film, it is anticipated that the largest stress will be localized near the free surface rather than near the film-substrate interface where the stress has been relaxed by creep in the early stages of growth. As a further consequence, the average of the stress through the thickness of the film is expected to be a diminishing function of the film thickness, in agreement with experimental observations.<sup>20</sup>

### THERMAL CONDUCTIVITY OF THIN FILMS AND INTERFACES

The thermal conductivity of thin films is often a strong function of the film thickness. Nath and Chopra<sup>27</sup> found that for Cu films thinner than about 1 micron the bulk conductivity values were not appropriate. Boikov *et al.*<sup>28</sup> studied the thermal conductivity of Ag and Al films, and Ogden *et al.*<sup>29</sup> the conductivity of anodic oxide coatings of Al of thickness in the range 25–110 microns. The common conclusion is that thin films exhibit a considerably lower thermal conductivity than bulk materials, and that a significant interfacial thermal resistance develops across the interface of thin films bonded to substrates. A comprehensive review of thermal conductivity measurements of thin films has been recently given by Guenther and McIver.<sup>18</sup>

For dielectric films (such as oxides and fluorides) the low film thermal conductivity leads to important implications about the laser damage resistance of such coatings. The energy density at damage  $E$ , is given by<sup>18</sup>

$$E_t \sim T_c \sqrt{\rho c_p k t_p} \quad (20)$$

where  $T_c$  is the temperature level at damage (typically the melting point of the material),  $\rho$  is the density,  $c_p$  the heat capacity,  $k$  the thermal conductivity, and  $t_p$  the laser pulse length which causes damage. Relationship (20) results from the work of Goldenberg and Tranter<sup>30</sup> who analyzed the time dependent heat transfer due to a spherical absorbing inclusion embedded within an infinite nonabsorbing matrix. Although  $c_p$  and  $\rho$  of optical thin films are close to those of the bulk solids, this is not the case for the thermal conductivity  $k$  which, being considerably lower for thin films, leads to lower values for the damage threshold energy densities.

The heat comparator is a technique which allows the rapid determination of the heat conductivity of bulk solids by bringing in contact a heated probe tip (of approximate diameter 200–300  $\mu\text{m}$ ) and the cooler solid. The temperature drop in the tip is directly related to the thermal conductivity of the solid, which can thus be measured. The technique was modified at the Laboratory for Laser Energetics at the University of Rochester to measure the thermal conductivity of thin films<sup>19</sup> of thickness  $h$  in the micron and submicron range. Denoting by  $k_{\text{app}}$  the value as measured by the thermal comparator, by  $k_{\text{eff}}$  the thermal conductivity of the film and any interfaces, and by  $k_f$  the film conductivity of the film material itself, Lambropoulos *et al.*<sup>19</sup> have used the work of Dryden<sup>31</sup> on the heat transfer of film-substrate assemblies to show that  $k_{\text{eff}}$  can be extracted from  $k_{\text{app}}$  via

$$\frac{1}{k_{\text{eff}}} = \frac{\pi a}{4 h} \left( \frac{1}{k_{\text{app}}} - \frac{1}{k_s} \right) \quad (21)$$

where  $a$  is the heat flow radius, and  $k_s$  is the conductivity of the substrate. Equation (21) is valid when  $h \ll a$  and  $k_{\text{eff}} \ll k_s$ , so that it can be used for thin films of low thermal conductivity. Otherwise, the relation between  $k_{\text{app}}$  and  $k_{\text{eff}}$  is more complex, although it is still easy to use.<sup>19</sup>

When  $k_{\text{eff}}$  is determined from (21), the film con-



ductivity  $k_F$  and the interfacial thermal resistance  $R_{int}$  (which is the ratio of the temperature drop across to the power flux through the interface) can be determined, respectively, as the inverse of the slope and the intercept in a plot of  $h/k_{eff}$  vs  $h$ .

Typical results for a wide range of oxide and fluoride films deposited by electron beam evaporation and by ion beam sputtering show that the film conductivity is considerably lower than that of the bulk.<sup>19</sup> For  $SiO_2$  films on Si the film conductivity was found to be 0.4–0.6 W/m/K (bulk value of 1.2–10.7 W/m/K); For  $TiO_2$  films on Si,  $k_F = 0.5$ –0.6 W/m/K (bulk value 7.4–10.4 W/m/K); For  $Al_2O_3$  on Si,  $k_F = 0.72$  W/m/K (bulk value 20–46 W/m/K); For  $MgF_2$  films on Si,  $k_F = 0.58$  W/m/K (bulk value 14.6–30 W/m/K). The measured interfacial thermal resistance was in the range of 0–3 K/(W/mm<sup>2</sup>) for the materials examined. Swartz and Pohl<sup>32</sup> have measured the interfacial thermal resistance of metal-oxide interfaces and have found values in the range 0.01–1.0 K/(W/mm<sup>2</sup>) at about 200 K. From extrapolating, their results seem to be valid at higher temperatures.

To examine whether or not these reduced values may be due to the increased porosity of the film, we use the work of Budiansky<sup>33</sup> who calculated the thermal conductivity of a composite containing spherical inclusions by using the self-consistent scheme. Budiansky found that

$$\frac{3c_1}{2 + \frac{k_1}{k}} + \frac{3(1 - c_1)}{2 + \frac{k_2}{k}} = 1 \quad (22)$$

where  $k_1$ ,  $k_2$ ,  $k$  are the thermal conductivities of the inclusions, of the matrix, and of the composite, respectively, and  $c_1$  is the volume concentration of the inclusions. Assuming that the spherical inclusions for the case of films are voids, the composite conductivity ( $k_F$  in our case) is related to the conductivity  $k_0$  corresponding to the completely dense solid by

$$\frac{k_F}{k_0} = 1 - \frac{3}{2}c \quad (23)$$

where  $c$  is the volume fraction of the voids. This equation implies that at a void fraction of 0.667, the conductivity of the film essentially vanishes.

The growth of thin films has been modelled numerically, and a comprehensive review for optical films can be found in the work of Bartholomeusz.<sup>34</sup> Muller<sup>35</sup> has calculated the packing density in thin films. He shows, for example, that for an angle of incidence of 30 degrees during deposition, the packing density is about 0.8 when  $T < 400$  K. Above that temperature atom surface migration sets in, and a structural change occurs, so that at about 450 K maximum packing is obtained. For an angle of incidence of 60 degrees, the low temperature packing density is between 0.5 and 0.6, it starts to increase

at about 400 K, and it becomes 1.0 at about 500 K. Thus, packing densities in the range of 0.5 to 1.0 are realistic in the case of deposited films, and they are compatible with the high porosity required, from Eq. (23), for the low measured value of the film thermal conductivity.

Typical data for the laser damage threshold of thin oxide and fluoride films are in the range of 5–20 J/cm<sup>2</sup> from the work of Walker *et al.*<sup>36–37</sup> Using the maximum value for the interfacial thermal resistance measured by the thermal comparator,<sup>19</sup> thus gives an upper bound on the temperature drop across the film-substrate interface of 0.6 K.

For a layer of thickness  $t_{int}$  and with thermal conductivity  $k_{int}$ , the interfacial thermal resistance is

$$R_{int} = \frac{t_{int}}{k_{int}} \quad (24)$$

so that, were the interface made of silica (with conductivity of 3 W/m/K), the corresponding thickness would be about 9 microns. The interface is known to create a large density of voids, and work is under way at the University of Rochester to try to correlate the interfacial void density to the details of the interfacial heat transfer in film-substrate assemblies. It is expected that, for a given areal void density, the shape of the voids will influence the interfacial thermal resistance.

## ACKNOWLEDGEMENT

This work has been supported by the Office of Naval Research under Grant N00014-87-K-0488 and the National Science Foundation under the 1988 Presidential Young Investigator Award MSM-8857096.

## REFERENCES

1. A. Bar-Cohen and A. D. Kraus (eds.), *Advances in Thermal Modeling of Electronic Component and Systems*, Vol. 1 (Hemisphere, New York), 1988.
2. A. G. Evans, M. D. Drory, and M. S. Hu, *J. Mater. Res.* 3, 1043 (1988).
3. J. R. Rice, *J. Appl. Mech.* 55, 98 (1988).
4. J. W. Hutchinson, M. E. Mear and J. R. Rice, Crack paralleling an interface between dissimilar materials, report MECH-95, Division of Applied Sciences, Harvard University (1987).
5. C. F. Shih and R. J. Asaro, *J. Appl. Mech.* 55, 299 (1988).
6. J. Qu and J. L. Bassani, *J. Mech. Phys. Solids* 37, 417 (1989).
7. V. L. Hein and F. Erdogan, *Int. J. Fract. Mech.* 7, 317 (1971).
8. B. J. Aleck, *J. Appl. Mech.* 16, 118 (1949).
9. R. Zeyfang, *Solid State Electron.* 14, 1035 (1971).
10. E. Suhir, *J. Appl. Mech.* 53, 657 (1986).
11. J. C. Lambropoulos and S.-M. Wan, in R. C. Sundahl *et al.* (eds.), *Electronic Packaging Materials Science*, Mater. Res. Soc. Proc., Vol. 108, 399 (1988).
12. J. C. Lambropoulos and S.-M. Wan, *Mater. Sci. and Eng. A107*, 169 (1989).
13. H. J. Frost and M. F. Ashby, *Deformation-Mechanism Maps* (Pergamon, New York), 1982.
14. B. A. Movchan and A. V. Demchishin, *Fiz. Met. Metalloved.* 28, 653 (1989).



15. J. A. Thornton, *J. Vac. Sci. Technol.* **11**, 666 (1974).
16. J. Thornton, in R. A. Huggins *et al.* (eds.), *Annual Review in Materials Science*, Vol. 7, 239 (1977).
17. W. Nakayama, *Appl. Mech. Rev.* **39**, 1847 (1986).
18. A. H. Guenther and J. K. McIver, in *Laser Optics for Intracavity and Extracavity Applications*, SPIE Vol. 895, 246 (SPIE, Washington), 1988.
19. J. C. Lambropoulos, M. R. Jolly, C. A. Amsden, S. E. Gilman, M. J. Sinicropi, D. Diacomihalis and S. D. Jacobs, *J. Appl. Phys.* **66**, 4230 (1989).
20. M. Murakami, in D. E. Schuele and R. W. Hoffman (eds.), *Critical Reviews in Solid State and Mat. Sci.* vol. 11, 317 (CRC Press, Boca Raton), 1984.
21. V. M. Koleshko, V. F. Belitsky and I. V. Kiryushin, *Thin Solid Films* **142**, 199 (1986).
22. R. L. Coble, *J. Appl. Phys.* **34**, 1679 (1963).
23. F. R. N. Nabarro, *Report of a Conf. on the Strength of Solids*, (Phys. Soc., London), 1948.
24. C. Herring, *J. Appl. Phys.* **21**, 437 (1950).
25. G. B. Gibbs, *Philos. Mag.* **13**, 589 (1966).
26. D. Goyal, A. H. King, and J. C. Bilello, R. C. Sundahl *et al.* (eds.), *Electronic Packaging Materials Science*, Mater. Res. Soc. Proc. Vol. 108, 395 (1988).
27. P. Nath and K. L. Chopra, *Thin Solid Films* **18**, 29 (1973).
28. B. T. Boikov, A. T. Pugachev and V. M. Bratsyshiv, *Thin Solid Films* **17**, 157 (1973).
29. T. R. Ogden, A. D. Rathsaam and J. T. Gilchrist, *Mater. Lett.* **5**, 84 (1987).
30. H. Goldenberg and M. A. Tranter, *Brit. J. Appl. Phys.* **3**, 296 (1952).
31. J. R. Dryden, *J. Heat Transfer* **105**, 408 (1983).
32. E. T. Swartz and R. O. Pohl, *Appl. Phys. Lett.* **51**, 2200 (1987).
33. B. Budiansky, *J. Composite Mater.* **4**, 286 (1970).
34. B. J. Bartholomeusz, K.-H. Muller, M. R. Jacobson, in M. R. Jacobson (ed), *Modeling of Optical Thin Films*, SPIE Vol. 821, 2 (SPIE, Washington) 1987.
35. K.-H. Muller, in M. R. Jacobson (ed), *Modeling of Optical Thin Films*, SPIE Vol. 821, 36 (SPIE, Washington) 1987.
36. T. W. Walker, A. H. Guenther and P. E. Nielsen, *IEEE J. Quantum Electron.* **QE-17**, 2041 (1981).
37. T. W. Walker, A. H. Guenther and P. E. Nielsen, *IEEE J. Quantum Electron.* **QE-17**, 2053 (1981).



## APPENDIX (5)

### Analysis of thermal stress, fracture strength, and the effect of ion exchange on high average power phosphate glass slab lasers

John C. Lambropoulos

*Department of Mechanical Engineering, University of Rochester, Rochester, New York 14627*

(Received 10 July 1989; accepted for publication 27 October 1989)

It has been recently demonstrated that it is possible to significantly alter the maximum power input required for mechanical failure of glass used for high average power laser applications by employing an ion exchange process that does not alter the optical properties of the strengthened glass. We present the analysis of the thermal stresses, fracture, and strengthening for the experimental geometry used. From this analysis the fracture strength of the untreated and treated glass can be estimated. Some suggestions for the control of thermal stresses during the operation of solid-state lasers using glass slab geometries are presented. The second part of this report presents a micromechanical analysis of the strengthening effect due to the ion exchange process in which the enhancement in fracture strength is correlated to the depth of the zone in which ion exchange has occurred, to the length of microscopic flaws present on the surface of the glass, and to the magnitude of the microscopic volume expansion due to the ion exchange process. In particular, we consider the cases where the depth of the treated zone is much smaller or much greater than the depth of surface flaws. The magnitude of the enhancement in fracture strength is calculated in terms of these microscopic quantities for some material properties typical of phosphate glasses.

#### I. INTRODUCTION

Recent technological advances in high repetition rate solid-state lasers with high average power have put increasing demands on the development of solid-state laser materials with increased mechanical strength under thermal loading conditions.<sup>1</sup> Since glass is an inherently brittle material, it is imperative to control the size of microscopic flaws present on its surface. These cracks eventually lead to the final fracture of the solid-state laser component. There are several ways to reduce the effect of such microscopic cracks while maintaining high thermal loadings. One is to reduce the size of the flaws on the glass surface: Such a method requires extensive and expensive polishing procedures. Another is to induce a compressive residual stress on the surface of the glass which thus tends to close the surface microflaws. This can be achieved by using compressed epitaxial layers,<sup>2</sup> polymer films,<sup>3</sup> or chemical treatments such as ion exchange.<sup>4,5</sup>

It has been recently demonstrated that ion exchange can significantly enhance the power input required for fracture in commercially available Nd-doped phosphate glass.<sup>4</sup> Thermal loading experimental studies of  $160 \times 15 \times 8$  mm<sup>3</sup> rectangular slabs showed a fivefold to sixfold increase in power input for the strengthened samples over the unstrengthened material. One important conclusion of that work was that the optical properties of the strengthened samples were very similar to the properties of the unstrengthened samples, thus making ion exchange a very viable technique for enhancing the mechanical properties while at the same time not altering the optical properties of phosphate glass used in high average power solid-state laser applications. It must be mentioned that one of the conclusions of the work of Cerqua and co-workers<sup>4</sup> was that the ion exchange treatment does not heal surface microflaws: Instead, the technique creates a thin layer of compressive stresses on the surface of the glass which, therefore, diminishes the driving force for crack

propagation. This force results from the superposition of the stresses due to the surface compressive layer produced by the ion exchange and of the thermal stresses due to the applied thermal load.<sup>4</sup>

The ion exchange process has been known to improve the mechanical strength of brittle materials.<sup>5</sup> Nevertheless, when such a technique is applied to phosphate glasses it creates a thin white film on the surface of the optical component which deteriorates the transmission of power to the interior host material. It also deteriorates the reflectivity of multiply reflected laser beams in the interior of the glass slab. The technique of Cerqua and co-workers<sup>4</sup> showed that the ion exchange, if carefully controlled and performed, preserves the optical integrity of the glass surface, thus making strengthened phosphate glass a viable alternative to solid-state lasers employing crystalline media, such as aluminas and garnets, which may have serious size limitations.

It is the objective of this report to analyze the thermal stresses during the thermal loading experiments of Cerqua and co-workers,<sup>4</sup> and to present a micromechanical analysis that correlates the enhancement in mechanical strength to the variables characterizing the ion exchange treatment such as the depth of the treated zone and the size mismatch between the exchanged ions. The report is presented in three parts: first, the temperature distribution in the thermally loaded glass slab is determined by solving the steady-state heat conduction equation. Second, the stresses are determined by using numerical and analytical techniques. The scaling of the surface stresses with a nondimensional Biot number is presented, the regions of maximum stressing are described, and the specific dependence of the various stress components on the magnitude of the thermal load is discussed. Third, the power input at fracture is related to the mechanical strength of the strengthened and unstrengthened materials and the size of the critical microflaws is estimated. These values are shown to lead to an estimate of the



volume expansion due to the ion exchange, and to the volume concentration of the ion exchange sites. An independent estimate of the depth of the surface layer can be combined with the parameters derived in order to predict from first principles the magnitude of the enhancement in fracture toughness of the strengthened material over the unstrengthened glass. Two specific cases are discussed: when the flaw size greatly exceeds the treated zone size, and when the flaw size is much smaller than the depth of the treated zone. It is shown that the induced enhancement in fracture toughness may easily exceed the fracture toughness of the untreated glass, and therefore the possibility of partial crack closure is discussed. In the discussion part of the report we use typical material parameters in order to derive some figures of merit for the maximum enhancement in fracture toughness due to ion exchange.

## II. TEMPERATURE DISTRIBUTION

The geometry of the slab is shown in Fig. 1. Due to the fact that the axial length greatly exceeds the cross-sectional dimensions, it is obvious that far from the faces  $z = \pm 1$  the temperature distribution is independent of  $z$ , and thus satisfies the heat diffusion equation

$$k\nabla^2 T(x,y,t) + Q(x,y,t) = \rho c \partial T(x,y,t) / \partial t, \quad (1)$$

where  $k$  is the thermal conductivity,  $\rho$  is the density, and  $c$  is the specific heat. The initial condition is  $T(x,y,t=0) = T_i$ , and the boundary condition is

$$k\partial T / \partial n + h(T - T_a) = 0. \quad (2)$$

In Eqs. (1) and (2)  $Q(x,y,t)$  is the power per unit volume absorbed by the glass due to thermal pumping.  $T_a$  is the temperature of the cooling medium, and  $h$  is the cooling coefficient which depends on the cooling medium.<sup>6</sup> The boundary condition (2) holds on the faces of the slab given by  $x = \pm L$  and  $y = \pm D$ . The temperature  $T_i$  is the initial temperature of the slab, and as will be shown later, does not affect the resulting stresses.

The rate of energy absorption  $Q(x,y,t)$  is a periodic function of time of the form<sup>7</sup>

$$Q(x,y,t) = Q_0(x,y) \sum_{m=0}^{\infty} \delta(t - m\tau), \quad m\tau < t < (m+1)\tau, \quad (3)$$

where the spatial variation is given by  $Q_0$  and  $\tau$  is the period of the repetition rate of the flashlamps that produce the thermal load on the glass slab. It has been shown<sup>7</sup> that if the period  $\tau$  is sufficiently low as compared to the characteristic

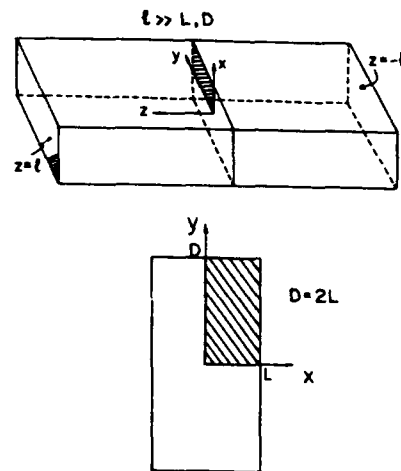


FIG. 1. The geometry of the thermally pumped glass slab. Due to symmetry, only the shaded region was used in the numerical calculation of the thermal stresses.

time required for heat to diffuse through the glass slab, then the time dependence in Eq. (1) can be neglected, so that the temperature can be found from the steady-state heat diffusion equation

$$k\nabla^2 T(x,y) + Q_0(x,y) = 0 \quad (4)$$

under the boundary condition of Eq. (2).

Following the analysis of Ref. 7, it can be shown that the minimum frequency of flashing for which the steady-state approximation is valid is given by

$$f_{\min} = k\pi^2 n^2 (1 + L^2/D^2) / (\rho c L^2), \quad (5)$$

where  $n$  is an integer that has a value of approximately 5 or higher. Such a value is required in order to make time-dependent effects negligible.<sup>7</sup>

For the case of uniform heat deposition, we have that  $Q(x,y) = Q_0$ , where  $Q_0$  is constant. Under this assumption, the solution to the steady-state equation of (4) under the boundary condition (2) has been given by Carslaw and Jaeger<sup>8</sup> as

$$\frac{T - T_a}{T_0} = B^{-1} + \frac{1}{2}(1 - x^2) - 4B \sum_{n=1}^{\infty} A_n \cos \lambda_n x \cosh \lambda_n y, \quad (6)$$

where the coefficients  $A_n$  are given by

$$A_n = \frac{\sin \lambda_n}{\lambda_n^2 (2\lambda_n + \sin 2\lambda_n) (\lambda_n \sinh \lambda_n D/L + B \cosh \lambda_n D/L)}. \quad (7)$$

The numbers  $\lambda_n$  are the roots of the transcendental equation  $\lambda_n \tan \lambda_n = B$ , the parameter  $B$  is the Biot number defined by

$$B = hL/k, \quad (8)$$

and  $T_0$  is a convenient unit for measuring changes in tem-

perature above  $T_a$  and it is given by

$$T_0 = Q_0 L^2 / k. \quad (9)$$

In Eq. (6) the distances  $x$  and  $y$  are measured in terms of the width  $L$  of the slab.



When  $B \ll 1$ , it is easily shown that the temperature becomes

$$\frac{T - T_a}{T_0} = B^{-1} + \frac{1}{2}(1 - x^2) - \frac{\cos\sqrt{B}x \cosh\sqrt{B}y}{B(1 + D/L)}, \quad (10)$$

whereas when  $B \gg 1$  the temperature becomes

$$\frac{T - T_a}{T_0} = \frac{1}{2}(1 - x^2) - \frac{16}{\pi^2(1 + \pi) \cosh \pi D/2L} \times \cos \frac{\pi x}{2} \cosh \frac{\pi y}{2} + O\left(\frac{1}{B}\right). \quad (11)$$

It is thus seen that when the cooling rate, as given by the cooling coefficient  $h$  or the Biot number  $B$ , is very small the temperature increases continuously. This is to be expected because for small  $B$  the cooling rate is not sufficient to remove the power deposition represented by  $Q_0$ . On the other hand, when the Biot number is very large, the temperature deposition becomes essentially independent of the Biot number. We also note that due to the rapid decrease of the coefficients  $A_n$  in the series solution for the temperature, a few terms in the infinite sum will suffice for the precise numerical computation of the temperature distribution.

### III. THERMOELASTIC STRESSES

Once the temperature has been determined, the stresses can be calculated as well. In this particular report, the stresses have been calculated under two modeling assumptions. First, that the faces  $z = \pm 1$  are completely constrained against displacement in the  $z$  direction, so that

$$\epsilon_{zz} = 0. \quad (12)$$

The other situation examined corresponds to the case where the slab is completely unconstrained against displacement in the  $z$  direction, so that there is no net force in the  $z$  direction, i.e.,

$$F_z = \int_{x=-L}^L dx \int_{y=-D}^D dy \sigma_{zz} = 0. \quad (13)$$

In either case, as long as we stay away from the end faces  $x = \pm L$  the deformation due to thermal stresses is two dimensional so that the displacements are  $u(x, y), v(x, y)$  in the  $x, y$  directions, respectively.

Under the plain strain conditions expressed in Eq. (12), the constitutive relation for the thermoelastic deformation of the slab is<sup>9</sup>

$$\epsilon_{\alpha\beta} = \frac{1 + \nu^*}{E^*} \left( \sigma_{\alpha\beta} - \frac{\nu^*}{1 + \nu^*} \sigma_{\gamma\gamma} \delta_{\alpha\beta} \right) + \alpha^* T \delta_{\alpha\beta}, \quad (14)$$

where  $T$  measures the temperature above  $T_a$  and the summation convention is used for repeated Greek lower case indices which take the values  $x, y$ .

The modified thermoelastic moduli  $E^*$ ,  $\nu^*$ , and  $\alpha^*$  are related to the actual Young's modulus  $E$ , coefficient of thermal expansion  $\alpha$ , and Poisson ratio  $\nu$  for the case of plane strain, Eq. (12), by Ref. 9

$$E^* = E/(1 - \nu^2), \quad \alpha^* = \alpha(1 + \nu), \quad \nu^* = \nu/(1 - \nu). \quad (15)$$

For the case of plane strain, Eq. (12), the out-of-plane component of stress  $\sigma_{zz}$  is given by

$$\sigma_{zz} = \nu(\sigma_{xx} + \sigma_{yy}) - \alpha ET. \quad (16)$$

On the other hand, in order to calculate  $\sigma_{zz}$  for the case of no constraint, it is necessary to first calculate  $\sigma_{zz}$  via Eq. (16), and then to subtract the average value (over the face  $-L < x < +L, -D < y < +D$ ) of the stress component  $\sigma_{zz}$ . This procedure leads to a stress distribution that satisfies Eq. (13).

It is interesting to note that the in-plane stresses  $\sigma_{xx}$ ,  $\sigma_{xy}$ , and  $\sigma_{yy}$  do not depend on the Biot number  $B$ . To see this, the Airy stress function is introduced by

$$\sigma_{xx} = \frac{\partial^2 \phi}{\partial y^2}, \quad \sigma_{yy} = \frac{\partial^2 \phi}{\partial x^2}, \quad \sigma_{xy} = -\frac{\partial^2 \phi}{\partial x \partial y} \quad (17)$$

so that the equations of equilibrium are satisfied automatically. Substitution from Eq. (17) into the constitutive equations (15), and further substitution for the strains into the compatibility equation

$$\frac{\partial^2 \epsilon_{xx}}{\partial y^2} + \frac{\partial^2 \epsilon_{yy}}{\partial x^2} = \frac{2\partial^2 \epsilon_{xy}}{\partial x \partial y} \quad (18)$$

leads to a single differential equation for the stress function, namely

$$\nabla^4 \phi + E^* \alpha^* \nabla^2 T = 0. \quad (19)$$

Noting that the temperature  $T$  satisfies the steady-state heat conduction Eq. (4), Eq. (19) finally yields

$$\nabla^4 \phi = E^* \alpha^* Q_0 / k. \quad (20)$$

Since the sides of the slab are free of tractions, these boundary conditions are cast in terms of derivatives of the stress function via Eq. (17). It is concluded that since the differential equation and the boundary conditions for the stress function do not depend on the Biot number, the in-plane stress components  $\sigma_{xx}$ ,  $\sigma_{xy}$ , and  $\sigma_{yy}$  are also independent of the Biot number and they depend only on the amount of power deposition per unit volume  $Q_0$ . On the other hand, the out-of-plane component of stress  $\sigma_{zz}$  does depend on the Biot number since it is calculated via Eq. (16) that involves the temperature distribution which depends on the Biot number  $B$ .

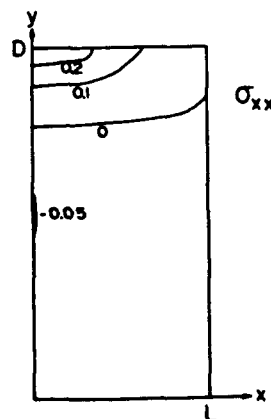


FIG. 2. Contours of the in-plane stresses  $\sigma_{xx}$  in units of  $\alpha E Q_0 L^2 / k$ . These stress components are independent of the Biot number  $hL/k$ . The Poisson ratio is 0.25.



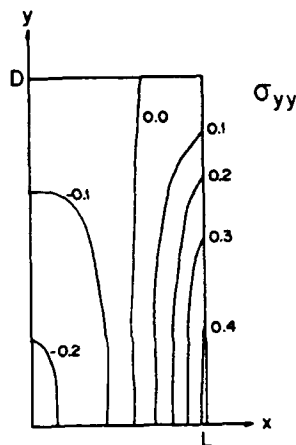


FIG. 3. Contours of the in-plane stresses  $\sigma_{yy}$  in units of  $\alpha E Q_0 L^2 / k$ . These stress components are independent of the Biot number  $hL/k$ . The Poisson ratio is 0.25.

The stresses were determined numerically for the Poisson ratio equal to 0.25 and for the aspect ratio  $D/L = 2$  by using bilinear isoparametric finite elements. The stress contours are shown in Figs. 2 and 3 for the in-plane stress components, which, as mentioned previously, do not depend on the Biot number. Due to the symmetry of the problem, only the quadrant  $0 < x/L < 1, 0 < y/L < D/L$  is shown. It can be seen immediately that the surface of the slab is in tension, whereas the interior is in a state of compression. The stresses are measured in units of  $\alpha E T_0$ , where the reference temperature rise is given by Eq. (9). The out-of-plane stress components  $\sigma_{zz}$  are shown in Figs. 4 and 5 for the constrained case satisfying Eq. (12). It is seen immediately that these stresses are compressive, and as such presumably do not lead to fracture.

On the other hand, for the unconstrained case satisfying Eq. (13), the out-of-plane stress components  $\sigma_{zz}$  are shown in Figs. 6–8 for the Biot number  $B = 0.1, 1, 10$ , respectively. It is seen that for the unconstrained case the  $\sigma_{zz}$  stress components are tensile near the surface of the slab and compressive in the interior. Depending on the Biot number, it is possible for  $\sigma_{zz}$  to exceed the in plane stresses  $\sigma_{xx}$  and  $\sigma_{yy}$ . For the case of unconstrained deformation in the  $z$  direction, the variation of the maximal values of the stresses with the Biot number  $B$  is shown in Fig. 9. Specifically, Fig. 9 includes the

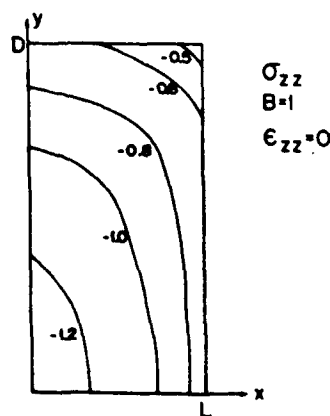


FIG. 4. Contours of the out-of-plane stress  $\sigma_{zz}$  in units of  $\alpha E Q_0 L^2 / k$  when the ends  $z = \pm 1$  are constrained against displacement in the  $z$  direction. The Biot number  $B = hL/k$  is 1, and the Poisson ratio is 0.25.

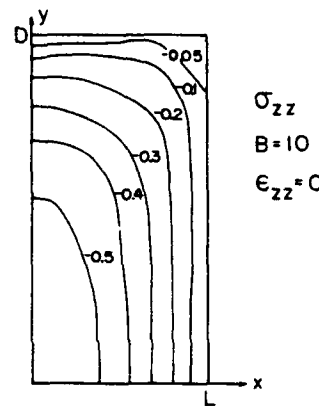


FIG. 5. Contours of the out-of-plane stress  $\sigma_{zz}$  in units of  $\alpha E Q_0 L^2 / k$  when the ends  $z = \pm 1$  are constrained against displacement in the  $z$  direction. The Biot number  $B = hL/k$  is 10, and the Poisson ratio is 0.25.

variation of the stresses with  $B$  for the three points A, B, and C all of which are located on the surface of the slab.

Were the plate of infinite extent in the  $y$  direction but of finite extent  $2L$  in the  $x$  direction, then the points on the surface of the slab would be in a state of balanced biaxial tension of magnitude

$$\sigma_{yy} = \sigma_{xx} = \frac{\alpha E T_0}{3(1-\nu)} \quad (21)$$

This value is also shown in Fig. 9 for comparison purposes. It can be seen from Fig. 9 that the result for the plate of infinite extent provides a good upper bound for the stresses when  $B > 1$ , as well as for the in-plane stress components  $xx$  and  $yy$  for all values of the Biot number. However, when  $B < 1$ , it is seen that the result for the infinite plate underestimates the  $zz$  components of stress at the point B where, as will be shown in the next section, the stress intensity factor is larger than the stress intensity factor at the points A and C for cracks of similar depths (quarter elliptical crack at the point B, half elliptical cracks at the points A and C).

The effect of the nonuniform power deposition rate  $Q$  was studied by examining a plate of infinite extent in the  $y$  direction, but of finite extent  $2L$  in the  $x$  direction. The power deposition profile was taken as

$$Q(x) = Q_0 \exp(-x/c) \quad 0 < x < 2L, \quad (22)$$

where  $x$  measures from the face of the plate. When  $c \gg 2L$  the power deposition rate is essentially uniform through the

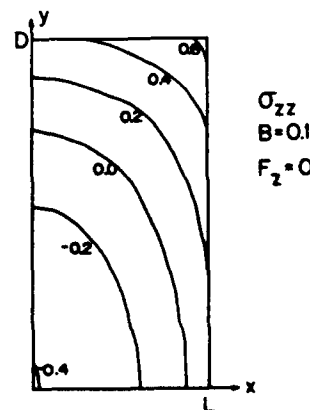


FIG. 6. Contours of the out-of-plane stress  $\sigma_{zz}$  in units of  $\alpha E Q_0 L^2 / k$  when the ends  $z = \pm 1$  are allowed to displace freely in the  $z$  direction. The Biot number  $B = hL/k$  is 0.1, and the Poisson ratio is 0.25.



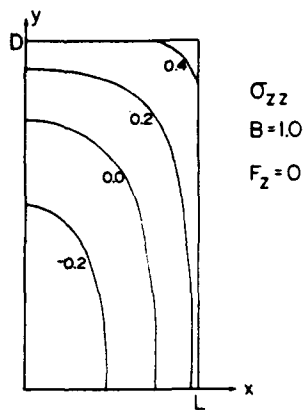


FIG. 7. Contours of the out-of-plane stress  $\sigma_{zz}$  in units of  $\alpha E Q_0 L^2 / k$  when the ends  $z = \pm 1$  are allowed to displace freely in the  $z$  direction. The Biot number  $B = hL/k$  is 1.0, and the Poisson ratio is 0.25.

thickness of the plate. When  $c \ll 2L$  the power deposition rate is localized near  $x = 0$ . The stresses at  $x = 0$ , which is in a state of balanced biaxial tension, are shown in Figs. 10(a) and 10(b) as functions of the ratio  $c/2L$ . The stresses were normalized either in terms of the maximum power deposition rate  $Q_0$ , which occurs at  $x = 0$ , Fig. 10(a), or in terms of the average power deposition rate per unit volume over the plate thickness  $Q_{ave}$ , Fig. 10(b). It is seen that the stresses are now smaller than what Eq. (21) predicts. Thus the previous analysis for uniform power deposition per unit volume, the results of which have been summarized in Fig. 9, provides an upper bound for the stresses due to inhomogeneous power deposition rates.

#### IV. TOUGHENING BY ION EXCHANGE

It has been shown previously<sup>4</sup> that an estimate for the efficiency of power transfer between the lamps and the glass material allows the calculation of the change in fracture strength due to the ion exchange process. It is important to note that such an estimate of the enhancement in fracture strength was based on the largest magnitude for the surface stresses  $\sigma_{xx}$  and  $\sigma_{yy}$ , which, as argued previously, do not depend on the Biot number. However, Fig. 9 shows that this is not necessarily the case; when the Biot number is less than 1,  $\sigma_{zz}$ , which depends on  $B$ , may exceed  $\sigma_{xx}$  and  $\sigma_{yy}$  considerably.

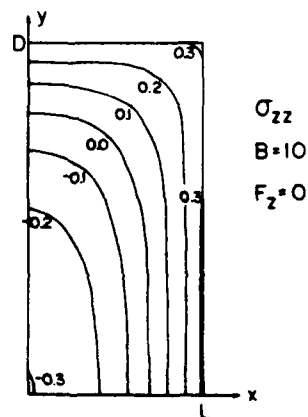


FIG. 8. Contours of the out-of-plane stress  $\sigma_{zz}$  in units of  $\alpha E Q_0 L^2 / k$  when the ends  $z = \pm 1$  are allowed to displace freely in the  $z$  direction. The Biot number  $B = hL/k$  is 10, and the Poisson ratio is 0.25.

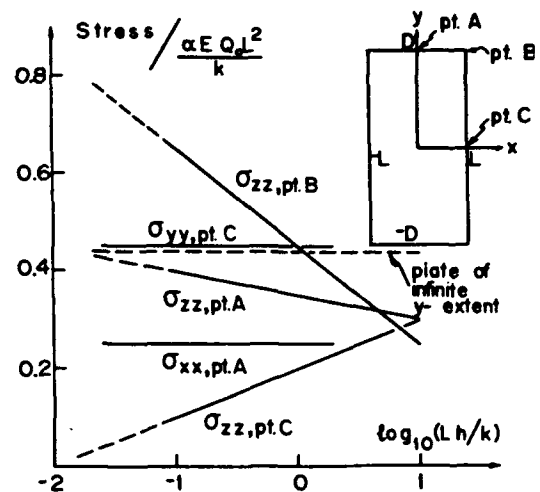
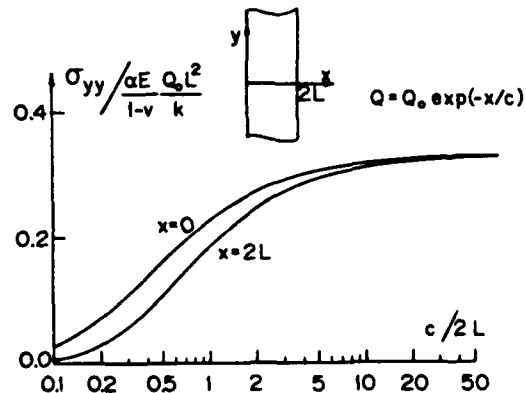
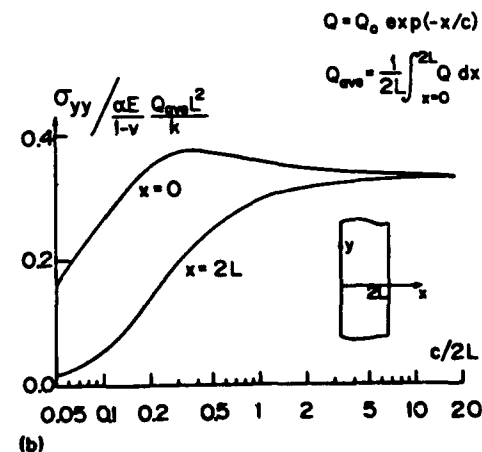


FIG. 9. Plots of the maximum stress on the surface of the slab vs  $\log_{10} B$ . These stresses occur at the points labeled A, B, and C. The result for the plate of width  $2L$  in the  $x$  direction and of infinite extent in the  $y$  direction is also shown. The Poisson ratio is 0.25.



(a)



(b)

FIG. 10. The effect of nonuniform power absorption on the tensile stresses in the front and back faces of a slab of width  $2L$  and of infinite extent in the  $y$  direction. The power absorbed per unit volume  $Q$  is nonuniform and it has a decay length  $c$ . (a) The stresses are normalized in terms of the maximum power  $Q_0$  absorbed per unit volume. (b) The stresses are normalized in terms of the average power  $Q_{ave}$  absorbed per unit volume.



It must be also mentioned that surface cracks, depending on where they are located, lead to different stress intensity factors. For example, for a surface semielliptical flaw of maximum depth  $b$  and under far field uniform tension of magnitude  $\sigma$ , the stress intensity factor is<sup>10</sup>

$$K = 1.12\sigma\sqrt{\pi b}, \quad (23)$$

whereas for a quarter-circular corner flaw of radius  $b$  the stress intensity factor is<sup>10</sup>

$$K = (2.6/\pi)\sigma\sqrt{\pi b}. \quad (24)$$

For a quarter-elliptical corner flaw the stress intensity factor is given by<sup>10</sup>

$$K = 1.3\sigma\sqrt{\pi b}, \quad (25)$$

where  $b$  is now the smallest depth of penetration.

Knowledge of the power input required for fracture for the strengthened and unstrengthened glass leads to an estimate of the fracture strength of the two materials. The difference in fracture strength is attributed to ion exchange, so that from the enhancement in fracture strength the microscopic details of the ion exchange can be estimated. Furthermore, knowledge of the difference in size between the exchanged ions allows the calculation of the volume concentration of the exchanged species. In deriving this result, the work of Nabarro was used<sup>11</sup>: When  $n$  sites within a solid of total volume  $V_0$  undergo a stress-free dilatation (in the sense of Eshelby<sup>12</sup>) whereby each site increases its volume by  $\Delta V^T$ , then the total dilatational strain  $e^T$  is given by

$$e^T = \Delta V^T (n/V_0). \quad (26)$$

The dilatation of Eq. (26) gives rise to a balanced biaxial compression on the surface of the glass which is determined by noting that the underlying glass does not allow any straining along directions parallel to the glass face. This balanced biaxial compression due to ion exchange is given by

$$\sigma = -\frac{Ee^T}{3(1-\nu)}. \quad (27)$$

Once the stresses due to the thermal power deposition and the stresses due to the ion exchange are known from Fig. 9 and Eq. (27), respectively, the fracture criterion for the unstrengthened glass is written as

$$\Omega\sqrt{\pi b}\eta(B)(\alpha EQ_0^*L^2/k) = K_{Ic}, \quad (28)$$

where  $Q_0^*$  is the power deposition rate per unit volume at failure,  $K_{Ic}$  is the fracture toughness of the unstrengthened glass,  $\Omega$  is a numerical factor that depends on the crack location and geometry and can be extracted from Eqs. (23)–(25), and  $\eta(B)$  is a dimensionless function of the Biot number  $B$  such that the thermal stresses are given by  $\sigma = \eta(B)\alpha EQ_0^*L^2/k$ . The factor  $\eta(B)$  depends on which stress component leads to fracture and can be found from Fig. 9.

On the other hand, for the glass strengthened by ion exchange, the fracture criterion becomes

$$\Omega\sqrt{\pi b}\left(\eta(B)\frac{\alpha EQ_0^{*T}L^2}{k} - \frac{Ee^T}{3(1-\nu)}\right) = K_{Ic}, \quad (29)$$

where  $Q_0^{*T}$  is now the power deposition rate per unit volume at fracture of the strengthened glass. In writing Eqs. (28)

and (29), it is assumed that the flaw size  $b$  and the fracture toughness of the bulk glass  $K_{Ic}$  does not change as a result of ion exchange at the surface.

Elimination of  $\Omega$ ,  $b$ , and  $K_{Ic}$  from Eqs. (28) and (29) gives

$$e^T = 3(1-\nu)\eta(B)\frac{\alpha L^2(Q_0^{*T} - Q_0^*)}{k} \quad (30)$$

from where the macroscopic dilatation  $e^T$  can be determined. Since  $\Delta V^T$  can be estimated from knowledge of the size of the exchanged ions, Eq. (26) allows the calculation of the volume concentration of the ion exchange sites. Finally, knowledge of the fracture toughness  $K_{Ic}$  of glass allows via Eq. (28) the calculation of the critical flaw size  $b$  responsible for fracture.

As an example, we used  $K_{Ic} = 0.3 \text{ MPa m}^{1/2}$ , which is typical of phosphate glass,<sup>13</sup> experimentally determined flashlamp power at failure of 660 and 3600 W for the unstrengthened and strengthened glass, respectively, which lead to power deposition rates per unit volume of 3.2 and 17 W/cm<sup>3</sup>, respectively (derived on the assumption of a 10% efficiency),<sup>4</sup>  $L = 0.4 \text{ cm}$ ,  $\eta(B) = 0.5$  (which corresponds to a value of the Biot number of about  $B = 1$ ),  $k = 0.82 \text{ W/m K}$ ,  $\alpha = 11 \times 10^{-6}$ ,  $E = 60 \text{ GPa}$ ,  $\nu = 0.25$ . These material properties are typical of phosphate glass.<sup>14</sup> These values lead to a macroscopic dilatation of  $e^T = 0.0034$ .

Using the values of 0.078 and 0.098 nm for the ionic radii of  $\text{Li}^+$  and  $\text{Na}^+$ , respectively,<sup>15</sup> so that  $\Delta V^T = 1.94 \times 10^{-3} \text{ nm}^{-3}$ , Eq. (26) yields a density of  $n/V_0 = 1.7 \times 10^{21} \text{ cm}^{-3}$  for the ion exchange sites. Finally, using the atomic weight of 7 and 23 for Li and Na, respectively, gives the weight percentage of  $\text{Na}^+$  as 2.1%. This value is in good agreement with independent measurements by electron microprobe analysis, where it was found that the weight percent of  $\text{Na}^+$  varies from 2.8% on the surface of the sample, to 1.4% at a depth of 12–13  $\mu\text{m}$ , to the error value of 0.2% at a depth of 60  $\mu\text{m}$ .

The compressive stress due to the ion exchange was found via Eq. (27) to be 90 MPa. The fracture stress of the unstrengthened glass was calculated to be 20 MPa. The fracture strength of the strengthened glass was determined as 110 MPa. Using  $B = 1$ , the critical flaw size was determined as 45–90  $\mu\text{m}$ . With  $B = 0.1$ , the critical flaw is 20–35  $\mu\text{m}$ . These values for the critical flaw size are comparable to the size of the powder used in the polishing process.

It must be pointed out that the use of Eqs. (23)–(25) assumes that the region over which the ion exchange has occurred greatly exceeds the crack length, so that the crack can be visualized as being embedded within a uniform stress level. Although the zone within which ion exchange had occurred was experimentally measured to be about 60  $\mu\text{m}$ , the residual stress spatial distribution due to ion exchange could not be determined besides the variation of the weight percent of Na ions with distance from the free surface or the estimate of the compressive strength induced, as described in Ref. 4.

The effect of nonuniform residual stresses on inducing a stress intensity factor which tends to close the crack faces and on the possible partial crack closure has been examined



by Green.<sup>16</sup> However, in Green's work it was assumed that the residual stress distribution is known *a priori*. Since for the case of ion exchange this is not necessarily the case, we intend to examine a limiting case, namely the case when the crack length greatly exceeds the depth of the zone over which ion exchange has occurred, and that the crack faces have undergone ion exchange up to a characteristic depth  $H$ , as shown in Fig. 11.

Figure 11(a) shows schematically the case where the face of the glass plate has undergone ion exchange up to a typical length  $H$ , but the crack faces have not undergone any exchange. Figure 11(b) shows the case where only the crack faces, up to the crack tip, have undergone ion exchange. It is most likely that the actual configuration will be a hybrid of the geometries shown in Fig. 11. Because these two geometries lead to different dependence of the strengthening effect on the geometrical parameters  $H$  and  $b$ , they are analyzed separately.

The free body diagram of the underlying glass substrate for the case of Fig. 11(a) is shown in Fig. 11(c). The forces per unit depth  $P_1 = P_2 = P = \sigma H$  with  $\sigma$  the magnitude of the compressive stress due to the ion exchange, see Eq. (27), which has a typical value of 90 MPa. The moments per unit depth  $M_1 = M_2 = M = \sigma H^2/2$ . In view of the fact that  $M_2$

and  $P_2$  are remotely located with respect to the crack tip, their contribution to inducing a stress intensity factor at the crack tip can be neglected. Furthermore, the contribution due to  $M_1$  is much smaller (of order  $H/b$ ) than the contribution of  $P_1$ , and can also be neglected. Thus, the largest contribution is due to  $P_1$  which can be found in Ref. 17. It is given by

$$\Delta K = -2.6(\sigma H / \sqrt{\pi b}), \quad (31)$$

where  $\Delta K$  is the change in the stress intensity factor at the crack tip. The fact that  $\Delta K < 0$  implies that there is a toughening or shielding effect.<sup>18</sup>

By setting  $\Delta K$  equal to the fracture toughness of the glass itself, say  $0.3 \text{ MPa m}^{1/2}$ ,<sup>13</sup> and using  $\sigma = 90 \text{ MPa}$ , we derive a relation between the crack length  $b$  and the ion exchange zone width. Using  $b = 10 \mu\text{m}$  yields  $H = 7 \mu\text{m}$ . If we take the fracture toughness as  $0.5 \text{ MPa m}^{1/2}$ ,<sup>13</sup> we find  $H = 12 \mu\text{m}$ . Since this analysis is valid only when  $b$  exceeds  $H$ , we conclude that for brittle materials of low fracture toughness ion exchange via the mechanism shown in Fig. 11(a) can enhance the apparent fracture toughness by as much as 100% with an ion exchange depth of only a few micrometers.

The other mechanism shown in Fig. 11(b) is analyzed by using the solution of Budiansky and co-workers,<sup>18</sup> whereby the stress intensity factor induced by a distribution of volumetric expansion  $\theta(r, \phi)$  over the area  $A$  was found under plane strain conditions to be

$$\Delta K = \frac{E}{3(1-\nu)\sqrt{2\pi}} \int_A \theta r^{-3/2} \cos \frac{3\phi}{2} dA, \quad (32)$$

where  $r, \phi$  are polar coordinates measuring from the crack tip ( $\phi = 0$  is the line ahead of the crack). It is seen from Eq. (32) that ion exchange occurring within a fan of  $120^\circ$  ahead of the tip ( $-\pi/3 < \phi < \pi/3$ ) induces a positive  $\Delta K$ , thus making the material more brittle. On the other hand, ion exchange over the crack faces induces a negative  $\Delta K$  so that the material at the crack tip appears shielded from the remotely applied thermal stresses. Following Ref. 18, the near tip stress intensity factor is given by

$$K_{\text{tip}} = K_{\text{appl}} + \Delta K, \quad (33)$$

where  $K_{\text{appl}}$  is the stress intensity due to the applied thermal loads, and  $\Delta K$  is due to ion exchange. The fracture criterion is

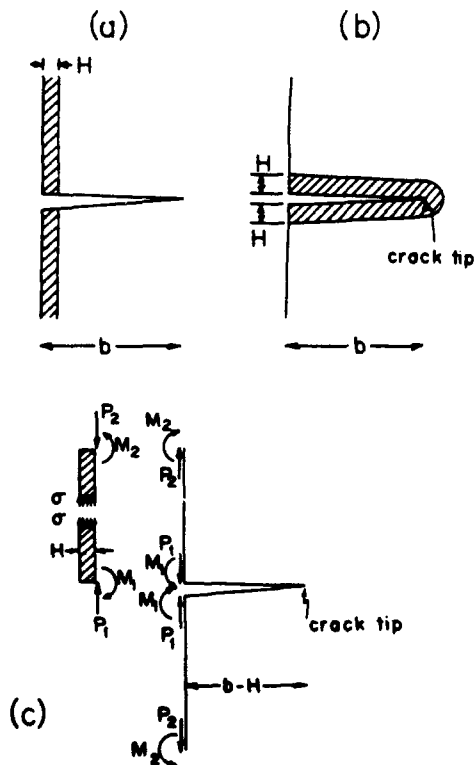


FIG. 11. The interaction of a zone of thickness  $H$  over which ion exchange has occurred with a crack of length  $b$ , where  $b$  greatly exceeds  $H$ . (a) Ion exchange over the surface of the slab. (b) Ion exchange over the crack faces and ahead of the crack tip. (c) The forces acting on the film which is in a state of compression of magnitude  $\sigma$ , and the forces acting on the underlying glass. These forces induce a stress intensity factor at the crack tip which tends to close the crack.

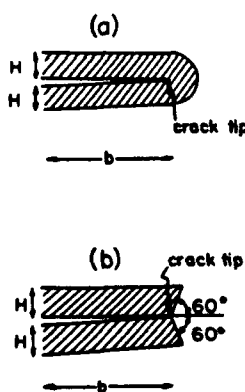


FIG. 12. The details of the ion exchange process near the crack tip are important, since exchange over the crack faces induces a shielding  $\Delta K$  ( $\Delta K < 0$ ), whereas exchange ahead of the crack tip induces an antishielding  $\Delta K$  ( $\Delta K > 0$ ). (a) Ion exchange over the crack faces and ahead of the crack tip. (b) Ion exchange over the crack faces only.



$$K_{ip} = K_{ic} \quad (34)$$

with  $K_{ic}$  the fracture toughness of the glass. It is noted that this calculation assumes that the ion exchange process does not alter the fracture toughness of the glass material, but that it only induces residual stresses which shield the crack tip from the thermal stresses induced by the cooling medium.

$\Delta K$  has been calculated via Eq. (32) for the two cases shown in Fig. 12. In Fig. 12(a) the ion exchange zone extends over the crack faces and in front of the crack tip. The detailed geometry ahead of the crack tip is described in Ref. 18. Assuming that  $\theta$  is uniform within the ion exchange zone, the work of Budiansky and co-workers<sup>18</sup> yields

$$\Delta K = -0.63\sigma\sqrt{H}, \quad (35)$$

$\sigma$  being the magnitude of the compressive stress due to ion exchange. On the other hand, the geometry of Fig. 12(b), in which ion exchange occurs over the crack faces but not ahead of the crack tip, leads to<sup>19</sup>

$$\Delta K = -1.3\sigma\sqrt{H}. \quad (36)$$

As an example of the toughening effect predicted by Eqs. (35) or (36), we note that an ion exchange layer thickness of  $H = 10\text{--}30\text{ }\mu\text{m}$  produces an enhancement in the stress intensity factor of  $\Delta K = -0.3\text{ MPa m}^{1/2}$ . A thickness of  $H = 30\text{--}70\text{ }\mu\text{m}$  produces  $\Delta K = -0.5\text{ MPa m}^{1/2}$ . These values of the layer thickness are of the same order of magnitude as the experimentally determined thickness of about  $60\text{ }\mu\text{m}$ . The induced enhancements in the fracture toughness are of the same magnitude as the fracture toughness  $K_{ic}$  of the glass itself. It is concluded that the mechanisms of ion exchange shown in Fig. 12 induce considerable enhancements of the fracture toughness of the glass. These enhancements may be as large as the intrinsic fracture toughness of the glass itself.

A basic assumption in deriving Eqs. (35) and (36) is that the volume expansion due to the ion exchange is uniformly distributed within the layer thickness  $H$ . This is not the case in reality since the depth profile of the exchange layer arises from the diffusion of the exchanging ions, so that the percentage of exchange sites is highest near the free surface and it diminishes as one moves into the glass. In view of this, Eqs. (35) and (36) are applicable when  $H$  is identified as an effective thickness over which the volume expansion is essentially uniform. Even so, the numerical examples discussed above show that ion exchange is a potent mechanism for enhancing the fracture toughness of brittle phosphate glasses.

Comparison of Eqs. (35) and (36) also shows that the details of the ion exchange process near the crack tip are important in determining the levels of the enhancement in the fracture toughness. Ion exchange over the crack faces shields the material from the applied loads; ion exchange ahead of the crack tip enhances the applied loads.

When the crack shielding mechanisms of Figs. 11 and 12 are superposed on the applied thermal loads, the fracture criterion becomes

$$K_{ip} = \Omega\eta(B)\frac{\alpha EQ_0^w L^2}{k}\sqrt{\pi b} - \chi_1\frac{\sigma H}{\sqrt{\pi b}} - \chi_2\sigma\sqrt{H} \\ = K_{ic}, \quad (37)$$

where the coefficients  $\chi_1$  and  $\chi_2$  are of order unity and depend on the details of the ion exchange process near the crack tip, see Eqs. (31), (35), and (36). It is seen that the thermal loads [the first term on the right-hand side of Eq. (37)], and the strengthening mechanisms due to ion exchange are characterized by different dependence of the induced stress intensity factor on the geometric quantities  $b$  (the crack length) and  $H$  (the depth of the ion exchange zone). In writing Eqs. (37) it is assumed that the ion exchange process near the crack tip does not alter the intrinsic fracture toughness of the glass material, i.e.,  $K_{ic}$  is the same as for the glass that has not undergone any ion exchange. As was shown previously, for brittle materials such as the phosphate glass under investigation here, the strengthening contributions are of the same order of magnitude as the stress intensity factor due to the applied loads. It is concluded that for microcracks long with respect to the depth of the ion exchange zone, ion exchange is a viable mechanism for enhancing the fracture toughness of brittle components. On the other hand, when the microcracks are much shorter than the ion exchange zone, the analysis leading to Eq. (29) shows that, again, ion exchange is a considerable strengthening mechanism. It is expected that the same strengthening phenomenon will occur when the crack length is comparable to the ion exchange zone.

## V. CONCLUSIONS

Numerical techniques were used to calculate the thermal stresses during the steady-state absorption of heat by thermal pumping of a slab of phosphate glass used for high average power solid-state laser applications. It was shown that the in-plane stress components are independent of the Biot number characterizing the surrounding cooling medium. These stress components depend only on the magnitude of the power per unit volume absorbed during thermal pumping. The out-of-plane stress components do depend on the Biot number and on the thermal loads. The state of stress near the outer surface of the glass contains tensile and compressive components. The in-plane stresses are always tensile. The out-of-plane stresses are compressive when no lateral displacement is allowed, and tensile when the lateral ends are allowed to displace freely. The calculated stresses were used in order to evaluate the compressive stresses induced by a thin zone within which ion exchange has occurred. From the compressive stresses the volume density of ion exchange sites and the magnitude of the weight percent of ions within the exchange layer were calculated. It was shown that for the case of long or short microcracks, with respect to the depth of the ion exchange zone, ion exchange induces a significant reduction of the near-tip stress intensity factor thus shielding the near-tip region from the applied thermal loads. The details of the ion exchange process near the crack tip were shown to be significant in altering the levels of crack tip shielding.



## ACKNOWLEDGMENTS

This work was supported by the Office of Naval Research under Grant No. N00014-87-K-0488, and the National Science Foundation under the Presidential Young Investigator Award MSM-8857096. The work was also supported by the General Electric Company Advance Laser Technology Group, Binghamton, NY under Contract No. A25-E-0580BS, the New York State Center for Advanced Optical Technology of the Institute of Optics, and the sponsors of the Laser Fusion Feasibility Project at the Laboratory for Laser Energetics whose sponsors are as follows: Empire State Electric Energy Research Corporation, General Electric Company, New York State Energy Research and Development Authority, Ontario Hydro, Southern California Edison Company, and the University of Rochester. Such support does not imply endorsement of the content by any of the above parties. The author also acknowledges helpful discussions with C. A. Cerqua and J. Kelly of the Laboratory for Laser Energetics at the University of Rochester. The comments and suggestions of S. D. Jacobs are also acknowledged.

<sup>1</sup>J. L. Emmett, W. F. Krupke, and W. R. Sooy, Lawrence Livermore National Laboratory Report No. UCRL-53571, 1984.

- <sup>2</sup>J. Marion, D. Gaultieri, and R. Morris, *J. Appl. Phys.* **62**, 2065 (1987).
- <sup>3</sup>K. L. Marshall, A. W. Schmid, D. J. Smith, A. A. Bevin, M. J. Guardalben, and S. D. Jacobs, *J. Appl. Phys.* **64**, 2279 (1988).
- <sup>4</sup>K. A. Cerqua, S. D. Jacobs, and A. Lindquist, *J. Non-Cryst. Solids* **93**, 361 (1987).
- <sup>5</sup>T. B. Troczynski and P. S. Nicholson, *J. Am. Ceram. Soc.* **70**, C112 (1987).
- <sup>6</sup>E. R. G. Eckert and R. M. Drake, Jr., *Heat and Mass Transfer*, 2nd ed. (McGraw-Hill, New York, 1959).
- <sup>7</sup>P. R. Manzo, H. R. Verdun, and E. A. Phillips, Science Applications, Inc. Report No. 168-201-014, 1980.
- <sup>8</sup>H. S. Carslaw and J. C. Jaeger, *Conduction of Heat in Solids* (Oxford University Press, London, 1959).
- <sup>9</sup>B. A. Boley and J. H. Weiner, *Theory of Thermal Stresses* (Wiley, New York, 1960).
- <sup>10</sup>A. S. Kobayashi and A. N. Enetanya, in *Mechanics of Crack Growth* (American Society for Testing and Materials, Philadelphia, 1976), ASTM STP 590, pp. 477-495.
- <sup>11</sup>F. R. N. Nabarro, *Proc. R. Soc. London Ser. A* **175**, 519 (1940).
- <sup>12</sup>J. D. Eshelby, *Proc. R. Soc. London Ser. A* **241**, 376 (1957).
- <sup>13</sup>J. E. Marion, *J. Appl. Phys.* **62**, 1595 (1987).
- <sup>14</sup>W. F. Krupke, M. D. Schinn, J. E. Marion, J. A. Caird, and S. E. Stokowski, *J. Opt. Soc. Am. B* **3**, 102 (1986).
- <sup>15</sup>C. J. Smithells, Ed., *Metals Reference Book* (Butterworth, New York, 1976).
- <sup>16</sup>D. J. Green, *J. Am. Ceram. Soc.* **66**, 807 (1983).
- <sup>17</sup>H. Tada, P. C. Paris, and G. R. Irwin, *The Stress Analysis of Cracks Handbook* (Del Research, Hellertown, PA, 1973).
- <sup>18</sup>B. Budiansky, J. W. Hutchinson, and J. C. Lambropoulos, *Int. J. Solids Structures*, **19**, 337 (1983).
- <sup>19</sup>A. G. Evans, A. Heuer, F. Lange, and M. V. Swain, *J. Am. Ceram. Soc.* **68**, i-iv (1986).



## APPENDIX (6)

### Toughening and crack tip shielding in brittle materials by residually stressed thin films

John C. Lambropoulos

Department of Mechanical Engineering and Laboratory for Laser Energetics, University of Rochester,  
Rochester, New York 14627

(Received 10 September 1990; accepted 5 February 1991)

The apparent fracture toughness of brittle components can be greatly enhanced via surface-deposited thin films which are under residual, possibly nonuniform compression since the residual compression counteracts the effect of the applied loads at the tip of a surface crack. Examples are epitaxial thin films on crystalline components, thin films in a state of compression due to the film deposition process, or thin films of ion-exchange in glass. We review the micromechanics of the strengthening process by considering a surface microcrack under the combined action of the residual stress in the film (which shields the crack tip and may cause partial crack closure) and of the externally applied loads (thermal or mechanical). We examine crack tip shielding as the interaction of microscopic dilatant spots with the crack tip. This model predicts rising crack growth resistance curves for limited amounts of crack growth. We review and analyze experimental results on ion exchange in thin films of glass in small-, medium-, and large-size glass components for high average power solid state lasers. These measurements show that the apparent fracture strength increases by as much as five to six times.

#### 1. INTRODUCTION

The apparent fracture toughness of brittle materials can be greatly enhanced by various surface modification methods, such as epitaxial thin films on crystalline substrates,<sup>1</sup> sol-gel films on optical materials,<sup>2</sup> physically deposited thin films,<sup>3</sup> or thin films of glass within which ion exchange has occurred.<sup>4-6</sup> It is currently accepted that the deposition of the thin film does not alter the inherent fracture toughness of the brittle material (which is usually quite low): Instead, it is believed that the stresses within the thin film (which are a direct result of the deposition process) shield the tip of a microcrack from the applied thermomechanical loads, so that a higher value of the applied load is required in order to fracture the specimen (as compared to a specimen without any films).

A standard technique for observing such enhancement in the fracture toughness of brittle materials has been indentation microcracking whereby a surface microcrack is introduced by using a sharp indenter.<sup>7,8</sup> The specimen is further cracked with the indenter, or by using standard mechanical loading, such as the four-point-bending configuration.<sup>9</sup> Another technique is the use of thermal shock tests whereby the specimen is uniformly heated and then rapidly cooled: The thermal stresses, resulting from the inhomogeneous temperature distribution within the specimen, will fracture the specimen when the difference between the initial (uniform) temperature of the specimen and the temperature of the quenching medium is sufficiently high.<sup>4,9,10</sup>

For linear elastic materials containing cracks, an asymptotic analysis of the stress distribution near a crack tip shows that the stresses are singular, with a spatial distribution varying like  $r^{-1/2}$  (where  $r$  is the distance from the crack tip), and that the magnitude of the singular term is governed by the stress intensity factor (SIF)  $K_{tip}$ , valid near the crack tip. For example, for mode I (or opening mode) cracking, the

stress distribution ahead of a crack tip is given by

$$\sigma_{yy} = \frac{K_{tip}}{\sqrt{2\pi x}}, \quad x > 0, \quad x \rightarrow 0, \quad (1)$$

where the crack (extending infinitely in the  $z$  direction) occupies the half line  $x < 0$ , the uncracked part extends along  $x > 0$ , and the axis  $y$  is perpendicular to the crack. It is noted that the stress intensity factor  $K_{tip}$  cannot be computed from the asymptotic analysis: A complete solution is required of the boundary value problem consisting of the crack under the action of the applied loads.

Since the stresses near a crack tip are uniquely determined by the stress intensity factor, for a brittle material it is assumed that fracture will occur when the near-tip stress intensity factor  $K_{tip}$  reaches a critical value  $K_{Ic}$ , called the fracture toughness, which is a material property, thus

$$K_{tip} = K_{Ic}. \quad (2)$$

In the absence of any mechanisms that shield the crack tip from the applied loads, the near-tip stress intensity factor  $K_{tip}$  is equal to the applied stress intensity factor  $K_{app}$ , so that

$$K_{tip} = K_{app}. \quad (3)$$

For example, for a crack under the action of uniformly applied far field stresses  $\sigma$  in a direction perpendicular to the crack plane, the applied stress intensity factor is

$$K_{app} = \Omega \sigma \sqrt{\pi a_0}, \quad (4)$$

where  $a_0$  is the half-length of the crack tip, and  $\Omega$  is a geometrical factor which includes the interaction of the crack with near-by free surfaces. For example, for an interior crack infinite in the  $z$  direction,  $\Omega = 1$ ; for an edge crack of depth  $a_0$ ,  $\Omega = 1.12$ ; for an interior penny-shaped crack  $\Omega = 2/\pi$ .

On the other hand, when the crack tip is shielded from the applied loads, the near-tip SIF  $K_{tip}$  is related to the far-field (or applied) SIF  $K_{app}$  by



$$K_{\text{tip}} = K_{\text{app}} + \Delta K, \quad (5)$$

where  $\Delta K$  is the contribution of any mechanisms that interact with the crack tip. When  $\Delta K < 0$ , then shielding occurs. In this case, combination of Eqs. (2), (4), and (5) shows that at fracture the required stress  $\sigma$  is higher than what it would be if no shielding was present. Similarly, when  $\Delta K > 0$ , the applied loads are enhanced near the tip, and the net effect is to make the material effectively more brittle by reducing the value of  $\sigma$  required for fracture.

As an example of the shielding effect of thin films, we mention the work of Lawn and Fuller,<sup>11</sup> and of Tandon and Green,<sup>5</sup> who considered an indentation crack as a semicircular penny-shaped crack of radius  $c$ . At fracture, the total SIF at the intersection of the crack front with the specimen's free surface is equal to the fracture toughness  $K_{\text{Ic}}$ , so that<sup>5,11</sup>

$$K_{\text{Ic}} = \chi \frac{P}{c^{3/2}} + \Omega \sigma \sqrt{\pi c} + 2\Omega \sigma_0 \sqrt{H}, \quad (6)$$

where the first term is the contribution of the residual stresses present as a result of the permanent plastic deformation under the maximum load  $P$  of the indenter, the second term is due to the applied stresses, and the third term is due to the presence of a thin film of thickness  $H \ll c$  under a state of biaxial tension ( $\sigma_0 > 0$ ) or compression ( $\sigma_0 < 0$ ) in the film's plane. The dimensionless quantities  $\chi$  and  $\Omega$  are geometric factors which account, respectively, for the interaction of the residual stresses due to the indentation and for the interaction of the specimen's free surface with the crack tip. The quantity  $\chi = 0.016 (E/HD)^{1/2}$  where  $E$  is the Young's modulus and  $(HD)$  is the hardness of the material.<sup>7,8</sup>

It is clear from Eq. (6) that when the film is in compression, the last term (due to the film) shields the second term (due to the applied loads) and the first term (due to the indentation itself), so that a higher value of the applied stress  $\sigma$  is required for fracture. We note from Eq. (6) that for the indentation crack the contribution due to the residually stressed film (which is valid only in the limit  $H \ll c$ ) is independent of the crack radius  $c$ .

As typical values of the interaction between very thin surface films and very deep surface cracks, the data of Kobrin and Harker<sup>3</sup> on sputtered submicron-thick films had a crack depth of 12–100  $\mu\text{m}$ , and a compressive film stress of 0.2, 1.0, and 1.6 GPa for films of  $\text{Al}_2\text{O}_3$ ,  $\text{SiO}_2$ , and  $\text{Si}_3\text{N}_4$ , respectively. The substrate was glass (with  $K_{\text{Ic}} = 0.62 \text{ MPa}\sqrt{\text{m}}$ ), Si ( $K_{\text{Ic}} = 0.74 \text{ MPa}\sqrt{\text{m}}$ ), sapphire ( $K_{\text{Ic}} = 1.7 \text{ MPa}\sqrt{\text{m}}$ ), or  $\text{Si}_3\text{N}_4$  ( $K_{\text{Ic}} = 4.1 \text{ MPa}\sqrt{\text{m}}$ ). The resulting shielding contribution ranged from  $(-\Delta K) = 0.1$  to  $1.7 \text{ MPa}\sqrt{\text{m}}$ .

Ion exchange in glass similarly creates a thin surface film which is in a state of residual compression. The work of Tandon and Green<sup>5</sup> on silicate glass ( $K_{\text{Ic}} = 0.73 \text{ MPa}\sqrt{\text{m}}$ ) where  $\text{Na}^+$  ions were exchanged for  $\text{K}^+$  ions had an exchange layer of thickness 3–7.5  $\mu\text{m}$ , and an indentation crack depth of at least 150  $\mu\text{m}$ . The average compressive stress in the ion exchange layer was in the range 150 to 320 MPa. Depending on the indentation load used, the fracture strength of the ion-exchanged specimens increased to 150–210 MPa, as compared to a fracture strength of about 80 MPa for the unstrengthened specimens.

It is not always the case that the thickness of the compres-

sive layer is much smaller than the depth of the surface crack at failure. Cerqua *et al.*<sup>4</sup> have shown that for the case of phosphate glass with the exchange of  $\text{Na}^+$  for  $\text{Li}^+$  ions, there is a remarkable improvement in the fracture strength of the glass when the surface crack is comparable in magnitude to the thickness of the compressive layer.

The tests of Cerqua *et al.*<sup>4</sup> were performed on three geometries: The first geometry was that of small disks (diameter of 20 mm, thickness of 3 mm); the second geometry was that of squat cylinders (diameter 6.4 mm, height 6.4 mm); These two geometries were tested in thermal shock tests, and a finite element analysis was performed (with a time-dependent temperature distribution) in order to correlate the temperature drop at fracture to the magnitude of the resulting thermal stresses.<sup>9</sup> For the small disks, the Biot number (based on the specimen's half thickness) was about 5; For the cylinder geometry the Biot number (based on the radius) was equal to 10. These tests were used to extract the value of the fracture strength. For the unstrengthened specimens, the fracture strength was about 25 MPa, whereas for the strengthened specimens it was about 135 MPa.

The third geometry tested by Cerqua *et al.*<sup>4</sup> was that of rectangular slabs ( $8 \times 15 \times 160 \text{ mm}^3$ ) which were thermally pumped to failure. A finite element analysis again correlated the thermal power input to the resulting thermal stresses under steady-state thermal pumping.<sup>6</sup> It was found that the unstrengthened specimens had a fracture strength of 19–23 MPa, whereas after ion exchange the strength was improved to about 110 MPa.

The conclusion from all these tests was that ion exchange can greatly improve the apparent fracture toughness of nominally brittle materials by imparting an average compressive surface stress of the order of 90–110 MPa for phosphate glass. The value of the average compressive surface stress was correlated to the amount of the average dilation, which was found to be about 0.0034. In turn, this dilation was converted to an average  $\text{Na}^+$  ion concentration of about 2.1%.

Independent measurement of the Na ion concentration by Cerqua *et al.*<sup>4</sup> showed that the maximum concentration of 2.8% occurred at the surface of the specimen, and that the thickness of the ion exchange layer was 50–60  $\mu\text{m}$ , with a monotonic decrease from the surface value. The distance over which the maximum concentration was halved was about 15–20  $\mu\text{m}$ . It is thus seen that the numerical predictions (which yielded an average  $\text{Na}^+$  ion concentration of 2.1%) are in good agreement with the experimental observations.

In order to correlate the depth of the ion exchanged layer to the depth of surface microcracks, a value of  $0.3 \text{ MPa}\sqrt{\text{m}}$ <sup>12</sup> was used for the fracture toughness of phosphate glass. In addition to this information, the use of a value for the unstrengthened fracture strength of 20–25 MPa, allows the application of Eqs. (2)–(4), from which the depth of the surface crack can be estimated as between 37 and 57  $\mu\text{m}$ . We observe that in the tests of Cerqua *et al.*,<sup>4</sup> fracture occurred when the glass specimen was in contact with water. This contact would diminish the fracture toughness of glass from the fracture toughness in air. For example, using a diminished value of  $K_{\text{Ic}} = 0.1 \text{ MPa}\sqrt{\text{m}}$  for the fracture toughness



in water yields a crack depth of 4–6  $\mu\text{m}$ . It is thus seen that, contrary to the indentation experiments, in the thermal shock tests the crack length is comparable to the thickness of the ion exchange layer.

It is the purpose of this report to present a simple model whereby the shielding imparted by a surface compressive layer is viewed as arising from the interaction of individual dilation sites with a crack tip. The dilation sites are arranged so as to create a thin layer of either uniform or varying magnitude of dilation, and we calculate the change  $\Delta K$  in the near-tip stress intensity factor due to this layer. We emphasize the relation of  $\Delta K$  to the crack length, rather than to the thickness of the compressive layer. The presented analysis aims at deriving closed form expressions for the shielding effect when the crack length is much smaller, comparable to, or much longer than the depth of the compressive layer.

## II. SHIELDING BY EXPANDING SPOTS AND LAYERS

Consider a semi-infinite crack in a linear elastic solid under plane strain conditions in the  $z$  direction. The crack extends along  $x < 0$ . The uncracked ligament is along  $x > 0$ . When the volume of two circular cylinders, located at the cylindrical coordinates  $(r, \beta)$  and  $(r, -\beta)$  with respect to the crack tip, changes isotropically by the stress-free amount  $\theta^T$ , then the resulting change in the near-tip stress intensity factor is given by<sup>13,14</sup>

$$dK = \frac{E\theta^T dA}{3\sqrt{2\pi}(1-\nu)} \frac{\cos(3\beta/2)}{r^{3/2}}, \quad (7)$$

where  $dA$  is the cross sectional area of each cylinder,  $E$  is the Young's modulus of the material, and  $\nu$  is the Poisson ratio, see Fig. 1(a). It is thus seen that when the spots are located in a forward cone of total angle  $2\pi/3$  ( $0 < \beta < \pi/3$ ), their effect is to open the crack tip ( $dK > 0$ ), whereas when they

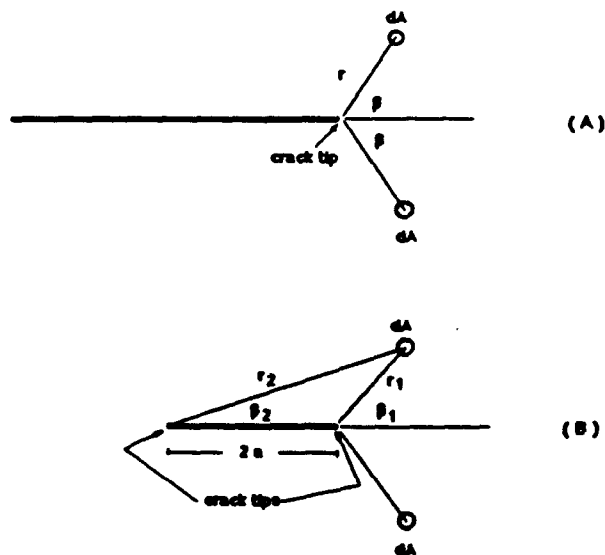


FIG. 1. The interaction of two symmetrically located circular cylinders, each of cross sectional area  $dA$ , with (a) a semi-infinite crack, and (b) with a finite crack.

lie in the range  $\pi/3 < \beta < \pi$  they cause crack tip shielding ( $dK < 0$ ).<sup>14</sup>

On the other hand when the dilating spots interact with a finite crack of length  $2a_0$ , as shown in Fig. 1(b), the resulting stress intensity factor at the nearest crack tip is

$$dK = \frac{E\theta^T dA}{3(1-\nu)} \sqrt{\frac{a_0}{\pi}} \frac{\cos[(3\beta_1 + \beta_2)/2]}{r_1^{3/2} r_2^{1/2}}, \quad (8)$$

where  $(r_1, \beta_1)$  are the polar coordinates with respect to the nearest crack tip, and  $(r_2, \beta_2)$  are the polar coordinates with respect to the furthest crack tip.

When the transforming spots are arranged in the form of a vertical strip (see Fig. 2) of width  $(dx)$  near a semi-infinite crack, then the resulting change in the near tip stress intensity factor can be found by integrating the expressions in Eq. (7). The result is

$$dK = 0, \quad (9a)$$

when the strip is located ahead of the crack tip [as shown in Fig. 2(a)], and

$$dK = -\frac{1}{3} \sqrt{\frac{2}{\pi}} \frac{E\theta^T}{1-\nu} \frac{dx}{\sqrt{D}}, \quad (9b)$$

when the strip is located behind the crack tip [as shown in Fig. 2(b)]. It is thus seen that the effect of an expanding layer is to either not interact with the crack tip when the layer is located ahead of the crack tip, or to shield the crack tip ( $dK < 0$ ) when the layer is located behind the crack tip. It is noted that the geometry of Fig. 2, which leads to the results

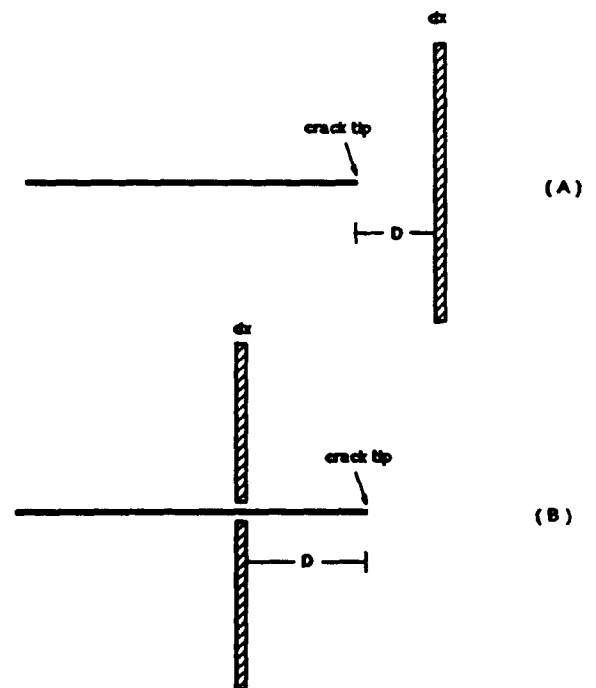


FIG. 2. The interaction of a vertical strip with a semi-infinite crack under plane strain conditions. The strip has a stress-free dilation  $\theta^T$ . (a) When the strip is located ahead of the crack tip  $\Delta K = 0$ . (b) When the strip is located behind the crack tip the shielding  $\Delta K < 0$  and is given by Eq. (9b).



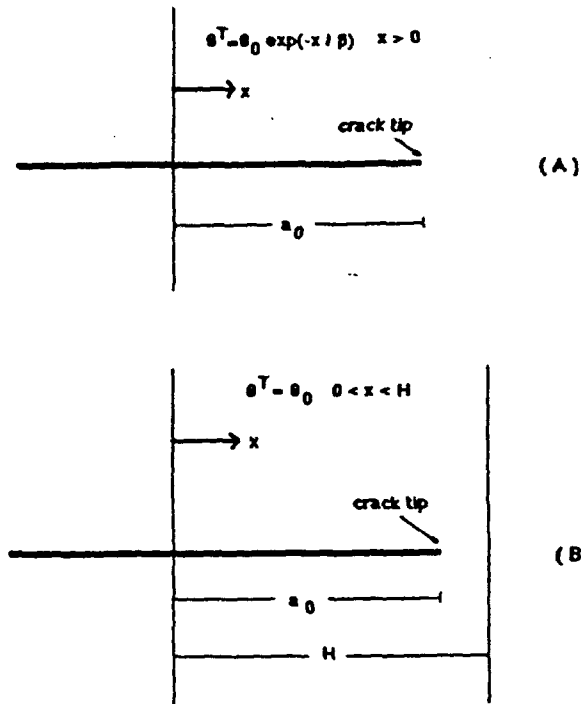


FIG. 3. The interaction of a layer with stress-free dilation with a crack tip. (a) Exponentially decaying dilation for  $x > 0$  with characteristic length scale  $\beta$ . (b) Uniform dilation within a layer of thickness  $H$ .

of Eq. (9), is equivalent to that of an embedded plate which is in a state of biaxial stress.

### III. SHIELDING BY SPATIALLY VARYING DILATIONS

Consider a semi-infinite crack which is embedded within a region where the stress-free dilation is decaying exponentially

$$\theta^T = \theta_0 \exp(-x/\beta), \quad x > 0 \quad (10)$$

with a characteristic length  $\beta$  [Fig. 3(a)], or is constant within a layer of width  $H$  [Fig. 3(b)]

$$\theta^T = \theta_0, \quad 0 < x < H. \quad (11)$$

In either case, the  $x$  coordinate measures from a plane at a distance  $a_0$  behind the crack tip, and  $\theta_0$  is the maximum dilation, which occurs at the surface  $x = 0$ . Thus, it is assumed that the surface  $x = 0$  is the free surface. In this way, the problem of the interaction between a surface crack of length  $a_0$  and the compressive layer is substituted by the analytically simpler model shown in Fig. 3, of the semi-infinite crack interacting with a layer of varying stress-free dilation. Thus, the simpler model of Fig. 3 does not account for the interaction between the crack tip and the free surface of the sample.

For the case of the exponentially decaying stress-free dilation, the expression in Eq. (9b) is used to find the induced shielding  $\Delta K$ . A vertical strip of width  $dx$  is at a distance  $H = a_0 - x$  behind the crack tip and the limits of integration are from  $x = 0$  to  $x = a_0$ . The result is

$$\Delta K = -\frac{1}{3} \sqrt{\frac{2}{\pi}} \frac{E\theta_0\sqrt{\beta}}{1-\nu} e^{-a_0/\beta} (-i)\sqrt{\pi} \text{Erf}\left(i\sqrt{\frac{a_0}{\beta}}\right) \quad (12a)$$

which, when the crack depth  $a_0$  greatly exceeds the characteristic length  $\beta$  of the compressive layer, reduces to

$$\Delta K = -\frac{1}{3} \sqrt{\frac{2}{\pi}} \frac{E\theta_0\sqrt{\beta}}{1-\nu} \frac{1-e^{-a_0/\beta}}{\sqrt{a_0/\beta}}, \quad a_0 \gg \beta. \quad (12b)$$

In Eq. (12a) the error function of imaginary argument is defined as<sup>15</sup>

$$\text{Erf}(i\sqrt{x}) = \frac{2i}{\sqrt{\pi}} \int_0^{\sqrt{x}} \exp(u^2) du. \quad (13)$$

Both Eq. (12a) and the asymptotic result of Eq. (12b) are shown in Fig. 4 in a non-dimensional form. It is seen that when  $a_0 > 3-4\beta$  the asymptotic expression provides a good approximation for the more involved result of Eq. (12a).

For the case of constant stress-free dilation, the integration of Eq. (9b) is again straightforward. As before,  $D = a_0 - x$ . When  $a_0 < H$  the limits of integration are from  $x = 0$  to  $x = a_0$ . When  $a_0 > H$ , the limits of integration are from  $x = 0$  to  $x = H$ . The result is

$$\Delta K = -\frac{2}{3} \sqrt{\frac{2}{\pi}} \frac{E\theta_0\sqrt{H}}{1-\nu} \times \begin{cases} \sqrt{a_0/H}, & a_0 < H \\ \sqrt{a_0/H} - \sqrt{(a_0/H) - 1}, & a_0 > H \end{cases}, \quad (14a)$$

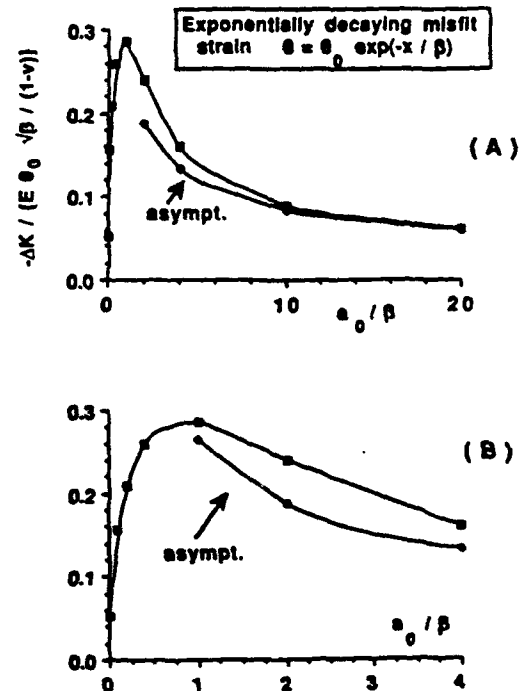


FIG. 4. Nondimensional shielding for the case of exponentially decaying stress-free dilation with characteristic length scale  $\beta$ . The asymptotic result is valid for  $a_0 \gg \beta$ . (b) is the same version as (a) with the horizontal axis magnified.



which reduces to

$$\Delta K = -\frac{1}{3} \sqrt{\frac{2}{\pi}} \frac{E\theta_0\sqrt{H}}{1-\nu} \frac{1}{\sqrt{a_0/H}}, \quad a_0 \gg H \quad (14b)$$

when the crack depth  $a_0$  greatly exceeds the thickness  $H$  of the compressive layer.

Figure 5 shows in non-dimensional form the shielding  $\Delta K$  versus the crack depth  $a_0$ . Again, it is seen that when  $a_0 > 2H$ , the asymptotic expression (14b) provides an accurate estimate of the shielding effect.

We observe that the results in Figs. 4 and 5 can be viewed as crack-growth resistance curves relating the shielding contribution  $\Delta K$  of  $K_{IIP}$  to the amount of crack growth  $a_0$ . Examination of Figs. 4 and 5 also shows that the dependence of the shielding  $\Delta K$  on the amount of crack growth  $a_0$  has the following main features: From a dimensional analysis argument, it is clear that the shielding  $\Delta K$  must be proportional to the Young's modulus  $E$ , to the maximum amount of stress-free dilation  $\theta_0$ , and to the square root of the characteristic length ( $\beta$  or  $H$ ) describing the spatial distribution of the stress-free dilation. A maximum in the shielding contribution is attained when the crack length is equal to the characteristic length over which the stress-free dilation occurs. When the crack length is considerably longer than this characteristic length, the shielding  $\Delta K$  depends weakly on crack length.

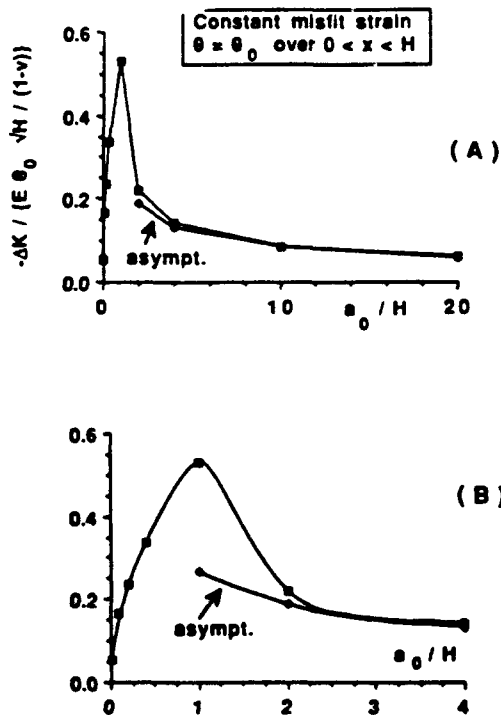


FIG. 5. Nondimensional shielding for the case of constant stress-free dilation in a layer of thickness  $H$ . The asymptotic result is valid for  $a_0 \gg H$ . (b) is the same version as (a) with the horizontal axis magnified.

#### IV. FREE SURFACE EFFECTS

The results expressed in Eqs. (12) and (14) do not explicitly account for the proximity to the crack tip of the free surface of the half space, since the basic solutions for the interaction of the dilating spots with a crack, Eqs. (7) and (8), are valid for a semi-infinite crack and a crack of length  $2a_0$  in the infinite solid, respectively.

In order to examine the effect of the proximity of the free surface to the crack tip, we use a solution from the *Stress Analysis of Cracks Handbook* (entry 8.4).<sup>16</sup> This solution is applied to the geometry of Fig. 3(b), in which there is a constant dilation of magnitude  $\theta_0$  extending from  $x = 0$  (which is the location of the free surface) to  $x = H$ . The result is

$$\Delta K = -\frac{E\theta_0\sqrt{H}}{1-\nu} \sqrt{\frac{a_0}{H}} \times \begin{cases} -0.663, & a_0 < H \\ -0.376 \sin^{-1}(H/a_0)F(H/a_0), & a_0 > H \end{cases} \quad (15)$$

where  $F$  is a slowly varying function which takes the value 1.30 when  $H/a_0 = 0$  and the value 1.122 when  $H/a_0 = 1$ .

The predictions of Eq. (15) which account for the presence of the free surface at  $x = 0$  are compared to those of Eq. (14) in Fig. 6. It is seen that both approaches predict similar trends on the dependence of toughening  $\Delta K$  on crack length  $a_0$ . The presence of the free surface leads to higher enhancement in the near-tip stress intensity factor because, in that case, the half-space is more compliant than the full space with the semi-infinite crack.

#### V. DISCUSSION

As an example of the applicability of the results in Figs. 4 and 5, we consider the data of Cerqua *et al.*<sup>4</sup> on ion exchange in phosphate glass. The Young's modulus is  $E = 60$  GPa, and the Poisson ratio is  $\nu = 0.25$ . The value of the maximum stress-free dilation  $\theta_0$  (occurring at the free surface) is about 0.0045, and the decay length  $\beta = 15 \mu\text{m}$ . Using  $K_{Ic} = 0.1$  MPa  $\sqrt{\text{m}}$  for the fracture toughness of the glass, and a base

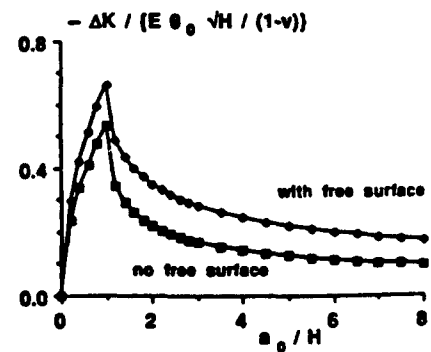


FIG. 6. Nondimensional shielding, due to a layer of thickness  $H$  on the surface of a half space with a crack of length  $a_0$  normal to the free surface, when the free surface effects are accounted and when they are neglected.



fracture stress of 20–25 MPa for the unstrengthened specimens, the crack size is found to be  $a_0 = 4\text{--}6\text{ }\mu\text{m}$ . As an example of the enhancement in the near tip stress intensity factor, a crack length of  $a_0 = 5\text{ }\mu\text{m}$  yields  $\Delta K = -0.33\text{ MPa}\sqrt{\text{m}}$ . Using  $K_{Ic} = 0.3\text{ MPa}\sqrt{\text{m}}$  yields  $\mu\text{m}$ . The value  $a_0 = 50\text{ }\mu\text{m}$  yields  $\Delta K = -0.28\text{ MPa}\sqrt{\text{m}}$ . It is concluded that for ion exchange in phosphate glass the shielding due to the residual stress-free dilation is comparable to or in excess of the intrinsic fracture toughness of the brittle material itself.

In the discussion above it has been assumed that the crack remains open at fracture so that no crack closure occurs. It is known, however, that crack closure may occur when the crack is subjected to nonuniform stresses that vary from compression to tension. Crack closure has been discussed by Green,<sup>17</sup> by Thresher and Smith,<sup>18</sup> and by Bakioglu *et al.*<sup>19</sup> Here we present a simple model which estimates the amount of crack closure in terms of the compressive stress due to the surface layer and of the tensile applied stress which leads to failure.

At failure the crack, of total depth  $a_0$ , is under the action of the (tensile) fracture stress  $\sigma_F$  and of the compressive stress  $\sigma = -\sigma_0 \exp(-x/\beta)$  due to the residually stressed layer. In our simple model, we assume that the crack closes over a distance  $c$  so that at  $x = c$  the net stress changes from compressive to tensile. This implies that the open portion of the crack has length  $2a = a_0 - c$ . A simple calculation yields

$$c = \beta \ln\left(\frac{\sigma_0}{\sigma_F}\right), \quad c < a_0 \quad (16)$$

where  $\sigma_0$  is the magnitude of the maximum compression at the surface, and is related to the maximum stress-free dilation  $\theta_0$  by

$$\sigma_0 = \frac{E\theta_0}{3(1-\nu)} \quad (17)$$

For example, using  $\beta = 15\text{ }\mu\text{m}$ ,  $\theta_0 = 0.0045$ ,  $\sigma_F = 110\text{ MPa}$ , Eq. (17) yields  $\sigma_0 = 120\text{ MPa}$ , and Eq. (16) yields  $c = 1.3\text{ }\mu\text{m}$  for the amount of crack closure.

The simple analysis presented above is valid in the limit when the crack depth  $a_0$  greatly exceeds the characteristic length  $\beta$  of the compressive layer. A more careful analysis of closure in the interior crack of total physical length  $2a_0$  is that of Thresher and Smith,<sup>18</sup> where it was assumed that the crack tip will close when the local stress intensity factor vanishes. This analysis was applied to the exponentially decaying compression due to the ion exchange layer to yield the following expression for the amount  $c$  of crack closure

$$c = D_1 \beta \ln\left(\frac{\sigma_0}{\sigma_F}\right) - D_2, \quad c < a_0, \quad (18)$$

where the coefficients  $D_1$  and  $D_2$  are weak functions of the ratio  $a_0/\beta$  as shown in Fig. 7. When Eq. (18) is applied to the same data discussed above ( $\beta = 15\text{ }\mu\text{m}$ ,  $\sigma_F = 110\text{ MPa}$ ,  $\sigma_0 = 120\text{ MPa}$ ,  $a_0 = 50\text{ }\mu\text{m}$ ) the resulting amount of crack closure is  $c = 1.34\text{ }\mu\text{m}$ . We also observe that when  $a_0 \gg \beta$ , the coefficient  $D_1$  approaches the value 1 and  $D_2$  approaches 0, thus recovering the simple result of Eq. (16). On the other hand, using  $a_0 = 5\text{ }\mu\text{m}$ , we get for the amount of crack clo-

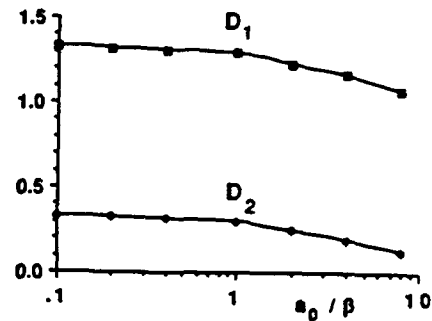


FIG. 7. The nondimensional coefficients entering the calculation of crack closure  $c$  for an interior crack of original length  $2a_0$ , whose length at fracture is  $2a$ .

sure  $c = 1.30\text{ }\mu\text{m}$  from Eq. (16), and  $c = 1.38\text{ }\mu\text{m}$  from Eq. (18).

It is concluded that the simple expression of Eq. (16) provides an accurate estimate of crack closure, and that crack closure may be a significant portion of the physical crack depth  $a_0$ . It is thus seen that the surface compressive layer has a double effect. It provides a shielding contribution  $\Delta K < 0$ , and it tends to close the physical crack depth so that the effective crack length  $2a$  is smaller than the original crack depth  $a_0$ .

## VI. CONCLUSIONS

A simple model has been presented to account for the interaction between a surface crack and a surface layer which is in a state of residual compression. The compression was viewed as arising from the stress-free dilation of infinitesimal spots within the layer. The emphasis was on deriving simple, closed-form solutions. The applications include epitaxial films, films in compression due to the deposition process, or ion exchange films.

The main result is that a shielding of the crack tip develops. The effective manifestation of shielding is to make the material appear tougher in the sense that higher applied loads are required for fracture, although the intrinsic fracture toughness of the material is not altered. The amount of shielding depends on the Young's modulus, the amount of stress-free dilation on the surface of the material, and the square root of the characteristic dimension of the layer. The shielding is localized in the sense that it exhibits a maximum when the crack depth is equal to the characteristic length scale of the compressive layer. When the crack length greatly exceeds the length of the layer, the amount of shielding depends weakly on the amount of crack growth. Another result of the surface compressive layer is to induce crack closure by amounts comparable to the characteristic length of the compressive layer.

## ACKNOWLEDGMENTS

This work was supported by the National Science Foundation under the Presidential Young Investigator Award



Grant No. MSM-8857096 and by the Office of Naval Research under Grant No. N00014-87-K-0488.

- <sup>1</sup>J. Marion, D. Gaultieri, and R. Morris, *J. Appl. Phys.* **62**, 2065 (1987).
- <sup>2</sup>B. D. Fabes and D. R. Uhlmann, *J. Am. Ceram. Soc.* **73**, 978 (1990).
- <sup>3</sup>P. H. Kobrin and A. B. Harker, *J. Mater. Sci.* **24**, 1363 (1989).
- <sup>4</sup>K. A. Cerqua, S. D. Jacobs, and A. Lindquist, *J. Non-Cryst. Solids* **93**, 361 (1987).
- <sup>5</sup>R. Tandon and D. J. Green, *J. Am. Ceram. Soc.* **73**, 970 (1990).
- <sup>6</sup>J. C. Lambropoulos, *J. Appl. Phys.* **67**, 1784 (1990).
- <sup>7</sup>D. B. Marshall and B. R. Lawn, in *Microindentation Techniques in Materials Science and Engineering*, edited by P. J. Blau and B. R. Lawn, (ASTM STP 889, city 1986, pp. 26-46).
- <sup>8</sup>R. F. Cook and G. M. Pharr, *J. Am. Ceram. Soc.* **73**, 787 (1990).
- <sup>9</sup>J. C. Lambropoulos, *J. Am. Ceram. Soc.* **71**, C-24 (1988).
- <sup>10</sup>W. P. Rogers, A. F. Emery, R. C. Bradt, and A. S. Kobayashi, *J. Am. Ceram. Soc.* **70**, 406 (1987).
- <sup>11</sup>B. R. Lawn and E. R. Fuller, Jr., *J. Mater. Sci.* **19**, 4061 (1984).
- <sup>12</sup>W. F. Krupke, M. D. Shinn, J. E. Marion, J. A. Caird, and S. E. Stokowski, *J. Opt. Soc. Am.* **3**, 102 (1986).
- <sup>13</sup>J. W. Hutchinson, Report No. DEAP S-8, Division of Engineering and Applied Physics, Harvard University, April 1974.
- <sup>14</sup>B. Budiansky, J. W. Hutchinson, and J. C. Lambropoulos, *Int. J. Solids Struct.* **19**, 337 (1983).
- <sup>15</sup>*Handbook of Mathematical Functions*, edited by M. Abramowitz and I. A. Stegun, (Dover, New York, 1965).
- <sup>16</sup>H. Tada, P. C. Paris, and G. R. Irwin, *The Stress Analysis of Cracks Handbook*, (Del Research Corporation, Hellertown, PA, 1973).
- <sup>17</sup>D. J. Green, *J. Am. Ceram. Soc.* **66**, 807 (1983).
- <sup>18</sup>R. W. Thresher and F. W. Smith, *Int. J. Fracture* **9**, 33 (1973).
- <sup>19</sup>M. Bakioglu, F. Erdogan, and D. P. H. Hasselman, *J. Mater. Sci.* **11**, 1826 (1976).



# APPENDIX (7)

## Thermal conductivity of dielectric thin films

J. C. Lambropoulos

Department of Mechanical Engineering, University of Rochester, Rochester, New York 14627

M. R. Jolly,<sup>a)</sup> C. A. Amsden,<sup>b)</sup> S. E. Gilman,<sup>c)</sup> M. J. Sinicropi, D. Diakomihalis,  
and S. D. Jacobs<sup>d)</sup>

Laboratory for Laser Energetics, University of Rochester, 250 East River Road, Rochester,  
New York 14623-1299

(Received 12 May 1989; accepted for publication 20 July 1989)

A direct reading thermal comparator has been used to measure the thermal conductivity of dielectric thin-film coatings. In the past, the thermal comparator has been used extensively to measure the thermal conductivity of bulk solids, liquids, and gases. The technique has been extended to thin-film materials by making experimental improvements and by the application of an analytical heat flow model. Our technique also allows an estimation of the thermal resistance of the film/substrate interface which is shown to depend on the method of film deposition. The thermal conductivity of most thin films was found to be several orders of magnitude lower than that of the material in bulk form. This difference is attributed to structural disorder of materials deposited in thin-film form. The experimentation to date has primarily centered on optical coating materials. These coatings, used to enhance the optical properties of components such as lenses and mirrors, are damaged by thermal loads applied in high-power laser applications. It has been widely postulated that there may be a correlation between the thermal conductivity and the damage threshold of these materials.

### I. INTRODUCTION

In 1984, Decker *et al.*<sup>1</sup> reported the measurement of thermal conductivity for thin films of SiO<sub>2</sub> and Al<sub>2</sub>O<sub>3</sub>. Values were found to be one or two orders of magnitude lower than those for the corresponding bulk materials. The authors attributed this difference to the unique microstructure of dielectric thin films which, along with defects and impurities, would be expected to reduce the phonon mean free path, and thus the thermal conductivity. Work by others has recently reinforced these findings for other dielectric coatings.<sup>2</sup>

Low thermal conductivity has important implications for electrical and optical applications, where heat deposited in a thin layer must be dissipated in order to prevent damage. A recent review by Guenther and McIver<sup>3</sup> discusses these implications which derive from the relation between the energy density at damage  $E_d$  and the material properties of the film

$$E_d \sim T_c \sqrt{(\rho c k t_p)}, \quad (1)$$

where  $T_c$  is the temperature level at damage (typically the melting point of the film material),  $\rho$  is the density,  $c$  is the heat capacity,  $k$  is the thermal conductivity of the film, and  $t_p$  is the laser pulse length which causes damage. Relation (1) results from the work of Goldenberg and Tranter<sup>4</sup> who analyzed the time-dependent heat transfer due to a spherical absorbing inclusion embedded within an infinite nonabsorbing matrix. Although the heat capacity and density of optical thin films are close to the properties of the bulk solids,<sup>1</sup> this is

not the case for the thermal conductivity which, being considerably lower for thin films, leads to lower values of the damage threshold energy densities. Thus, models which account for thermal transport in thin-film structures may have no predictive value if they employ bulk thermal conductivity data. For example, lack of film conductivity data imposes serious limitations on heat dissipation models in optical elements and arrays.<sup>5</sup>

Most techniques utilized to measure the thermal conductivity of thin solid films are difficult and time consuming. In Decker's work a thin-film thermocouple was deposited directly onto a sapphire substrate, subsequently overcoated with the test film and a second thin-film thermocouple.<sup>1</sup> Ono *et al.*<sup>6</sup> developed a technique for measuring the thermal conductivity of diamond films, which involved the application of black paint to the front and rear surfaces of the free-standing film sample. Other techniques involve complex optical systems.<sup>7</sup> When applied to free-standing films, such techniques do not allow the estimation of any interfacial thermal properties, such as the interfacial thermal resistance, which are expected to become increasingly important as the films become thinner.

This article describes a method developed at the Laboratory for Laser Energetics<sup>8</sup> which is relatively rapid, non-destructive, and can be applied to samples in a conventional film-on-substrate geometry. The thermal conductivity values obtained are those in the direction normal to the film surface. The interfacial thermal properties can also be evaluated from the experimental measurements. Our data suggest that thermal conductivity of many materials in thin-film form is significantly lower than in bulk form, and that the interfacial thermal resistance depends on the method of film deposition.

<sup>a)</sup> Now at Lord Corp., Cary, NC.

<sup>b)</sup> Now at Coherent, Inc., Palo Alto, CA.

<sup>c)</sup> Now at Meadowlark Optics, Longmont, CO.

<sup>d)</sup> Author to whom all correspondence should be addressed.



## II. THE THERMAL COMPARATOR

The thermal comparator technique for measuring the thermal conductivity of bulk solids has been extensively described by Powell.<sup>9,10</sup> A thermal comparator, consisting of a sample stage and a control module was purchased in 1975 (Ref. 11) to perform conductivity measurements of bulk materials. The commercial unit was converted to a high-precision device by temperature controlling both the samples and the sample stage, and by averaging the output signal. The thermal conductivity apparatus now consists of an environmentally controlled sample chamber enclosing a sample stage, a control and readout module, and signal processing equipment, as shown schematically in Fig. 1.

The principle of operation and calibration procedure for the apparatus are shown in Fig. 2. After placing a test sample on the sample stage, a thermocouple junction sensing tip is raised into contact with the sample surface. The two surfaces are kept in contact by applying a small force, usually 5 or 10 g, which compresses the sensing tip onto the film/substrate assembly. Heat flows from the hot tip (56 °C) to the cooler sample (36 °C). Within a short time, typically 10 s, a steady-state condition is established. A voltage, generated by the temperature difference between the sensing tip and a reference junction, is acquired by the control module. A personal computer collects several voltage signals, averages them, and stores them. Bulk materials of known conductivity are used to generate a thermal conductivity calibration curve. Unknowns are compared to these standards to find their apparent conductivity.

Substrates of highly conductive materials such as sapphire and silicon are preferred for studying the thermal conductivity of insulative thin films. When a coated substrate is evaluated, the presence of a film causes the substrate to register a substantially reduced value of thermal conductivity. Knowing the thermal conductivity of the substrate, an analytical model provides the means of extracting the film's thermal conductivity.

## III. ANALYTICAL MODELING

The thermal comparator technique is useful for making thermal conductivity measurements on bulk materials. When a substrate coated with an insulating film is tested, the comparator indicates a reduction in the apparent conductivity of the specimen. Modeling is required to extract the film conductivity from the apparent conductivity measured by the apparatus. In what follows, the subscript "app" denotes

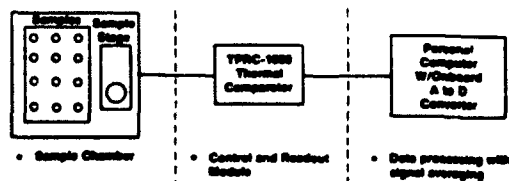


FIG. 1. High precision thermal comparator apparatus. Samples and sample stage are contained in a sealed environmental chamber where temperature is controlled to within 0.1 °C, and humidity is held constant at 6%  $\pm$  1%. A personal computer is used to average the millivolt signals from the comparator readout module.

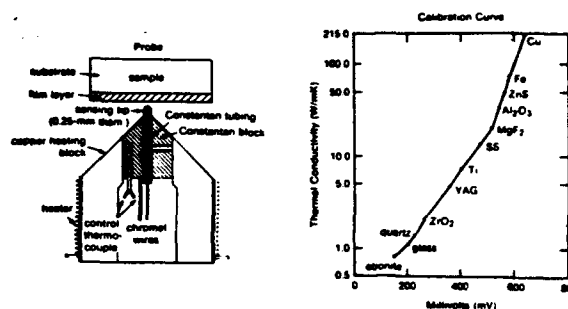


FIG. 2. Principle of operation. The tip of the heated thermocouple probe (56 °C) is cooled when contacted to the coated substrate (36 °C). A voltage generated between the probe junction and an internal, heated control junction reaches a steady-state value and is recorded. Thermal conductivity is determined by comparing calibration standard signals with unknowns. The thin-film coating causes a reduction in the conductivity of the substrate material, which is usually silicon or sapphire. Note: Bulk calibration constants supplied by the instrument manufacturer are for specific materials as follows: Glass—Corning Code 7740. Ti—A110 AT (Ti-5Al-2.5Sn) Alloy. SS—316 stainless steel. Fe—Armco Iron. Quartz—fused silica. Cu—Berlco copper.

the apparent conductivity for the film/interface/substrate assembly as measured by the thermal comparator. The subscript "eff" denotes the effective conductivity for the film which includes any interfacial effects due to the interface between film and substrate, or between film and sensing probe tip. The subscript "F" denotes the conductivity of the thin film material. The analytical model consists of two parts: first, the extraction of  $k_{eff}$  from the measured  $k_{app}$ , and then the extraction of  $k_F$  from  $k_{eff}$ .

The analytical treatment of heat flow, from a circular region of radius  $a$  on the surface of a semi-infinite half-space of uniform conductivity  $k$ , can be found in Carslaw and Jaeger,<sup>12</sup> where the thermal constriction is defined as the ratio of temperature increase to power flowing through a spot of size  $a$ . We define the thermal resistance  $R$  in a slightly different manner, namely as

$$R = \Delta T / (Q/A), \quad (2)$$

where  $\Delta T$  is the average change in temperature over the area  $A$  of the circle of radius  $a$  ( $A = \pi a^2$ ) as compared to the temperature of the substrate far from the heated spot, and  $Q$  is the net power passing through  $A$ . The thermal resistance can be calculated if the distribution of power flux  $q(r)$  (power per unit area) is known. The power flux  $q(r)$  is related to the power  $Q$  by

$$Q = \int_0^a q(r) 2\pi r dr. \quad (3)$$

For the specific power flux distribution

$$q(r) = Q / (2\pi a \sqrt{a^2 - r^2}), \quad (4)$$

over  $0 < r < a$  and vanishing otherwise (which makes the area within the circle of radius  $a$  isothermal) the thermal resistance can be calculated based on the analysis of Carslaw and Jaeger.<sup>12</sup> It is given by

$$R = (\pi/4) (a/k). \quad (5)$$

Numerical analysis by using finite elements<sup>13</sup> was also employed in order to establish that the thermal resistance as



calculated in (5) is not very sensitive to the specific power flux distribution over the circle. For example, when

$$q(r) = \frac{Q}{\pi a^2} \quad \text{or} \quad q(r) = \frac{3Q}{2\pi a^2} \left(1 - \frac{r^4}{a^4}\right) \quad (6)$$

over  $0 < r < a$  and vanishing otherwise, it was found that the thermal resistance increased by 10% and 15%, respectively, over the value of Eq. (5).

Dryden<sup>14</sup> extended the analysis of Carslaw and Jaeger to the case of a film of thickness  $t$  and thermal conductivity  $k_{eff}$  which is bonded to a substrate of thermal conductivity  $k_s$  and of semi-infinite extent. Employing the power flux profile of Eq. (4), Dryden's work is used to evaluate the thermal resistance as

$$R = \frac{\pi}{4} \frac{a}{k_{eff}} + 2 \frac{a}{k_{eff}} \sum_{n=1}^{\infty} \theta^n I_n(t/a), \quad (7a)$$

where  $I_n$  is a definite integral involving trigonometric and Bessel functions, and

$$\theta \equiv \theta(k_{eff}/k_s) = \frac{(k_{eff}/k_s) - 1}{(k_{eff}/k_s) + 1}. \quad (7b)$$

On the other hand, treating the film/interface/substrate assembly as a semi-infinite solid of apparent thermal conductivity  $k_{app}$ , where  $k_{app}$  is measured directly by the thermal comparator, the thermal resistance is given by

$$R = (\pi/4)(a/k_{app}). \quad (8)$$

Equating the thermal resistance given by Eq. (7a) to the thermal resistance given by Eq. (8) yields the relation

$$\frac{1}{k_{eff}} + \frac{8}{\pi} \frac{1}{k_{eff}} \sum_{n=1}^{\infty} \theta^n I_n\left(\frac{t}{a}\right) = \frac{1}{k_{app}}, \quad (9)$$

with  $\theta = \theta(k_{eff}/k_s)$  given by Eq. (7b). Equation (9) relates the experimentally measured  $k_{app}$  to the thermal conductivity of the film/interface  $k_{eff}$  and the thermal conductivity  $k_s$  of the substrate if the heat flow radius  $a$  and the thickness  $t$  of the film are known.

When the film thickness  $t$  is much smaller than the size  $a$  of the heat flow radius  $t \ll a$  and with  $k_{eff} \ll k_s$ , then Eq. (7a) is simplified to

$$R = \frac{\pi}{4} \frac{a}{k_s} + \frac{t}{k_{eff}}. \quad (10)$$

This equation provides the thermal resistance as a perturbation from the case when there is no film at all. The first term in Eq. (10) gives the thermal resistance for a spot of radius  $a$  on a half-space of thermal conductivity  $k_s$  and the second term gives the effect of the film. When the thermal resistance of Eq. (10) is set equal to the thermal resistance of Eq. (8), the relation between the measured  $k_{app}$  and the film/interface  $k_{eff}$  becomes

$$\frac{1}{k_{eff}} = \frac{\pi}{4} \frac{a}{t} \left( \frac{1}{k_{app}} - \frac{1}{k_s} \right). \quad (11)$$

Equation (11) is to be seen as the limiting case of Eq. (9) which is valid for arbitrary  $t/a$ . Still, Eq. (11) is mentioned here because it shows explicitly the dependence of  $k_{eff}$  on the measured  $k_{app}$  and on the ratio  $t/a$  for  $t/a \ll 1$ . The predicted relation between  $k_{eff}$  and  $k_{app}$  as given by Eq. (9) and asymptotically by Eq. (11) is shown in Fig. 3 for several

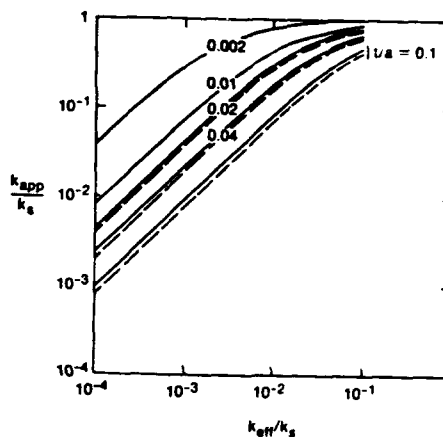


FIG. 3. Comparison of exact and asymptotic relation between the measured  $k_{app}$  and the film/interface conductivity  $k_{eff}$  as predicted from Dryden's work (see Ref. 14). Dryden's expression, Eq. (9), is indicated by the solid line. The asymptotic approximation, Eq. (11), is indicated by the dashed line.

ratios  $t/a$ . For the thickest films considered in Fig. 3 ( $t/a = 0.1$ ), the discrepancy between  $k_{eff}$  (for a given  $k_s$ ) as given by Eq. (9) and as given asymptotically by Eq. (11) is less than 20%.

As will be discussed below, in our measurements, the condition  $a \gg t$  was satisfied for the values of  $a$  used, so that Eqs. (10) and (11) were used in our data analysis.

A lower bound for the size  $a$  of the heat flow radius is given by the size  $a_c$  of physical contact between the sensing probe tip and the film/substrate assembly. Using the Hertzian theory of elastic contact,<sup>15</sup> a compressing force corresponding to a mass of 5–10 g, a radius of curvature of 320  $\mu\text{m}$  for the probe tip (assumed hemispherical), and elastic properties for the material of the probe tip (Young's modulus of 165 GPa) and the film material,<sup>16</sup>  $a_c$  is estimated as being between 10  $\mu\text{m}$  (for oxide films such as  $\text{TiO}_2$  and  $\text{SiO}_2$ ) and 20  $\mu\text{m}$  (for fluoride films such as  $\text{MgF}_2$ ).

Optical shadowgraphy was used to observe contact characteristics between the probe tip and a test sample. Taking into account the relative proximities of the probe tip geometry and the test sample, an upper bound for the heat flow radius was estimated to be 180  $\mu\text{m}$ . Furthermore, finite element analysis of the heat flow from the probe tip to the film/substrate assembly showed that the region over which significant heat transfer occurs may exceed the region of actual physical contact. Thus, the heat flow radius is estimated to be between 20 and 180  $\mu\text{m}$ .

In view of the fact that the lower bound is based on an elastic calculation assuming that the probe tip is perfectly hemispherical, it is expected that the actual value for the heat flow radius is closer to the upper bound of 180  $\mu\text{m}$  rather than to the lower bound of 20  $\mu\text{m}$ . Besides these observations, the actual value of the heat flow radius could not be estimated to a better degree. Still, the error introduced via the uncertainty in the value of the heat flow radius was estimated as described below. Thus, our results can be easily scaled if a more precise value for the heat flow radius can be determined.



We note from Eq. (11) that for a given  $k_{app}$  measured on a film of thickness  $t$  on a substrate of conductivity  $k_s$ , the chosen value of  $a$  and the resulting value of  $k_{eff}$  satisfy

$$ak_{eff} = \text{constant} \quad (12a)$$

from where the uncertainty  $\Delta a$  in the chosen value of  $a$  and the uncertainty  $\Delta k_{eff}$  in the resulting value of  $k_{eff}$  are related by

$$\Delta k_{eff}/k_{eff} = -\Delta a/a. \quad (12b)$$

Thus, with  $a$  between 20 and 180  $\mu\text{m}$ , the value of  $a$  chosen was 100  $\mu\text{m}$ , so that the uncertainty in  $k_{eff}$  due to the uncertainty in  $a$  is estimated at about 80%.

It must be noted that due to convection and conduction via the surrounding fluid (air or other gas) to the film/substrate sample, the heat flow radius may exceed the actual contact size  $a_c$ , especially when the surrounding fluid is highly conductive, or the film is thick, or the film/interface conductivity  $k_{eff}$  is very low. In such cases, a considerable amount of heat flux occurs parallel to the film, thus making the appropriate value of the heat flow radius larger than the actual contact size.

In order to account for such effects and thus find more appropriate values of  $a$  for use in Eq. (9) or (11), the heat transfer from the probe to the film/substrate sample was analyzed using the finite element code ANSYS.<sup>17</sup> Because the film conductivity is specified in the finite element model, Eq. (7a) can be used to extract the appropriate heat flow radius, which is called  $a_A$ . It was found that for a given geometry and environment, the appropriate heat flow radius  $a_A$  is solely a function of the actual contact size  $a_c$  and the film/interface conductivity  $k_{eff}$ . The heavy solid line in Fig. 4 shows how the ratio  $a_A/a_c$  depends on  $k_{eff}$  for a 10- $\mu\text{m}$ -thick film deposited on sapphire and assumed to be surrounded by air. The light lines were derived analytically by noting, from Eq. (10), that the effect of the film is felt only through the term  $t/k_{eff}$ . Thus, the light lines in Fig. 4 were fitted to the equation

$$a_A/a_c = f(t/k_{eff}), \quad (13)$$

where the function  $f(\ )$  was evaluated from the finite ele-

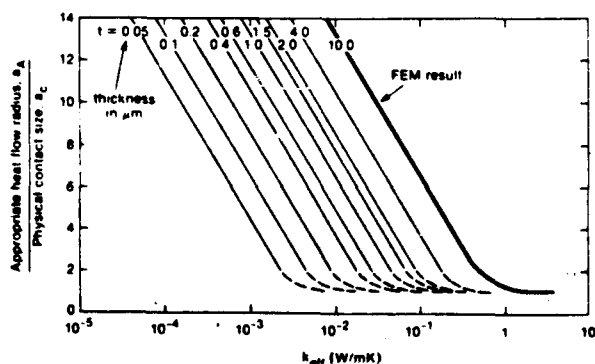


FIG. 4. The appropriate heat flow radius  $a$  to be used in Dryden's expression (see Ref. 14) in terms of the size of physical contact, of the film/substrate conductivity  $k_{eff}$ , and of the film thickness  $t$ . The heavy solid line is from a finite element model (FEM); the other lines are from dimensional analysis. The medium is air and the substrate is sapphire.

ment results (the heavy solid line in Fig. 4). It is seen that when the film/interface conductivity  $k_{eff}$  is lower than some critical value, the appropriate  $a_A$  to be used in Eq. (9) considerably exceeds the size of physical contact.

The asymptotic Eq. (11) relating the measured  $k_{app}$  and the extracted  $k_{eff}$  can be further used to ascertain the effect of various substrates through the substrate conductivity  $k_s$ . It is immediately seen that when the measured  $k_{app}$  is close to the substrate conductivity  $k_s$ , the resolution of Eq. (11) rapidly diminishes. For this reason, we try to avoid evaluation of films which give readings close to the substrate conductivity. In this range, the presence of noise in the system is sufficient to produce extremely large errors in the output film conductivity. Results are most reliable when the film has a conductivity which is much lower than the substrate conductivity  $k_s$ . The measured  $k_{app}$  is then measurably reduced due to the presence of the film, and the potential error due to factors such as system noise is minimized.

Another limitation imposed by the model leading to Eq. (11) is that we need supporting substrates which are large enough to be considered semi-infinite half spaces, i.e., the films must be deposited on substrates which are large enough that they may be considered to be perfect heat sinks. Minimum sample size depends on film and substrate thermal properties. For example, for most films on silicon or sapphire substrates, the minimum sample size is about 25 mm in diameter by about 10 mm thick.

A final limitation arises from the fact that the application of the load that compresses the probe tip onto the film/substrate sample causes a localized thinning of the film immediately underneath the probe tip. The elastic solution by Yu, Sanday, and Rath<sup>18</sup> for the indentation by a hemispherical probe tip of a film/substrate assembly was used in order to estimate that for  $t \ll a$ , as was the case in our measurements to be reported in the sequel, the thinning  $\Delta t$  of the film sample can be estimated from

$$\Delta t = \left( \frac{3P^2}{4R_{tip}} \right)^{1/3} \left[ \left( \frac{1-\nu_p^2}{E_p} + \frac{1-\nu_s^2}{E_s} \right)^{2/3} - \left( \frac{1-\nu_F^2}{E_F} \right)^{2/3} \right], \quad (14)$$

where  $P$  is the load,  $R_{tip}$  is the radius of curvature of the probe tip, and  $\nu, E$  are Poisson's ratio and Young's modulus of the probe tip (subscript  $p$ ), the substrate (subscript  $s$ ), and the film (subscript  $F$ ). Table I shows the thinning in terms of  $E_s$  and  $E_F$  when the probe tip has  $E_p = 165$  GPa, for a load of 5 g, and for  $R_{tip} = 320$   $\mu\text{m}$ . For stiff films (e.g., oxides) on stiff substrates (such as sapphire or silicon) the

TABLE I. Approximate values of film thinning with load of 5 g and radius of curvature of probe tip 320  $\mu\text{m}$ .  $E_F$  and  $E_s$  are the Young's modulus of the film and of the substrate, respectively.

$\Delta t$ ( $\mu\text{m}$ )	$E_s = 200$ GPa	$E_s = 60$ GPa
$E_F$ (GPa) 200	0.03	0.02
60	0.03	0.02
12	0.24	0.18
6	0.42	0.37



thinning is a few hundredths of a micron. For compliant films (e.g., fluorides) on stiff substrates, the thinning is on the order of  $0.05\text{--}0.030\text{ }\mu\text{m}$ . Thus, when the film thickness of compliant films is on the order of  $0.1\text{--}0.5\text{ }\mu\text{m}$ , the changes in geometry due to localized thinning are significant and the local value of the film thickness is quite different from the nominal film thickness.

It must be pointed out that Eq. (7a) or (10) results from a two-dimensional heat flow analysis which couples an axial length scale (the film thickness  $t$ ) to a transverse length scale (the heat flow radius  $a$ ). When a one-dimensional heat flow analysis is carried out (which would be strictly valid when the heat flow radius  $a$  greatly exceeds the film thickness  $t$  and the substrate thickness  $L$ , although we still have  $L \gg t$ ) the result is

$$\frac{1}{k_{\text{eff}}} = \frac{L}{t} \left( \frac{1}{k_{\text{app}}} - \frac{1}{k_s} \right). \quad (15)$$

In view of the fact that the thickness of the substrate (typically several millimeters in our experiments) can greatly exceed the heat flow radius  $a$  ( $\sim 100\text{ }\mu\text{m}$ ), it is concluded that a one-dimensional analysis may greatly underestimate  $k_{\text{eff}}$  unless precautions are taken to actually validate the assumptions upon which such a one-dimensional calculation, viz. Eq. (15), is derived.

Once the conductivity of the film/interface  $k_{\text{eff}}$  is determined from Eq. (9) or (11) for a specific film thickness  $t$  (typically in the range of a few microns, as will be presented in the sequel), the film conductivity  $k_F$  is evaluated by noting that, since  $a \gg t$ , the heat flow within the film is essentially one-dimensional and normal to the film/substrate interface or to the interface between the probe tip and the film. Denoting by  $R_{\text{int}}$  the thermal resistance due to any interfaces,  $R_{\text{int}}$  is defined by

$$R_{\text{int}} = \Delta T_{\text{int}} / (Q/A_{\text{int}}), \quad (16)$$

where  $\Delta T_{\text{int}}$  is the temperature drop across the interface (of cross-sectional area  $A_{\text{int}}$ ) and  $Q/A_{\text{int}}$  is the power flux across the interface. A one-dimensional heat flow analysis is now applicable; it yields

$$t/k_{\text{eff}} = (t/k_F) + R_{\text{int}}, \quad (17)$$

which implies that a plot of  $t/k_{\text{eff}}$  vs  $t$ , with  $k_{\text{eff}}$  found from Eq. (9) or (11), has slope equal to  $1/k_F$  and intercept of  $R_{\text{int}}$ .

In view of the fact that the uncertainty  $\Delta a$  in the heat flow radius  $a$  produces an uncertainty  $\Delta k_{\text{eff}}$  in  $k_{\text{eff}}$  as shown in Eqs. (12a) and (12b), and since  $k_{\text{eff}}$  is linearly related to  $k_F$  viz., Eq. (17), the resulting uncertainty  $\Delta k_F$  in the film conductivity  $k_F$  also satisfies

$$ak_F = \text{constant} \quad (18a)$$

or

$$\Delta k_F/k_F = -\Delta a/a. \quad (18b)$$

In a similar fashion, the resulting value for  $R_{\text{int}}$  depends on the value  $a$  used for the heat flow radius via

$$R_{\text{int}}/a = \text{constant} \quad (19a)$$

or

$$\Delta R_{\text{int}}/R_{\text{int}} = \Delta a/a. \quad (19b)$$

Since the uncertainty in  $a$  has been previously estimated at  $\Delta a/a = 80\%$ , it is concluded that a similar amount of error is present in  $\Delta k_F/k_F$  and in  $\Delta R_{\text{int}}/R_{\text{int}}$ .

#### IV. PROCEDURE

The experimental and analytical procedure used to determine the thermal conductivity of thin films and the thermal resistance of any interfaces is summarized in flow chart form in Fig. 5, which shows one run in which about five film samples and six calibration standards are evaluated. Each run takes approximately 1 h. Generally, six similar runs are conducted on a given sample set. The results of these runs are averaged to provide the value of  $k_{\text{app}}$ . Once the value of  $k_{\text{app}}$  is determined, the value of the film/interface conductivity  $k_{\text{eff}}$  is calculated from Eq. (11). The value of the heat flow radius used in this step was taken to be  $100\text{ }\mu\text{m}$ , as discussed previously. Finally,  $t/k_{\text{eff}}$  is plotted versus film thickness  $t$  in order to extract the film conductivity  $k_F$  from the slope of the straight line and the interfacial thermal resistance  $R_{\text{int}}$  from the intercept of the straight line with the ordinate.

#### V. RESULTS

Tables II–VII show the results of testing in the form of the measured value of  $k_{\text{app}}$  vs film thickness  $t$ . These tables include the film material, the substrate, the load used, as well as the extracted values for the film conductivity  $k_F$  and for the interfacial thermal resistance  $R_{\text{int}}$ . The data shown are for films deposited either on sapphire (of conductivity  $k_s = 35\text{ W/m K}$ )<sup>19</sup> or single-crystal silicon (38 mm diameter by 6 mm thickness) with a crystal orientation of (111) (of conductivity  $k_s = 150\text{ W/m K}$ )<sup>19</sup> or for films deposited on fused silica (of conductivity  $k_s = 1.41\text{ W/m K}$ ).<sup>20</sup> The plots of  $t/k_{\text{eff}}$  versus film thickness  $t$  are shown in Figs. 6–11, where the straight lines used to extract  $k_F$  and  $R_{\text{int}}$  are also

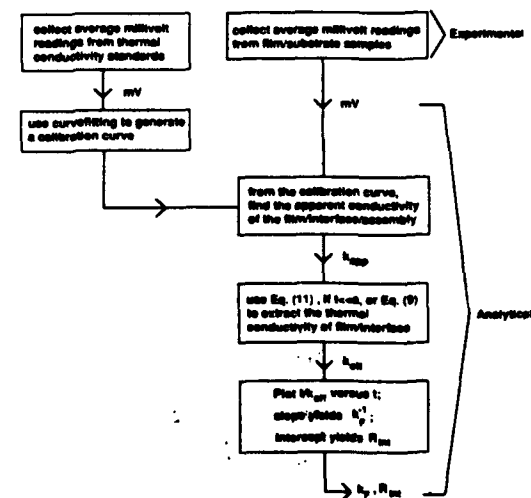


FIG. 5. Experimental and analytical procedure for finding the conductivity of the thin film. For a given thickness, six runs are typically conducted and averaged.



TABLE II. Measured  $k_{app}$  (W/m K) vs thickness ( $\mu\text{m}$ ) for  $\text{SiO}_2$  on silicon substrates with two deposition techniques and loads of 5 and 10 g. The extracted film conductivity  $k_f$  (W/m K) and interfacial thermal resistance  $R_{int}$  ( $\text{mm}^2 \text{K/W}$ ) are also shown.

Method/material/substrate	Thickness	$k_{app}$	$k_f$	$R_{int}$
EBE $\text{SiO}_2$ /silicon load: 5.0 g	0.52	$30.9 \pm 3.0$	0.61	1.07
	1.01	$21.7 \pm 1.3$		
	2.00	$15.8 \pm 1.3$		
	4.03	$13.7 \pm 0.6$		
EBE $\text{SiO}_2$ /silicon load: 10.0 g	0.50	$42.2 \pm 6.5$	0.45	0.11
	1.00	$23.6 \pm 4.0$		
	2.00	$15.0 \pm 0.8$		
IBS $\text{SiO}_2$ /silicon load: 5.0 g	0.50	$26.8 \pm 10.7$	1.05	1.78
	1.01	$23.3 \pm 4.1$		
	1.95	$18.4 \pm 1.6$		
	4.40	$16.0 \pm 1.2$		
IBS $\text{SiO}_2$ /silicon load: 10.0 g	0.50	$43.8 \pm 3.4$	0.41	0.00
	1.01	$21.9 \pm 2.4$		
	1.95	$14.7 \pm 1.1$		
	4.40	$12.5 \pm 1.2$		

TABLE III. Measured  $k_{app}$  (W/m K) vs thickness ( $\mu\text{m}$ ) for  $\text{TiO}_2$  films on silicon substrates with two deposition techniques and loads of 5 and 10 g. The extracted film conductivity  $k_f$  (W/m K) and interfacial thermal resistance  $R_{int}$  ( $\text{mm}^2 \text{K/W}$ ) are also shown.

Method/material/substrate	Thickness	$k_{app}$	$k_f$	$R_{int}$
EBE $\text{TiO}_2$ /silicon load: 5.0 g	0.52	$19.3 \pm 4.5$	0.59	2.7
	1.01	$16.0 \pm 2.2$		
	1.57	$13.5 \pm 2.1$		
	2.05	$14.3 \pm 2.2$		
IBS $\text{TiO}_2$ /silicon load: 5.0 g	0.50	$52.0 \pm 7.4$	0.48	0.54
	1.01	$24.7 \pm 7.3$		
	1.99	$15.0 \pm 1.8$		
IBS $\text{TiO}_2$ /silicon load: 10.0 g	0.50	$36.0 \pm 6.4$	0.48	0.52
	1.01	$24.2 \pm 2.0$		
	1.99	$18.9 \pm 1.6$		
	4.02	$12.7 \pm 0.7$		

TABLE IV. Measured  $k_{app}$  (W/m K) vs thickness ( $\mu\text{m}$ ) for  $\text{TiO}_2$  films on various substrates.

Method/material/substrate	Thickness	$k_{app}$	$k_f$	$R_{int}$
EBE $\text{TiO}_2$ /sapphire load: 5.0 g	0.060	$20.9 \pm 1.5$	...	...
	1.184	$22.2 \pm 2.7$		
	1.246	$25.7 \pm 4.0$		
EBE $\text{TiO}_2$ /sapphire load: 10.0 g	0.060	$18.8 \pm 2.6$	...	...
	1.184	$21.1 \pm 2.6$		
	1.246	$29.2 \pm 6.1$		
EBE $\text{TiF}_3$ /fused silica load: 5.0 g	0.060	$1.46 \pm 0.18$	...	...
	1.184	$1.48 \pm 0.19$		
	1.246	$1.51 \pm 0.15$		

TABLE V. Measured  $k_{app}$  (W/m K) vs thickness ( $\mu\text{m}$ ) for various oxide films deposited on sapphire. The extracted film conductivity  $k_f$  (W/m K) and interfacial thermal resistance  $R_{int}$  ( $\text{mm}^2 \text{K/W}$ ) are also shown.

Method/material/substrate	Thickness	$k_{app}$	$k_f$	$R_{int}$
EBE $\text{HfO}_2$ /sapphire load: 5.0 g	0.257	$18.9 \pm 2.0$	0.052	<0
	0.442	$10.2 \pm 0.6$		
	0.495	$46.6 \pm 2.5$		
EBE $\text{Sc}_2\text{O}_3$ /sapphire load: 5.0 g	0.146	$17.2 \pm 1.4$	0.053	<0
	0.292	$10.7 \pm 0.4$		
	0.462	$28.0 \pm 1.6$		
EBE $\text{ZrO}_2$ /sapphire load: 5.0 g	0.151	$19.0 \pm 1.9$	0.04	<0
	0.317	$9.8 \pm 0.5$		
	0.465	$18.1 \pm 0.6$		
EBE $\text{ThO}_2$ /sapphire load: 5.0 g	0.174	$25.1 \pm 2.9$	0.67	0.60
	0.350	$23.2 \pm 2.9$		
	0.396	$24.9 \pm 3.5$		
EBE $\text{Al}_2\text{O}_3$ /sapphire load: 5.0 g	0.173	$18.3 \pm 1.7$	...	...
	0.292	$26.0 \pm 1.6$		
	0.462	$20.5 \pm 1.8$		
EBE $\text{CeO}_2$ /sapphire load: 5.0 g	0.128	$19.4 \pm 2.0$	...	...
	0.257	$20.9 \pm 2.0$		
	0.357	$17.2 \pm 2.0$		

TABLE VI. Measured  $k_{app}$  (W/m K) vs thickness ( $\mu\text{m}$ ) for various fluoride films deposited on sapphire. The extracted film conductivity  $k_f$  (W/m K) and interfacial thermal resistance  $R_{int}$  ( $\text{mm}^2 \text{K/W}$ ) are also shown.

Method/material/substrate	Thickness	$k_{app}$	$k_f$	$R_{int}$
EBE $\text{AlF}_3$ /sapphire load: 5.0 g	0.194	$18.5 \pm 0.8$	0.31	1.40
	0.388	$16.1 \pm 1.2$		
	0.544	$37.0 \pm 4.0$		
EBE $\text{HfF}_4$ /sapphire load: 5.0 g	0.173	$9.7 \pm 1.1$	0.27	2.40
	0.347	$13.2 \pm 0.6$		
	0.520	$11.9 \pm 1.6$		
EBE $\text{YF}_3$ /sapphire load: 5.0 g	0.162	$22.9 \pm 2.2$	0.75	0.97
	0.325	$22.3 \pm 2.6$		
	0.403	$21.0 \pm 2.3$		
EBE $\text{CeF}_3$ /sapphire load: 5.0 g	0.150	$24.4 \pm 2.1$	0.08	<0
	0.300	$15.4 \pm 1.9$		
	0.470	$28.9 \pm 2.3$		
EBE $\text{ScF}_3$ /sapphire load: 5.0 g	0.189	$23.7 \pm 1.8$	0.09	<0
	0.379	$14.8 \pm 1.3$		
	0.539	$40.4 \pm 3.0$		
EBE $\text{ThF}_4$ /sapphire load: 5.0 g	0.162	$20.5 \pm 1.2$	0.10	<0
	0.337	$14.3 \pm 1.4$		
	0.506	$27.2 \pm 3.2$		
EBE $\text{LaF}_3$ /sapphire load: 5.0 g	0.160	$19.3 \pm 1.0$	...	...
	0.321	$23.7 \pm 2.8$		
	0.473	$23.9 \pm 2.5$		
EBE $\text{MgF}_2$ /sapphire load: 5.0 g	0.209	$35.3 \pm 2.3$	...	...
	0.420	$36.7 \pm 2.9$		
	0.583	$58.3 \pm 2.1$		



TABLE VII. Measured  $k_{app}$  (W/m K) vs thickness ( $\mu\text{m}$ ) for ZnS and cryolite films deposited on sapphire. The extracted film conductivity  $k_F$  (W/m K) and interfacial thermal resistance  $R_{int}$  ( $\text{mm}^2 \text{K/W}$ ) are also shown.

Methor <sup>1</sup> /material/substrate	Thickness	$k_{app}$	$k_F$	$R_{int}$
EBE ZnS/sapphire load: 5.0 g	0.190	$20.7 \pm 2.6$	...	...
	0.477	$33.1 \pm 2.1$		
	0.592	$28.8 \pm 1.8$		
EBE cryolite/sapphire load: 5.0 g	0.155	$20.3 \pm 1.6$	0.15	0.6
	0.464	$13.2 \pm 0.5$		

shown. Also, in these figures, the variation of  $k_{eff}$  itself with  $t$  is also shown. Table VIII summarizes our extracted values for the thin-film thermal conductivities and interfacial thermal resistances in addition to data from the work of Decker<sup>1</sup> and Ristau,<sup>7</sup> and thermal conductivity data for the bulk materials.

The materials tested were oxides ( $\text{SiO}_2$ ,  $\text{TiO}_2$ ,  $\text{HfO}_2$ ,

$\text{Sc}_2\text{O}_3$ ,  $\text{ZrO}_2$ ,  $\text{ThO}_2$ ,  $\text{Al}_2\text{O}_3$ ,  $\text{CeO}_2$ ), fluorides ( $\text{AlF}_3$ ,  $\text{HfF}_4$ ,  $\text{YF}_3$ ,  $\text{CeF}_3$ ,  $\text{ScF}_3$ ,  $\text{ThF}_4$ ,  $\text{LaF}_3$ ,  $\text{MgF}_2$ ), and a few other films (ZnS, Cryolite). The films were tested by using a load of either 3.5, 5.0, or 10.0 g. The films were deposited in either of two ways: ion beam sputtering (IBS) or electron beam evaporation (EBE).

For  $\text{SiO}_2$  films, viz. Figs. 6(a)–6(d) and Table II, in the range of thicknesses  $0 < t < 4 \mu\text{m}$ , it is observed that the film conductivity  $k_F$  is not constant, but instead varies with the thickness  $t$ , since the plot of  $t/k_{eff}$  is not a straight line over this thickness range. Still, for thickness  $< 2 \mu\text{m}$ , the results can be fitted in a straight line to give the value of  $k_F$  reported in Table II. Table II also shows that the method of film deposition does not appear to significantly alter the film conductivity  $k_F$  or the interfacial thermal resistance  $R_{int}$  at the 10-g load. This is not the case, however, at the 5-g load. As can be seen in Table II, IBS deposited  $\text{SiO}_2$  films show a higher value for both the film conductivity and interfacial thermal resistance than do the EBE deposited  $\text{SiO}_2$  films at this load. At this point in time, the dependence of these values on the load used has not been precisely determined.

A similar discussion follows the results for the  $\text{TiO}_2$

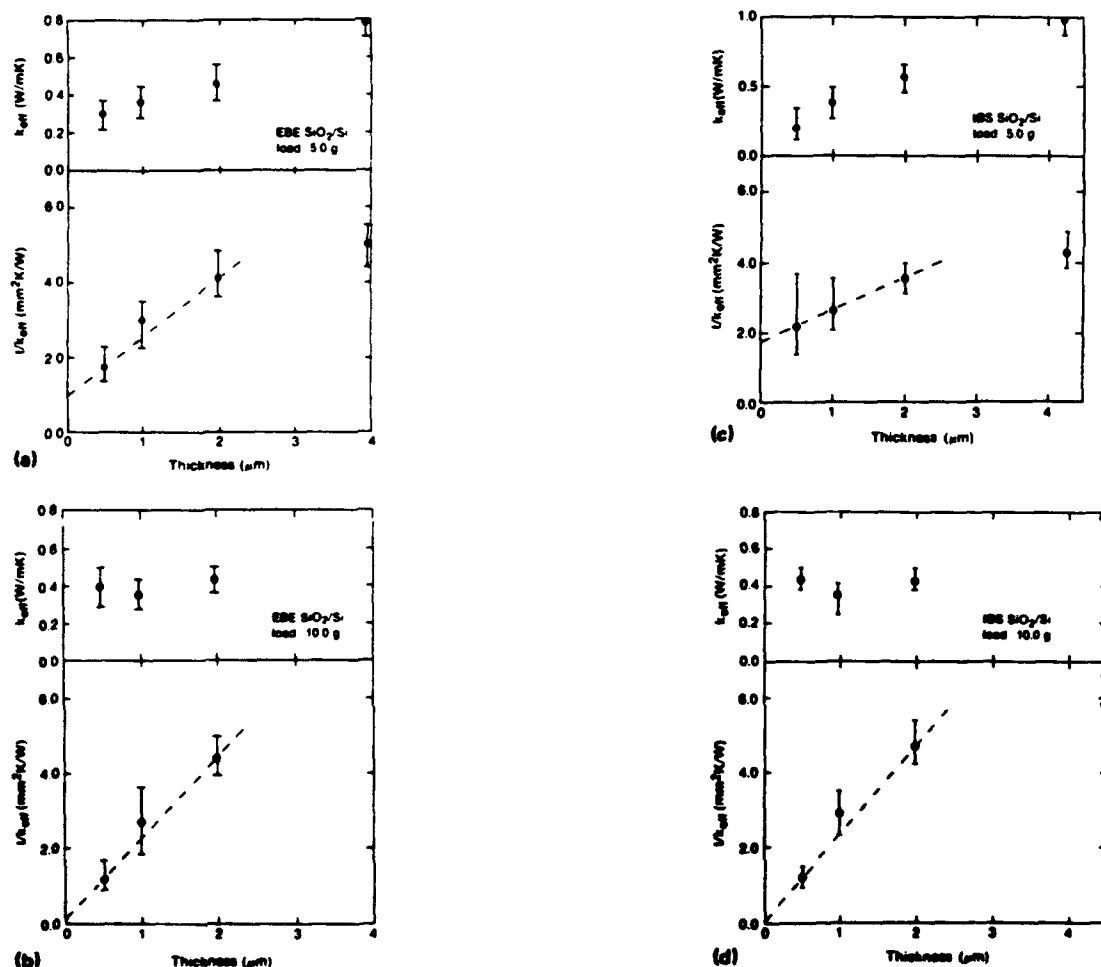
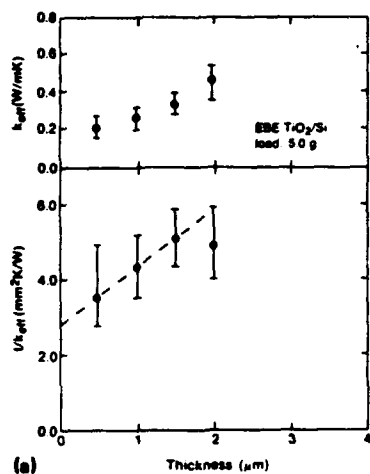
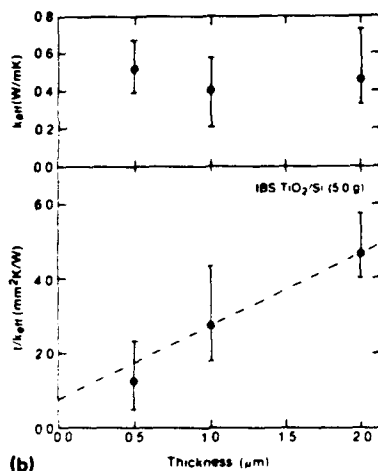


FIG. 6. Variation of  $k_{eff}$  and  $t/k_{eff}$  vs  $t$  for: (a) EBE  $\text{SiO}_2/\text{Si}$  at a 5-g load; (b) EBE  $\text{SiO}_2/\text{Si}$  at a 10-g load; (c) IBS  $\text{SiO}_2/\text{Si}$  at a 5-g load; (d) IBS  $\text{SiO}_2/\text{Si}$  at a 10-g load.

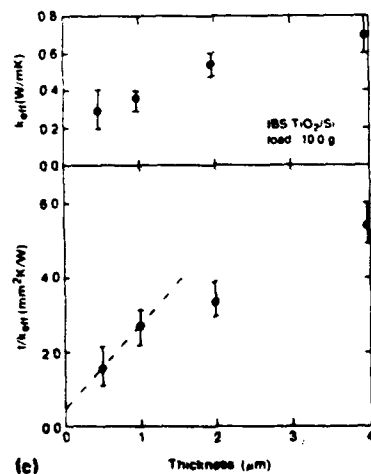




(a)



(b)



(c)

FIG. 7. Variation of  $k_{app}$  and  $t/k_{app}$  vs  $t$  for: (a) EBE  $\text{TiO}_2/\text{Si}$  at a 5-g load; (b) IBS  $\text{TiO}_2/\text{Si}$  at a 5-g load; (c) IBS  $\text{TiO}_2/\text{Si}$  at a 10-g load.

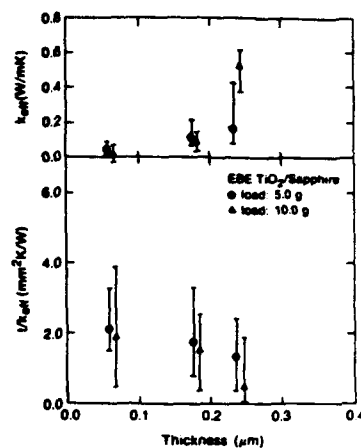


FIG. 8. Variation of  $k_{app}$  and  $t/k_{app}$  vs  $t$  for EBE  $\text{TiO}_2/\text{Al}_2\text{O}_3$  at 5- and 10-g loads.

films deposited on silicon [Table III, Figs. 7(a)–7(c)]. Table III also shows that the method of deposition does not alter significantly the value of the film conductivity. Still it appears that the method of deposition does affect the interfacial thermal resistance for the  $\text{TiO}_2$  films as the EBE deposited films appear to have higher interfacial thermal resistance than the IBS deposited films. The applied load, however, seems to have little effect on the interfacial thermal resistance for the IBS deposited  $\text{TiO}_2$  films. Clearly, more data are required in order to quantify more precisely the effect of method of deposition and applied load on the interfacial thermal resistance.

Figure 8 and Table IV show the data for  $\text{TiO}_2$  films but now deposited on substrates such as sapphire and fused silica, which have considerably lower thermal conductivity than silicon. As discussed previously and as shown explicitly in Eq. (11), when the measured value  $k_{app}$  is close to the substrate conductivity  $k_s$ , the resolution of the measurement deteriorates considerably. This is shown when we compare Fig. 7 with Fig. 8, where the error bars are now so significant that the data cannot be fitted by a straight line. It is thus shown that silicon is a much better substrate than sapphire or fused silica for measuring the thermal conductivity of dielectric thin films.

The measurements for other oxide films deposited on sapphire (and using a load of 5 g) are shown in Table V and in Figs. 9(a)–9(d) for thicknesses  $< 0.5 \mu\text{m}$ . For several film materials, the thickest films gave values for  $k_{app}$  which were close to, if not exceeding as in the case of  $\text{HfO}_2$ , the thermal conductivity of the substrate. In such cases, the measurement was discarded, viz. Figs. 9(a)–9(c), since the experimental noise in the apparatus significantly affects the measured  $k_{app}$  when the latter is close to the substrate conductivity  $k_s$ . Consequently, only two points (corresponding to the lower thicknesses) were used in the determination of the film thermal conductivity and of the interfacial thermal resistance. It is interesting to note that some materials, viz. Figs. 9(a) and 9(c) gave negative value of the interfacial thermal resistance. Such negative values were discarded by observing that it is possible that  $t/k_{app}$  vs  $t$  may have a sig-



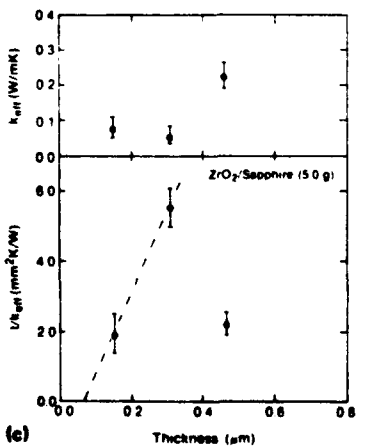
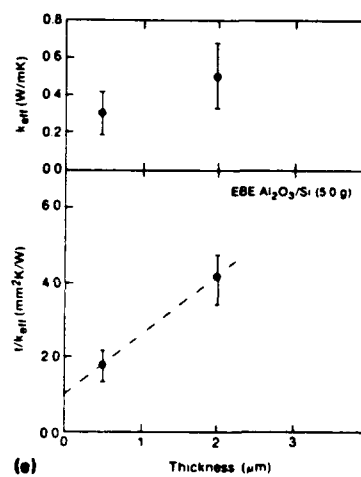
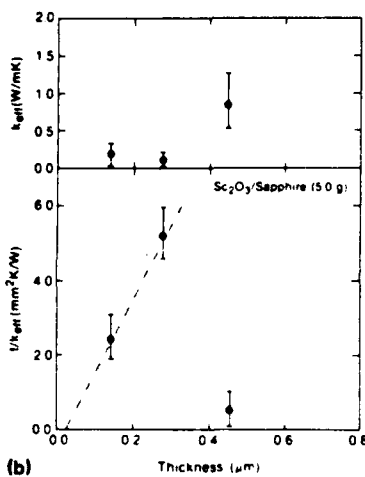
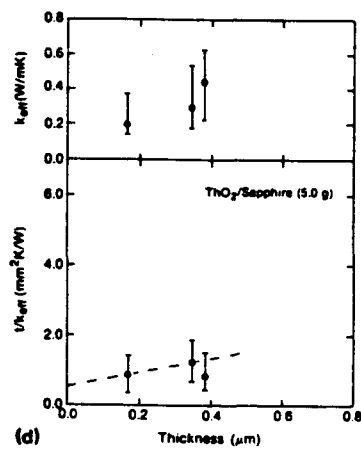
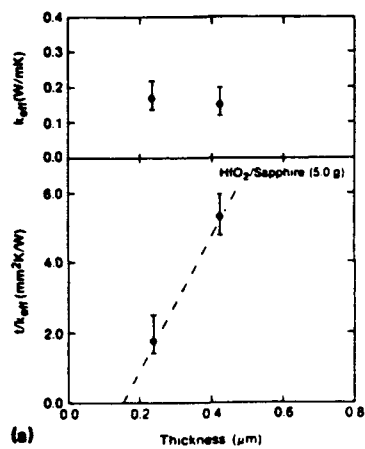


FIG. 9. Variations of  $k_{eff}$  and  $t/k_{eff}$  vs  $t$  for: (a)  $\text{HfO}_2/\text{Al}_2\text{O}_3$ ; (b)  $\text{Sc}_2\text{O}_3/\text{Al}_2\text{O}_3$ ; (c)  $\text{ZrO}_2/\text{Al}_2\text{O}_3$ ; (d)  $\text{ThO}_2/\text{Al}_2\text{O}_3$ ; and (e)  $\text{Al}_2\text{O}_3/\text{Si}$ .



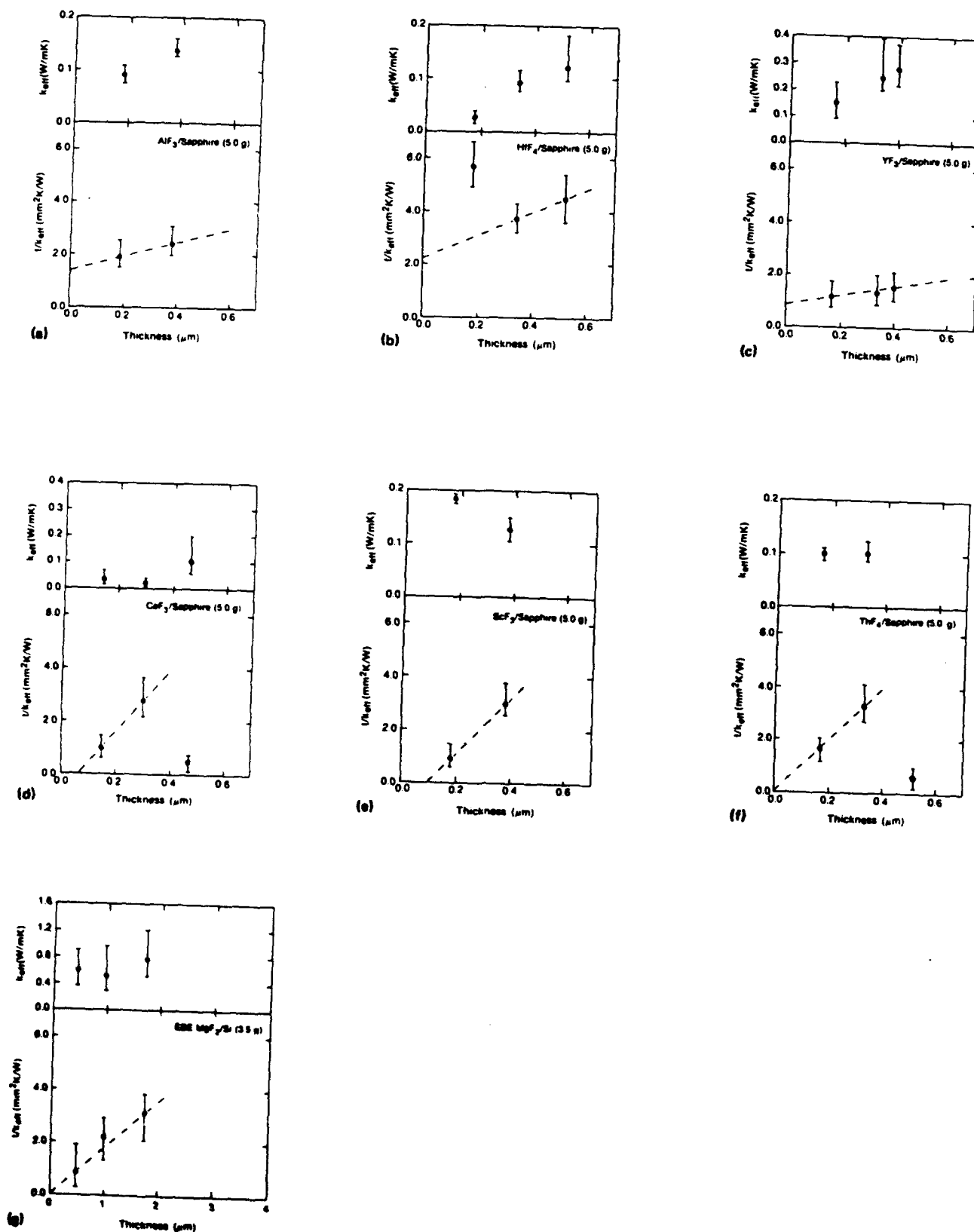


FIG. 10. Variation of  $k_{eff}$  and  $U/k_{eff}$  vs  $t$  for: (a)  $AlF_3/Al_2O_3$ ; (b)  $HfF_4/Al_2O_3$ ; (c)  $YF_3/Al_2O_3$ ; (d)  $CeF_3/Al_2O_3$ ; (e)  $ScF_3/Al_2O_3$ ; (f)  $ThF_4/Al_2O_3$ ; and (g)  $MgF_2/Si$ .



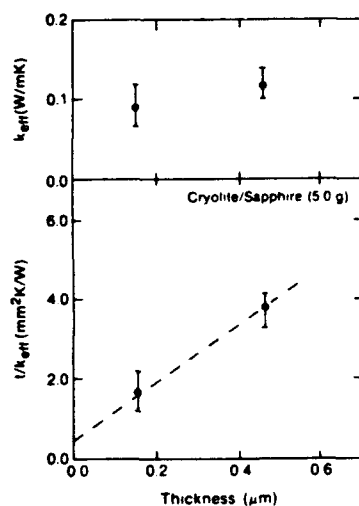


FIG. 11. Variation of  $k_{\text{eff}}$  and  $t/k_{\text{eff}}$  vs  $t$  for Cryolite/ $\text{Al}_2\text{O}_3$ .

moidal shape so that the slope of  $t/k_{\text{eff}}$  vs  $t$  at small thicknesses is smaller than the slope at larger thicknesses, where fitting to a straight line is actually done. If the middle part of such a sigmoidal curve is used to extrapolate to  $t = 0$ , it will lead to a negative intercept. Figure 9(c) shows the results for  $\text{Al}_2\text{O}_3$  films deposited on silicon. These  $\text{Al}_2\text{O}_3$  films were in the range of 0.5–4  $\mu\text{m}$ .

The data for fluoride films deposited on sapphire are shown in Table VI and in Figs. 10(a)–10(f). Again, in some materials, the thickest film data had to be discarded since they gave readings which were too close to the substrate

thermal conductivity. It must be noted that in some cases the data corresponding to the thinnest film had to be discarded. This is shown in Fig. 10(b), where a film of 0.2  $\mu\text{m}$  thickness gave too large a value for  $t/k_{\text{eff}}$ . This observation is explained by noting that fluorides are considerably softer than oxides, and even a load of 5 g can produce a large amount of localized elastic thinning which can be as large as 0.2–0.3  $\mu\text{m}$ . Furthermore, due to the material's softness, it is possible that the application of the load by the probe tip leads to decohesion along the film/substrate interface. Such a decohesion leads to considerably lower values of the film/interfacial conductivity  $k_{\text{eff}}$ , thus producing an abnormally large value for  $t/k_{\text{eff}}$ . Figure 10(g) shows the data for  $\text{MgF}_2$  films deposited on silicon. These films were in the range of 0.5–4  $\mu\text{m}$ . None of the problems with the fluoride films, mentioned above, were encountered in this case. Most fluoride films had a film conductivity in the range of 0–0.3 W/m K, with the exception of  $\text{YF}_3$ , which had a conductivity of 0.75 W/m K (although the error bars in the  $\text{YF}_3$  data are large enough that a line of larger slope can also be fitted through the data).

Data for a zinc-sulfide film and for a cryolite film are reported in Table VII and plotted for the latter in Fig. 11.

The values for the thermal conductivity of the film materials discussed above are summarized in Table VIII. As a general conclusion, the film material conductivity is < 1.1 W/m K, and the interfacial thermal resistance due to the probe tip/film and film/substrate interface is typically < 2–3  $\text{mm}^2\text{K/W}$ . These values lead to the conclusion that the conductivity of a material in thin-film form is considerably less than the thermal conductivity of the same material in bulk form.

TABLE VIII. Thermal conductivity  $k_f$  (W/m K) and thermal interfacial resistance  $R_{\text{int}}$  ( $\text{mm}^2\text{K/W}$ ) for various film materials on several substrates. Values from the work of Decker<sup>1</sup> and Ristau<sup>7</sup> are also shown.

Film/substrate (EBE deposited except as noted)	Load	Present work		Decker <sup>1</sup> $k_f$	Ristau <sup>7</sup> $k_f$	Bulk $k$
		$k_f$	$R_{\text{int}}$			
$\text{SiO}_2/\text{silicon}^b$	10,5	0.45,0.61	0.1,1.1	0.17 ( $t = 1 \mu\text{m}$ )	0.10 ( $t = 1 \mu\text{m}$ )	1.2 <sup>16</sup> –10.7 <sup>20</sup>
IBS $\text{SiO}_2/\text{silicon}^b$	10,5	0.41,1.05	0.0,1.8	0.28 ( $t = 0.5 \mu\text{m}$ )		
$\text{TiO}_2/\text{silicon}^b$	5	0.59	2.7			
IBS $\text{TiO}_2/\text{silicon}^b$	10,5	0.48,0.48	0.52,0.54		0.018 ( $t = 1 \mu\text{m}$ )	7.4–10.4 <sup>20</sup>
$\text{HfO}_2/\text{sapphire}^c$	5	0.052	...			
$\text{Sc}_2\text{O}_3/\text{sapphire}^c$	5	0.053	...			
$\text{ZrO}_2/\text{sapphire}^c$	5	0.04	...			
$\text{ThO}_2/\text{sapphire}^c$	5	0.67	0.6			
$\text{Al}_2\text{O}_3/\text{silicon}^c$	5	0.72	1.0		33 ( $t = 1 \mu\text{m}$ )	20 <sup>1</sup> –46 <sup>20</sup>
$\text{CeO}_2/\text{sapphire}^c$	5	...	...			
$\text{AlF}_3/\text{sapphire}^c$	5	0.31	1.4			
$\text{HfF}_4/\text{sapphire}^c$	5	0.27	2.4			
$\text{YF}_3/\text{sapphire}^c$	5	0.75	0.97			
$\text{CeF}_3/\text{sapphire}^c$	5	0.08	...			
$\text{ScF}_3/\text{sapphire}^c$	5	0.09	...			
$\text{ThF}_4/\text{sapphire}^c$	5	0.10	...			
$\text{LaF}_3/\text{sapphire}^c$	5	...	...			
$\text{MgF}_2/\text{silicon}^b$	3.5	0.58	0.0			14.6 <sup>16</sup> –30 <sup>21</sup>
$\text{ZnS}/\text{sapphire}^c$	5	...	...			
Cryolite/ $\text{sapphire}^c$	5	0.15	0.6			

<sup>a</sup>Samples from A. Steward, AFWL.

<sup>b</sup>Samples from T. Allen, OCLI, Inc.

<sup>c</sup>Samples from D. J. Smith, LLE.



By assuming that the surface morphology of the film essentially replicates the surface morphology of the underlying substrate (this assumption appears more reasonable for the stiff, harder films such as oxides, whereas its validity is questionable for the case of the softer fluoride films), and since any interfacial thermal resistance between the probe tip and the surface of the bulk standards used in establishing the calibration curves, viz. Fig. 2, is thus seen to be the same as the resistance between the probe tip and the film surface, we are led to the conclusion that any interfacial thermal resistance extracted from the intercept with the ordinate axis in the plots of  $t/k_{\text{eff}}$  vs  $t$  must thus be attributed to the interface between the film and the supporting substrate. The resolution of our experimental measurement and the fact that for small thicknesses  $t/k_{\text{eff}}$  may not be linearly related to the thickness  $t$  (our measurements at discrete thicknesses cannot reveal this dependence, especially at small  $t$ ) does not presently allow a precise determination of the value of  $R_{\text{int}}$  or a correlation of this thermal resistance with other variables such as film deposition method or film microstructure.

Experiments were also carried out in helium gas which has a much greater thermal conductivity (0.15 W/m K) than air. The large value of  $k$  for He implies that the heat flow radius for the experiments in He is greater than the heat flow radius for the air measurements. Since the extracted values of  $k_{\text{eff}}$  are of the same order of magnitude as the thermal conductivity of He, the value of the heat flow radius in He is very close to the actual size of the probe tip. Using a value of 300  $\mu\text{m}$  for the heat flow radius in He, and the value of 100  $\mu\text{m}$  for the heat flow radius in air, the plots of  $t/k_{\text{eff}}$  vs  $t$  for the He and air data had thermal resistance within 1–2  $\text{mm}^2 \text{ K/W}$  of each other. It is concluded that any thermal resistance between the probe tip and the film surface is probably due to solid–solid contacts, rather than solid–fluid (He or air) contacts. This conclusion is in agreement with previously published experimental and analytical work.<sup>21</sup>

If the thermal resistance extracted is due to the film/substrate interface, as argued above, it becomes clear that in addition to the film conductivity  $k_F$ , the value of the film/interface thermal conductivity  $k_{\text{eff}}$  (which includes the interfacial thermal resistance  $R_{\text{int}}$ ) is also of interest, especially for applications where the film/substrate interface is important as in studies of thin-film laser damage. It is noted that the film/interface thermal conductivity does depend on the film thickness, whereas the dependence of the film conductivity  $k_F$  on the thickness (over the range of thicknesses studied in this report) is much weaker. The temperature drop across the film/substrate interface, which is directly related to the interfacial thermal resistance  $R_{\text{int}}$ , is an important quantity. Large values of the interfacial thermal resistance imply that the temperature is essentially discontinuous across the interface, and that the amount of the temperature discontinuity depends on the heat flux across the interface.

The inhomogeneous structure of the film/substrate interface (which contains voids, cracks, and other inhomogeneities) is expected to be directly related to the magnitude of the interfacial thermal resistance.<sup>22</sup> Such inhomogeneities create a barrier to heat flow, and thus lead to the interfacial thermal resistance. This explanation seems particularly val-

id for evaporated films which are known to have a high level of internal tensile stress and a propensity for crazing.<sup>23,24</sup> The same observation may be made for thin films prepared by ion beam sputtering.<sup>25</sup> Other measurements of the interfacial thermal resistance in terms of phonon scattering at the film/substrate interface have been provided by Swartz and Pohl<sup>26</sup> who measured the thermal resistance at the interface between Rh:Fe films deposited on sapphire.

Although the discussion and present analysis has focused on dielectric thin films, similar measurements have been made for metallic thin films. A comprehensive review of such measurements of the thermal conductivity of thin films is provided by Guenther and McIver.<sup>3</sup> As typical examples we mention the work of Nath and Chopra<sup>27</sup> on thin films of copper, who found that for films thinner than about 1  $\mu\text{m}$  the bulk conductivity values were not appropriate, the work of Boikov *et al.*,<sup>28</sup> who studied the thermal conductivity of silver and aluminum films, and the work of Ogden *et al.*<sup>29</sup> on anodic oxide coatings of aluminum, although the thicknesses used in latter work were in the 15–110  $\mu\text{m}$  range. The common conclusion is that thin films exhibit a considerably lower thermal conductivity than bulk materials, and that a significant interfacial thermal resistance develops across the interface of thin films bonded to substrates.

The limitations imposed by the experimental technique, as described above, must be borne in mind when interpreting the measurements of  $k_{\text{app}}$  versus thickness. The effect of the substrate conductivity, the effect of the finite size of the sample used, the effect of small film thickness (especially for the softer films), and the effect of the precise value of the heat flow radius are all important considerations whose contributions were discussed previously.

Our data analysis involves knowledge of the heat flow radius  $a$  in order to extract the effective film/interface conductivity  $k_{\text{eff}}$  from the measured value of  $k_{\text{app}}$ . Although an upper and a lower bound were established for the heat flow radius, the uncertainty in  $a$  leads to an uncertainty of about 80% in the extracted values of  $k_{\text{eff}}$ ,  $k_F$ , and  $R_{\text{int}}$ . Furthermore, the variation of these quantities with the heat flow radius was established in Eqs. (12a), (18a), and (19a), respectively. In addition to this error, the analytical expression from Dryden's work<sup>14</sup> for the thermal resistance used a heat influx profile which may contain an error of 10%–20% when compared to other profiles, as shown above. Thus, the combined uncertainty in our measurements has allowed the calculation of the thin-film conductivity to within a factor of 2. Even so, the conclusion of our measurements stands, namely that thin films are characterized by a thermal conductivity considerably lower than that of bulk samples.

The uncertainty in the value of the heat flow radius  $a$  can be eliminated to some extent by using a self-aligning probe tip of, say, a flat profile so that the heat flow radius is well approximated by the width of the probe tip. The design of such a probe tip is currently under way at the Laboratory for Laser Energetics.

It is clear that several questions cannot be definitely answered from our present work due to the error margins in our data, and due to the lack of data on the continuous variation of the effective film conductivity with film thickness,



especially at small values of the film thickness. Such data are expected to provide quantitative information about the effect of the inhomogeneous structure of the film/substrate interface and of the film microstructure on the phenomenological aspects of the film thermal behavior (thermal conductivity, interface thermal resistance). Thus, the next step would involve the measurement of  $k_{app}$  versus thickness for a much larger number of thicknesses in the range of 0.2–4  $\mu\text{m}$ .

## VI. CONCLUSIONS

The thermal conductivity of thin dielectric films of optical materials used in high-power laser applications has been measured by using the thermal comparator technique. This technique allows the extraction of the thermal conductivity of the film material and of the film/substrate interfacial thermal resistance in a rapid, inexpensive, and nondestructive manner. The largest error in the data reduction is due to the uncertainty in the value of the heat flow radius. Estimating upper and lower bounds for the heat flow radius allowed the calculation of the film conductivity within a factor of 2. Our results can be easily scaled to accommodate other values of the heat flow radius.

It was found that the thermal conductivity of oxide and fluoride films is as much as two orders of magnitude lower than the thermal conductivity of the corresponding bulk solids, implying that bulk values are inappropriate in the design of thin optical films. The thin film thermal conductivity was found to be not very sensitive to the method of film preparation. The thermal conductivity of the silica films exhibited a strong thickness dependence in the range 0–4  $\mu\text{m}$ . The other films exhibited a weaker dependence of the conductivity on the film thickness. These results are in qualitative agreement with other measurements of the thermal conductivity in metallic and dielectric films. Further work is necessary in order to correlate the film and film/substrate interface microstructure to the measured values of thermal conductivity and interfacial thermal resistance, and to provide a more precise determination of the heat flow radius.

## ACKNOWLEDGMENTS

The authors would like to thank D. J. Smith (LLE), T. Allen (OCLI, Inc.), and A. Steward (AFWL) for the provision of selected coating samples. C. A. Amsden gratefully acknowledges the help and support of Professor J. S. Torok of the Rochester Institute of Technology. S. D. Jacobs acknowledges the help of Professor A. Entenberg of RIT in proofing the manuscript.

This work was supported by the U.S. Air Force under Contract No. F2965088WU164; Optical Coating Laboratory, Inc. of Santa Rosa, CA; the New York State Center for Advanced Optical Technology of the Institute of Optics; the U.S. Department of Energy Division of Inertial Fusion under Agreement No. DE-FC03-85DP40200; and by the Laser Fusion Feasibility Project at the Laboratory for Laser Energetics which has the following sponsors: Empire State Electric Energy Research Corporation, New York State Energy Research and Development Authority, Ontario Hydro, and

the University of Rochester. Such support does not imply endorsement of the content by any of the above parties. The work of J. C. Lambropoulos was also supported by the Office of Naval Research under Grant No. N00014-87-K-0488 and the National Science Foundation under the 1988 Presidential Young Investigator Award No. MSM-8857096.

- <sup>1</sup>D. L. Decker, L. G. Koshigoe, and E. J. Ashley, *NBS Special Publication 727, Laser Induced Damage in Optical Materials: 1984* (Government Printing Office, Washington, DC, 1986), pp. 291–297.
- <sup>2</sup>S. M. J. Ahkter and D. Ristau, "Thermal conductivity of dielectric films and correlation to damage threshold at 1064 nm," edited by H. E. Bennett, A. H. Guenther, D. Milam, and B. E. Newman, presented at the 18th Annual Symposium on Optical Material for High Power Laser, Boulder, CO, 3–5 November 1986.
- <sup>3</sup>A. H. Guenther and J. K. McIver, *Laser Optics for Intracavity and Extracavity Applications* (SPIE, Washington, DC, 1988), Vol. 895, pp. 246–253.
- <sup>4</sup>H. Goldenberg and M. A. Tranter, *Br. J. Appl. Phys.* **3**, 296 (1952).
- <sup>5</sup>J. M. Halley and J. E. Midwinter, *J. Appl. Phys.* **62**, 4055 (1987).
- <sup>6</sup>A. Ono, T. Baba, H. Funamoto, and A. Nishikawa, *Jpn. J. Appl. Phys.* **25**, Part 2, L808 (1986).
- <sup>7</sup>D. Ristau and J. Ebert, *Appl. Opt.* **25**, 4571 (1986).
- <sup>8</sup>C. A. Amsden, S. E. Gilman, S. D. Jacobs, and J. S. Torok, *Optical Interference Coatings*, 1988 Tech. Digest Series (Optical Society of America, Washington, DC, 1988), Vol. 6, pp. 78–81.
- <sup>9</sup>R. W. Powell, *J. Sci. Instrum.* **34**, 485 (1957).
- <sup>10</sup>R. W. Powell, in *Thermal Conductivity*, edited by R. P. Tye (Academic, London, 1969), Part 2, pp. 275–338.
- <sup>11</sup>TC-1000 Thermal Comparator, Lafayette Instrument Company, Lafayette, IN.
- <sup>12</sup>H. S. Carslaw and J. C. Jaeger, in *Conduction of Heat in Solids* (Oxford University Press, London, 1959), Chap. VIII, p. 216.
- <sup>13</sup>C. A. Amsden, MS thesis, Rochester Institute of Technology (1988).
- <sup>14</sup>J. R. Dryden, *J. Heat Trans.* **105**, 408 (1983).
- <sup>15</sup>S. Timoshenko and J. N. Goodier, *Theory of Elasticity*, 2nd ed. (McGraw-Hill, New York, 1951), pp. 372–377.
- <sup>16</sup>M. L. Scott, H. E. Bennett, A. H. Guenther, D. Milam, and B. E. Newman, *Laser Induced Damage in Optical Materials: 1983* (Government Printing Office, Washington, DC, 1985), pp. 329–339.
- <sup>17</sup>G. J. DeSalvo and J. A. Swanson, ANSYS Engineering Analysis System User's Manual, Swanson Analysis System, Inc., 1 June 1985 (unpublished).
- <sup>18</sup>H. Y. Yu, S. C. Sanday, and B. R. Rath, "Film elastic properties determined by the indentation test—Theoretical consideration," Naval Research Laboratory Report, NRL 9168 (12 January 1989).
- <sup>19</sup>*CRC Handbook of Chemistry and Physics* 68th Ed. (CRC, Florida, 1987–1988).
- <sup>20</sup>Y. S. Touloukian, R. W. Powell, C. Y. Ho, and P. G. Klemens, *Thermophysical Properties of Matter, Volume 2, Thermal Conductivity, Non-metallic Solids* (IFI/Plenum Data Corporation, New York, 1970), p. 208.
- <sup>21</sup>E. Fried, in *Thermal Conductivity*, edited by R. P. Tye (Academic, London, 1969), Part 2, pp. 253–273.
- <sup>22</sup>K. H. Guenther, *Appl. Opt.* **23**, 3806 (1984).
- <sup>23</sup>H. K. Pulker and J. Maser, *Thin Solid Films* **59**, 65 (1979).
- <sup>24</sup>M. F. Doerner and W. D. Nix in *CRC Critical Reviews in Solid State and Materials Sciences* (CRC, Boca Raton, FL, 1988), Vol. 14, pp. 225–268.
- <sup>25</sup>H. Windischmann, *J. Appl. Phys.* **62**, 1800 (1987).
- <sup>26</sup>E. T. Swartz and R. O. Pohl, *Appl. Phys. Lett.* **51**, 2200 (1987).
- <sup>27</sup>P. Nath and K. L. Chopra, *Thin Solid Films* **18**, 29 (1973).
- <sup>28</sup>B. T. Boikov, A. T. Pugachev, and V. M. Bratsykhiv, *Thin Solid Films* **17**, 157 (1973).
- <sup>29</sup>T. R. Ogden, A. D. Rathsam, and J. T. Gilchrist, *Mater. Lett.* **5**, 84 (1987).
- <sup>30</sup>S. S. Ballard and J. S. Browder, *CRC Handbook of Laser Science and Technology*, edited by M. J. Weber (CRC, Boca Raton, FL, 1986), Vol. IV, Part 2 in Section 1.1.1.3.
- <sup>31</sup>W. A. Hargreaves, *Laser Focus* **18**, 86 (1982).



## APPENDIX (8)

J. C. Lambropoulos and S.-S. Hwang, Implications of low film thermal conductivity for the laser damage resistance of optical thin films, Electro-Optics and Nonlinear Optics, ed. K.M. Nair, A. S. Bhalla, and E.M. Vogel, Ceramic Transactions, 14, 219-227 (1990).

### IMPLICATIONS OF LOW FILM THERMAL CONDUCTIVITY FOR THE LASER DAMAGE RESISTANCE OF OPTICAL THIN FILMS

John C. Lambropoulos and S.-S. Hwang  
Department of Mechanical Engineering  
University of Rochester  
Rochester, NY 14627

#### ABSTRACT

Recent measurements of the thermal conductivity of thin films of dielectric materials (oxides and fluorides) have shown that the value for thin films (with thickness in the micron and submicron range) may be as much as two orders of magnitude lower than the value for the corresponding bulk solid. We examine the implications of such low values on the laser damage resistance of thin optical films in view of a micromechanics model consisting of an absorbing inclusion embedded within a non-absorbing thin film which is attached to a substrate. Finite element techniques are used to calculate the temperature in the inclusion, in the film's free surface, and along the film/substrate interface.

#### 1. INTRODUCTION

The resistance to laser damage in optical thin films is an important design consideration towards the development of powerful solid-state lasers. Many experimental data on the critical energy density per unit area have been reported by Walker et al.<sup>(1)</sup> for nine dielectric films as a function of laser pulse length (5 and 15 ns), wavelength (1.06, 0.53, 0.35, and 0.26  $\mu\text{m}$ ), and film thickness (1/8 to 2 wavelengths). These data are in the range 1-40 J/cm<sup>2</sup> for the oxide and fluoride films tested<sup>(1)</sup>. Experimental results on laser damage for 1 ns pulses have been reported by Lowdermilk and Milam<sup>(2)</sup> for surfaces of optically polished glass and thin optical films in addition to observations of laser damage in such films. Austin et al.<sup>(3)</sup> have shown that the film's internal stress also influences the laser damage resistance of the film: They reported that the laser damage resistance increases by a factor of 2-3 when the film's internal stress vanishes, and that either tensile or compressive internal stress lead to diminished laser damage resistance. Walker et al.<sup>(4)</sup> have discussed the mechanisms that lead to laser damage in dielectric materials (avalanche ionization, multiphoton absorption, and impurity-initiated damage) and have concluded that the impurity model appears more likely.



According to the impurity model, which has been discussed by Hopper and Uhlmann<sup>[5]</sup> for bulk materials, an absorbing inclusion within a non-absorbing infinite matrix is heated due to the absorption of the incident radiation. The high temperature within the inclusion leads to failure when the temperature reaches some critical value<sup>[5]</sup>. The model uses the solution by Goldenberg and Tranter<sup>[6]</sup> who considered the time-dependent heat conduction due to the absorption of radiation  $Q$  (power per unit volume) within the inclusion of radius  $R$  embedded within the non-absorbing infinite matrix. Due to the dependence of  $Q$  on the radius  $R$  of the inclusion (which absorbs according to the cross section  $R^2$ , so that  $Q$  varies like  $1/R$ ) the laser damage resistance is minimum when the size of the absorbing inclusion is of order  $0.2 \mu\text{m}$ <sup>[4]</sup>.

Further analysis of the absorbing inclusion within the infinite, non-absorbing matrix has been carried out by Lange et al.<sup>[7,8]</sup> who showed that this model leads to an expression for the laser damage resistance of the form

$$E_0 = \frac{16}{\pi} T_c (\rho c k t)^{1/2} \quad (1)$$

where  $E_0$  is the value of the critical energy density per unit area,  $T_c$  is the critical temperature at failure (typically the melting point of the host), and  $\rho$ ,  $c$ ,  $k$  are the density, heat capacity, and thermal conductivity of the host material (i.e. the matrix) and  $t$  is the duration of the laser pulse. In the work by Lange et al.<sup>[7,8]</sup> bulk values were used for the thin film thermal conductivity.

Although the density and heat capacity of thin films are close to the values for the bulk materials, this is not the case for the thermal conductivity of thin films. Guenther and McIver<sup>[9]</sup> have recently discussed the measurement and the effect of the thermal conductivity of thin films in view of recent experimental measurements which show that the thermal conductivity of thin films can be considerably lower than the thermal conductivity of the corresponding bulk solid. The discussion by Guenther and McIver<sup>[9]</sup> is based on eqn. (1) once the host thermal conductivity is identified with the value for the film. Thus, the question is raised of whether or not eqn. (1) is applicable to thin films of very low thermal conductivity, in view of the fact that eqn. (1) has been derived for an inclusion within an infinite matrix, so that other effects such as the proximity of the inclusion to the free surface, the proximity to the film/substrate interface, the size of the inclusion, or the film thickness do not enter the model.

Recent work by Lambropoulos et al.<sup>[10]</sup> at the Laboratory for Laser Energetics at the University of Rochester has used a modified thermal comparator method to measure in-situ the thermal conductivity of a large variety of optical thin films (oxides and fluorides) deposited on Si or sapphire substrates. The method is quick and non-destructive. It is based on the work of Powell<sup>[11]</sup>, and operates on the principle that when a heated tip touches a cooler solid, the temperature at the tip soon reaches a steady state value which depends on the thermal conductivity of the solid in contact with the tip. The method also allows the determination of the interfacial thermal resistance  $R_{int}$ , defined as the temperature drop per unit power



flux across the film/substrate interface. Typical values for the thermal conductivity  $k_F$  of submicron thin films are in the range 0.04 to 1 W/m/K for oxide films, and in the range 0.08 to 0.75 W/m/K for fluoride films. Some of these values are two orders of magnitude lower than the corresponding bulk values for the same material. Typical values of the interfacial thermal resistance are in the range 0 to 2.7 K/(W/mm<sup>2</sup>).

It is the objective of this report to discuss some of the implications of the low values for the film thermal conductivity on the laser damage resistance of such films, and in particular to discuss the applicability of the scaling expressed in eqn. (1) for film/substrate assemblies involving submicron thin films of low thermal conductivity. We will show that when the film thermal conductivity is low, the model of Goldenberg and Tranter [6] which treats the host as infinite does not properly account for the low film thermal conductivity and for the proximity of the inclusion to the substrate. Thus, the predictions of such a model, encapsulated in the failure criterion of eqn. (1), must be viewed with caution, especially in comparing such predictions to experimental data.

## 2. MODEL OF ABSORBING INCLUSION EMBEDDED WITHIN FILM

Consider a spherical inclusion of radius  $R$  embedded within a film of thickness  $H$ , such that the center of the inclusion is at a distance  $D$  below the free surface of the film which is assumed to be insulated. The film is supported on a semi-infinite substrate as shown in Fig. 1. The subscripts "F", "I", and "S" identify the film, inclusion, and substrate, respectively. At time  $t \geq 0$  the inclusion absorbs power at the rate  $Q$  per unit volume, whereas the film and substrate do not absorb any incident radiation. The temperature and the heat flux are assumed to be continuous at all interfaces and to decay to zero sufficiently far from the inclusion.

For the case of the inclusion embedded within an infinite matrix, Goldenberg and Tranter [6] have shown that the temperature distribution has a sigmoidal time dependence, being low at small times and achieving its maximum value at steady state ( $t \rightarrow \infty$ ). The steady state solution is given by (here we identify the matrix or host material with the film material)

$$\begin{aligned} T &= \frac{R^2 Q}{k_I} \left( \frac{1}{3} \frac{k_I}{k_F} + \frac{1}{6} \left( 1 - \frac{r^2}{R^2} \right) \right), \quad r < R \\ T &= \frac{1}{3} \frac{R^2 Q}{k_F} \frac{R}{r}, \quad r > R \end{aligned} \quad (2)$$

where  $r$  is the spherical radial coordinate measuring from the center of the absorbing sphere. It is clear that such a model cannot account for the proximity of the inclusion to a free surface or to a film/substrate interface, nor can it account for a film/substrate geometry where the inclusion is within an insulating film which is deposited on a conducting substrate.



To account for these effects, we assumed  $R=H/5$  (since inclusions of 0.2 micron size give the least damage resistance and typical film thickness is 1 micron), and we used finite elements to solve the time-dependent heat conduction equations

$$\begin{aligned} k_I \nabla^2 T_I + Q &= (\rho c)_I \frac{\partial T_I}{\partial t}, \quad r < R \\ k_F \nabla^2 T_F &= (\rho c)_F \frac{\partial T_F}{\partial t}, \quad r > R, \quad -(H-D) < z < D \\ k_S \nabla^2 T_S &= (\rho c)_S \frac{\partial T_S}{\partial t}, \quad z < -(H-D) \end{aligned} \quad (3)$$

where  $z$  is the axial coordinate in a cylindrical system with origin in the center of the inclusion, and  $\nabla^2$  is the axisymmetric Laplacian operator in the cylindrical coordinates  $r$ , and  $z$ . Note that  $r^2 = r_1^2 + z^2$ . The initial condition for the temperature is  $T(r_1, z, t=0)=0$ . As boundary conditions we assume that the film's free surface at  $z=D$  is insulated, and that the temperature and heat flux is continuous at the surface of the inclusion and at the film/substrate interface. For the finite element solution we also assumed that the ratio of the thermal diffusivities  $d=k/(\rho c)$  is equal to the ratio of the thermal conductivities.

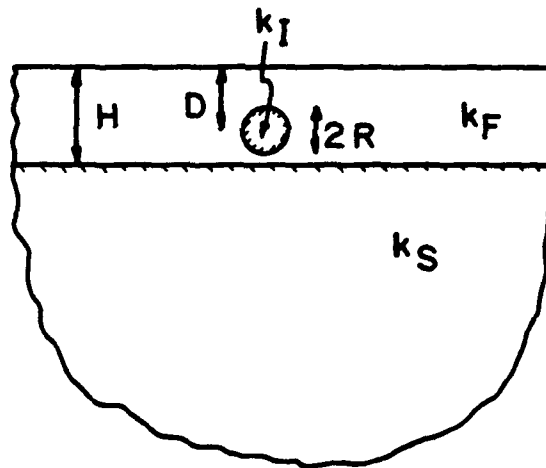


Figure 1. The geometry of a film of thickness  $H$  containing an absorbing spherical inclusion of radius  $R$ . A cylindrical coordinate system has origin in the center of the inclusion. The film's free surface is located at  $z=D$  (assumed insulated). The film/substrate interface is located at  $z=-(H-D)$ .



The numerical solution showed that the time dependence of the temperature distribution still has the characteristic sigmoidal shape and that the steady state gives the largest temperature values. Figure 2 shows the variation of the steady state temperature (measured in units of  $QR^2/2k_s$ ) at the center of the inclusion vs. the nondimensional ratio of film to substrate thermal conductivity for several values of the ratio of inclusion to substrate thermal conductivity. The dashed lines show the steady state temperature in the center of the inclusion as determined by the model of Goldenberg and Tranter, eqn. (2).

We observe that the infinite matrix results are in good agreement with the numerical results for the inclusion embedded within the film, see Figure 1, when  $k_f/k_s$  is of order unity. This would be the usual case were the film conductivity the same as the corresponding bulk value. When  $k_f/k_s \ll 1$ , the infinite matrix results overestimate the temperature as determined from the more accurate numerical model. When the inclusion is very conducting,  $k_f/k_s \gg 1$ , the expressions of eqn. (2) overestimate the temperature in the inclusion. It is thus seen that the model of Goldenberg and Tranter<sup>[6]</sup> as used by Lange et al.<sup>[7,8]</sup>, on which the scaling law of eqn. (1) is based, is not accurate when the film thermal conductivity is low compared to that of the substrate, and that the model of the inclusion in the infinite matrix does not always accurately describe the actual temperature in the inclusion even though the matrix is identified with the film material.

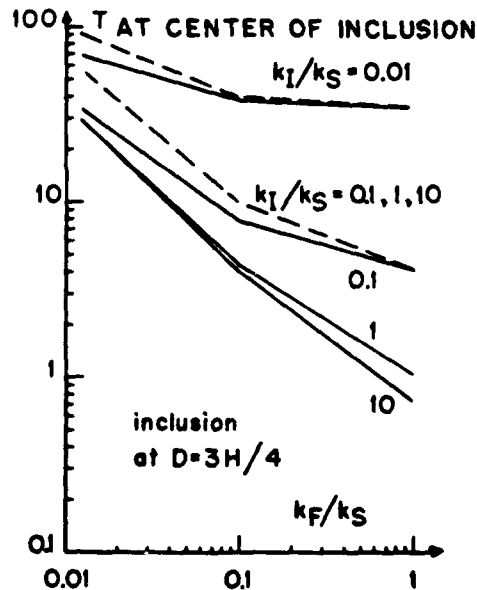


Figure 2. Steady state temperature in the center of the inclusion (measured in units of  $QR^2/2k_s$ ) vs. the ratio of film to substrate thermal conductivity for several values of the inclusion thermal conductivity. The dashed lines correspond to eqn. (2) by Goldenberg and Tranter<sup>[6]</sup> for the absorbing inclusion within the infinite matrix. The solid lines are from the finite element solution.



Figure 3 shows the steady state temperature at the center of the film/substrate interface immediately below the inclusion. The result from the infinite matrix model is shown as calculated via eqn. (2) with the identification  $r=H-D>R$ . When compared to the numerical results, it is seen that this model overestimates the temperature at the center of the interface. The numerical result suggests that the temperature at the interface is not only low (as compared to the inclusion temperature), but it is also fairly independent of the film thermal conductivity. Thus, the experimentally measured low values for the thermal conductivity of thin films are not expected to affect significantly the temperature along the interface. In this context, we note the observation of Lowdermilk and Milam [2] that no correlation was found between the damage threshold and coating adhesion.

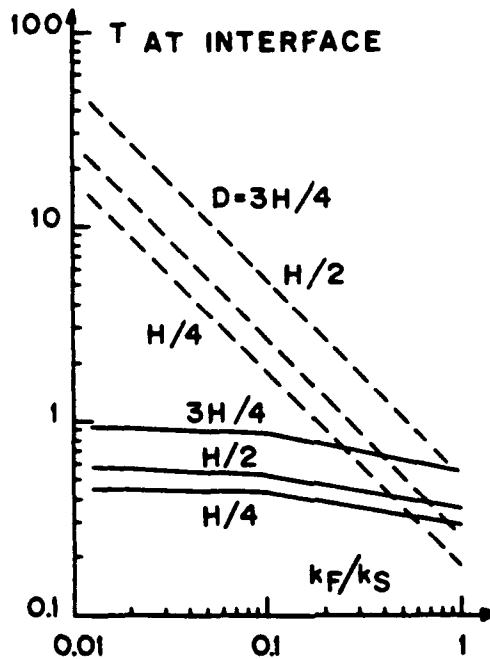


Figure 3. Steady state temperature in the center of the film/substrate interface  $r_1=0, z=-(H-D)$  (measured in units of  $QR^2/2k_S$ ) vs. the ratio of film to substrate thermal conductivity for several locations of the inclusion below the film's free surface. The inclusion thermal conductivity varies from  $k_I/k_S=0.01$  to 10. The dashed lines correspond to eqn. (2) by Goldenberg and Tranter [6] for the absorbing inclusion within the infinite matrix. The solid lines are from the finite element solution.

On the other hand, Figure 4 shows that the steady state temperature in the center of the film's free surface depends considerably on the film thermal conductivity, and that it may increase by two orders of magnitude when the film thermal conductivity is reduced by the same amount. The proximity of the inclusion to the free surface also plays a crucial role in view of the insulated boundary at  $z=D$ . The temperature can increase by an order of magnitude when the inclusion is moved from  $D=3H/4$  to  $H/4$ . Comparison of Figure 2 to Figure 4 shows that another implication of low



film thermal conductivity is that the temperature in the free surface becomes comparable to the temperature in the center of the inclusion when  $k_F \ll k_S$ . This is not the case when the film conductivity is comparable to that of the substrate. Thus, the present numerical model suggests that the film's free surface is another location where excessive temperatures may lead to laser damage, especially when the inclusion is situated near the free surface. We also note that the free surface temperature from the infinite matrix model, see eqn. (2), shows approximately the same dependence on  $k_F$  as the more accurate numerical solution.

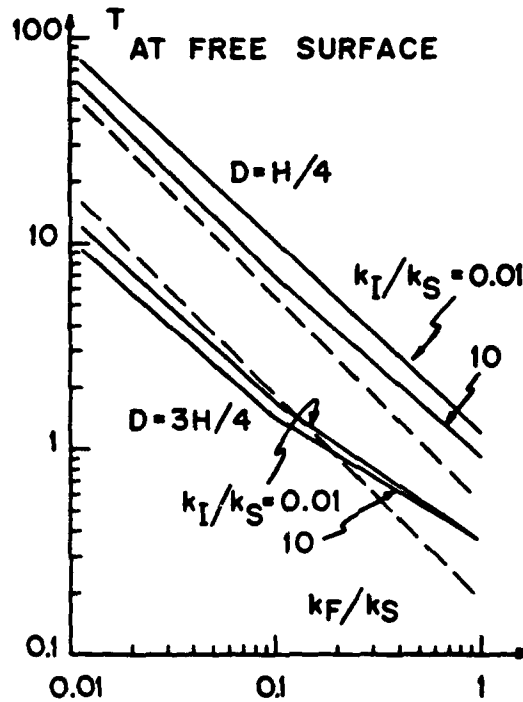


Figure 4. Steady state temperature in the center of the film's free surface at  $r_1=0$ ,  $z=D$  (measured in units of  $QR^2/2k_S$ ) vs. the ratio of film to substrate thermal conductivity for several locations of the inclusion below the film's free surface. The inclusion thermal conductivity varies from  $k_I/k_S=0.01$  to 10. The dashed lines correspond to eqn. (2) by Goldenberg and Tranter<sup>[6]</sup> for the absorbing inclusion within the infinite matrix. The solid lines are from the finite element solution.

### 3. CONCLUSIONS

The very low values for the thermal conductivity of dielectric thin films imply that the predictions of the model of an absorbing inclusion embedded within a non-absorbing infinite matrix, and specifically eqn. (1) for the scaling of the critical energy density at damage with the film's conductivity, may not be accurate. Nevertheless, such a scaling establishes the importance of the film thermal conductivity in determining the laser damage resistance. Eqn. (2) or Figures 2-4



show that the temperature in the inclusion is very high when the film material has a low thermal conductivity compared to the substrate. When the thermal conductivity of the film is comparable to that of the substrate, then the model leading to eqn. (1) is accurate. In addition to the inclusion, the present work also identifies the importance of the free film surface as a possible site for damage when the film conductivity is low, and when the inclusion is located near the free surface of the film.

The more accurate model presented in this report accounts for the thickness of the film, for the proximity of the absorbing inclusion to the free surface and to the film/substrate interface, as well as for the different thermal conductivities of the film, inclusion, and substrate materials. The results presented refer to steady state temperatures which are known to be the largest. In that sense, the discrepancy discussed above between the model of the inclusion within the infinite matrix and the more accurate numerical model accounting for the presence of the film is largest under steady state conditions. Since laser damage is a time dependent phenomenon, it is clear that the variation of the temperature with time must be explicitly accounted in addition to the film thickness, inclusion size, and low film thermal conductivity in a manner analogous to the work of Lange et al. [7,8].

#### ACKNOWLEDGEMENTS

This work was supported by the U.S. Air Force under contract F2965088WU164; Optical Coating Laboratory, Inc. of Santa Rosa, CA; the New York State Center for Advanced Optical Technology of the Institute of Optics; the U.S. Department of Energy Division of Inertial Fusion under agreement No. DE-FC03-85DP40200; and by the Laser Fusion Feasibility Project at the Laboratory for Laser Energetics which has the following sponsors: Empire State Electric Energy Research Corporation, New York State Energy Research and Development Authority, Ontario Hydro, and the University of Rochester. Such support does not imply endorsement of the content by any of the above parties.

The authors also acknowledge the support of the National Science Foundation under the Presidential Young Investigator Award MSM-8857096 and of the Office of Naval Research under Grant N-00014-87-K-0488.

#### REFERENCES

1. T.W. Walker, A.H. Guenther, and P.E. Nielsen, Pulsed laser-induced damage to thin-film optical coatings-Part I: Experimental, IEEE J. Quantum Electronics, QE-17, 2041 (1981).
2. W.H. Lowdermilk and D. Milam, Laser-induced surface and coating damage, IEEE J. Quantum Electronics, QE-17, 1888 (1981).
3. R.R. Austin, R. Michaud, A.H. Guenther, and J. Putman, Effects of structure, composition, and stress on the laser damage threshold of homogeneous and inhomogeneous single films and multilayers, Appl. Optics, 12, 665 (1973).



4. T.W. Walker, A.H. Guenther, and P.E. Nielsen, Pulsed laser-induced damage to thin-film optical coatings-Part II: Theory, IEEE J. Quantum Electronics, QE-17, 2053 (1981).
5. R.W. Hopper and D.R. Uhlmann, Mechanism of inclusion damage in laser glass, J. Appl. Phys., 41, 4023 (1970).
6. H. Goldenberg and C.J. Tranter, Heat flow in an infinite medium heated by a sphere, Brit. J. Appl. Phys., 3, 296 (1952).
7. M.R. Lange, J.K. McIver, and A.H. Guenther, The influence of the thermal and mechanical properties of optical materials in thin film form on the damage resistance to pulsed lasers, Thin Solid Films, 118, 49 (1984).
8. M.R. Lange, J.K. McIver, and A.H. Guenther, Pulsed laser damage in thin film coatings: fluorides and oxides, Thin Solid Films, 125, 143 (1985).
9. A.H. Guenther and J.K. McIver, The role of thermal conductivity in the pulsed laser damage sensitivity of optical thin films, Thin Solid Films, 163, 203 (1988).
10. J.C. Lambropoulos, M.R. Jolly, C.A. Amsden, M. Sinicropi, D. Diakomihalis, and S.D. Jacobs, Thermal conductivity of dielectric thin films, J. Appl. Phys., 66, 4230 (1989).
11. R.W. Powell, Thermal conductivity determinations by thermal comparator methods, in: Thermal Conductivity, vol. 2, p. 276 (ed. R.P. Tye), Academic Press, New York (1969).



# APPENDIX (9)

HTD-Vol. 184, Thin Film Heat Transfer:  
Properties and Processing  
ASME 1991

## THERMAL CONDUCTIVITY OF THIN FILMS: MEASUREMENT AND MICROSTRUCTURAL EFFECTS

J. C. Lambropoulos

Department of Mechanical Engineering  
Laboratory for Laser Energetics

S. D. Jacobs

Laboratory for Laser Energetics

S. J. Burns

Department of Mechanical Engineering

L. Shaw-Klein

Department of Mechanical Engineering  
Laboratory for Laser Energetics

S.-S. Hwang

Department of Mechanical Engineering  
University of Rochester  
Rochester, New York

### ABSTRACT

We review the thermal comparator method and its application to the measurement of the thermal conductivity of thin films with thickness in the sub-micron range. The technique measures the apparent thermal conductivity of a film/interface/substrate composite by recording the temperature drop when a heated tip comes into contact with the film's free surface, and by comparing to a set of bulk standards of known conductivity. The main result has been that the thermal conductivity of thin films for a large variety of materials (oxides, fluorides, nitrides, amorphous metals, and superconductors with thickness of 0.2-1.0  $\mu\text{m}$ ) may be as much as two orders of magnitude lower than that of the corresponding bulk solid, and that a significant interfacial thermal resistance may develop. To explain the reduced film thermal conductivity, we have considered microstructural effects that may be modelled with continuum assumptions (porosity and columnar film microstructure) and phonon scattering. For the case of AlN, we consider the effect of phonon scattering due to the interaction with the phonon mean free path with the film thickness and with impurities. We also discuss the implications of reduced film thermal conductivity for the laser damage resistance of thin dielectric films via the model of the absorbing inhomogeneity. The main conclusion is that bulk thermal conductivity data are not applicable to designs using thin films, and that a database is required for thin film thermal conductivity measurements.

### INTRODUCTION

Many electronic, optical, and optoelectronic devices have layered microstructures. Examples are laser diodes, transistors and integrated circuits, and multilayer dielectric thin film laser mirrors. During use in an electronic or optical system, heat generated within these layered structures must be rapidly removed to prevent element failure. This problem has become much more severe recently, due to (1) the increase in speed of electronic devices (which implies in most cases a much higher power dissipation, i.e., more heat being

generated and the need to remove it), and (2) the emergence of high-power, short-pulse lasers.

The removal of heat from bulk components like power transistors, integrated circuits, or solid metal laser mirrors is straightforward. For the former, 0.3-mm thick silicone pads containing highly conductive ceramic fillers like boron nitride, magnesium oxide, or aluminum oxide, serve as heat transfer agents to heat sinks. The conductivities of these pads are on the order of 3 W/m-K, which is within a factor of three of ceramic alumina. For the latter, subsurface channels allow coolant under high pressure to remove heat from the metal mirror surface. The conductivities of water and copper are 0.5 W/m-K and 500 W/m-K, respectively. Heat removal from thin, dielectric multilayers is another matter entirely.

In 1984, Decker et al. (1986) reported the measurement of thermal conductivity of free-standing thin films of  $\text{SiO}_2$  and  $\text{Al}_2\text{O}_3$ . Values were found to be one or two orders of magnitude lower than those for the corresponding bulk materials (see Table 1). The authors attributed this difference to the unique microstructure of dielectric thin films, which prevents them from exhibiting bulk-like properties. When deposited with physical deposition methods like sputtering or evaporation, these films are best described as somewhat inhomogeneous, anisotropic, and either polycrystalline or amorphous. Columnar growth is often observed. These films may also contain voids, pinholes, and nodular defects, which reduce the density and integrity of the film. The result is a reduced phonon mean free path and lower thermal conductivity. A number of films have been examined to date, and the trend is summarized in Table 1.

In a recent review, Guenther and McIver (1988) discuss implications for multilayer dielectric thin film laser mirrors, which are derived from the relation between the areal energy density at damage  $E_d$  and the material properties of the thin film

$$E_d \sim T_c \sqrt{\rho c k l_p} \quad (1)$$

where  $T_c$  is the temperature level at damage (typically the melting point of the film material),  $\rho$  is the density,  $c$  the heat capacity per



unit mass,  $k$  the thermal conductivity of the film, and  $t_p$  the laser pulse length that causes damage. Relation (1) results from the work of Goldenberg and Tranter (1952) who analyzed the time dependent heat transfer due to a spherical absorbing inclusion embedded within an infinite nonabsorbing matrix. Although the heat capacity and density of optical thin films are close to the properties of the bulk solids (Decker et al., 1986), this is not the case for the thermal conductivity which, being considerably lower for thin films, leads to lower values of the damage threshold energy densities. Thus, models that account for thermal transport in thin film structures may have no predictive value if they employ bulk thermal conductivity data. For example, lack of film conductivity data imposes serious limitations on heat dissipation models in optical elements and arrays (Halley and Midwinter, 1987).

Current optical recording technologies involve laser marking of thin organic or metal films, laser-heating induced local phase changes, and thermomagnetic recording. Laser marking is a melt/ablate process, whereas thermomagnetic recording involves a change in the direction of magnetization in a film. All involve the absorption of laser radiation to bring a local area of the film above some threshold energy per unit volume, where the "writing process" occurs.

In this application it is often desirable to maximize the local temperature induced by the laser, thereby accelerating the writing process. Much numerical modeling work is done to understand lateral heat flow in thin films, for this defines the size of "bits" of information recorded by the process. Edge definition is an especially important concern.

A survey of the current literature is given below. It reveals a strong interest in the thermal conductivity of thin layers, and a glaring lack of hard thermal conductivity data for thin metal, polymer, and dielectric films. This survey does not include all film thermal conductivity measurements to date; it merely shows the necessity of measuring and understanding the range of thin film thermal conductivity for a large variety of technical applications.

In their finite element analysis of blister formation and thermal stress, Evans and Nkansah (1988) and Nkansah and Evans (1990) used "assumed" values for the thermal conductivities of a 100-nm dye-polymer layer (0.2 W/m-K) and a 30-nm tellurium layer (1.5 W/m-K). Both were taken from the literature for bulk solids.

Anderson (1990) estimated the total thermal conductivity for sputtered rare-earth-transition-metal films (30–100 nm thick) from electrical conductivity measurements, and from a comparison with known amounts of laser power required to record in the medium. The result... "Values estimated in this way are approximately one order of magnitude smaller than those of the bulk constituents of the films".

Koyanagi et al. (1989) developed... "a new estimation method for thermal conductivity of the thin-film recording media... The estimated thermal conductivity of the film recording media was found to be 50% lower than that of the bulk." No explanation was given; the reproducibility of the result was not discussed.

Bartholomew (1989) addressed both the uncertainty in thermal conductivity data and the lack of knowledge regarding resistance to heat flow at film-substrate interfaces. The author concluded that, at present "... The thermal properties of thin film

layers are, in general, unknown; but they can be treated as adjustable parameter and estimated from the results of marking experiments".

In a 1990 review of x-ray lithography, Maldonado (1990) stressed the importance of high thermal conductivity, high hardness, and high stiffness for the mask used to absorb x rays. Each mask currently consists of an absorbing pattern on a free standing 5- $\mu$ m thick boron-doped silicon membrane film. This mask is resistant to x-ray damage, but is otherwise inferior to possible alternatives like boron nitride, silicon carbide, or diamond. The thermal conductivities that can be achieved in these alternative thin film materials will, in part, determine their success in replacing B-doped Si.

Most techniques utilized to measure the thermal conductivity of thin solid films are difficult and time consuming. For example, Decker's technique (1986) included the application of thermocouples to free-standing films. Ono et al. (1986) developed a technique for measuring the thermal conductivity of diamond films, which involved the application of black paint to the front and rear surfaces of the free-standing film sample.

Tai et al. (1988) developed a complex silicon microbridge structure to evaluate the lateral thermal conductivity of liquid phase chemical vapor deposition (LPCVD) polycrystalline silicon films that were 1.5  $\mu$ m thick. They obtained a value of 32 W/m-K, a lower number than the bulk values of ~150 W/m-K, which will effect the future design of polycrystalline silicon-bridge flow sensors.

Morelli et al. (1988) grew polycrystalline diamond films with hot-filament assisted CVD. They etched away the silicon substrate, mounted the free-standing films in a cryostat, and measured film thermal conductivities at room temperature that were comparable to a type 1a natural diamond (100 W/m-K). This prompted them to promote the broad industrial use of these low cost films for thermal management in "... any application requiring good heat conductivity".

Saenger (1989) used an interferometric calorimetric method to measure thin film diffusivity of 5- $\mu$ m and 10- $\mu$ m thick polyimide polymer films bonded to optically transparent glass substrate. The author constructed special surface and subsurface coatings to properly deposit, heat, and reflect a probe beam from the sample film. The author's technique required a displacement to be measured, which was on the order of a few angstroms. Saenger's motivation was the search for improved nondestructive methods for studying thermal properties of thin films.

There are other complex optical approaches (Ristau and Ebert, 1986). When applied to free-standing films, such techniques do not allow the estimation of any interfacial thermal properties, such as the interfacial thermal resistance, which are expected to become increasingly important as the films become thinner.

Cahill et al. (1989) and Swartz (1987) have discussed techniques for measuring the thermal resistance of interfaces. These techniques essentially use as thermometers electrically heated strips which have been deposited onto a substrate. Cahill et al. (1989) have observed that the presence of a thin amorphous SiO<sub>2</sub> layer (with thicknesses in the range 7 to 115 nm) on various substrates greatly increased the boundary resistance. They found that in the temperature range 2–50 K the film thermal conductivity is considerably lower than that of the bulk amorphous SiO<sub>2</sub>. However, for greater temperatures, the conductivity of the film approached that of the substrate. The



effect of thin amorphous layers on the boundary resistance has been discussed by Matsumoto et al. (1977) who showed that the thermal resistances of films in series do not necessarily add due to the fact that phonons (i.e. elastic vibrations) of different frequencies contribute differently to the total thermal conductivity (which includes contributions from phonons of all frequencies lower than some upper limit). These works (Cahill et al., 1989; Swartz, 1987; Matsumoto et al., 1977) among others (to be discussed in the sequel) have convincingly shown that the basic reason for the reduced film conductivity is the scattering of phonons from the film boundaries. However, the precise dependence of the film conductivity on the film thickness has not been discussed.

The measurement of thermal conductance for thin films has been so specialized that it has not been possible to construct any reliable database. Modelling to optimize the design of multilayer structures, either by changing the types of materials or their microstructure, has not occurred. Yet it is reasonably expected that the method of film deposition, the rate of film growth, and the substrate temperature could all be modified to improve thermal properties of films. A lack of analytical instrumentation has prevented this work from beginning.

In this report we briefly review the thermal comparator technique (Powell, 1969) as it applies to the measurement of the thermal conductivity of thin films. This technique is non-destructive, rapid, and inexpensive, and it has been used by Lambropoulos et al. (1989) for the measurement of conductivities of thin dielectric films in the micron and submicron range. Section 1 reviews and summarizes the basic principles of the thermal comparator. Some more recent measurements on ceramic, metallic, and superconducting thin films are reported. Section 2 presents several models which are used to understand the diminished thermal conductivity of thin films. These models are categorized into continuum effects (such as porosity and grain microstructure) and into phonon scattering effects (inclusions, dislocations, stacking faults, grain boundaries). Section 3 shows the effect of the reduced film thermal conductivity for the specific problem of laser damage resistance of thin dielectric films used for optical applications. All these effects clearly show that the thermal conductivity of thin films is reduced as compared to that of the corresponding bulk solid, and that the use of bulk data is inappropriate when heat transfer in thin films is considered.

## 1. MEASUREMENT OF THE THERMAL CONDUCTIVITY OF THIN FILMS WITH THE THERMAL COMPARATOR

The thermal comparator was originally developed for the measurement of the thermal conductivity of bulk solids. A comprehensive review has been published by Powell (1969). The application of the thermal comparator to the measurement of the conductivity of thin films has been described in detail by Lambropoulos et al. (1989). The principle of operation is as follows: An assembly terminating in a probe tip (of diameter approximately 320  $\mu\text{m}$ ) is heated to about 20 degrees above ambient. The tip is brought into contact with a half-space which is maintained at room temperature. The steady-state drop in the temperature of the tip with respect to that of the rest of its assembly is measured by a thermocouple. The temperature drop is directly related to the thermal conductivity of the half-space which can be measured in this manner. The largest contribution to the experimental error is the heat flow radius of the area of contact between the tip and the specimen, which

is expected to lie in the range of 30-180  $\mu\text{m}$ . The value used for the extraction of the thin film thermal conductivities reported below was 100  $\mu\text{m}$  (Lambropoulos, 1989).

Table 2 shows bulk and thin film thermal conductivities for various systems. These measurements illustrate the effects of microstructure on thermal conductivity. Microstructural effects will be further discussed in the next section.

The results on the oxides and fluorides are from Lambropoulos et al. (1989). These films are dielectric and used as optical thin films. The data for AlN are from Shaw-Klein et al. (1991), and show the large effect of boundary scattering and inclusions. This effect is manifest in a markedly lower thermal conductivity for thinner films.

The data for the amorphous metal films show the effect of the columnar microstructure. Since the films are conductive, the thermal conductivity in the film plane (denoted by "par") can be measured via the Wiedemann-Franz law (Anderson, 1990) which states that for metallic solids the thermal conductivity is proportional to the electrical conductivity. These data are compared with data from the thermal comparator, which measures the thermal conductivity normal to the plane of the film (denoted with "per"). The high degree of anisotropy resulting from the columnar microstructure is clear. The table also shows a superconducting thin film.

These results all show the typical lowering of thin film thermal conductivity as compared to the bulk values. The correlation between the diminished film thermal conductivity and the film microstructure will be discussed in the next section.

**TABLE 1: Thermal conductivity of selected bulk materials**

Materials	k(W/m-K)
Diamond (I and II)	1200-2300
Cu (polycrystalline)	200-500
Si (single crystal)	150
Al <sub>2</sub> O <sub>3</sub> (single crystal)	35
Al <sub>2</sub> O <sub>3</sub> (sintered)	20
Many oxides and fluorides, bulk solids	1.0 to 10
Oxide and fluoride films, nominally 1 $\mu\text{m}$ thick	0.05 to 1.0
Air	0.025



**TABLE 2: Measured thermal conductivity of various thin films**

Film material	Microstructure	Thickness ( $\mu\text{m}$ )	$k_{\text{film}}$ (W/ m-K)	$k_{\text{bulk}}$ (W/ m-K)
$\text{SiO}_2$	Amorphous	0.50-2.0	0.4-1.1	1.2-10.7
$\text{TiO}_2$	-	0.50-2.0	0.5-0.6	7.4-10.4
$\text{ZrO}_2$	-	0.15-0.47	0.04	
$\text{Al}_2\text{O}_3$	-	0.17-0.46	0.72	20-46
$\text{MgF}_2$	-	0.21-0.58	0.58	15-30
$\text{AlN}$	Dense, polycrystalline	<0.15 0.25-1.0	0.5 16	70-180
Tb-Fe compound	dense, amorphous	0.25-1.0	5.3 (par) 7.0 (per)	30-40
Tb-Fe compound	columnar, amorphous	0.25-1.0	0.3 (par) 4.3 (per)	
$\text{YBa}_2\text{Cu}_3\text{O}_7$	crystalline	0.25-1.0	0.1-0.2	8-10

Notice that (par) denotes the conductivity parallel to the film, and (per) perpendicular to the film.

## 2. MICROSTRUCTURAL EFFECTS IN FILM THERMAL CONDUCTIVITY

All of the thermal resistance mechanisms in bulk materials are also present in thin films. In thin films, however, there are often more defects than are typically seen in bulk solids. These defects lower the thermal conductivity below expected values.

The defects are roughly divided into two categories: defects whose effects can be treated using continuum models (for example, film porosity and film columnar microstructure) and those which must be treated using models for phonon (or electron) scattering.

### A. CONTINUUM EFFECTS

#### Porosity effects

The density of conventionally deposited (sputtered or evaporated) thin films is often lower than that of bulk materials. An example of the familiar columnar microstructure which often results from physical vapor deposition (Movchan and Demchishin, 1969; Thornton 1974, 1977; Messier, 1986) is shown in Fig. 1. Voids between the columns account for much of the decreased density. Chemical vapor deposited films (CVD) are often denser, although their dendritic growth pattern can also lead to lowered densities. Finally, sol-gel films, which originate as liquids spun or dipped onto substrates and subsequently dried, are even more porous, and may even exhibit open porosity, see Fig. 2. Messier (1986) has pointed out that the microstructural features of thin films (voids, columns) can

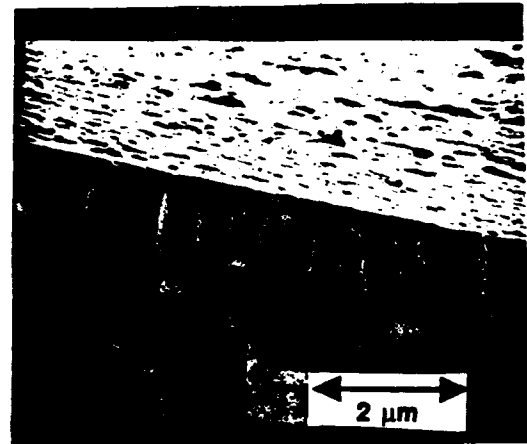


**FIGURE 1:** Scanning electron micrograph of a thin film of an amorphous metal exhibiting the columnar microstructure.

no longer be described as individual entities; instead, they must be described by distribution functions. For example, for low adatom mobility, a fractal model can be used to describe the natural clustering occurring during the aggregation of atoms.

Many models account for the effect of porosity on thermal conductivity. For example, Maxwell (1904) showed that for a dilute concentration (volume fraction  $p$ ) of a dispersed phase of inclusions of spherical shape and of conductivity  $k_i$  embedded within a continuous matrix of conductivity  $k_m$ , the thermal conductivity  $k$  of the composite is given by



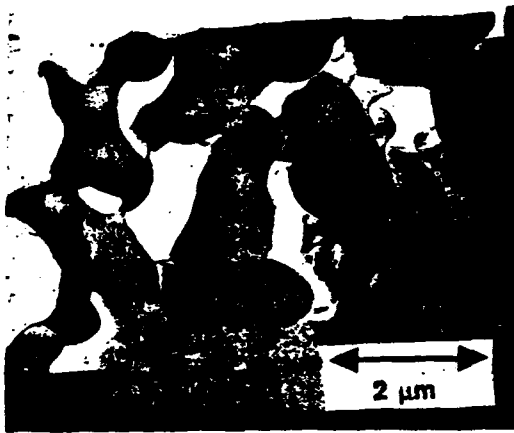


FIGURE 2: Scanning electron micrograph of a thin amorphous sol-gel film of  $\text{SiO}_2$  exhibiting open porosity.

$$\frac{k}{k_m} = \frac{\frac{k_i}{k_m} + 2 - 2p \left(1 - \frac{k_i}{k_m}\right)}{\frac{k_i}{k_m} + 2 + p \left(1 - \frac{k_i}{k_m}\right)} \quad (2)$$

The effect of finite concentration for spherical dispersed phase has been considered by Brailsford and Major (1964), and by Budiansky (1970) who used effective medium theory. According to this theory, an individual sphere of the dispersed phase is embedded within an infinite medium of the (as yet undetermined) thermal conductivity  $k$ . The result is

$$\frac{p}{2 + \frac{k_i}{k}} + \frac{1-p}{2 + \frac{k_m}{k}} = \frac{1}{3} \quad (3)$$

The analysis of Budiansky (1970), which is applicable to more than two phases, shows that the matrix can be seen as an inclusion of volume fraction  $(1-p)$ . Hashin and Shtrikman (1962) derived bounds for the thermal conductivity of the composite. Their result is identical to that in eqn (2). However, Hashin and Shtrikman (1962) show that the result of eqn (2) is an upper bound for  $k$  when  $k_m > k_i$  (and a lower bound for  $k_m < k_i$ ).

Schulz (1981) has developed a general expression for the thermal conductivity of a solid containing inclusions of various shapes. The result of Schulz is applicable to the case of dispersions of spheres, or of parallel and series arrangements of the phases. For spherical inclusions, the result is

$$1-p = \left(\frac{k_m}{k}\right)^{1/3} \frac{k_i - k}{k_i - k_m} \quad (4)$$

If the porosity in the film is due to spaces between columns, randomly distributed pores may not be an accurate model. Instead, we treat the porosity as slabs of bulk material (columns) separated by slabs of air (porosity). Using the analogy of parallel or series resistors,  $k$  normal to the columns (i.e. parallel to the film plane) is

$$\frac{1}{k_{\perp}} = \frac{p}{k_i} + \frac{1-p}{k_m} \quad (5a)$$

whereas parallel to the columns the result is

$$k_{\parallel} = p k_i + (1-p) k_m \quad (5b)$$

The predictions of eqns (2)-(5) are shown in Fig. 3. Notice that eqn (2) is actually an upper bound for the dependence of  $k/k_m$  on  $p$  for spherically shaped dispersions, according to Hashin and Shtrikman (1962). The result for  $k_{\parallel}$  exceeds that of eqn (2) because the arrangement of the dispersed inclusions used in deriving eqn (5b) for  $k_{\parallel}$  is obviously that of slabs rather than that of spheres.

Pores of shapes other than spherical have been considered by Reynolds and Hough (1957), by Rocha and Acrivos (1972, 1973) for dilute suspensions, by Redondo and Beery (1986) and by Miloh and Benveniste (1988) for cracked solids.

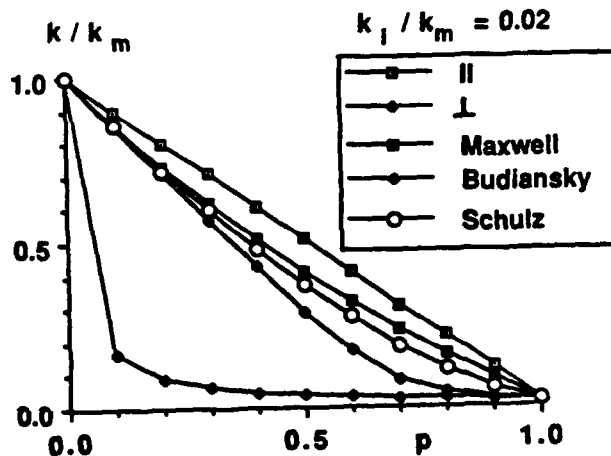


FIGURE 3: The ratio of film to bulk thermal conductivity vs. film porosity  $p$  according to various models.  $\perp$  denotes the direction normal to the columns comprising the film microstructure (i.e. parallel to the film plane).  $\parallel$  denotes the direction parallel to the columns (i.e. normal to the film plane).



## Columnar effects

From the discussion above, it is clear that columnar structures, which often result from physical vapor deposition, not only lower the thermal conductivity of the film, but also introduce anisotropic effects.

Even if the columns are touching and porosity effects discussed above are ignored, we can expect a decrease in film thermal conductivity due to the interfacial thermal resistance  $R_{col}$  of the column contacts. Treating the film as a composite made up of columnar grains, the anisotropic thermal conductivity is now given by

$$\frac{k(\phi)}{k_m} = \frac{\frac{k_{\perp}}{k_m}}{\frac{R_{col} k_m}{D} \frac{k_{\perp}}{k_m} + 1} \sin^2 \phi + \frac{k_{\parallel}}{k_m} \cos^2 \phi \quad (6)$$

where  $D$  is the grain diameter,  $\phi=0$  is the direction parallel to the column (i.e. normal to the film), and  $k_{\perp}$ ,  $k_{\parallel}$  are given by eqn (5).

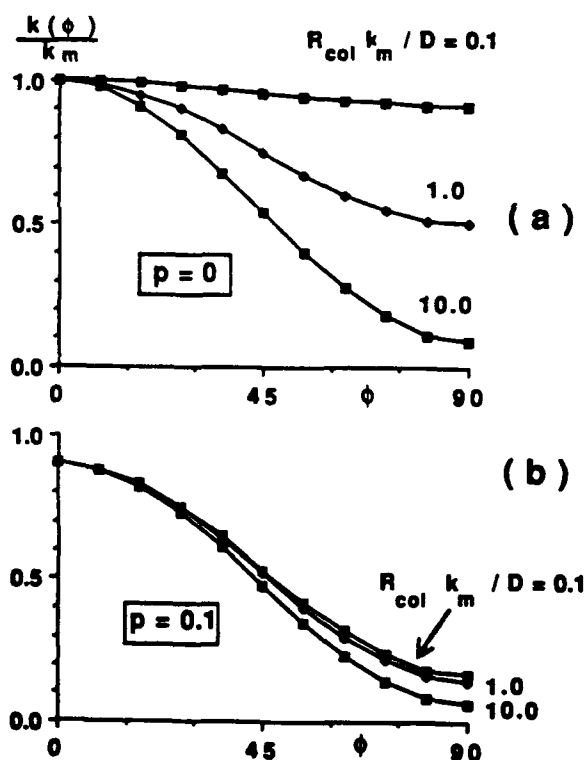


FIGURE 4: The ratio of film to bulk thermal conductivity vs. angle away from the column axis. For low levels of porosity, the columnar microstructure introduces anisotropy. For larger amounts of porosity, the anisotropy is due to the porosity itself.

Figure 4 shows the dependence of  $k(\phi)/k_m$  on the angle  $\phi$ . It is seen that for small porosity, the effect of  $R_{col}$  is significant, see Fig. 4A. As soon as the porosity takes a small but non-zero value, the effect of the interfacial resistance  $R_{col}$  becomes small due to the fact that the thermal resistance due to the porosity exceeds that due to the contacts between different grains.

Although it was assumed in deriving eqn (6) that the columns are perfectly perpendicular to the interface, this may not be necessarily so. Models of film growth suggest that the grains have a distribution of directions, and this is consistent with Messier's observations (1986).

Another way to treat the effect of columnar structure on heat flow is to consider the scattering of heat carriers (phonons or electrons) from column surfaces, from interfaces, or from other defects. These heat carriers are referred to as quasi-particles in the brief explanation that follows.

## B. QUASIPARTICLE SCATTERING EFFECTS

Some heat resistance sources, for example impurity atoms, can not be accurately modeled using a continuum approach. In such cases, it is useful to envision heat flow resistance arising from the scattering of electrons or phonons (i.e. lattice vibrations). The theory of the thermal conductivity of solids from the point of view of quasiparticle scattering has been extensively discussed by Klemens (1955; 1958; 1969) who has expanded on Peierls' theory of thermal conductivity of bulk solids, and by Klemens and Williams (1986) for metals.

Phonons and electrons can be treated similarly as particles of momentum proportional to their frequency. In general, the total thermal conductivity of a system can be expressed as (Kingery et al., 1976)

$$k = k_e + k_p + k_r \quad (7)$$

where  $k_e$  is the thermal conductivity due to electronic charge carrier transport (which vanishes for dielectric materials),  $k_p$  is the thermal conductivity due to the lattice vibrations (phonons), and  $k_r$  the thermal conductivity due to radiation (negligible for most materials at room temperature).

The quasiparticle contributions to thermal conductivity depend on their specific heat per unit volume  $C$ , velocity  $v$ , and mean free path  $\lambda$ , as follows (Klemens, 1958)

$$k = \frac{1}{3} \int_0^\infty c(\omega) v(\omega) \lambda(\omega) d\omega \quad (8)$$

where  $c(\omega)d\omega$  is the contribution to the specific heat per unit volume  $C = \int c(\omega)d\omega$  from particles with frequencies in the range  $\omega$  to  $\omega+d\omega$ . Debye's approximation is often used according to which phonons have frequencies only in the range from 0 to the Debye frequency  $\omega_D$  so that the upper limit in eqn (8) is set to  $\omega_D$ . According to Debye's theory (Reissland, 1973)



$$c(\omega) = \frac{3 k_B}{2 \pi^2 v^3} \left( \frac{k_B T}{h/2\pi} \right)^2 \frac{x^4 e^x}{(e^x - 1)^2}, \quad x = \frac{h \omega}{2 \pi k_B T} \quad (9)$$

where  $T$  is the absolute temperature,  $h$  is Planck's constant, and  $k_B$  is Boltzmann's constant. The Debye frequency  $\omega_D$  is related to the Debye temperature  $\theta_D$  via  $\theta_D = h\omega_D/(2\pi k_B)$ . For phonons, the velocity  $v$  is the same as the speed of sound in the solid.

While the specific heat of thin films is generally unchanged from its bulk value, the mean free path  $\lambda$  is governed by the interaction of the particles with each other and with microstructural imperfections or defects. These changes are expressed in terms of changes in the scattering event relaxation time  $\tau$ , which is defined as the time for a perturbation from an equilibrium value to decay back to the equilibrium value (Klemens, 1958; 1969). The relaxation time  $\tau$  is related to the mean free path  $\lambda$  by

$$\tau = \lambda / v \quad (10)$$

where  $v$  is the particle velocity. When several types of interactions are at work, the relaxation rates rather than times add as

$$\frac{1}{\tau} = \sum_i \frac{1}{\tau_i} \quad (11)$$

Notice that, in the presence of several scattering mechanisms, eqn (11) shows that the mechanism with the fastest scattering time will dominate the overall relaxation time.

Once the total relaxation time is computed, the phonon thermal conductivity is found via eqns (8)-(10) as (Klemens, 1958; 1969)

$$k = \frac{k_B}{2 \pi^2 v} \left( \frac{k_B T}{h/2\pi} \right)^3 \int_0^{\theta_D/T} \tau(x) \frac{x^4 e^x}{(e^x - 1)^2} dx \quad (12)$$

In this way, if the dependence of the relaxation time on the phonon frequency is known, eqn (12) provides the dependence of the phonon conductivity on the absolute temperature  $T$  and on the details of the scattering imperfection. In the absence of any imperfections, the only scattering is of phonons by other phonons due to the anharmonic nature of the bonding between atoms (Reissland, 1973). For example, for scattering of phonons off other phonons so that the total momentum is not conserved (termed Umklapp or U-processes), the relaxation time is given by (Klemens, 1958; Parrott and Stuckes, 1975)

$$\tau_U^{-1} = A x^2 T^4 \exp(-B/T) \quad (13)$$

where  $A$ ,  $B$  are material parameters,  $B$  being proportional to the Debye temperature of the solid. These constants are often treated as empirical constants, which can be determined by fitting the temperature dependence of the thermal conductivity of the perfect bulk crystal to an expression of the form shown in eqns (12) and (13). For the perfect crystal, eqns (12)-(13) predict that at low

temperatures ( $T/\theta_D \ll 1$ ) the intrinsic phonon thermal conductivity increases with diminishing temperature like  $T^3 \exp(B/T)$ ,  $B$  being a material constant, whereas at high temperatures ( $T/\theta_D \gg 1$ ) it decreases with temperature like  $1/T$ .

Based on perturbation theory, theoretical scattering relaxation times have been calculated for several types of microstructural imperfections (Klemens, 1955; 1958). For boundary scattering, the relaxation time due to phonon scattering off external surfaces (e.g. the film surface or the film/substrate interface) or internal surfaces (grain or boundary scattering) is given by

$$\tau_g^{-1} = \frac{v}{d} \quad (14)$$

where  $d$  is the dimension defining the boundaries, i.e. the film thickness or the grain size. Casimir (1938) showed that for long, rectangular grains  $d$  is nearly equal to the square cross section's side, whereas for long, cylindrical grains  $d$  is the grain diameter.

As an example of the application of eqns (11)-(14), we calculate the effect of film thickness on the thermal conductivity of AlN at room temperature as compared to the value of bulk, single crystal AlN. For the bulk solid  $k=320$  W/m-K,  $\theta_D=950$  K (Dinwiddie and Onn, 1990). For the bulk single crystal, the intrinsic thermal conductivity is governed by the relaxation time  $\tau_U$  for Umklapp processes given by eqn (13). In this case, the constants are approximately  $A=10 \text{ s}^{-1} \text{ K}^{-4}$  and  $B=160$  K (Dinwiddie and Onn, 1990). On the other hand, for a thin film of AlN, the relaxation time has contributions from Umklapp scattering and grain boundary scattering, eqn (14), where the length scale  $d$  is identified with the film thickness  $t$ . Fig. 5 shows the dependence on the film thickness  $t$  of the film thermal conductivity relative to that of the bulk single crystal. It is immediately clear that for submicron thin films the thermal conductivity is a strong function of film thickness, in agreement with the experimental results discussed in the previous section.

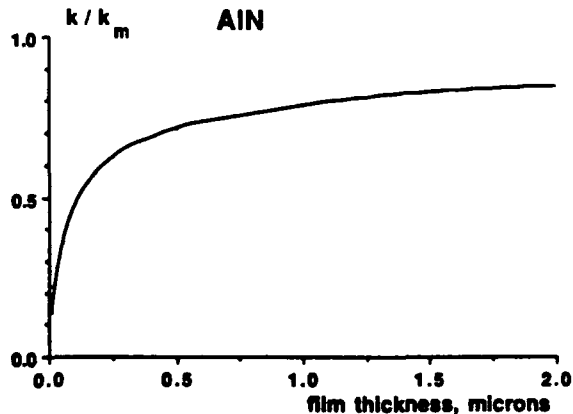


FIGURE 5: Predictions of a model accounting for phonon scattering due to the presence of a thin film of AlN. The model gives the variation of the thermal conductivity at room temperature of a thin AlN film with thickness.  $k_m$  is the conductivity of bulk single crystal AlN.



Impurity atoms also scatter phonons strongly. The effect of impurity atoms consists of three contributions: due to the mass difference between the impurity and solvent atoms, due to the strain created by the size difference, and due to the difference in binding energy (Klemens, 1955; Parrott and Stuckes, 1975). The relaxation time is given by an expression of the form

$$\tau_i^{-1} = I x^4 T^4 \quad (15)$$

where the parameter  $I$  incorporates the effects mentioned above, and  $x$  is given by eqn (9). The dominant effect in the parameter  $I$  is due to the mass difference between an impurity atom and the solvent atom. The impurity effect is considerable; experiments (Dinwiddie and Onn, 1990) have shown that there is a large drop in the thermal conductivity of AlN due to small amounts of oxygen impurities which replace nitrogen in the AlN lattice. This effect is shown in Fig. 6, which was derived for bulk AlN on the basis of eqns (12) and (15). In thin film deposition (sputtering or evaporation) the impurity concentration is controlled by impurities present in the vacuum chamber during deposition. Such impurities are often minimized by sufficiently lowering the deposition backing pressure and by keeping the chamber free of organic contaminants. Careful control often results in thin films of very high purity and theoretically high thermal conductivity.

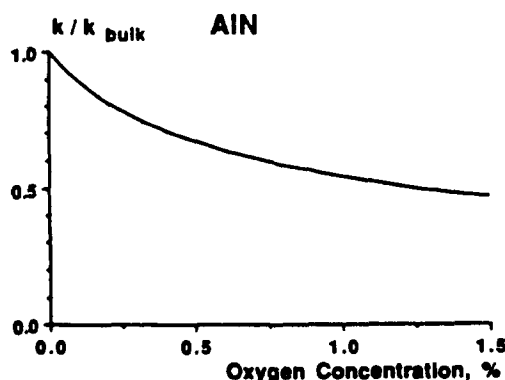


FIGURE 6: Predictions of a model accounting for phonon scattering due to impurities. The model gives the variation of the thermal conductivity of AlN at room temperature with the concentration of impurities (for AlN the impurity is oxygen).

The contribution of dislocations and stacking faults to thermal resistance may be low compared to other defects at room temperature. Still, they often appear in thin films, and they may dominate the relaxation time in the absence of other defects. For a random array of screw dislocations (Klemens, 1955)

$$\tau_d^{-1} = 0.033 N_d b^2 \gamma_0 \omega \quad (16)$$

where  $N_d$  is the dislocation density,  $b$  the Burgers vector, and  $\gamma_0$  the Gruneisen constant, a material parameter which measures the deviation of the lattice bonds from being derived via a purely harmonic potential. The Gruneisen constant is typically between 1 and 2 for many solids (Klemens and Williams, 1986). It is expected

that phonon scattering from dislocations will be important in epitaxial thin films resulting from molecular beam epitaxy or liquid phase epitaxy. Such films are often characterized by large densities of misfit dislocations when the film thickness exceeds some critical value. Klemens (1955) has also calculated the relaxation times for arrays of edge dislocations, stacking faults, and tilt grain boundaries.

### 3. LASER DAMAGE OF OPTICAL THIN FILMS

The resistance to laser damage in optical thin films is an important design consideration towards the development of powerful solid-state lasers. Many experimental data on the critical energy density per unit area have been reported by Walker et al. (1981a) for nine dielectric films as a function of laser pulse length (5 and 15 ns), wavelength (1.06, 0.53, 0.35, and 0.26  $\mu\text{m}$ ), and film thickness (1/8 to 2 wavelengths). These data are in the range 1–40 J/cm<sup>2</sup> for the oxide and fluoride films tested. Experimental results on laser damage for 1 ns pulses have been reported by Lowdermilk and Milam (1981) for surfaces of optically polished glass and thin optical films in addition to observations of laser damage in such films. Walker et al. (1981b) have discussed the mechanisms that lead to laser damage in dielectric materials (avalanche ionization, multiphoton absorption, and impurity-initiated damage) and have concluded that the impurity model appears more likely.

According to the impurity model, which has been discussed by Hopper and Uhlmann (1970) for bulk materials, an absorbing inclusion within a non-absorbing infinite matrix is heated due to the absorption of the incident radiation. The high temperature within the inclusion leads to failure when the temperature reaches some critical value. The model uses the solution by Goldenberg and Tranter (1952) who considered the time-dependent heat conduction due to the absorption of radiation  $q$  (power per unit volume) within the inclusion of radius  $R$  embedded within the non-absorbing infinite matrix. Due to the dependence of  $q$  on the radius  $R$  of the inclusion (which absorbs according to the cross section  $R^2$ , so that  $q$  varies like  $1/R$ ) the laser damage resistance is minimum when the size of the absorbing inclusion is of order 0.2  $\mu\text{m}$  (Lange et al., 1984; 1985).

Further analysis of the absorbing inclusion within the infinite, non-absorbing matrix has been carried out by Lange et al. (1984; 1985) who showed that this model leads to the expression for the laser damage resistance of eqn (1), thus establishing the importance of the thermal conductivity of the host material within which the absorbing inclusion is embedded. Still, the question is raised of whether or not eqn. (1) is applicable to thin films of very low thermal conductivity, in view of the fact that eqn. (1) has been derived for an inclusion within an infinite matrix, so that other effects such as the proximity of the inclusion to the free surface, the proximity to the film/substrate interface, the size of the inclusion, or the film thickness do not enter the model.

Consider a spherical inclusion of radius  $R$  embedded within a film of thickness  $H$ , such that the center of the inclusion is at a distance  $D$  below the free surface of the film which is assumed to be insulated. The film is supported on a semi-infinite substrate as shown in Fig. 7. The subscripts "F", "I", and "S" identify the film, inclusion, and substrate, respectively. At time  $t=0$  the inclusion absorbs power at the rate  $q$  per unit volume, whereas the film and substrate do not absorb any incident radiation. The temperature and



the heat flux are assumed to be continuous at all interfaces and to decay to zero sufficiently far from the inclusion.

For the case of the inclusion embedded within an infinite matrix, Goldenberg and Tranter (1952) have shown that the temperature distribution has a sigmoidal time dependence, being low at small times and achieving its maximum value at steady state (when the time  $t \rightarrow \infty$ ). The effect of the film conductivity on the steady state values of the temperature has been discussed by Lambropoulos and Hwang (1990).

We used finite elements to solve the time-dependent heat conduction equations

$$\begin{aligned} k_I \nabla^2 T_I + q &= (\rho c)_I \frac{\partial T_I}{\partial t}, \quad r < R \\ k_F \nabla^2 T_F &= (\rho c)_F \frac{\partial T_F}{\partial t}, \quad r > R, \quad -(H-D) < z < D \\ k_S \nabla^2 T_S &= (\rho c)_S \frac{\partial T_S}{\partial t}, \quad z < -(H-D) \end{aligned} \quad (17)$$

where  $z$  is the axial coordinate in a cylindrical system  $(r, z)$  with origin in the center of the inclusion, and  $\nabla^2$  is the axisymmetric Laplacian operator in the cylindrical coordinates  $r, z$ . Note that  $r^2 = r_1^2 + z^2$ . The initial condition for the temperature is  $T(r, z, t=0) = 0$ . As boundary conditions we assume that the film's free surface at  $z=D$  is insulated, and that the temperature and heat flux is continuous at the surface of the inclusion and at the film/substrate interface. For the finite element solution we also assumed that the ratio of the thermal diffusivities  $d=k/(\rho c)$  is equal to the ratio of the thermal conductivities.

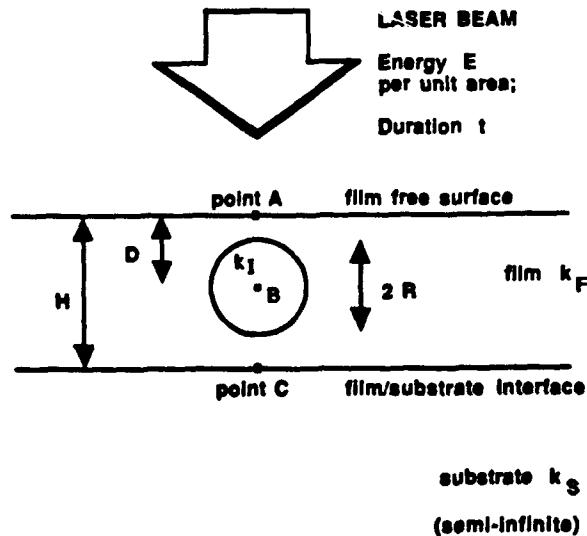


FIGURE 7: The geometry of a thin film containing an embedded inclusion. Only the inclusion absorbs the incident radiation. The rate of power absorption per unit volume in the inclusion is  $q$ .

Fig. 8 shows the temperature evolution with time when the film is insulating ( $k_F/k_S=0.01$ ) or has the same conductivity as the substrate. In Fig. 8 the inclusion is conducting (thus modeling a metallic inclusion,  $k_I/k_S=1$ ), has a radius  $R=H/5$ , and is located at  $D=H/4$  below the free surface of the film. The power absorbed per unit volume  $q$  can be converted to energy absorbed per unit area  $E$  by assuming that the inclusion absorbs in proportion to its cross-sectional area so that

$$q = \frac{3}{4} \frac{E}{tR} \quad (18)$$

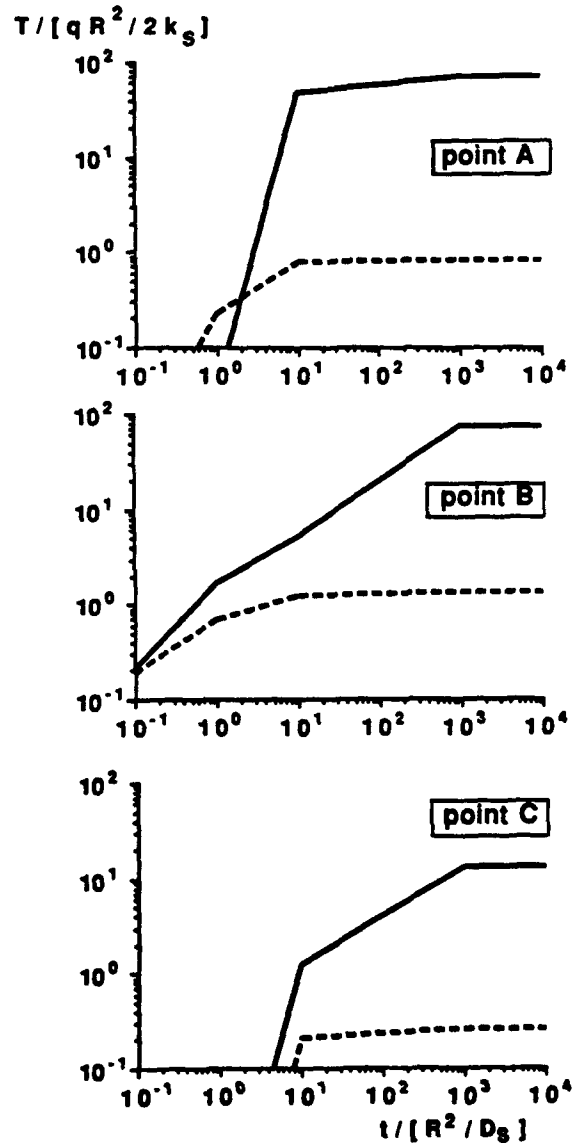


FIGURE 8: Variation with time of the temperature at the free surface (point A), the center of the inclusion (point B), and the film/substrate interface (point C). The inclusion is located at  $D=H/4$ , and its size is  $R=H/5$ . The inclusion has  $k_I/k_S=1$ . The solid lines (—) correspond to  $k_F/k_S=0.01$  (i.e. low film thermal conductivity). The dashed lines (---) correspond to  $k_F/k_S=1$ .



where  $t$  is the time elapsed from the beginning of the pulse. Thus, the temperature is effectively measured in units of  $3 E R / (8 t k_f)$ .

It is clear from Fig. 8 that the effect of a reduced film thermal conductivity is significant at points on the free surface (point A), inside the inclusion (point B), and at the film-substrate interface (point C). However, the effect of reduced  $k_f$  becomes significant only after certain times. For example, using  $D_S = 2E-4 \text{ m}^2/\text{s}$  (typical of Si), an inclusion size  $R = 0.1 \text{ }\mu\text{m}$ , and a pulse length of 1 ns, the non-dimensional time  $t/(R^2/D_S)$  is such that the effect of the reduced film conductivity is significant. For these parameters, and using  $E = 1 \text{ J/cm}^2$ , a value of 1 for the non-dimensional temperature corresponds to an actual temperature of about 3,750 K.

Fig. 8 also shows that the temperature at the film/substrate interface (point C) is much lower than that at the inclusion center or the film free surface. This implies that a significant temperature gradient develops within the film, whereas the temperatures at the substrate remain low. Of course, the use of a more insulating substrate will increase the interfacial temperature.

#### 4. CONCLUSIONS

The thermal comparator is well suited to the measurement of the thermal conductivity of thin films of a variety of materials. Such measurements are required in order to estimate the rate of heat removal from configurations involving thin films. The data in Table 2 show that the thermal conductivity of thin films is not a material property; indeed, the thermal conductivity is a property that is strongly influenced by microstructural defects such as porosity, grain microstructure, impurities, dislocations, and stacking faults. In addition, the presence of length scales which are comparable to the phonon mean free path, makes the thermal conductivity depend on these length scales. As an example, the analysis of the thermal conductivity of AlN shows clearly the effect of film thickness and impurity content.

The thermal conductivity is calculated in terms of an integral over all phonon frequencies which involves the combined relaxation time for all scattering events. Since the total relaxation time is the geometric mean of the individual relaxation times, all these mechanisms interact with each other, thus inducing a complex dependence of the film conductivity on the details of the individual scattering mechanisms.

An important consequence of this interaction is that thermal resistances may not simply add when several geometries involving thin films are arranged in parallel. This is due to the fact that the phonon density within a thin film may not be in thermal equilibrium, and that only phonons of low frequency are allowed to pass to the substrate. This idea has been discussed by Matsumoto et al. (1977) and by Cahill et al. (1989).

Both phonon scattering models and experimental data for thin film thermal conductivity show that bulk values are clearly inappropriate. Thus, a database is necessary containing the thermal conductivity of thin films for a variety of thicknesses and for a variety of microstructural features. The thermal comparator is inexpensive, rapid, non-destructive and thus convenient for carrying out such measurements. The current design of the comparator can only measure film/substrate specimens at room temperature. Since the temperature dependence of the thermal conductivity also provides

important microstructural information at temperatures lower than the Debye temperature, this proposed database should also contain the temperature as a parameter.

#### ACKNOWLEDGEMENTS

This work was supported by the U.S. Department of Energy Division of Inertial Fusion under agreement No. DE-FC03-85DP40200, and by the Laser Fusion Feasibility Project at the Laboratory for Laser Energetics which has the following sponsors: Empire State Electric Energy Research Corporation, New York State Energy Research and Development Authority, Ontario Hydro, and the University of Rochester. The work was also sponsored by Texaco. Such support does not imply endorsement of the content by any of the above parties.

The authors also acknowledge the support of the National Science Foundation under the Presidential Young Investigator Award MSM-8857096 and of the Office of Naval Research under Grant N-00014-87-K-0488.

#### REFERENCES

- Anderson, R.J., 1990, "The thermal conductivity of rare-earth-transition-metal films as determined by the Wiedemann-Franz law", *Journal of Applied Physics*, vol. 67, p. 6914.
- Bartholomeusz, B.J., 1989, "Thermomagnetic marking of rare-earth-transition-metal thin films", *Journal of Applied Physics*, vol. 65, p. 262.
- Brailsford, A.D. and K. G. Major, K.G., 1964, "The thermal conductivity of aggregates of several phases, including porous materials", *British Journal of Applied Physics*, vol. 15, p. 313.
- Budiansky, B., 1970, "Thermal and thermoelastic properties of isotropic composites", *Journal of Composite Materials*, vol. 4, p. 286.
- Cahill, D.G., Fischer, H.E., Klitsner, T., Swartz, E.T. and Pohl, R.O., 1989, "Thermal conductivity of thin films: measurements and understanding", *Journal of Vacuum Science and Technology*, vol. A7, p. 1259.
- Casimir, H.B.G., 1938, "Note on the conduction of heat in crystals", *Physica*, vol. 5, p. 495.
- Decker, D.L., Koshigoe, L.G., and Ashley, E.J., 1986, "Thermal properties of optical thin film materials", *NBS Special Publication 727, Laser Induced Damage in Optical Materials: 1984*, p. 291, Government Printing Office, Washington, DC.
- Dinwiddie, R.B. and Onn, D.G., 1990, "Temperature dependence of the thermal conductivity of materials for microelectronic packaging: measuring and modelling effects of microstructure and impurities", in *Advanced Electronic Packaging Materials*, Materials Research Society Symposium Proceedings, vol. 167, ed. A. T. Barfknecht et al., p. 241, MRS, Pittsburgh.
- Evans, K.E. and Nkansah, M.A., 1988, "Finite element analysis of thermal stresses in optical storage media", *Journal of Applied Physics*, vol. 64, p. 3398.
- Nkansah, M.A. and Evans, K.E., 1990, "Modeling delamination due to thermal stress in optical storage media", *Journal of Applied Physics*, vol. 67, p. 3242.



Goldenberg, H. and Tranter, M.A., 1952, "Heat flow in an infinite medium heated by a sphere", *British Journal of Applied Physics*, vol. 3, p. 296.

Guenther, A.H. and McIver, J.K., 1988, "The role of thermal conductivity in the pulsed laser damage sensitivity of optical thin films", *Proceedings of Society of Photo-instrumentation Engineers* (SPIE), vol. 895, p.246.

Halley, J.M. and Midwinter, J.E., 1987, "Thermal analysis of optical elements and arrays on thick substrates with convective cooling", *Journal of Applied Physics*, vol. 62, p. 4055.

Hashin, Z. and Shtrikman, S., 1962, "A variational approach to the theory of the effective magnetic permeability of multiphase materials", *Journal of Applied Physics*, vol. 33, p. 3125.

Hopper, R.W. and Uhlmann, D.R., 1970, "Mechanism of inclusion damage in laser glass", *Journal of Applied Physics*, vol. 41, p. 4023.

Kingery, W.D., Bowen, H.K., and Uhlmann, D.R., 1976, *Introduction to Ceramics*, 2nd ed., John Wiley, New York.

Klemens, P.G., 1955, "The scattering of low-frequency lattice waves by static imperfections", *Proceedings of the Physical Society*, vol. 68, p. 1113.

Klemens, P.G., 1958, "Thermal conductivity and lattice vibrational modes", in *Solid State Physics*, vol. 7, ed. F. Seitz and D. Turnbull, Academic Press, New York, p. 1.

Klemens, P.G., 1969, "Theory of the thermal conductivity of solids", in *Thermal Conductivity*, vol. 1, ed. R. P. Tye, Academic Press, New York, p. 1.

Klemens, P.G. and Williams, R.K., 1986, "Thermal conductivity of metals and alloys", *International Metals Reviews*, vol. 31, p. 197.

Koyanagi, H., Ito, T., Miyamoto, N., Sato, Y., and Ando, H., 1989, "Optical and thermal analyses on multilayered thin films of a phase-change optical recording disk", *Journal of Applied Physics*, vol. 66, p. 1045.

Lange, M.R., McIver, J.K., and Guenther, A.H., 1984, "The influence of the thermal and mechanical properties of optical materials in thin film form on the damage resistance to pulsed lasers", *Thin Solid Films*, vol. 118, p. 49.

Lange, M.R., McIver, J.K., and Guenther, A.H., 1985, "Pulsed laser damage in thin film coatings: fluorides and oxides", *Thin Solid Films*, vol. 125, p. 143.

Lambropoulos, J.C., Jolly, M.R., Amsden, C.A., Sinicropi, M., Diakomihalis, D., and Jacobs, S.D., 1989, "Thermal conductivity of dielectric thin films", *Journal of Applied Physics*, vol. 66, p. 4230.

Lambropoulos, J.C. and Hwang, S.-S., 1990, "Implications of low film thermal conductivity for the laser damage resistance of optical thin films", in *Electro-Optics and Nonlinear Optic Materials*, Ceramic Transactions vol. 14, ed. K. M. Nair, A. S. Bhalla, and E. M. Vogel, American Ceramic Society, p. 219.

Lowdermilk, W.H. and D. Milam, D., 1981, "Laser-induced surface and coating damage", *IEEE Journal of Quantum Electronics*, vol. QE-17, p. 1888.

Maldonado, J.A., 1990, "X-Ray lithography, where it is now, and where it is going", *Journal of Electronic Materials*, vol. 19, p. 699.

Matsumoto, D.S., C. L. Reynolds, C.L. Jr., and A. C. Anderson, A.C., 1977, "Thermal boundary resistance at metal-epoxy interfaces", *Physical Review*, vol. B16, p. 3303.

Maxwell, J.C., 1904, *A Treatise on Electricity and Magnetism*, Clarendon Press, Oxford, p. 435.

Messier, R., 1986, "Toward quantification of thin film morphology", *Journal of Vacuum Science and Technology*, vol. A4, p. 490.

Miloh, T. and Benveniste, Y., 1988, "A generalized self-consistent method for the effective conductivity of composites with ellipsoidal inclusions and cracked bodies", *Journal of Applied Physics*, vol. 63, p. 789.

Morelli, D.T., Beetz, C.P., and Perry, T.A., 1988, "Thermal conductivity of synthetic diamond films", *Journal of Applied Physics*, vol. 65, p. 3063.

Movchan, B.A. and Demchishin, A.V., 1969, *Fiz. Met. Metalloved.*, vol. 28, p. 653 (in Russian).

Ono, A., Baba, T., Funamoto, H., and Nishikawa, A., 1986, "Thermal conductivity of diamond films synthesized by microwave plasma CVD", *Japanese Journal of Applied Physics*, vol. 25, p. L808.

Parron, J.E. and Stuckes, A.D., 1975, *Thermal Conductivity of Solids*, Pion Limited, London, pp. 44-122.

Powell, R.W., 1969, "Thermal conductivity determinations by thermal comparator methods", in *Thermal Conductivity*, vol. 2, ed. R. P. Tye, Academic Press, New York, p. 276.

Redondo, A. and Beery, J.G., 1986, "Thermal conductivity of optical coatings", *Journal of Applied Physics*, vol. 60, 3882.

Reissland, J.A., 1973, *The Physics of Phonons*, John Wiley, London, p. 117.

Reynolds, J.A. and Hugh, J.M., 1957, "Formulae for dielectric constants of mixtures", *Proceedings of the Physical Society*, vol. B70, p. 769.

Ristau, D. and Ebert, J., 1986, "Development of a thermographic laser calorimeter", *Journal of Applied Optics*, vol. 25, p. 4571.

Rocha, A. and Acrivos, A., 1972, "On the effective thermal conductivity of dilute dispersions, general theory for inclusions of arbitrary shape", *Quarterly Journal of Mechanics and Applied Mathematics*, vol. 26, p. 217.

Rocha, A. and Acrivos, A., 1973, "On the effective thermal conductivity of dilute dispersions, highly conducting inclusions of arbitrary shape", *Quarterly Journal of Mechanics and Applied Mathematics*, vol. 26, p. 441.

Saenger, K.L., 1989, "An interferometric calorimeter for thin-film thermal diffusivity measurements", *Journal of Applied Physics*, vol. 65, p. 1447.

Schulz, B., 1981, "Thermal conductivity of porous and highly porous materials", *High Temperature-High Pressure*, vol. 13, p. 649.

Shaw-Klein, L., Burns, S.J., and Jacobs, S.D., 1991, "Thermal conductivity of aluminum nitride thin films", in *Electronic Packaging Materials Science*, ed. E. D. Lillie et al., Materials Research Society Symposium Proceedings, vol. 203, MRS, Pittsburgh, (to be published).

Swartz, E.T., 1987, "Solid-solid thermal boundary resistance", Ph. D. thesis, Cornell University.

Tai, Y.C., Mastrangelo, C.H., and Muller, R.S., 1988, "Thermal conductivity of heavily doped low-pressure chemical vapor deposited polycrystalline silicon films", *Journal of Applied Physics*, vol. 63, p. 1442.

Thornton, J.A., 1974, "Influence of apparatus geometry and deposition conditions on the structure and topography of thick sputtered coatings", *Journal of Vacuum Science and Technology*, vol. 11, p. 666.

Thornton, J.A., 1977, "High rate thick film growth", in *Annual Review in Materials Science*, vol. 7, ed. R. A. Huggins et al., p. 239.



Walker, T.W., Guenther, A.H., and Nielsen, P.E., 1981a,  
"Pulsed laser-induced damage to thin-film optical coatings-Part I:  
Experimental", *IEEE Journal of Quantum Electronics*, vol. QE-17, p.  
2041.

Walker, T.W., Guenther, A.H., and Nielsen, P.E., 1981b,  
"Pulsed laser-induced damage to thin-film optical coatings-Part II:  
Theory", *IEEE Journal of Quantum Electronics*, vol. QE-17, p.  
2053.